Probing the Structure-Property Relationships of Metal Oxide Nanocatalysts

A Dissertation Presented for the

Doctor of Philosophy

Degree

The University of Tennessee, Knoxville

Sreya Paladugu

August 2023

© by Sreya Paladugu, 2023
All Rights Reserved.

Dedication

I dedicate this work to my parents.

Acknowledgements

I would like to thank my advisor, Dr. Katharine Page, for being an amazing mentor. Her guidance, dedication and encouragement throughout my graduate career have been instrumental to my growth as a scientist, and as an individual, and have made this work possible. The time I have spent in her research group has been invaluable.

Thank you to my SCGSR mentor and committee member, Dr. Cheng Li, for his valuable insights into my neutron total scattering analysis, his willingness to discuss all things science and his continued support and encouragement.

I would also like to thank my committee members, Dr. Claudia Rawn and Dr. Mariya Zhuravleva for their advice on my research projects, their encouragement throughout my graduate studies and their support of my outreach efforts.

I would like to express my gratitude to the many scientists at Oak Ridge National Lab, Dr. Stephen Purdy, Dr. Jue Liu, Dr. Michelle Everett, Dr. Luke Daemen, Dr. Zili Wu, and Dr. Matt Tucker for their support of my professional development and research efforts.

Thank you to Dr. Palani Jothi, Dr. Peter Metz, Xin Wang and all my current and past research group members at the University of Tennessee, for providing support, encouragement, and feedback on my research.

Thank you to my mom, dad and sister for their unwavering support, patience and encouragement.

Abstract

This work is aimed at uncovering the role of structural defects and disorder on the properties of metal oxide nanoparticles for emissions control and electrochemical catalytic applications. This understanding is achieved through: (i) synthesis of traditional and novel catalysts; (ii) catalytic performance testing; and (iii) *in-situ* structural characterization via neutron scattering.

Metal oxide nanomaterials impregnated with noble metals serve as benchmark catalysts for a wide range of catalytic reactions. We investigate the influence of noble metals on the defect structure of the underlying support with a focus on emissions control catalysis. Neutron total scattering was employed to investigate the structural evolution of CeO_2 and Pt-CeO_2 nanorods *in-situ* under oxidation and reduction. The need for *in-situ* characterization environments motivated the design of a hazardous gas handling system (HGHS), high temperature furnace and quartz sample cell designed to enable *in-situ* gas flow at the Nanoscale-Ordered Materials Diffractometer (NOMAD) instrument at the Spallation Neutron Source. This new *in-situ* gas flow set up was commissioned by studying the structural evolution of $CeZrO_4$ and Pd-$CeZrO_4$ under oxidation, methane oxidation and methane reduction. In this system, Pd is found to have a profound impact on the evolution of the underlying support. In both studies, neutron total scattering proves to be a valuable tool in uncovering the nature and evolution of oxygen vacancies and local cation ordering within catalyst supports, which may be challenging to resolve using other characterization techniques.

Despite their high activity, the scarcity, high cost and instability of noble metal based catalysts presents major drawbacks. We leverage compositional complexity to design $RE_{0.5}Ce_{0.5}O_{2-x}$ catalysts, where RE = a single or multiple rare earth cation(s), as noble metal-free electrocatalysts for the oxygen evolution reaction (OER). Incorporating a single RE cation into the fluorite lattice boosts OER activity, further enhanced by the compositionally complex oxide composition that increases oxygen vacancies, reducing the energy required for OH* adsorption. Thus, tuning compositional complexity may offer promising improvements in OER catalytic activity.

Our findings yield new perspectives on designing industrially viable metal oxide nanocatalysts and advance the applicability of neutron total scattering for studying materials *in-situ* under gas flow.

Table of Contents

1 Introduction **1**

1.1 Importance of Metal Oxide Nanoparticles in Catalysis 2

1.2 Synthesis Strategies for Optimizing Catalytic Performance 3

1.2.1 Tuning Nanoparticle Morphology 3

1.2.2 Tuning Bulk and Surface Chemistry 8

1.3 Select Applications of Metal Oxide Nanocatalysts 11

1.3.1 Automotive Emissions Control 11

1.3.2 Electrochemical Oxygen Evolution Reaction 12

1.4 Advanced Structural Characterization using Neutron Total Scattering 13

1.5 Objectives and Research Significance 15

2 *In-situ* Redox Behavior of CeO_2 and Pt-CeO_2 Nanorods **16**

2.1 Abstract 17

2.2 Introduction 17

2.3 Materials Synthesis 20

2.4 Materials Characterization and Methods 20

2.4.1 Neutron Total Scattering 20

2.4.2 Near Ambient Pressure-X-ray Photoelectron Spectroscopy . . . 23

2.4.3 Structure Models and Refinements 24

2.5 Results and Discussion 27

2.5.1 Rietveld Refinement Results 27

2.5.2 PDF Refinement Results 31

2.5.3 NAP-XPS Results . . . 43
2.6 Conclusion . . . 43
2.7 Acknowledgements . . . 45

3 *In-situ* methane oxidation behavior of $CeZrO_4$ and Pd-$CeZrO_4$ 47
3.1 Abstract . . . 48
3.2 Introduction . . . 49
3.3 Methods . . . 51
3.3.1 Materials . . . 51
3.3.2 Synthesis of $CeZrO_4$ and Pd-$CeZrO_4$ . . . 51
3.3.3 Neutron Total Scattering Measurements . . . 52
3.3.4 Neutron Diffraction and PDF Analysis . . . 56
3.3.5 Density Functional Theory Calculations . . . 57
3.4 Results and Discussion . . . 58
3.4.1 Average Structure . . . 58
3.4.2 Local Structure . . . 63
3.5 Conclusion . . . 72
3.6 Acknowledgements . . . 73

4 Mesoporous $RE_{0.5}Ce_{0.5}O_{2-x}$ Fluorite Electrocatalysts for the Oxygen Evolution Reaction 74
4.1 Abstract . . . 75
4.2 Introduction . . . 75
4.3 Materials Synthesis . . . 78
4.3.1 Materials . . . 78
4.3.2 Synthesis of Porous Binary Fluorites via Evaporation Induced Self Assembly (EISA) . . . 79
4.3.3 Fabrication of the Working Electrode for OER. . . . 80
4.4 Materials Characterization and Methods . . . 80
4.4.1 Structure and Morphology . . . 80

4.4.2 Electrochemical Measurements . . . 81
4.4.3 Density Functional Theory (DFT) . . . 82
4.5 Results and Discussion . . . 82
4.5.1 Phase purity and sample morphology . . . 82
4.5.2 Electrocatalytic performance for the OER . . . 90
4.5.3 OER Electrocatalytic Stability . . . 98
4.6 Conclusion . . . 102
4.7 Acknowledgements . . . 103
Appendix . . . 104

5 Tailored $(La_{0.2}Pr_{0.2}Nd_{0.2}Tb_{0.2}Dy_{0.2})_2Ce_2O_7$ as a Highly Active and Stable Nanocatalyst for the Oxygen Evolution Reaction 135
5.1 Abstract . . . 136
5.2 Introduction . . . 137
5.3 Materials Synthesis . . . 141
5.3.1 Materials . . . 141
5.3.2 Synthesis of Mesoporous Fluorites via Evaporation Induced Self Assembly (EISA) . . . 142
5.3.3 Fabrication of the Working Electrode for OER . . . 142
5.4 Materials Characterization and Methods . . . 143
5.4.1 Structure and Morphology . . . 143
5.4.2 Electrochemical Measurements . . . 145
5.5 Results and Discussion . . . 146
5.5.1 Structure and Morphology . . . 146
5.5.2 Defect Chemistry . . . 151
5.5.3 Catalytic Performance for the Oxygen-Evolution Reaction . . . 157
5.6 Conclusion . . . 165
5.7 Acknowledgements . . . 166
Appendix . . . 167

6 Summary and Outlook **185**

6.1 Role of Noble Metals on Defect Formation in CeO_2-Based Oxides for Heterogeneous Catalysis 185

6.2 *In situ* Neutron Total Scattering of Catalysts under Real Operating Conditions 187

6.3 Leveraging Compositional Complexity To Enhance Activity and Stability of Electrocatalysts for the Oxygen Evolution Reaction 188

Bibliography **191**

Vita **233**

List of Tables

2.1 Rietveld refinement results for CeO_2 and Pt-CeO_2 nanorods under various flow conditions, using an ideal Fluorite model. 29
2.2 Rietveld refinement results for CeO_2 and Pt-CeO_2 nanorods under various flow conditions using a single phase fluorite structure model with Frenkel-type oxygen defects. 30

4.1 Lattice parameter a, isotropic atomic displacement parameters U_{iso}s, average crystalline correlation length L, and resulting goodness of fit R_{wp} resulting from XRD Rietveld refinements of the fluorite sample series data. Measured BET surface area (SA) is also shown for the samples. 86
4.2 Electrocatalytic performance of fluorite catalysts in the series. 99
S4.1 Chemical composition results from X-ray Fluorescence (XRF) of binary fluorites. 105

5.1 Catalytic performance of fluorite catalysts. 164
S5.1 Chemical composition results from Energy Dispersive X-ray Spectroscopy (EDS) elemental mapping and X-ray Fluorescence (XRF) of $RE_2Ce_2O_7$ prepared by calcination at 600°C for 4 hours. 169
S5.2 Parameters of equivalent circuit obtained from fitting of EIS experimental data. 175

List of Figures

1.1 Pressurized autoclave set up used in a typical hydrothermal synthesis reaction. 5
1.2 Schematic of the EISA synthesis procedure. 7
1.3 Schematic of the IWI synthesis procedure. 10

2.1 CeO_2 and Pt-CeO_2 nanorods were exposed *in-situ* to stepped temperature profiles and furnace gas flow conditions at NOMAD, as indicated here. 22
2.2 The CeO_2 fluorite crystal structure and its known oxygen defect sites. (a) The fluorite structure (S. G. $Fm\bar{3}m$) features Ce at the 4*a* sites and O on the 8*c* sites. Oxygen atoms (red spheres) form cubeoctahedron around Ce atoms (green spheres). The oxygen can be partially occupied, as depicted here. The resulting CeO_{2-x} formula corresponds to the defect fluorite crystal structure. (b) Ce atoms can be seen to form close-packed {111} planes, with O occupying tetrahedral interstitial positions (8*c* sites). A single red OCe_4 tetrahedron is depicted for clarity. (c) Oxygen are also known to take up positions within the octahedral interstitial sites of the Ce close-packed planes, highlighted as a purple polyhedron. This interstitial oxygen site is displaced randomly from the center of the octahedron along one of six ⟨001⟩ directions, partially occupying the 24*e* site in the lattice (purple spheres) and resulting in the formation of Frenkel-type oxygen defects. 25

2.3 Rietveld refinement results for (a) CeO_2 and (b) Pt- CeO_2 rod data, collected under D_2 and O_2 flow at 400°C. Data was fit to an ideal Fluorite model. Measured data are shown as circles, fits as colored lines through the data, and difference curves fall below the data and fits. Tick marks indicate *hkl* indices for the cubic fluorite crystal structure. 28
2.4 Lattice parameters of (a) CeO_2 and (b) Pt-CeO_2 rods, determined from Rietveld and 2-50 Å PDF refinements using an ideal Fluorite model. . . 32
2.5 2-50 Å PDF fit results for (a) CeO_2 and (b) Pt-CeO_2 rod data, collected under D_2 and O_2 flow at 400°C. Data was fit to an ideal Fluorite model. Data are shown as circles, fits as colored lines through the data, and difference curves fall below the data and fits. 33
2.6 Crystallographic domain sizes of (a) CeO_2 and (b) Pt-CeO_2 rods, determined from 2-50 Å PDF refinements using an ideal Fluorite model. 35
2.7 2-10 Å PDF fit results for (a) CeO_2 and (b) Pt- CeO_2 nanorod data measured under D_2 flow at 400 °C. Data was fit to a single phase ideal Fluorite model and a two phase structure model with a bulk ideal fluorite structure and a secondary surface structure containing oxygen Frenkel-type defects. 8*c* and 24*e* oxygen occupancies were refined in the secondary phase structure. Data are shown as circles, fits as colored lines through the data, and difference curves fall below the data and fits. 36
2.8 2-10 Å PDF fit results for (a) CeO_2 and (b) Pt-CeO_2 nanorod data measured under D_2 flow at 400°C and fit with a two phase Frenkel Defect-Fluorite model for CeO_2 rods and three phase Frenkel Defect and Metallic Pt model for Pt-CeO_2 nanorods. Each phase contribution is shown. 38

2.9 2-10 Å PDF fit results for (a) CeO_2 and (b) Pt-CeO_2 nanorod data, collected under D_2 and O_2 flow at 400°C. Data was fit to a Frenkel defect-fluorite model for CeO_2 rods and Frenkel Defect and Metallic Pt model for Pt- CeO_2 nanorods. 8*c* and 24*e* oxygen occupancy's were refined in the secondary phase structure in both cases. Data are shown as circles, fits as colored lines through the data, and difference curves fall below the data and fits. 39

2.10 Lattice parameters for the bulk fluorite phase and surface Frenkel-type defect phase of (a) CeO_2 and (b) Pt-CeO_2 nanorods determined based on 2-10 Å PDF refinements fit with a Frenkel Defect-Fluorite model for CeO_2 rods and Frenkel Defect and Metallic Pt model for Pt- CeO_2 nanorods. 41

2.11 Occupancy values of the 24*e* octahedral interstitial oxygen site in the fluorite lattice for (a) CeO_2 and (b) Pt- CeO_2 nanorod data determined based on 2-10 Å PDF refinements with a Frenkel defect-fluorite model for CeO_2 rods and Frenkel Defect and Metallic Pt model for Pt- CeO_2 nanorods. 42

2.12 Change in percentage of Ce^{3+} for the Pt-CeO_2 rods, shown as a solid green square and circle to represent D_2 flow and O_2 flow respectively, as determined by NAP-XPS. Lattice parameters of Pt-CeO_2 nanorods as determined by PDF analysis are shown as a solid black square and circle to represent D_2 flow and O_2 flow respectively. The Frenkel Defect and Metallic Pt model was used for PDF refinements of the Pt-CeO_2 nanorods. 44

3.1 Schematic showing new low background high temperature furnace (left), dimensions of new quartz gas flow cell (center) and new quartz flow cell with Pd-$CeZrO_4$ sample loaded on NOMAD sample stick (right). 53

3.2 Schematic showing new low background high temperature furnace (left), dimensions of new quartz gas flow cell (center) and new quartz floe cell with Pd-$CeZrO_4$ sample loaded on NOMAD sample stick (right). 54

3.3 (a) Neutron diffraction patterns of $CeZrO_4$ and Pd-$CeZrO_4$ under oxidation (red line) at 400°C, methane oxidation reaction (purple line) at 550°C and methane reduction (green line) gas flow at 550°C. (b) Rietveld refinements of the neutron diffraction data of Pd-$CeZrO_4$ measured under methane oxidation reaction (top panel), methane reduction immediately upon switching gas flow environments (beginning at t = 0 min and including the first 12 minutes of data, labeled t = 0 min) (middle panel) and methane reduction gas flow beginning at t = 12 min of flow and including the subsequent 12 minutes of data, labeled t = 12 min. Measured data is shown as colored circles, structural fits are shown as black lines through the data and the difference curves in green fall below the data and fits. Pd-$CeZrO_4$ measured under methane reaction and methane reduction t = 0 min gas flow conditions were refined using two phase models comprising of a $CeZrO_4$ primary phase with (S.G.) $P4_2/nmc$ (hkl indices indicated by tick marks in black) and a secondary CeO_2 impurity phase with (S.G.) $Fm\bar{3}m$ (hkl tick marks in red). Pd-$CeZrO_4$ measured under methane reduction at t = 12 min was refined using a two phase model composed of $CeZrO_4$ and an impurity CeO_2 phases both with (S.G.) $Fm\bar{3}m$ (hkl tick marks in red). (c) Corresponding crystal structures used to refine the primary phases of Pd-$CeZrO_4$ measured under methane oxidation reaction, methane reduction at t = 0 min and methane reduction at t = 12 minutes, with corresponding refined oxygen atom occupancy shown. 59

3.4 Refined parameters from Rietveld refinements of neutron diffraction data for $CeZrO_4$ and Pd-$CeZrO_4$ under oxidation, reaction, and reduction gas flow environments. $CeZrO_4$ under all measured gas environments and Pd-$CeZrO_4$ under oxidation, reaction and reduction at t = 0 min were refined using a two phase structural model composed of S.G. $P4_2/nmc$ and a secondary CeO_2 impurity phase with $(S.G.)$ $Fm\bar{3}m$. In the tetragonal phase, O_{occ} did not vary from 1 and was thus fixed to 1. Pd-$CeZrO_4$ measured under methane reduction at t = 12 min was refined using a two-phase model composed of $CeZrO_4$ and an impurity CeO_2 phase both with $(S.G.)$ $Fm\bar{3}m$. 61

3.5 Tetragonal unit cell volume of (a) $CeZrO_4$ and (b) Pd-$CeZrO_4$ under all measured gas flow conditions calculated from Rietveld refinements of neutron diffraction data. Pd-$CeZrO_4$ has a fluorite crystal structure with (S.G.) $Fm\bar{3}m$ under methane reduction. The fluorite unit cell volume was converted to a psuedo tetragonal unit cell volume ($V_{tetragonal}$=$V_{cubic}/2$) for comparison. 62

3.6 1.5-30 Å PDF fit results for (a) $CeZrO_4$ and (b) Pd-$CeZrO_4$ under all measured gas flow conditions. $CeZrO_4$, under all measured gas conditions, and Pd-$CeZrO_4$ under oxidation and methane reaction gas flow were refined using a two phase model composed of a tetragonal $CeZrO_4$ primary phase with (S.G.) $P4_2/nmc$ and an impurity CeO_2 phase with (S.G.) $Fm\bar{3}m$. Pd-$CeZrO_4$ was refined using a two phase model with S.G. $Fm\bar{3}m$ composed of $CeZrO_4$ and an impurity CeO_2 phase. Data are shown as colored circles, fits as black lines through the data, and difference curves in green fall below the data and fits. Note that data below 10 Å is shown at enlarged scale relative to data above 10 Å. 64

3.7 1.5-10 Å Refinement results of PDF analysis for Pd-$CeZrO_4$ reduction data derived from various attempted structural models known to exist in $CeZrO_x$ solid solutions: (a) tetragonal (T), (b) pyrochlore (P), (c) T + P model, (d) beta $Ce_2Zr_2O_{7.5}$ phase, (e) fluorite $CeZrO_4$ and (f) K-$CeZrO_{8-x}$ phase. A 5% secondary CeO_2 cubic phase is included in all fits. In (e) and (f), a comparison of each phase contribution and partial PDFs of $CeZrO_4$ (dotted lines) are shown below the measured data. Subset figures (a), (c) and (e) show structural models where the cation sublattice is disordered and occupied on average 50/50 by Ce/Zr. Subset figures (b), (d) and (f) show structural models with varying degrees of cation ordering. (No.) indicates the total number of refined parameters in each model. Black circles and orange lines correspond to the experimental and calculated PDF data, respectively. The difference curves are presented at the bottom of each panel, and the R_{wp} values for comparison are indicated at the top right. 65

3.8 (a) 1.5-30 Å PDF fit results for Pd-$CeZrO_4$ for methane reaction (purple), reduction (t=0 min, shown in green) and reduction (t=12 min, shown in dark green) upon switching gas. Methane reaction and reduction at t=0min data was fit using a two phase structural model consisting of a $CeZrO_4$ phase with S.G. $P4_2/nmc$ and an impurity CeO_2 phase with S.G. $Fm\bar{3}m$. Methane reduction at t=12min data was refined using a a two phase cubic model with S.G. $Fm\bar{3}m$ composed of $CeZrO_4$ and an impurity CeO_2 phase. Data are shown as colored circles, fits as black lines through the data, and difference curves in green fall below the data and fits. (b) Experimental local PDFs for Pd-$CeZrO_4$ measured under methane reaction (purple), reduction (t=0 min, shown in green) and reduction (t=12 min, shown in dark green) along with simulated partial PDFs computed from a cubic $CeZrO_4$ model with S.G. $Fm\bar{3}m$. (c) Schematic illustrations depicting the structural evolutions of DFT optimization at increasing concentrations of oxygen vacancies. (d) Computed partial PDFs showing the oxygen-related atom pairs after DFT optimization, along with inset schematics highlighting the changes in Ce/Zr-O polyhedron distortions. 68

3.9 DFT optimization plots illustrating the total energy versus volume for unit cell models of $CeZrO_4$ with (a) 3/64 and (c) 4/64 oxygen vacancies. The $CeZrO_4$ models with 1/64 and 2/64 oxygen vacancies were optimized by DFT directly with cell shapes/volumes relaxed. The relationship between the cell volume (c) and the formation energy (d) in relation to the number of oxygen vacancies is depicted here. 70

4.1 (a) Salient features of the $RE_{0.5}M_{0.5}O_{2-x}$ rare earth fluorite oxide structure family. When the 4+ fluorite metal M site is substituted with mainly trivalent RE (3+) species, charge compensation occurs through point defects on the oxygen sublattice. The unit cell on the top depicts a system where cation sites are occupied, on average, with equal parts of a RE ion and Ce ion. The defect-fluorite can be written as $RE_{0.5}Ce_{0.5}O_{2-x}$. In the unit cell on the bottom, the VIII-fold cation coordination polyhedra are depicted as light purple cubes with O atoms at the vertices. (b) Rietveld refinements of X-ray powder diffraction data of the fluorite samples. Measured data are shown as colored circles, structure model fits as a black line through the data, and the difference curves in black fall below the data and fits. CeO_2 was refined using a cubic fluorite structure as indicated by the hkl tick marks in black. The binary fluorites in the series were refined using a defect fluorite structure(with 50% RE and 50% Ce on each M site and 7/8ths of O sites occupied). (c) Variation in lattice parameters from Rietveld refinements of the binary fluorite samples, as a function of ionic radius of the RE^{3+} cations in assumed VII-fold coordination with oxygen. . . 83

4.2 O 1s core level binding energy spectra of (a) CeO2; (b) $La_2Ce_2O_7$; (c) $Pr_2Ce_2O_7$; (d) $Nd_2Ce_2O_7$; (e) $Tb_2Ce_2O_7$ and (f) $Dy_2Ce_2O_7$ catalysts. The area ratios of vacancy-related (O_v, green) and lattice-related (O_L, purple) are provided. 89

4.3 Electrocatalytic performance of CeO_2, $La_2Ce_2O_7$, $Pr_2Ce_2O_7$, $Nd_2Ce_2O_7$, $Tb_2Ce_2O_7$, and $Dy_2Ce_2O_7$ catalysts (a) LSVs; (b) Overpotential at current density of 10 $mAcm^{-2}$; (c) Cyclic voltammograms; (d) Tafel plots. All electrocatalysis data are measured in N_2 saturated 1 M KOH at a 10 mV s^{-1} scan rate. 91

4.4 Electrocatalytic performance of CeO_2 (mustard), $La_2Ce_2O_7$ (pink), $Pr_2Ce_2O_7$ (green), $Nd_2Ce_2O_7$ (blue-green), $Tb_2Ce_2O_7$ (blue), and $Dy_2Ce_2O_7$ (violet) catalysts (a) Mass activity of different catalysts; (b) Turnover frequency (TOF) and (c) Nyquist plots in the AC frequency range between 100 kHz and 0.1 Hz at 0.45 V. 94
4.5 (a) Slab models of the (100) surface of $Nd_2Ce_2O_7$ used to calculate differential charge densities of adsorbed OH on Nd (top) and Ce (bottom) sites; (b) OH adsorption energy of the fluorite sample series calculated using the DFT VASP package; (c) Comparison of the trends in ECSA, area ratios of vacancy-related (O_V) and lattice-related (O_L) oxygen calculated from the O1s core level binding spectra from XPS measurements and overpotential at current density of 10 $mAcm^{-2}$ for the fluorite series. 96
4.6 (a) Multistep chronopotentiometry study at various currents for (a) $Dy_2Ce_2O_7$; (b) $Nd_2Ce_2O_7$. Chronopotentiometry stability at a constant current of 10 mA (c) $Dy_2Ce_2O_7$; (d) $Nd_2Ce_2O_7$. 100
S4.1 Scanning electron microscopy images showing the heterogeneous morphology of $Nd_2Ce_2O_7$ calcined at 600°C including (a) spherical nanoparticles and (b) porous flakes. (c) Elemental Dispersive microscopy image of $Nd_2Ce_2O_7$ calcined at 600°C with elemental mapping shown to the right. 104
S4.2 Parameters of equivalent circuit obtained from fitting of electrochemical impedance spectroscopy (EIS) experimental data. 109
S4.3 High resolution XPS spectra of CeO_2 (a) Ce 3d; (b) O 1s. 110
S4.4 High resolution XPS spectra of $La_2Ce_2O_7$ (a) Ce 3d; (b) La 3d; (c) O 1s; (d) C 1s. 111
S4.5 High resolution XPS spectra of $Pr_2Ce_2O_7$ (a) Ce 3d; (b) Pr 3d; (c) O 1s; (d) C 1s. 112

S4.6 High resolution XPS spectra of $Nd_2Ce_2O_7$ (a) Ce 3d; (b) Nd 3d; (c) Nd 4d; (d) O 1s. 113
S4.7 High resolution XPS spectra of $Tb_2Ce_2O_7$ (a) Ce 3d; (b) Tb 3d; (c) O 1s; (d) C 1s. 114
S4.8 High resolution XPS spectra of $Dy_2Ce_2O_7$ (a) Ce 3d; (b) Dy 3d; (c) O 1s; (d) C 1s. 115
S4.9 (a) Cyclic voltammograms measured at different scan rates for CeO_2; (b) Plots of anodic and cathodic currents measured as a function of different scan rates for CeO_2 in N_2 saturated 1 M KOH at a scan rate of 10 mV s^{-1}. 116
S4.10 (a) Cyclic voltammograms measured at different scan rates for $La_2Ce_2O_7$; (b) Plots of anodic and cathodic currents measured as a function of different scan rates for $La_2Ce_2O_7$ in N_2 saturated 1 M KOH at a scan rate of 10 mV s^{-1}. 117
S4.11 (a) Cyclic voltammograms measured at different scan rates for $Pr_2Ce_2O_7$; (b) Plots of anodic and cathodic currents measured as a function of different scan rates for $Pr_2Ce_2O_7$ in N_2 saturated 1 M KOH at a scan rate of 10 mV s^{-1}. 118
S4.12 (a) Cyclic voltammograms measured at different scan rates for $Nd_2Ce_2O_7$; (b) Plots of anodic and cathodic currents measured as a function of different scan rates for $Nd_2Ce_2O_7$ in N_2 saturated 1 M KOH at a scan rate of 10 mV s^{-1}. 119
S4.13 (a) Cyclic voltammograms measured at different scan rates for $Tb_2Ce_2O_7$; (b) Plots of anodic and cathodic currents measured as a function of different scan rates for $Tb_2Ce_2O_7$ in N_2 saturated 1 M KOH at a scan rate of 10 mV s^{-1}. 120

S4.14 (a) Cyclic voltammograms measured at different scan rates for $Dy_2Ce_2O_7$; (b) Plots of anodic and cathodic currents measured as a function of different scan rates for $Dy_2Ce_2O_7$ in N_2 saturated 1 M KOH at a scan rate of 10 mV s^{-1}. 121
S4.15 Electrocatalytic performance of CeO_2: Cyclic voltammograms measured in N_2 saturated 1 M KOH at different scan rates. 122
S4.16 Electrocatalytic performance of $La_2Ce_2O_7$: Cyclic voltammograms measured in N_2 saturated 1 M KOH at different scan rates. 123
S4.17 Electrocatalytic performance of $Pr_2Ce_2O_7$: Cyclic voltammograms measured in N_2 saturated 1 M KOH at different scan rates. 124
S4.18 Electrocatalytic performance of $Nd_2Ce_2O_7$: Cyclic voltammograms measured in N_2 saturated 1 M KOH at different scan rates. 125
S4.19 Electrocatalytic performance of $Tb_2Ce_2O_7$: Cyclic voltammograms measured in N_2 saturated 1 M KOH at different scan rates. 126
S4.20 Electrocatalytic performance of $Dy_2Ce_2O_7$: Cyclic voltammograms measured in N_2 saturated 1 M KOH at different scan rates. 127
S4.21 Electrocatalytic chronopotentiometry stability at constant current of 10 mA (a) CeO_2; (b) $La_2Ce_2O_7$; (c) $Pr_2Ce_2O_7$; (d) $Tb_2Ce_2O_7$; measured in N_2 saturated 1 M KOH after 16h chronoamperometry. 128
S4.22 High resolution XPS spectra of CeO_2 after activity (a) Ce 3d; (b) O 1s. . 129
S4.23 High resolution XPS spectra of $Nd_2Ce_2O_7$ after activity (a) Ce 3d; (b) Nd 3d; (c) Nd 4d; (d) O 1s. 130
S4.24 High resolution XPS spectra of $Tb_2Ce_2O_7$ after activity (a) Ce 3d; (b) Tb 3d; (c) O 1s; (d) C 1s. 131
S4.25 High resolution XPS spectra of $Pr_2Ce_2O_7$ after activity (a) Ce 3d; (b) Pr 3d; (c) O 1s; (d) C 1s. 132
S4.26 High resolution XPS spectra of $La_2Ce_2O_7$ after activity (a) Ce 3d; (b) La 3d; (c) O 1s; (d) C 1s. 133

S4.27 High resolution XPS spectra of $Dy_2Ce_2O_7$ after activity (a) Ce 3d; (b) Dy 3d; (c) O 1s; (d) C 1s. 134

5.1 Synthesis schematic of mesoporous fluorite catalysts using a soft templating strategy via Evaporation Induced Self Assembly (EISA); calcination temperatures between 400°C and 1000°C are used in this work. The fluorite unit cell is shown on the top left with VIII-fold cation coordination polyhedron depicted as purple cubes with red O atoms at the vertices. The cation sites are occupied, on average, with equal parts of 5 RE ions and 1 M ion. When the fluorite A site is doped with a trivalent (+3) species, a multivalent cation like Ce is reduced from a +4 to a +3 state, and charge compensation occurs through point defects on the oxygen lattice sites resulting in a defect fluorite structure where Ce is VII-fold coordinated with oxygen. The CCO with a defect-fluorite structure can be written as $RE_{0.5}M_{0.5}O_{2-x}$. 140

5.2 XRD patterns of CeO_2, $Nd_2Ce_2O_7$ and $RE_2Ce_2O_7$ shown in (a),(d) and (g) respectively, prepared by calcination at 400°C, 600°C, 800°C and 1000°C (from top to bottom of each panel). The XRD pattern of $Nd_2Ce_2O_7$ calcined at 1000°C shows the formation of superstructure peaks as indicated by the blue stars. Refined values from Rietveld refinements of data for CeO_2, $Nd_2Ce_2O_7$ and $RE_2Ce_2O_7$ are shown for (b) lattice parameter, (e) crystallite size and (h) BET surface area. Rietveld refinement results of XRD data of samples prepared by calcination at 600°C are shown in (c), where the data was fit to a tetragonal phase with S.G. $P4_2/nmc$ for CeO_2 and a cubic phase with S.G. $Fm\bar{3}m$ for $Nd_2Ce_2O_7$ and $RE_2Ce_2O_7$. Measured data are shown as colored circles, structural model fits as a black line through the data, and the difference curves in green fall below the data and fits. (f) Scanning Electron Microscopy (SEM) images of $RE_2Ce_2O_7$ prepared by calcination at 400°C for 4 hours (shown in the column on the left) and 1000°C for 4 hours (shown in the column on the right). (i) SEM image (left) and corresponding EDS spectra maps (right, in color) for $RE_2Ce_2O_7$ prepared by calcination at 400°C for 4 hours. A region displaying heterogeneous morphology (larger flakes and smaller spheres) was intentionally selected. 147

5.3 Raman, neutron PDF and XPS results for fluorite catalysts prepared by calcination at 600°C where the top row represents CeO_2, the middle row shows $Nd_2Ce_2O_7$ and the bottom row represents $RE_2Ce_2O_7$. Raman spectra (λ_{ex} = 632.8 nm) are shown in the panel on the left as (a), (d) and (g). Preliminary 2-10 Å neutron PDF refinements using a two phase model comprising of Frenkel-type defects with S.G. $Fm\bar{3}m$ and $Pnn2$- type Ce_3O_{5+x} for CeO_2, $Nd_{1.5}Ce_{1.5}O_{5+x}$ for $Nd_2Ce_2O_7$ and $RE_{1.5}Ce_{1.5}O_{5+x}$ for $RE_2Ce_2O_7$ are shown in the panel in the middle as (b), (e) and (h). High resolution XPS O 1s core level binding energy spectra are shown in the panel on the right in (c), (f) and (i) where the area ratios of vacancy-related (O_V ,green) and lattice-related (O_L , red) oxygen are computed. 152

5.4 Electrocatalytic performance of CeO_2 (purple), $Nd_2Ce_2O_7$ (blue) and $RE_2Ce_2O_7$ (purple) calcined at 600°C: (a) LSVs measured in N_2 saturated 1 M KOH at a scan rate of 10 mV s^{-1}, (b) overpotential at a current density of 10 mA cm^{-2}, (c) cyclic voltammograms measured in N_2 saturated 1 M KOH at a scan rate of 10 mV s^{-1}, (d) Tafel plots and (e) overpotential benchmark at 10 mA cm^{-2} for recent reports on CeO_2 –based catalysts compared to $RE_2Ce_2O_7$. [1, 2, 3, 4, 5, 6, 7, 8, 9] 158

5.5 Electrocatalytic performance of CeO_2 (purple), $Nd_2Ce_2O_7$ (blue) and $RE_2Ce_2O_7$ (orange) calcined at 600°C: (a) mass activity, (b) turnover frequency (TOF), (c) electrochemically active surface area (ECSA) shown in black and roughness factor (RF) shown in green and (d) Nyquist plots in the AC frequency range between 100 kHz and 0.1 Hz at 0.55 V; (e) multistep chronoamperometry study of $RE_2Ce_2O_7$ at various current densities and (f) chronoamperometric stability of $RE_2Ce_2O_7$ at 0.46 V, where the inset displays OER polarization plots of $RE_2Ce_2O_7$ before and after chronoamperometry. 161

S5.1 Rietveld refinement of powder XRD data of $Nd_2Ce_2O_7$, calcined at 1000°C, using a cubic C-type (bixbyite) structure with space group $Ia\bar{3}$. 167
S5.2 Rietveld refinements of neutron diffraction data of $RE_2Ce_2O_7$, $Nd_2Ce_2O_7$ and CeO_2 (from top to bottom) calcined at 600°C. CeO_2 was fit using a tetragonal structure model with S.G. $P4_2/nmc$. $RE_2Ce_2O_7$ and $Nd_2Ce_2O_7$ were fit using a two phase structure model comprising of a primary cubic phase with S.G. $Fm\bar{3}m$ and a secondary oxygen vacancy ordered phase with orthorhombic S.G. $Pnn2$. The secondary phase has a stoichiometry of $RE_{1.5}Ce_{1.5}O_{5+x}$ in the case of $RE_2Ce_2O_7$ and $Nd_{1.5}Ce_{1.5}O_{5+x}$ for $Nd_2Ce_2O_7$. 168
S5.3 Wide-scan survey XPS spectra of (a) CeO_2, (b) $Nd_2Ce_2O_7$ and (c) $RE_2Ce_2O_7$. The C 1s spectra were deconvoluted with the peak at 284.9 eV corresponding to a Sp^3-C bond, and the peak at 288.8 eV corresponding to a C-O bond of ether, or carbonyl functional groups, and the peak at 292.1 and 295.7 eV corresponding to C=O bond of carbonyl groups. [10, 11, 12] 170
S5.4 High resolution XPS spectra of $RE_2Ce_2O_7$: (a) La 3d; (b)Ce 3d; (c) Pr 4d; (d) Nd 3d; (e)Nd 4d; (f) Tb 3d; (g) Dy 3d; (h) O 1s; (h) C 1s. . . . 171
S5.5 High resolution XPS spectra of CeO_2: (a) Ce 3d and (b) O 1s. 172
S5.6 High resolution XPS spectra of $Nd_2Ce_2O_7$: (a) Ce 3d; (b)Nd 3d; (c) Nd 4d; (d) O 1. 173
S5.7 Comparison of the catalytic performances between different Ceria-based catalysts. 174
S5.8 Electrocatalytic performance: cyclic voltammograms measured in N_2 saturated 1 M KOH at different scan rates for (a) $RE_2Ce_2O_7$; (b) $Nd_2Ce_2O_7$; and (c) CeO_2. 176
S5.9 (a) Cyclic voltammograms in non-Faradaic region measured at different scan rates for $RE_2Ce_2O_7$. (b) Plots of anodic and cathodic currents measured as a function of different scan rates for $RE_2Ce_2O_7$. 177

S5.10 (a) Cyclic voltammograms in non-Faradaic region measured at different scan rates for $Nd_2Ce_2O_7$. (b) Plots of anodic and cathodic currents measured as a function of different scan rates for $Nd_2Ce_2O_7$. 178
S5.11 (a) Cyclic voltammograms in non-Faradaic region measured at different scan rates for CeO_2. (b) Plots of anodic and cathodic currents measured as a function of different scan rates for CeO_2. 179
S5.12 Electrocatalytic chronoamperometry stability of (a) CeO_2 at 0.65 V and (b) $Nd_2Ce_2O_7$ at 0.54 V measured in N_2 saturated 1 M KOH after 16h chronoamperometry. 180
S5.13 Raman Spectra before and after OER activity for (a) CeO_2, (b) $Nd_2Ce_2O_7$ and (c) $RE_2Ce_2O_7$ ($\lambda_{ex} = 632.8$ nm). 181
S5.14 High resolution XPS spectra of $RE_2Ce_2O_7$ after OER activity: (a) La 3d; (b) Ce 3d; (c) Pr 4d; (d) Nd 3d; (e) Nd 4d; (f) Tb 3d; (g) Dy 3d; (h) O 1s and (h) C 1s. 182
S5.15 High resolution XPS spectra of $Nd_2Ce_2O_7$ after OER activity: (a) Ce 3d; (b) Nd 3d; (c) Nd 4d and (d) O 1s. 183
S5.16 High resolution XPS spectra of CeO_2 after OER activity: (a) Ce 3d, (b) O 1s. 184

Chapter 1

Introduction

1.1 Importance of Metal Oxide Nanoparticles in Catalysis

Over 80% of industrial processes involve the use of heterogeneous catalysts for a range of applications including the synthesis of specialty chemicals, refinement of petroleum and production of renewable energy. [13, 14, 15, 16] In heterogeneous catalysis, the catalyst exists in a different phase than the reactants; typically, the catalyst is a solid and the reactants are in gas or liquid form. [17] The role of a catalyst in these processes is to increase the rate of the reaction by lowering the activation energy and, in a multi-product reaction, to increase the selectivity towards a targeted product. [15, 16] Designing highly active, selective and stable catalysts is key for a sustainable society as catalysts play a crucial role in the efficiency, environmental impact and economic viability of the chemical and energy industries.

Metal oxides constitute an expansive class of inorganic materials, and represent one of the most important and widely used categories of solid heterogeneous catalysts. [15, 18] Metal oxides are employed as catalytic supports or used as catalysts themselves due to the flexibility in tuning their atomic structure and composition. As a result of this tunability, they have been found to effectively catalyze a wide variety of reactions, including oxidation, reduction, hydrogenation, transesterification, etc. [15, 18]

Engineering metal oxide catalysts on the nanometer scale has been demonstrated as an effective strategy for improving catalytic activity. Nanoparticles exhibit much larger total exposed surface areas per volume or weight and increased number of catalytically active sites compared to their bulk counterparts. They also display various combinations of surface chemistries and structures that can be tuned to optimize the selectivity and regeneration of the catalyst. [19, 20, 21]

The important characteristics of metal oxide nanoparticles that govern catalytic performance include:

- Surface area
- Exposed crystal facet terminations
- Edge/step defects
- Porosity
- Chemical composition.

A fundamental understanding of how these parameters affect catalytic performance is key to designing catalysts with high activity and selectivity. In this work, we aim to optimize catalytic performance by tuning: (i) nanoparticle morphology and (ii) bulk and surface chemistry through the synthesis of traditional and novel metal oxide nanocatalysts. This chapter will describe the various synthesis strategies employed, the target applications of the catalysts and the use of neutron total scattering to develop a fundamental structural understanding of how optimizing processing parameters is influencing the resulting catalytic properties. Finally, we frame the major research objectives of our work which are designed to uncover the role of structural defects and disorder on the catalytic properties of metal oxide nanoparticles under real-world conditions.

1.2 Synthesis Strategies for Optimizing Catalytic Performance

1.2.1 Tuning Nanoparticle Morphology

The synthesis method used in the preparation of metal oxide nano catalysts has a significant influence on the resulting surface area, porosity, morphology and

surface chemistry of the material. Commonly used synthesis methods include co-precipitation, sol-gel and hydrothermal/solvothermal approaches. [21, 22, 23, 24, 25, 26]

This work includes synthesis of traditional catalysts and catalytic supports via hydrothermal and incipient wetness impregnation methods, respectively. Synthesis of novel catalytic materials is explored using a soft templating evaporation induced self assembly (EISA) approach.

Hydrothermal Synthesis

The hydrothermal synthesis method takes advantage of the synergistic effect of high pressure and temperature, to produce highly nanocrystalline materials. [27] As there is no post annealing treatment required in this procedure, it can be used to synthesize nanoparticles with high surface areas. Improving the surface area of a catalyst leads to an increased number of catalytically active sites, thus improving catalytic activity.

In the hydrothermal synthesis method, shown in Figure 1.1, an aqueous mixture of inorganic precursors is sealed in a stainless steel autoclave and heated above the boiling point of water, resulting in elevated pressures. [28] Reaction parameters such as type and concentration of precursor, solvent, stabilizing agents, pressure, pH and the reaction temperature and time can be tuned to alter the phase selectivity, particle size distribution and morphology (rods, cubes, spheres) of the product. [27]

Soft-templating via Evaporation Induced Self Assembly

Evaporation Induced Self Assembly (EISA) is a highly tunable synthesis method that can be used to obtain mesoporous (2 nm - 50 nm) metal oxide structures. In heterogeneous catalysis, the activity of a catalyst can be largely enhanced by controlling its accessible porosity. Catalyst porosity is responsible for accessibility of active sites, diffusion rates of reactants to and products from active sites and selectivity through control of secondary reactions. [29]

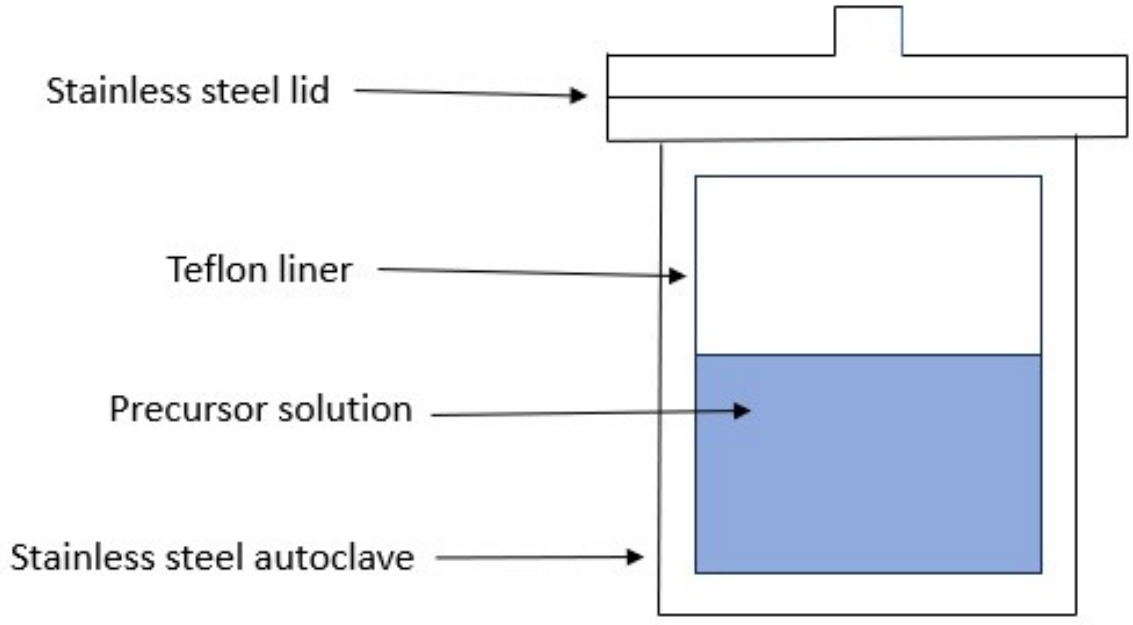


Figure 1.1: Pressurized autoclave set up used in a typical hydrothermal synthesis reaction.

Microporous materials (<2 nm) have high surface area but relatively small pore sizes, which prevents bulky organic molecules from entering the pores and participating in chemical reactions. This limits their use in the petroleum refinement and pharmaceutical industries. In contrast, macroporous materials (>50 nm) have large pore sizes but low surface areas. [30] Thus mesoporous materials (2 nm - 50 nm) provide an ideal pore size range for a variety of catalytic applications. In EISA, a homogeneous solution of inorganic precursors and surfactant are prepared in a volatile solvent (usually a mixture of water, ethanol and HCl). An overview of the synthesis method is shown in Schematic 1.2. [31] The process can be divided into four steps:

1. Solvent evaporation;
2. Water content of the film reaching equilibrium with the atmosphere;
3. Formation and stabilization of hybrid mesostructures;
4. Stiffening of the structure through condensation;

These four steps do not need to occur simultaneously and may overlap with the thin film deposition process.[32] The formation of mesostructures occurs through the self assembly of the structuring agent as micelles. In the condensation process, the thin film is calcined to remove the solvent and micelles and obtain the final solid mesostructured product. [33, 34] In this work, EISA is used to synthesize metal oxide nano catalysts, being a wet chemical synthesis route which allows for intimate mixing of metal oxide precursors at the atomic/molecular scale. [35] EISA can be used to achieve pure phases at lower temperatures relative to solid state methods due to increased diffusion kinetics of the cation in solution. Furthermore, EISA is inexpensive and easily scalable, making it feasible for industrial manufacturing. Finally, processing parameters such as surfactant type, solvent/water/surfactant mole ratio, solvent type, etc. can be straightforwardly varied to optimize the mesoporous architecture.

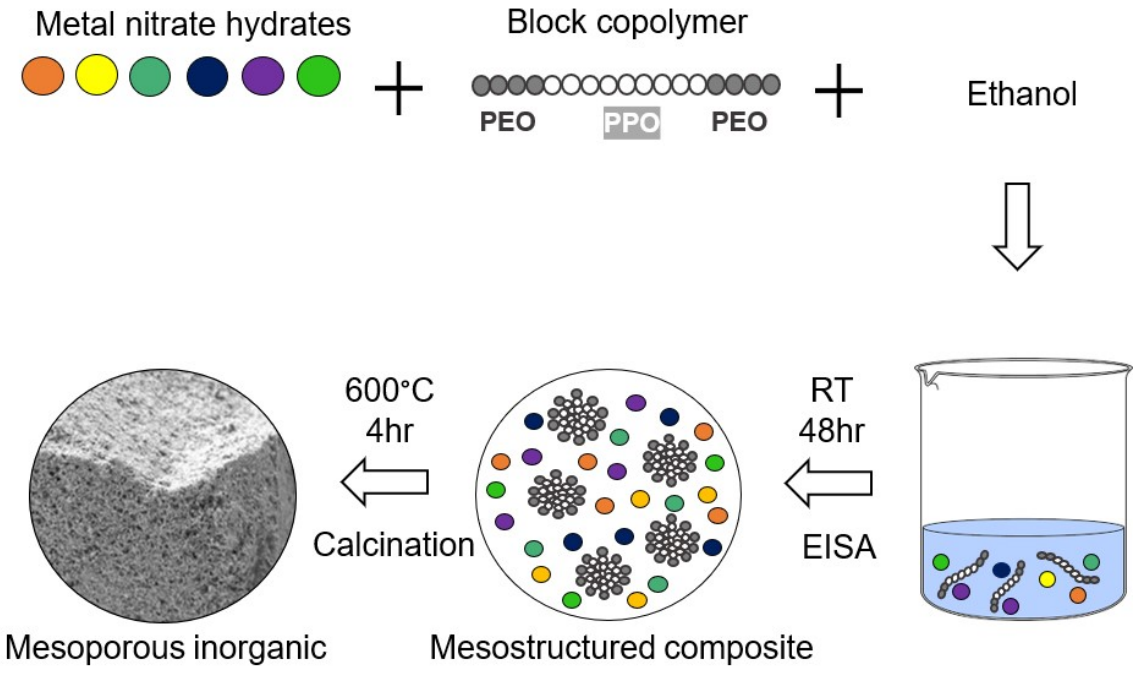


Figure 1.2: Schematic of the EISA synthesis procedure.

1.2.2 Tuning Bulk and Surface Chemistry

Heterogeneous catalysis occurs on the surface of solid catalysts and involves surface chemical processes such as adsorption of reactants on active sites, surface diffusion and reaction of adsorbed species and desorption of reaction products; thus surface chemistry plays a crucial role in the catalytic mechanism. [36] A common approach to tuning the surface chemistry of metal oxides involves dispersing metal nanoparticles on them, simultaneously enhancing catalytic activity and durability. As oxide supports are typically not inert, dispersing metal nanoparticles on the support gives rise to new interfacial phenomena, collectively described as the metal-support interaction (MSI). The synthesis method and processing parameters chosen to produce supported metal oxide catalysts determine whether the metal nanoparticles form highly dispersed single atoms or clustered configurations and influences the MSI and resulting catalytic activity.

MSI phenomena relate to charge transfer, the interfacial interaction, chemical composition, nanoparticle morphology and strong metal-support interaction.[37, 38, 39] In this work, we use an Incipient Wetness Impregnation method to produce noble metal supported metal oxide catalysts.

Incipient Wetness Impregnation

Incipient Wetness Impregnation (IWI) is a commonly used technique for the preparation of metal loaded catalyst supports. Low percentages of loading, often of precious metals, are achieved through adsorption of the precursor solution onto surface groups of the support.[29] In IWI, the volume of precursor solution used is equivalent to the pore volume of the support, ensuring that only the pores of the support are filled with precursor and preventing deposition on the external surface of the support.[40, 29] The catalyst is dried and calcined to eliminate residual volatile compounds from the precursor solution and deposit the metal on the catalyst surface. Figure 1.3 shows an IWI procedure where a catalytic support is impregnated with Pt metal. At low percentages of metal loading, this method can

be used to achieve small and highly dispersed metal nanoparticles on metal oxide catalytic supports.

Compositionally Complex Oxides

In addition to tuning the surface chemistry of catalysts through the MSI, we tune the bulk and surface chemistry of metal oxide catalysts and metal oxide supports by engineering defects in compositionally complex oxides. The surface chemistry of catalysts is often distinct from the bulk chemistry as surface atoms have fewer nearest neighbors and can display different types or concentrations of defects.[36] Although catalytic reactions proceed at the surface of a catalyst, vacancies can migrate between the surface/subsurface and bulk, thus influencing the catalytic activity. The type, size, location and concentration of defects in the bulk, surface and subsurface of catalysts play a key role in various oxidation and reduction applications.[41, 42]

Recently, significant research efforts have focused on investigating the influence of compositional complexity on the catalytic performance of metal oxides. High-entropy oxides (HEOs) are a class of multi-component complex oxides comprised of five or more cations randomly arranged in an equal or near-equal atomic ratio on specific crystallographic sub-lattices. The construct was first reported in 2015, yet the field is still in its infancy. [43] The concept of HEO's falls under the umbrella of the larger class of materials known as Compositionally Complex Oxides (CCO's), which includes non-equimolar compositions. [44] CCOs have attracted interest for catalysis due to the increased opportunity to tune catalytically active sites compared to traditional catalysts. The CCO concept can be used to introduce different isovalent/aliovalent cations with varying sizes, radii, and valence states into the host lattice to create more structural defects and oxygen vacancies than known systems and to influence the surface chemistry and charge distribution of the catalyst. [45, 46]

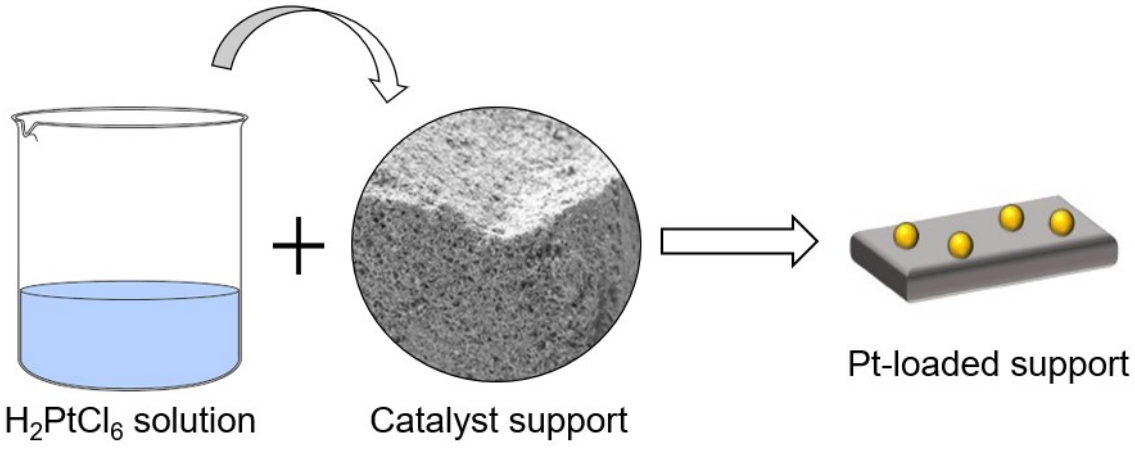


Figure 1.3: Schematic of the IWI synthesis procedure.

The lattice distortion in CCOs can potentially be controlled to lower the overall energy of the system and facilitate activation and transport of active species. CCOs have been reported to improve catalytic performances for various oxidation reactions and display enhanced thermal stability compared to traditional catalysts. [47, 48] However, carefully controlled studies that limit the number of variables and indicate clear synthesis-structure-property relationships for CCO and HEO catalysts are lacking.

1.3 Select Applications of Metal Oxide Nanocatalysts

Developments in the synthesis and characterization of nanomaterials has allowed us to achieve precise control over the shape, size and composition of metal oxide nanoparticles. These advancements have led to the use of supported metal oxides and metal oxide nanoparticles for a variety of heterogeneous catalysis applications including chemical refinement, food processing, environmental remediation and energy conversion and storage. In this work, we explore the synthesis-structure-property relationships of metal oxide nanoparticles as catalysts and supports for automotive emissions abatement and the electrochemical oxygen evolution reaction.

1.3.1 Automotive Emissions Control

In the late 1970s, the United States implemented stringent emissions control standards that require the use of catalytic converters in automobiles, to convert the pollutants in exhaust emissions into gases that are less harmful for the environment and human health. [49] Three-way catalysts (TWCs), present in the catalytic converters in traditional gasoline engines, are designed to perform multiple oxidation and reduction reactions (redox) simultaneously to convert the pollutants to less harmful gases. [50] TWCs oxidize carbon monoxide and hydrocarbons to form carbon dioxide and water, while reducing nitrogen oxides to nitrogen gas. To reduce our reliance on fossil fuels in traditional gasoline engines and combat

climate change, methane gas been proposed as a cleaner-burning fuel in natural gas vehicles (NGVs). However, exhuast emissions from NGVs often contain unburnt methane, which is a potent greenhouse gas.[51] Thus, significant research efforts have been devoted to developing efficient catalysts for the complete oxidation of methane.

A majority of high efficiency and robust catalysts used in emissions control comprise of metal oxide supports loaded with noble metals (typically platinum, palladium, rhodium). [52] The ability of the metal oxide support to dynamically and reversibly absorb and release oxygen, to facilitate the oxidation and reduction of pollutants in the emissions exhaust, is crucial to its catalytic performance. While extensive research efforts have focused on the synthesis and characterization of emissions control catalysts with various morphologies, few detailed *in-situ* structural studies have been performed. Studying the structural evolution of emissions control catalysts under conditions that mimic the environment in a catalytic converter or NGV, is key to determining the role of defects and disorder on catalytic activity and stability and extracting design strategies for industrially relevant catalysts.

1.3.2 Electrochemical Oxygen Evolution Reaction

A major factor limiting our transition to a sustainable society is the intermittent nature of energy generation from renewable energy sources such as wind, solar and hydrothermal energy. Hydrogen, produced via the water splitting reaction, presents a promising sustainable solution for the storage of electricity produced from renewable sources in the form of a chemical fuel or as a reactant for the production of value-added chemicals. [53, 54]

The electrochemical water splitting reaction uses an applied potential to convert water into hydrogen and oxygen. This reaction proceeds via the hydrogen evolution reaction (HER) which takes place at the cathode and the oxygen evolution reaction (OER) which occurs at the anode.

The rate determining step of the water splitting reaction, which prevents its widespread implementation in H_2 production, is the sluggish reaction kinetics of the OER, which results in a larger overpotential. [53, 54] The half-reaction describing OER is shown below:

$$2H_2O \rightarrow O_2 + 4\left(H^+ + e^-\right) \tag{1.1}$$

Thus far, the majority of catalysts that exhibit high OER activity are based on noble metals or their oxides (such as iridium (IV) oxide and ruthenium (IV) oxide). However, noble metal oxide OER catalysts are expensive, scarce and exhibit poor stability in alkaline media, preventing their large scale industrial implementation. [55, 9] Thus it is crucial to develop OER catalysts with high activity and stability without the use of precious metals. [56]

1.4 Advanced Structural Characterization using Neutron Total Scattering

Rational design of catalysts with high activity and selectivity relies on a fundamental understanding of the nature of active sites and the specific features (size, shape, surface area) of metal oxide nanoparticles that direct catalytic performance. Many present-day catalytic studies are pursued under ideal laboratory conditions, which may limit the understanding necessary to develop industrially relevant catalysts. Therefore, it is crucial to study the structure of catalysts *in-situ* under conditions that mimic industrial applications, to extract design strategies for next generation catalysts.

Total scattering is a promising technique for the study of the structural evolutions of catalysts as it can provide a fundamental understanding of which atomic features and defects, chemical short-range order, and local atomic distortions correlate to improved noble metal dispersion, regeneration, and overall improved catalytic performance. [57, 58, 59] *In-situ* total scattering measurements under

non-ambient conditions including variable pressure, temperature and reactive chemical environments can provide valuable information about catalytic synthesis, mechanism or deactivation. [58]

While Bragg scattering can lead to loss of structural information in nanomaterials due to peak broadening effects from finite size, total scattering can provide valuable insights into the structure of nanomaterials as well as gas-solid interactions as it can measure the long and short-range order of materials regardless of their crystallinity. Total scattering is usually represented by the structure function, *S(Q)*, given by:

$$S(Q) = \frac{I_{coh}(Q) - \sum c_i |b_i|^2}{|\sum c_i b_i|^2} + 1 \quad Q = \frac{4\pi \sin\theta}{\lambda} \tag{1.2}$$

In this equation, I_{coh} is the coherent scattering intensity (corrected), Q is the scattering vector, λ is the wavelength of the x-ray/neutron probe, c_i is the atomic concentration and b_i is the scattering length in the case of neutrons and atomic form factor when x-rays are used as the probe. A Fourier transform of *S(Q)* yields the pair distribution function (PDF) as shown:

$$G(r) = \frac{2}{\pi} \int_{Q_{\min}}^{Q_{\max}} Q[S(Q) - 1] \sin(Qr) dQ \tag{1.3}$$

Here Q_{max} and Q_{min} are the maximum and minimum momentum transfer, respectively. Neutron total scattering in particular offers advantages for the study of catalytic systems as heterogeneous catalytic reactions often involve light elements (such as hydrogen, oxygen) that neutrons have a larger sensitivity to relative to x-ray or electron probes. Neutron scattering also has excellent penetration depth, offering greater possibilities for the use of sample environments. Thus neutrons are able to facilitate the study of phenomena effectively "invisible" by other techniques.

In this work, *in-situ* and *ex-situ* neutron total scattering will be used to explore the nature of defects, local atomic structure, chemical short range or long range

order and atomic distortions (strains) from nearest neighbor correlations up to tens of nanometers in traditional and novel metal oxide nano catalysts.

1.5 Objectives and Research Significance

The aim of this work is to develop a comprehensive understanding of the role of structural defects and disorder on the properties of select metal oxide nanocatalysts under real working conditions. To achieve this aim, we follow a closely scrutinized feedback loop involving exploratory synthesis efforts, optimization of catalyst morphology, evaluation of catalytic functionality, and advanced structure-property characterization.

In Chapters 2 and 3, we evaluate the hypothesis that studying the structural evolution of metal oxide nanocatalysts impregnated with noble metals *in-situ* is crucial to elucidating the nature of defects and disorder and their role on the catalytic properties under real operating conditions.

In Chapters 4 and 5, we evaluate the hypothesis that compositional complexity can be leveraged as a materials design strategy to enhance catalytic activity and stability for the electrochemical OER, unrealized via more traditional materials approaches.

Results from these studies will provide new insights into materials design strategies for industrially relevant metal oxide nanocatalysts and will lead to advancements in the technique of neutron total scattering for the study of metal oxide nanocatalysts and other advanced materials, *in-situ* under gas flow.

Chapter 2

In-situ Redox Behavior of CeO_2 and Pt-CeO_2 Nanorods

A version of this chapter was originally published by Sreya Paladugu, Peter C. Metz, Si Luo, Meijun Li, Jue Liu, Harry Meyer (III), Yiqing Wu, Zili Wu and Katharine Page* [60]: Paladugu, S., Metz, P. C., Luo, S., Li, M., Liu, J., Meyer, H. I. I. I., Wu, Y., Wu, Z., and Page, K. (2023). In Situ Neutron Scattering Studies on the Oxidation and Reduction of CeO_2 and Pt–CeO_2 Nanorods. *The Journal of Physical Chemistry C*, 127(7), 3689–3697.

2.1 Abstract

The oxygen vacancy structure of ceria plays a key role in its performance as a favored material for catalysis applications. Here, we develop an understanding of the effects of Pt loading on the structural evolution of ceria nanorods under redox gas environments that mimic real automotive catalytic converters. *In-situ* neutron scattering studies under redox flow reveal that both CeO_2 and Pt-CeO_2 nanorods share a bulk fluorite structure with the presence of surface Frenkel-type oxygen defects. However, Pt-CeO_2 nanorods are more easily reducible than CeO_2 rods as evidenced by an increased concentration of Ce^{3+}, determined by NAP-XPS. Importantly, this work finds no evidence of oxygen vacancy ordered surface reconstruction which has been reported in earlier *ex-situ* investigations. Thus, this work highlights the discrepancy between *ex-situ* and *in-situ* structural observations and emphasizes the need for robust *in-situ* investigations of catalysts to develop industrially relevant materials.

2.2 Introduction

Ceria, CeO_2, has been extensively investigated for a broad range of catalytic applications. [61, 62, 63, 64, 65, 66, 67] The efficacy of CeO_2 as both a catalyst and support is due in part to its high oxygen storage capacity (OSC), enabled by its robust structural stability and extensive reversibility regarding formation of oxygen lattice defects. [68, 69, 70, 71, 72, 73] The dynamic and reversible formation

of oxygen vacancies in CeO_2 is charge-balanced by reduction of Ce^{4+} to Ce^{3+}. Consequently CeO_2 can store and release oxygen under oxidation and reduction environments. [74, 75, 76, 77, 73]

The rate determining step in the conversion of redox states of ceria is the formation of oxygen vacancies in the surface and bulk. The nature of these vacancies (type, size, concentration) and their location in the surface and/or the bulk play a key role in the oxygen diffusion mechanism and the resulting redox properties. [70, 77, 71] Thus, controlling the defect chemistry of ceria based materials is an important means for optimizing their performance for redox applications.

Nanocrystalline ceria exhibits superior performance for catalytic applications, compared to bulk counterparts, due to its larger surface area to volume ratio. Various studies have demonstrated that the desired surface defect chemistry of nanocrystalline ceria can be achieved by modifying the morphology and the resulting exposed crystal facet planes. [78, 79, 80, 81] Ceria reactive planes of {110} and {100} have been shown to have the lowest formation energy for surface oxygen vacancies and thus morphologies with these exposed facet terminations exhibit superior catalytic reactivity. [82] Ceria nanorods have high surface area to volume ratio, predominantly expose {110} and {100} planes and thus have a higher concentration of oxygen defects compared to other morphologies such as cubes or octahedra. [82]

In addition to controlling the morphology, the redox behavior of nanocrystalline ceria can be enhanced by surface modification with a noble metal. [83, 84, 85] Significant research efforts have focused on platinum supported on nanosized ceria due to their strong electronic interaction, leading to high metal dispersion and effective optimization of price-performance ratio. [86] Pt on ceria can be used for catalysis under both oxidizing (CO oxidation) and reducing (water-gas shift) conditions and the nature of Pt has been reported to evolve based on the redox environment. [62, 87, 88, 83, 84].

While detailed studies have been performed on ceria supported Pt nanoparticles under redox conditions, an atomic level understanding of the catalyst support with a rod shaped morphology under redox is lacking. As demonstrated by Wu et al., [89] Pt dispersed on cubic shaped and octahedral shaped ceria displays drastically different thermal stability behavior under redox environments. Pt nanoparticles can re-disperse on cubic shaped ceria with {100} exposed planes under an alternating oxidative and reductive atmosphere while this re-dispersion is unfavorable for Pt supported on octahedral shaped ceria with {111} terminations. [89] Ceria nanorods featuring {110} planes exhibiting high catalytic activity thus provide an attractive support for investigating the structural evolution of Pt-CeO_2 under redox conditions.

Additionally, the bare oxide nanoparticle surface is likely more complicated than idealized surface termination models suggest. Recently, Luo et al. reported the first experimental observation of a partially reduced Ce_3O_{5+x} surface defect phase, present on the surface of CeO_2 nanorods. This partially reduced ceria surface defect phase was discovered through an *ex-situ* neutron diffraction experiment where the samples were pre-reduced in H_2/Ar. [41] Many present-day catalytic studies are pursued under *ex-situ* ideal laboratory conditions, which may limit the understanding necessary to meet future energy infrastructure needs. In this context, the question arises, how do Pt-CeO_2 and CeO_2 rods behave under operating conditions?

In this work, we investigate the defect structure of CeO_2 and Pt-CeO_2 nanorods, under oxidizing and reducing gas atmospheres, through a comprehensive *in-situ* neutron diffraction and pair distribution function (PDF) study. The as-synthesized and Pt-decorated CeO_2 nanorods were studied *in-situ*, under oxidation and reduction conditions, closely mimicking the conditions of real automotive catalytic converters. Neutron scattering was used to investigate the structure of the nanorods as it is highly sensitive to oxygen and can capture intricate details of metal-oxygen bonding. The neutron results are complemented by Near Ambient

Pressure-X-ray Photoelectron Spectroscopy (NAP-XPS) which was performed to quantitatively track reduction behavior of the nanorods, as a function of gas environment, to probe the concentration of Ce^{3+}.

2.3 Materials Synthesis

CeO_2 nanorod samples were synthesized by a hydrothermal process as reported previously. [79, 90, 91] 0.868 g of $Ce(NO_3)_3{\cdot}6H_2O$ and 9.6 g of NaOH were dissolved in 5 and 35 mL of deionized water, respectively. Both solutions were mixed in a Teflon bottle with magnetic stirring, for 30 min, resulting in the formation of a milky slurry. Subsequently, the Teflon bottle containing this mixture was placed in a stainless steel autoclave and heated at 100 °C for 24 hours. The white precipitate obtained after hydrothermal treatment was separated by centrifugation, washed with deionized water and ethanol several times, followed by drying at 60 °C in air overnight. Pt-CeO_2 rods, were prepared via a traditional incipient wetness impregnation method with H_2PtCl_6 solution to achieve 1% Pt loading over CeO_2. The catalyst was dried and calcined at 400 °C for 4 hours. [92, 93, 94]

2.4 Materials Characterization and Methods

2.4.1 Neutron Total Scattering

Medium resolution powder neutron diffraction (NPD) and atomic pair distribution function (PDF) data was collected on NOMAD (Spallation Neutron Source, Oak Ridge National Laboratory). [95] The beam line was equipped with a high-precision gas-flow cell, furnace, and residual gas analyzer (RGA) to facilitate *in-situ* observation of the CeO_2 under non-ambient conditions. [96]

In the *in-situ* NPD and PDF study, 1 g of CeO_2 rod sample was loaded into a specialized quartz gas flow cell, mounted within a vacuum furnace (with 300-1473 K capability) and connected to the gas-flow system. The surface of the mounted

sample was cleansed of any adsorbed species by flushing with Ar. The sample was then oxidized in 4% O_2, Ar at 400 °C and subsequently cooled down to 100 °C with a 5°C per minute ramp. The sample was exposed to Ar to remove any residual oxygen prior to proceeding with further measurements. Finally, the sample was reduced under 4% D_2, Ar at 100 °C and was sequentially heated up to 260 °C, 350 °C and 400 °C with a 5°C per minute ramp between each temperature. The Pt-CeO_2 rod sample was measured using the same set-up and measurement conditions. A profile of all measurement conditions can be seen in Figure 2.1.

The previously light yellow powder samples were observed to be black in color after measurement, confirming reduction of the sample. Signal from the empty quartz container was also collected at all temperature conditions, to facilitate background subtraction from the sample data. A series of 12 minute scans were collected over a 1.5 hour duration at each temperature and gas flow condition. Isothermal data were summed together to improve statistics. Each 12 minute data set was time focused, normalized, and histogrammed and a Q_{max} of 25 $Å^{-1}$ was applied for generation of PDF data. However, PDF extraction required several additional data treatment steps. The background subtraction was complicated by variations (e.g. in thickness) between the empty container scattering signal, and the container scattering produced *in-situ*. Additionally, the pressure gradient generated by the gas flow across the sample bed compacted the sample, changing the packing fraction and beam fill. Thus, it was necessary to estimate a scaled background correction to obtain a silica-free scattering signal. Further, the incoherent scattering produced by adsorbed hydrogen produces an approximately Pseudo Voigt (half) like background that results in large amplitude artefacts in the low-r region of the PDF. [97, 98] This effect is not well described analytically for TOF instruments and is generally removed in ad-hoc fashion. [97, 99]

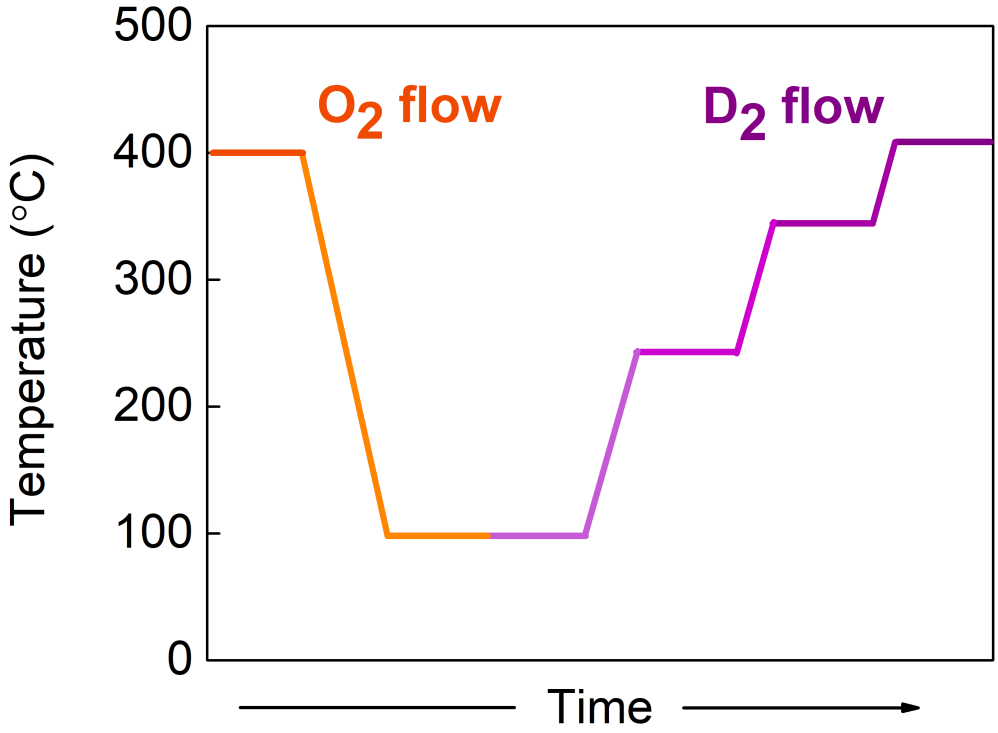


Figure 2.1: CeO_2 and Pt-CeO_2 nanorods were exposed *in-situ* to stepped temperature profiles and furnace gas flow conditions at NOMAD, as indicated here.

In this work, we corrected the reduced PDF by applying Fourier filtering to produce the expected limiting behavior [100] of the total scattering structure function *F(Q)* and the reduced pair distribution function *G(r)*

$$\lim_{Q\to\infty} F(Q) = 0 \tag{2.1}$$

$$\lim_{r\to 0} G(r) = -4\pi r\rho_0. \tag{2.2}$$

The background scale factor was estimated by least-squares refinement of the low-r portion of the PDF, subject to minimization of the target function

$$G(r|r_{O\ldots H} < r < r_{Ce\ldots O}) - 4\pi r\rho_0. \tag{2.3}$$

That is, the scaled background subtraction was optimized such the the Si...O pair correlation from the quartz sample cell ca. 1.6 Å in *G(r)* was eliminated.

2.4.2 Near Ambient Pressure-X-ray Photoelectron Spectroscopy

Laboratory near-ambient pressure X-ray photoelectron spectroscopy (NAP-XPS) measurements were completed using a EnviroESCA (SPECS GmbH, Berlin, Germany) with a monochromatic Al Kα X-ray source (1486.71 eV, 43 W, 14.5 kV). The binding energy scale of the instrument was calibrated according to ISO Standard 15472.22. The energy shift of the binding energy scale after environmental charge compensation by the gas was corrected for all spectra with respect to the Ce 3d (4+) photoemission line at 916.5 eV.

To prepare samples for the NAP-XPS measurement, CeO_2 and Pt-CeO_2 rods were first added to water, followed by sonication to form a well-mixed suspension. The suspension was added dropwise to a thick aluminum foil while heating on a hot plate to form a thin layer of particles after evaporation of water. Coated foil samples were attached to the heater stage using three metal clips that held the sample to the ceramic button heater. A Type K thermocouple was held in place between one of

the metal clips and the foil sample. After positioning the sample for analysis, NAP conditions were realized by back-filling the measurement chamber with pure O_2 or pure H_2 gas maintained at approximately 2 mbar. Data was collected at each sample temperature and gas environment condition for 1 hour. The following experimental sequence was followed: (1) 400 °C O_2; (2) 100 °C O_2; (3) 100 °C H_2; (4) 260 H_2; and (5) 350 °C H_2. For each temperature and environment setting a Ce 3d core level spectrum was acquired.

To determine changes in the valence state of Ce, a difference curve was constructed between the fully oxidized state (400 °C O_2) and each of the other four temperature and gas flow environments measured. To construct the difference curve, the spectra were aligned to the Ce^{4+} peak at ~916.5 eV. Next, the peak intensity was normalized to the same height so that the resulting difference is due to changes in peak shape and not peak intensity. After aligning and normalizing the spectra, each of the measured temperature and gas flow environments were subtracted from the spectrum measured at 400 °C, O_2. The resulting difference curves for the four temperature and gas flow states showed intensities in the regions where Ce^{3+} is typically observed. The area under the resulting difference curve was compared to the total area of the corresponding temperature and gas environment state curve to determine percent change of Ce^{3+}.

2.4.3 Structure Models and Refinements

Ceria crystallizes in a cubic fluorite structure with space group (S.G.) $Fm\bar{3}m$ where the Ce cations occupy the face-centered Wyckoff position 4*a* and the oxygen anions occupy the tetrahedral 8*c* position. [68, 101] In this structure, referred to hereafter as the ideal Fluorite model, (Figure 2.2a), the octahedral site (position 24*e*) is vacant. The fluorite lattice is known to form anion vacancies, leading to non-stoichiometric defect chemistry in CeO_{2-x}. [61, 101] Previous studies report a ceria defect structure where some of the oxygen anions relocate to the more spacious octahedral site, creating vacancies on the original tetrahedral site (Figure 2.2c).

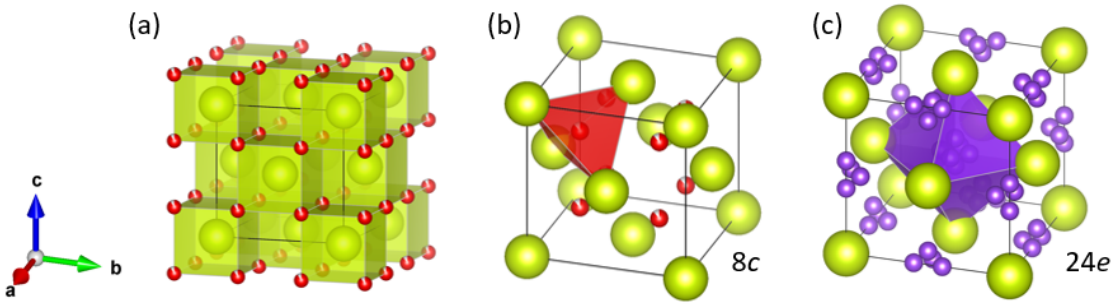


Figure 2.2: The CeO_2 fluorite crystal structure and its known oxygen defect sites. (a) The fluorite structure (S. G. $Fm\bar{3}m$) features Ce at the 4a sites and O on the 8c sites. Oxygen atoms (red spheres) form cubeoctahedron around Ce atoms (green spheres). The oxygen can be partially occupied, as depicted here. The resulting CeO_{2-x} formula corresponds to the defect fluorite crystal structure. (b) Ce atoms can be seen to form close-packed {111} planes, with O occupying tetrahedral interstitial positions (8c sites). A single red OCe_4 tetrahedron is depicted for clarity. (c) Oxygen are also known to take up positions within the octahedral interstitial sites of the Ce close-packed planes, highlighted as a purple polyhedron. This interstitial oxygen site is displaced randomly from the center of the octahedron along one of six $\langle 001 \rangle$ directions, partially occupying the 24e site in the lattice (purple spheres) and resulting in the formation of Frenkel-type oxygen defects.

These Frenkel pairs provide a facile mechanism for oxygen mobility in the ceria lattice. [102] As the oxygen ions are less tightly bound when occupying the octahedral site, they can escape the lattice more readily, improving the redox efficiency of ceria. [68] While the original tetrahedral site has a multiplicity of 8, the interstitial octahedral site has a multiplicity of 24, and anions that move to this position will fractionally occupy the 24*e* "split" site, leaving a corresponding vacancy on the 8*c* site. In this work, we investigate the presence of Frenkel defects in the surface of the nanorods with an anion vacancy defect structure model, hereafter termed Frenkel defect-fluorite model, which is depicted in Figure 2.2c. This structural model consists of a bulk fluorite phase with a secondary surface phase containing oxygen Frenkel defects.

To account for the presence of Pt in the Pt-CeO_2 ceria nanorods, a three-phase structural model was used for PDF fitting, comprising of a bulk fluorite structure, a fluorite structure with surface oxygen Frenkel defects, and a face centered cubic Pt model. This three phase structural model is referred to as the Frenkel Defect and Metallic Pt model.

To determine the average structure of the CeO_2 and Pt-CeO_2 rods, Rietveld refinements were performed in the TOPAS v6 software [103] using the ideal fluorite model and using a single phase fluorite structure model with Frenkel-type oxygen defects. The a lattice parameter, scale factor, and isotropic atomic displacement parameters (B_{iso}) were refined. The B_{iso} values for the 8*c* and 24*e* O atomic positions were constrained to be identical. The occupancy of the 8*c* oxygen site was refined with a dependent 24*e* oxygen interstitial site occupancy, constrained to form a Frenkel-defect pair.

To elucidate length-scale dependent defect ordering, PDF analysis was applied to the low-r (2-10 Å) and the long-range (2-50 Å) regions. PDF refinements were performed using the aforementioned structural models and the TOPAS v6 software. [103] The characteristic shape function for nanorod particles [104] was used to correct for the influence of particle shape. In all cases, the instrumental

resolution parameters Q_{broad} and Q_{damp} were fixed as 0.02018 $Å^{-1}$ and 0.06085 $Å^{-1}$ respectively, as refined from a Si standard. [105] The occupancies of the 8*c* and 24*e* oxygen atoms in the surface defect phase were again refined as a Frenkel-defect pair and the surface defect phase was assumed to be spherical with an ordering of 1 nm based on exploratory refinements. The FCC Pt phase was also assumed spherical and particle diameter fit with a spherical shape function parameter.

2.5 Results and Discussion

2.5.1 Rietveld Refinement Results

The results of Rietveld analysis using the Fluorite model, for the most oxidizing and reducing environments measured, are summarized in Figure 2.3. Upon comparing the diffraction patterns of the CeO_2 and Pt-CeO_2 rods, we find that the Pt-CeO_2 rods display narrower Bragg peaks, indicative of a higher degree of crystallinity. The enhanced crystallinity of the Pt-CeO_2 rods is a result of the synthesis procedure where they undergo an additional calcination step to decorate the surface of the CeO_2 rods with Pt atoms. As seen in Figure 2.3, the patterns for both CeO_2 and Pt-CeO_2 rods are reasonably fit by the ideal cubic fluorite structure, under both gas flow and temperature conditions, with no additional Bragg peaks detected. Refined parameters from Rietveld analysis of all measured environments are shown in Table 2.1 for the CeO_2 and Pt-CeO_2 rods.

To determine if Frenkel-type oxygen defects are present in the CeO_2 and/or Pt-CeO_2 rods, the Frenkel defect-fluorite model introduced above was applied to Rietveld refinements. The results of the series fitting are summarized in Table 2.2, with overall goodness-of-fit for the Frenkel defect-fluorite model provided. In both cases, additional site occupancy parameters worsened the overall fit to the powder diffraction data. The average structure was therefore determined to be an ideal fluorite structure.

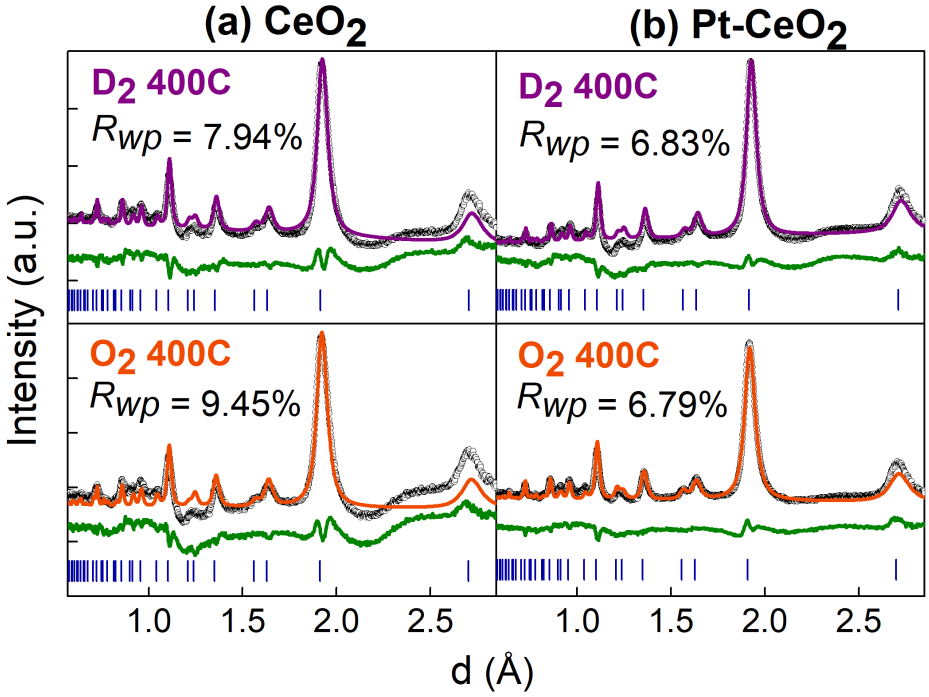


Figure 2.3: Rietveld refinement results for (a) CeO_2 and (b) Pt- CeO_2 rod data, collected under D_2 and O_2 flow at 400°C. Data was fit to an ideal Fluorite model. Measured data are shown as circles, fits as colored lines through the data, and difference curves fall below the data and fits. Tick marks indicate *hkl* indices for the cubic fluorite crystal structure.

Table 2.1: Rietveld refinement results for CeO_2 and Pt-CeO_2 nanorods under various flow conditions, using an ideal Fluorite model.

CeO_2 Nanorods				
Flow Condition	a (Å)	*Beq*(Ce) (Å^2)	*Beq*(O) (Å^2)	R_{wp}
O_2 100 °C	5.3961 ± 0.0052	0.1102 ± 0.0682	2.6262 ± 0.1857	11.18
O_2 400 °C	5.4042 ± 0.0055	0.3189 ± 0.1238	2.6406 ± 0.1828	9.45
D_2 100 °C	5.3974 ± 0.0057	0.3019 ± 0.1251	2.5359 ± 0.1914	11.07
D_2 260 °C	5.4014 ± 0.0046	0.3795 ± 0.1411	1.7931 ± 0.1433	8.47
D_2 350 °C	5.4055 ± 0.0048	0.4551 ± 0.1477	2.0173 ± 0.1547	8.52
D_2 400 °C	5.4107 ± 0.0049	0.5072 ± 0.1655	1.8605 ± 0.1559	7.94
Pt-CeO_2 Nanorods				
Flow Condition	a (Å)	*Beq*(Ce) (Å^2)	*Beq*(O) (Å^2)	R_{wp}
O_2 100 °C	5.3949 ± 0.0049	0.8198 ± 0.1883	2.1379 ± 0.1693	6.79
O_2 400 °C	5.3958 ± 0.0044	1.1453 ± 0.2221	1.6568 ± 0.1398	5.72
D_2 100 °C	5.4139 ± 0.0052	0.5952 ± 0.1471	2.5101 ± 0.1797	8.19
D_2 260 °C	5.4173 ± 0.0052	0.7452 ± 0.1686	2.5642 ± 0.1856	6.87
D_2 350 °C	5.4179 ± 0.0056	0.8924 ± 0.1869	2.8140 ± 0.2018	7.14
D_2 400 °C	5.4185 ± 0.0054	1.0310 ± 0.2212	2.5007 ± 0.1941	6.83

Table 2.2: Rietveld refinement results for CeO_2 and Pt-CeO_2 nanorods under various flow conditions using a single phase fluorite structure model with Frenkel-type oxygen defects.

CeO_2 Nanorods				
Flow Condition	a (Å)	*Beq*(Ce) (Å^2)	*Beq*(O) (Å^2)	R_{wp}
O_2 100 °C	5.3968 ± 0.0058	1.1950 ± 0.2329	1.3259 ± 0.1538	12.69
O_2 400 °C	5.4043 ± 0.0057	0.6762 ± 0.1265	2.4625 ± 0.1584	9.78
D_2 100 °C	5.3967 ± 0.0053	0.5241 ± 0.1603	1.3797 ± 0.1452	11.39
D_2 260 °C	5.4017 ± 0.0032	0.4963 ± 0.0734	1.6498 ± 0.0867	9.58
D_2 350 °C	5.4055 ± 0.0049	0.7389 ± 0.1345	1.8829 ± 0.1364	9.35
D_2 400 °C	5.4107 ± 0.0047	0.5449 ± 0.1168	1.8474 ± 0.1290	8.59
Pt-CeO_2 Nanorods				
Flow Condition	a (Å)	*Beq*(Ce) (Å^2)	*Beq*(O) (Å^2)	R_{wp}
O_2 100 °C	5.3954 ± 0.0049	1.1729 ± 0.1535	1.9482 ± 0.1257	6.95
O_2 400 °C	5.3968 ± 0.0045	1.8129 ± 0.1754	1.5025 ± 0.0948	6.69
D_2 100 °C	5.4134 ± 0.0059	1.1535 ± 0.1787	2.2308 ± 0.1584	8.04
D_2 260 °C	5.4024 ± 0.0066	2.2909 ± 0.2630	2.1381 ± 0.1582	7.59
D_2 350 °C	5.4176 ± 0.0060	1.4594 ± 0.1809	2.4740 ± 0.1566	7.35
D_2 400 °C	5.4184 ± 0.0055	1.4397 ± 0.1811	2.1337 ± 0.1400	7.10

The effects of redox on CeO_2 and Pt-CeO_2 rods were explored by extracting the lattice parameters determined from Rietveld refinements as seen in Figure 2.4. Inspection of the resulting lattice parameters reveals that the transition from an oxidizing to reducing atmosphere leads to an increase in lattice parameter for both CeO_2 and Pt-CeO_2 rods. The increase in lattice parameter due to reduction is suggestive of Ce conversion from a 4+ to 3+ valence state as Ce^{3+} has a larger ionic radius (1.034 Å) relative to Ce^{4+} (0.92 Å). [61, 77, 70, 106] Furthermore, the increase in lattice parameter upon switching from O_2 to D_2 flow is more significant for the Pt-CeO_2 rods than for the CeO_2 rods, suggesting that Pt-CeO_2 is more readily reducible.

The measured Bragg data presents several challenges that limit the extent of quantitative information that can be extracted about the nature of oxygen defects in the bulk structure and at the surfaces of the nanorods. There is significant noise in the data due to the small sample volumes studied and significant peak broadening due to the nanocrystalline nature of the rods. Hence, PDF analysis was pursued to clarify the oxygen vacancies of the average structure and determine any local structure features of the nanorods.

2.5.2 PDF Refinement Results

To resolve the average structure through PDF analysis, the Fluorite model was applied to refinements in the long range (2-50 Å) as seen in Figure 2.5 and the shape function for nanorods described by Usher et al.[107] was used to account for nanocrystalline shape and size effects on the PDF data. Qualitative assessment of the PDFs in Figure 2.5 shows larger amplitude in the high-r region for the Pt-CeO_2 rods than the CeO_2 rods, indicating a larger particle size. Ceria, among other metal oxides, has been broadly reported to display an increase in lattice parameter with decreasing particle size. [108, 109, 110, 106]

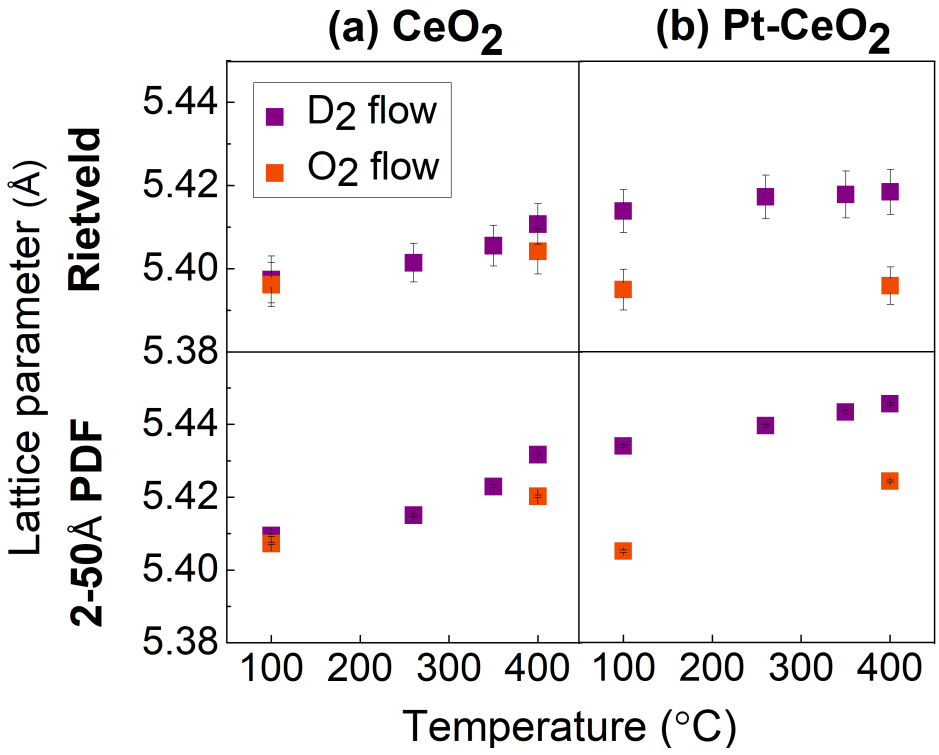


Figure 2.4: Lattice parameters of (a) CeO_2 and (b) Pt-CeO_2 rods, determined from Rietveld and 2-50 Å PDF refinements using an ideal Fluorite model.

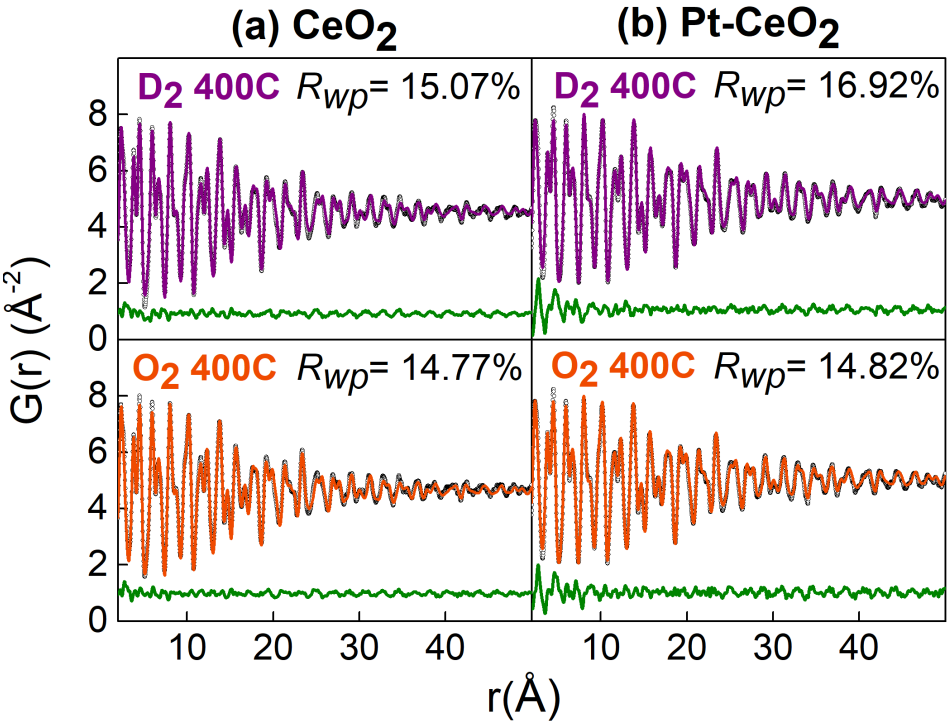


Figure 2.5: 2-50 Å PDF fit results for (a) CeO_2 and (b) Pt-CeO_2 rod data, collected under D_2 and O_2 flow at 400°C. Data was fit to an ideal Fluorite model. Data are shown as circles, fits as colored lines through the data, and difference curves fall below the data and fits.

Contrary to this trend, the Pt-CeO_2 rods exhibit a larger lattice parameter and larger overall particle size than the CeO_2 rods, indicating that the reduction behavior of the Pt-CeO_2 rods overrides particle size effects.

While we are able to extract the length and diameter of the shape dependent crystallite domain size for the CeO_2 rods, the coherent domain length of the Pt-CeO_2 rods exceeds the sensitivity of the PDF analysis technique. However, we are able to determine the diameter parameter of the crystallite domains of the Pt-CeO_2 rods and qualitatively demonstrate that it is larger than the diameter parameter of the CeO_2 rods (Figure 2.6). The larger coherent scattering domain size of the Pt-CeO_2 rods can be explained by the synthesis procedure where the CeO_2 rods undergo an additional calcination step, leading to increased crystallinity.

In accordance with Bragg diffraction results, Figure 2.5 shows that CeO_2 and Pt-CeO_2 nanorods share the same bulk ideal fluorite structure, as evidenced by the successful fitting of the Fluorite model to the data above 10 Å. However, there are significant discrepancies in fit to the low-*r* region for both CeO_2 and Pt-CeO_2 rods.

Comparison of the lattice parameters determined from PDF and Bragg analysis, shown in Figure 2.4, reflect similar trends which indicate that the Pt-CeO_2 nanorods have an expanded lattice relative to the CeO_2 rods due to an increased concentration of Ce^{3+}. It is well known Ce^{3+} in CeO_2 is charge balanced by oxygen vacancies. [70]

To investigate the deviation in the local structure from the bulk, the Frenkel Defect-Fluorite model was used to model the data below 10 Å. Figure 2.7 shows a fit to the data collected under D_2 flow at 400 °C, which is representative of the most reducing condition measured and the highest concentration of oxygen defects. As seen in the figure, inclusion of surface oxygen Frenkel-defects helps to capture the asymmetry observed in the peak at 2.9 Å in the CeO_2 rod data and improve the overall fit to the data below 10 Å. While the Frenkel Defect-Fluorite model helps improve the fit quality of the Pt-CeO_2 rod data relative to the Fluorite model, misfit of the peak at 2.9 Å remains.

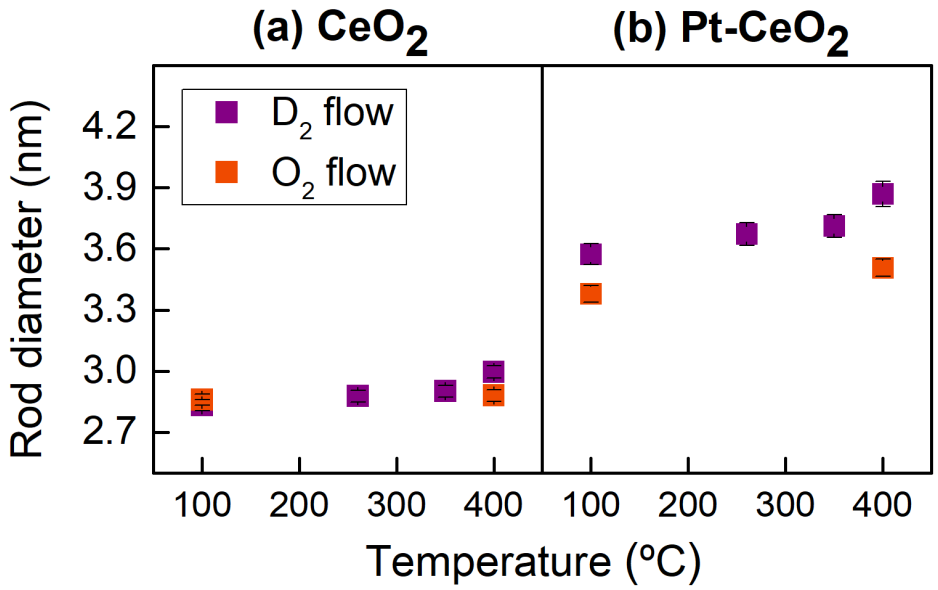


Figure 2.6: Crystallographic domain sizes of (a) CeO_2 and (b) Pt-CeO_2 rods, determined from 2-50 Å PDF refinements using an ideal Fluorite model.

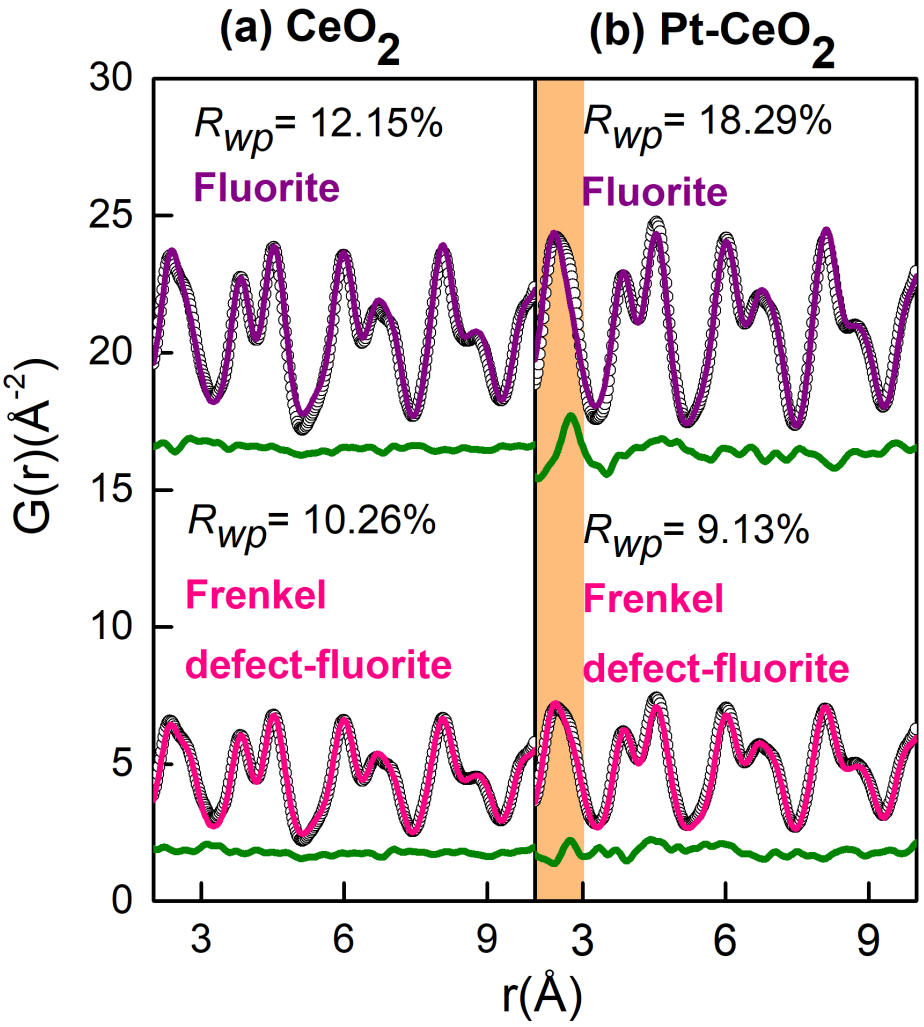


Figure 2.7: 2-10 Å PDF fit results for (a) CeO_2 and (b) Pt- CeO_2 nanorod data measured under D_2 flow at 400 °C. Data was fit to a single phase ideal Fluorite model and a two phase structure model with a bulk ideal fluorite structure and a secondary surface structure containing oxygen Frenkel-type defects. 8*c* and 24*e* oxygen occupancies were refined in the secondary phase structure. Data are shown as circles, fits as colored lines through the data, and difference curves fall below the data and fits.

This indicates that the Pt-CeO_2 rods have a surface structure that is distinct from the CeO_2 rods and that the Frenkel Defect-Fluorite model alone does not accurately represent the local structure of the Pt-CeO_2 rods.

Additionally, oxygen vacancy ordered ceria defect structures reported by Luo et al. [41] and Kummerle et al. [111] were applied to the CeO_2 and Pt-CeO_2 nanorods. It is important to note that these defect structures are derived from pre-reduced ceria nanorod and ceria single crystal samples, respectively, studied using *ex-situ* measurements and hence may not resemble the defect states of the ceria and Pt- CeO_2 ceria nanorods used in this study and in industrial catalytic converters. Neither of these models produced a significant improvement in fit quality compared to the Frenkel Defect-Fluorite model despite the inclusion of additional refineable parameters.

Therefore, oxygen Frenkel defects were found to most accurately describe the surface CeO_{2-x} structure of the CeO_2 and Pt-CeO_2 rods used in this study. The difference in the observed oxygen vacancy structures in the ceria nanorods derived from the *ex-situ* study by Luo et al,[41] and the present *in-situ* study brings in to question the relevancy of *ex-situ* laboratory characterization to real-word catalyst development.

Since oxygen vacancy ordered ceria defect structures were not able to entirely model the peak present at 2.9 Å in the Pt-CeO_2 rod data, the possibility of this peak having contributions from a Pt correlation was considered. As shown in Figure 2.8, applying the Frenkel Defect and Metallic Pt model to the Pt-CeO_2 rod data resolves the peak misfit at 2.9 Å. Furthermore, Figure 2.9 indicates that the Frenkel Defect and Metallic Pt model produces Pt-CeO_2 nanorod PDF fits which are similar in quality to that obtained for the CeO_2 rods using the Frenkel defect-fluorite model.

The nature of platinum bonding on the surface of ceria is highly dependent on the synthesis method and redox environment. [84]

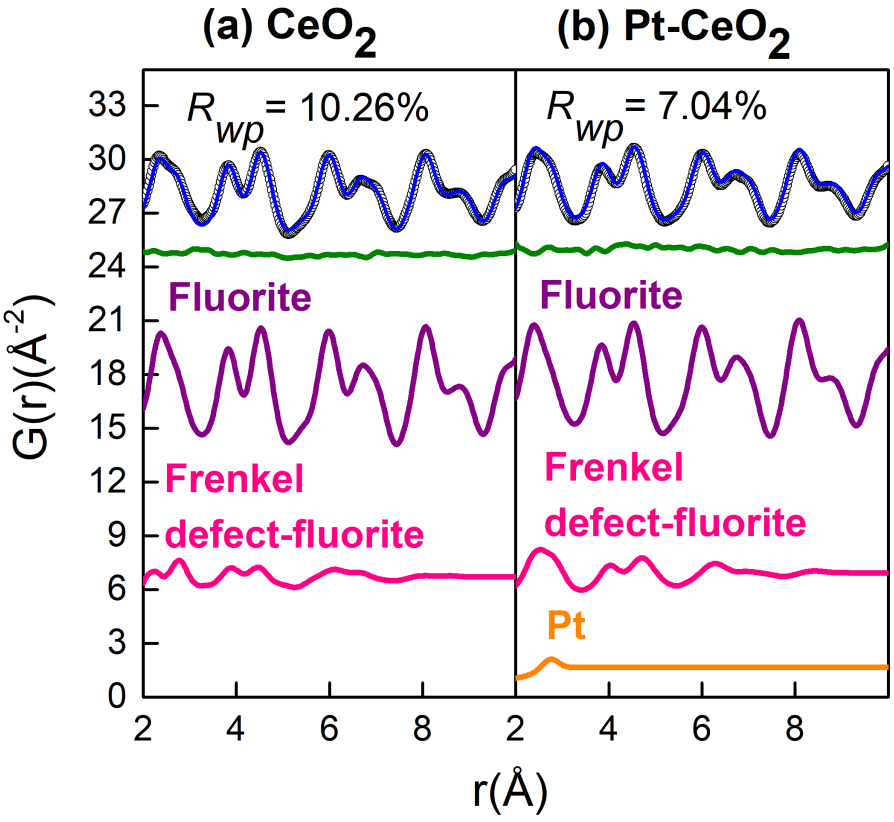


Figure 2.8: 2-10 Å PDF fit results for (a) CeO_2 and (b) Pt-CeO_2 nanorod data measured under D_2 flow at 400°C and fit with a two phase Frenkel Defect-Fluorite model for CeO_2 rods and three phase Frenkel Defect and Metallic Pt model for Pt-CeO_2 nanorods. Each phase contribution is shown.

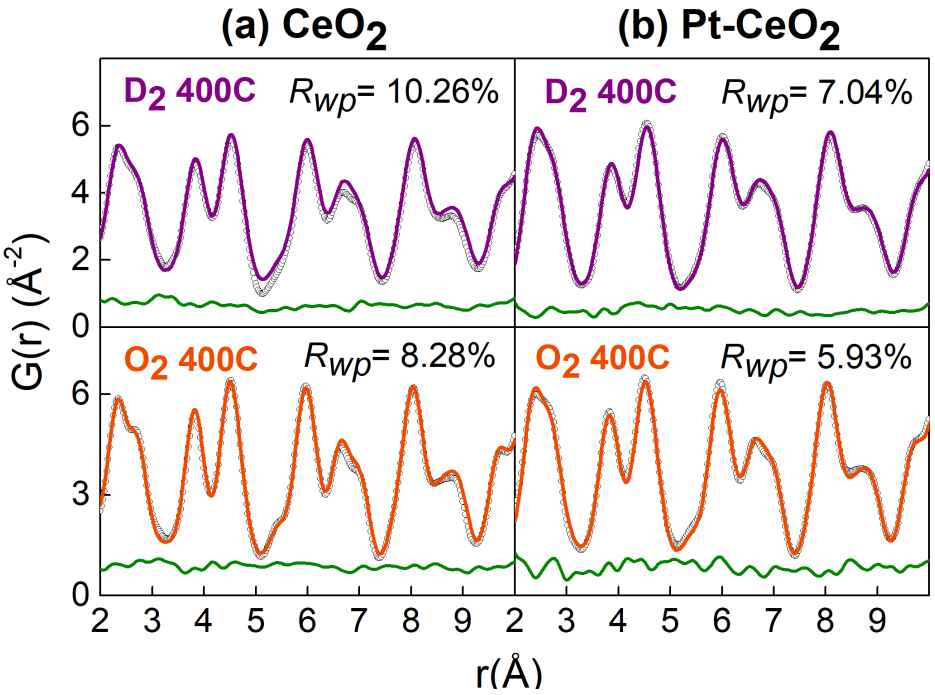


Figure 2.9: 2-10 Å PDF fit results for (a) CeO_2 and (b) Pt-CeO_2 nanorod data, collected under D_2 and O_2 flow at 400°C. Data was fit to a Frenkel defect-fluorite model for CeO_2 rods and Frenkel Defect and Metallic Pt model for Pt- CeO_2 nanorods. 8*c* and 24*e* oxygen occupancy's were refined in the secondary phase structure in both cases. Data are shown as circles, fits as colored lines through the data, and difference curves fall below the data and fits.

While Pt is known to be present in the form of PtO_2 and Pt-O-Ce bonds on the surface of Pt-CeO_2 nanoparticles, attempts to model the Pt-CeO_2 rod data with these structure types were unsuccessful as the reported bond lengths associated with these structures do not correspond with the correlation observed at 2.9 Å. [112, 84, 113] The data instead suggests the possible presence of small Pt nanometallic clusters on the surface of ceria in Pt-CeO_2 rods. However, it is important to note that this correlation could arise from contributions other than Pt-Pt and it is challenging to definitively determine the source based on a single peak correlation and PDF analysis alone.

Based on the 2-10 Å refinements shown in Figure 2.9, lattice parameters were extracted for the fluorite phase and the surface defect fluorite phase of the CeO_2 and Pt-CeO_2 rods. As seen in Figure 2.10 the lattice parameters of the fluorite and defect fluorite phase are similar for the CeO_2 rods while there is a significant difference in lattice parameters for both phases in the case of the Pt-CeO_2 rods. The lattice parameter from the local structure model of the defect phase of the Pt-CeO_2 rods is significantly larger than that of the fluorite phase, indicating the greater surface reducibility of the Pt-CeO_2 rods compared to the CeO_2 rods.

The nanoscale and phase complexity of the samples impedes the reliable refinement of absolute oxygen occupancy values. However, Figure 2.11 shows that the occupancy of the 24*e* oxygen interstitial site in the Frenkel defect pair shows sensitivity to redox flow conditions for the Pt-CeO_2 rods but not for the CeO_2 rods. To quantitatively determine if reduction effects are responsible for the lattice expansion observed in Pt-CeO_2 rods and CeO_2 rods, the change in Ce^{3+} percentage as a function of temperature and gas flow was determined using NAP-XPS measurements.

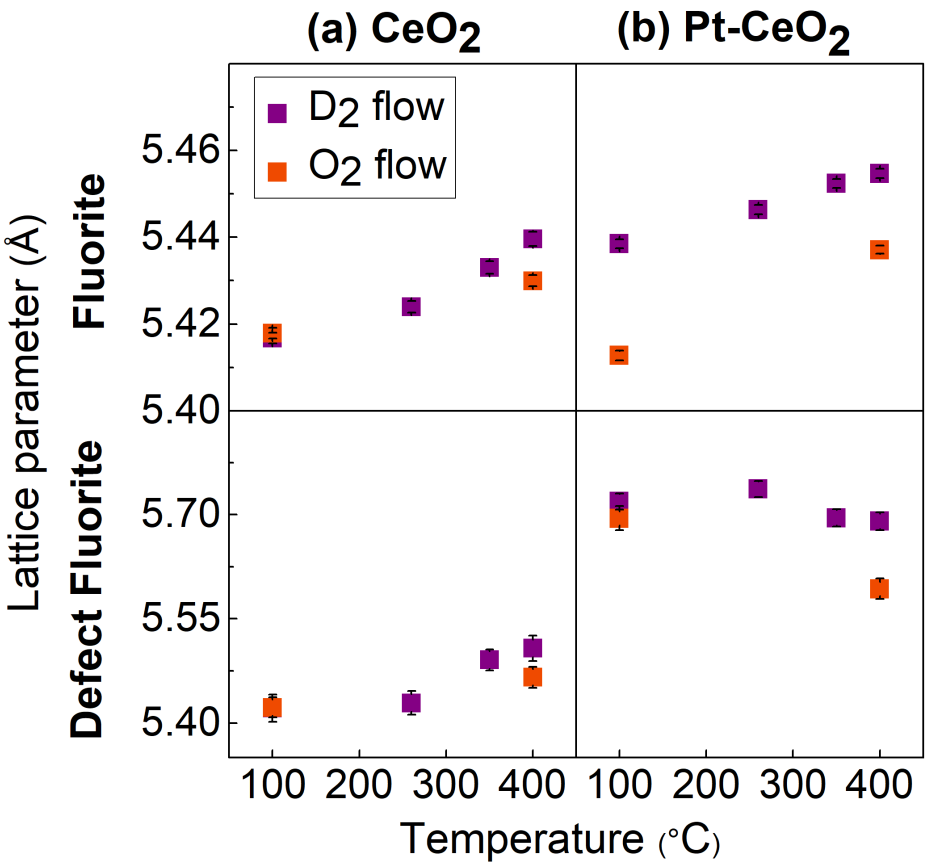


Figure 2.10: Lattice parameters for the bulk fluorite phase and surface Frenkel-type defect phase of (a) CeO_2 and (b) Pt-CeO_2 nanorods determined based on 2-10 Å PDF refinements fit with a Frenkel Defect-Fluorite model for CeO_2 rods and Frenkel Defect and Metallic Pt model for Pt- CeO_2 nanorods.

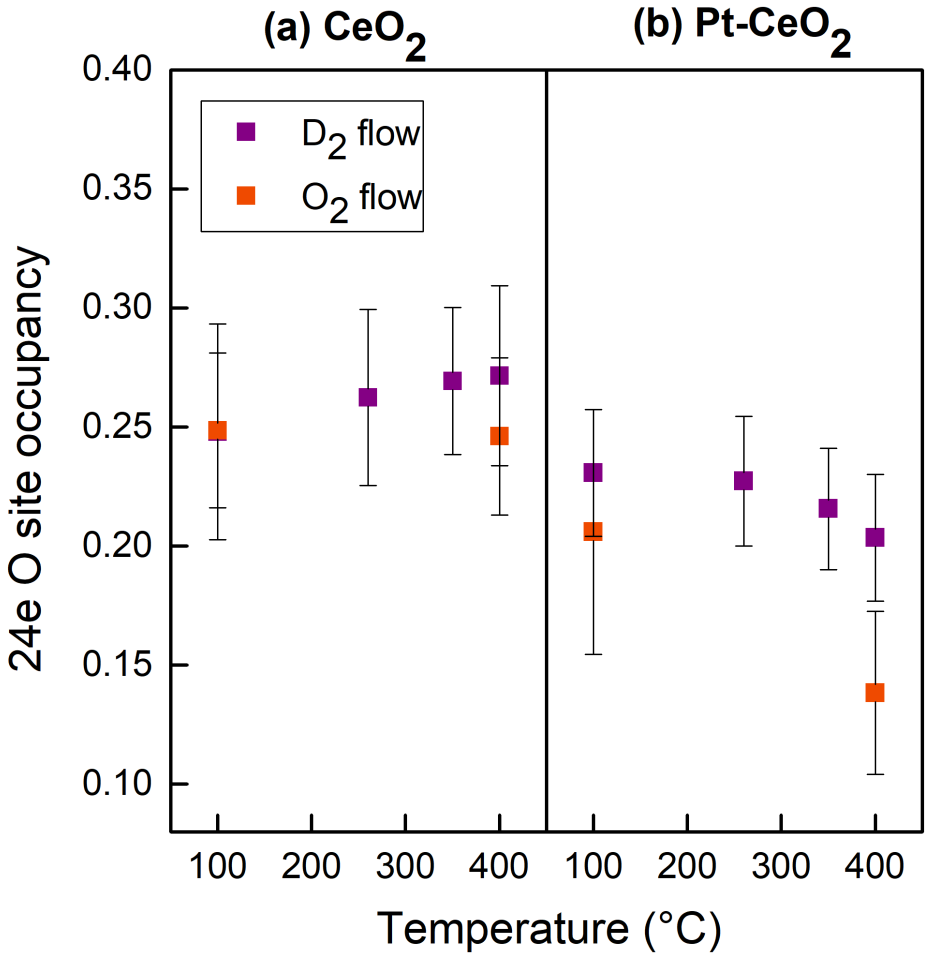


Figure 2.11: Occupancy values of the 24*e* octahedral interstitial oxygen site in the fluorite lattice for (a) CeO_2 and (b) Pt- CeO_2 nanorod data determined based on 2-10 Å PDF refinements with a Frenkel defect-fluorite model for CeO_2 rods and Frenkel Defect and Metallic Pt model for Pt- CeO_2 nanorods.

2.5.3 NAP-XPS Results

The change in Ce^{3+} percentage and lattice parameter estimated by PDF analysis for the measured temperature/gas flow conditions are shown in the Figure 2.12 for Pt-CeO_2 rods. Neutron diffraction and PDF analysis results show an increase in lattice parameter when switching from O_2 to D_2 flow and with increasing temperature under D_2 flow. A possible source of this lattice expansion is attributed to conversion of smaller Ce^{4+} cations to larger Ce^{3+} cations due to reduction effects.

For the case of Pt-CeO_2 rods, the percentage of Ce^{3+} increases from 3% to 13% when switching from O_2 to H_2 flow and from 13% under H_2 flow at 100°C to 22% H_2 flow at 350°C. This confirms the influence of reduction effects on lattice parameter in the Pt-CeO_2 rods, distinct from thermal expansion.

In the case of undecorated CeO_2 rods, no difference was observed between the Ce 3d spectrum for the fully oxidized state measured under O_2 environment at 400°C and spectra for H_2 environment at 260°C or H_2 environment at 350 °C. A difference was observed for the spectra measured under O_2 at 100°C and H_2 at 100°C, but the differences could not be correlated with changes in the valence state of Ce. Rather, spectral differences were caused by peak broadening effects, which were the result of sample charging during the measurement.

Thus, it appears that surface decoration by platinum plays an active role mediating the effect of ambient gas molecules upon Ce oxidation state and charge-compensating oxygen vacancy formation.

2.6 Conclusion

We have investigated the structural evolution of CeO_2 and Pt-CeO_2 nanorods *in-situ* under oxidizing and reducing gas environments. Neutron diffraction and PDF analysis indicates that both CeO_2 and Pt-CeO_2 nanorods share a bulk fluorite structure with the presence of surface Frenkel-type oxygen defects.

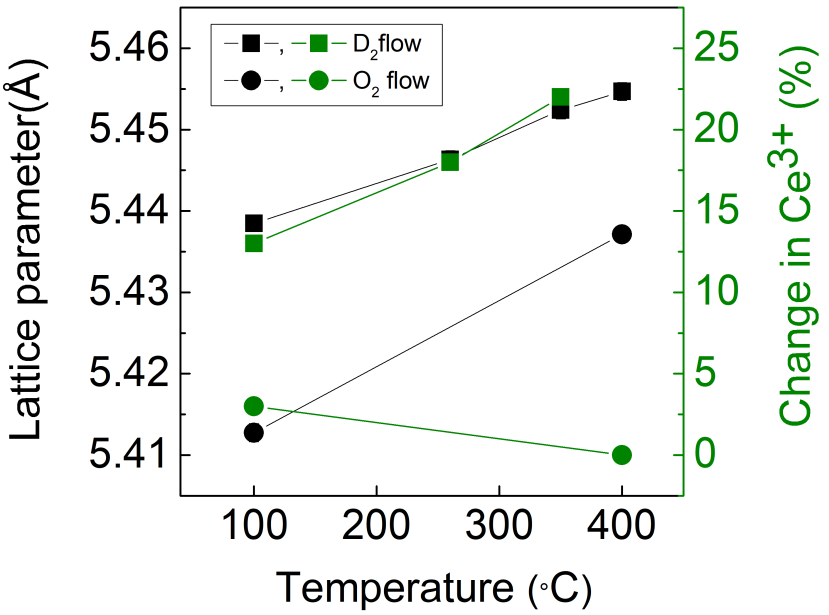


Figure 2.12: Change in percentage of Ce^{3+} for the Pt-CeO_2 rods, shown as a solid green square and circle to represent D_2 flow and O_2 flow respectively, as determined by NAP-XPS. Lattice parameters of Pt-CeO_2 nanorods as determined by PDF analysis are shown as a solid black square and circle to represent D_2 flow and O_2 flow respectively. The Frenkel Defect and Metallic Pt model was used for PDF refinements of the Pt-CeO_2 nanorods.

Contrary to earlier *ex-situ* investigations, this work finds no evidence of oxygen vacancy ordered surface reconstruction.

The lattice parameter of CeO_2 rods is indistinguishable under O_2 vs. D_2 flow while there is an appreciable increase in the lattice parameter of the Pt-CeO_2 rods when under reducing atmosphere. The lattice expansion of the Pt-CeO_2 rods is attributed to an increase in concentration of Ce^{3+}, corroborated by NAP-XPS. Given Ce redox is accompanied by charge and mass transport across the particle surface, it is inferred that Pt surface decoration enhances the kinetics of this process.

Short-range PDFs of the CeO_2 and Pt-CeO_2 rods exhibit additional features that can not be modeled by a bulk fluorite structure alone. Inclusion of oxygen Frenkel-type defects in the surface structure resolves all unfit peak correlations in the case of the CeO_2 rods. While the Frenkel-type defect structure improves the quality of the Pt- CeO_2 PDF fits, an unfit peak correlation remains at 2.9 Å which can be modeled using Pt nanometallic clusters. Based on the low percentage of Pt loading and limitations of the PDF technique, alternate characterization techniques are needed to confirm the presence of Pt in the form of clusters.

Finally, the discrepancy between *ex-situ* and *in-situ* structural observations are noteworthy. This work emphasizes the need for robust *in-situ* investigations of functional catalytic materials to confirm the mechanistic underpinnings of this important class of materials and extract design strategies for industrially relevant materials.

2.7 Acknowledgements

This work was supported by the U.S. Department of Energy, Office of Science, Office of Basic Energy Sciences Early Career Research Program Award KC040602, under Contract No. DE-AC05-00OR22725. Data analysis and interpretation was supported by the Graduate Advancement and Training Education fellowship and sponsored by the Science Alliance. Sample preparation was supported as part of UNCAGE-ME, an Energy Frontier Research Center funded by the U.S. Department of

Energy, Office of Science (Basic Energy Sciences), under Award No. DE-SC0012577. This research used beamline BL-1B (NOMAD) at the Spallation Neutron Source, a DOE Office of Science User Facility operated by the Oak Ridge National Laboratory.

Chapter 3

In-situ methane oxidation behavior of $CeZrO_4$ and Pd-$CeZrO_4$

A version of this chapter is under preparation to be submitted for publication by Sreya Paladugu, Bo Jiang, Stephen C. Purdy, Michelle S. Everett, Bekki Mills, Cheng Li* and Katharine Page*: Paladugu, S., Purdy, S., Jiang, B., Mills, B., Everett, M. M., Li, C., and Page, K. (2023). *In-situ* Neutron Total Scattering Studies on the Methane Oxidation and Reduction of $CeZrO_4$ and Pd-$CeZrO_4$. In preparation.

3.1 Abstract

The catalytic oxidation of methane (CH_4) is a promising strategy for mitigating CH_4 emissions and combating climate change. Pd-$CeZrO_4$ has demonstrated potential as a catalyst for methane oxidation due to its improved thermal stability and high oxygen storage capacity. In this work, we study the *in-situ* structural evolution of $CeZrO_4$ and Pd-$CeZrO_4$ under methane oxidation and reduction conditions using *in-situ* neutron total scattering to unravel the role of Pd on the nature of oxygen vacancies in $CeZrO_4$. The results from *in-situ* neutron diffraction reveal that Pd-$CeZrO_4$ exhibits an increased concentration of oxygen vacancies under methane oxidation reaction and reduction relative to pristine $CeZrO_4$. Additionally, the formation of oxygen vacancies in Pd-$CeZrO_4$, when switching from methane reaction to reduction, is accompanied by a phase transition of Pd-$CeZrO_4$ from a tetragonal to a cubic average structure. This intriguing observation is consistent with the improved reducibility and superior oxidation catalytic performance of Pd-$CeZrO_4$. Furthermore, *in-situ* neutron pair distribution function (PDF) analysis demonstrates that the generation of oxygen vacancies in Pd-$CeZrO_4$, when transitioning from methane oxidation to reduction, is associated with distinct cation local distortions for Ce and Zr, which is known to influence oxygen mobility and thus overall catalytic performance. This study provides fundamental insights into the role of Pd on enhancing the reducibility and methane oxidation catalytic activity of $CeZrO_4$ by increasing the concentration of oxygen vacancies and inducing distinct cation local distortions for Ce and Zr.

3.2 Introduction

Methane, an abundant greenhouse gas released into the atmosphere through industrial and automotive emissions, significantly contributes to environmental pollution and exacerbates climate change. [114, 115, 116, 117] The catalytic oxidation of methane (CH_4) has attracted interest as a potential approach to mitigate CH_4 emissions in an effort to combat climate change. [114, 118, 115, 119, 120] However, the complete oxidation of CH_4 at a low temperature has remained a long-standing challenge in the field of heterogeneous catalysis. [121, 115, 51, 122] Thus far, Pd loaded oxide supports have been regarded as the most active catalysts for the methane oxidation reaction. [123, 124, 125, 126, 127, 128, 119] Despite their high activity, Pd- based catalysts suffer from poor thermal stability and undergo rapid deactivation under reaction conditions due to sintering of the active phase of Pd into larger particles, resulting in a loss of surface area and reduction in catalytic activity. [122, 120, 129] Thus, the development of more efficient catalysts for the complete oxidation of CH_4 hinges on the design of scalable, low-cost, earth-abundant and sinter-resistant catalysts that can maintain higher surface area and facilitate long-term catalytic operation.

CeO_2- based oxides have been widely investigated as catalyst supports for methane oxidation due to their dynamic ability to store and release active oxygen by accommodating a high concentration of oxygen vacancies and due to the strong interfacial interaction between Pd and Ce which enables stabilization of the active phase of Pd. [120, 121, 122, 127, 128, 130, 123] Although pure CeO_2 is known to sinter at high temperatures, resulting in a decrease in oxygen storage capacity and catalytic activity, doping CeO_2 with Zr has been demonstrated as an effective materials design strategy to significantly improve thermal stability and oxygen storage capacity. [128, 131, 132] Ding et al. demonstrated that Pd- $CeZrO_4$ is active for the CH_4 oxidation reaction and that the crystal structure of the $CeZrO_4$ support can significantly impact methane oxidation catalytic activity by influencing

the (1) nature and stability of Pd active sites and (ii) concentration of oxygen vacancies in the support. [131] Literature studies on the structural characterization of Pd-$CeZrO_4$ for methane oxidation focus primarily on the behavior of Pd and its transformations, leaving unanswered questions about the nature of the underlying support and its interaction with Pd. Furthermore, while it is known that the concentration and location of oxygen vacancies in the surface/bulk of Pd-$CeZrO_4$ influences the resulting catalytic activity for methane oxidation [133, 134, 135], the evolution of oxygen defects and chemical short range order in neat and Pd-$CeZrO_4$ under operating reaction conditions has not been investigated.

Studying the structural evolution of catalysts *in-situ* can provide key insights into the nature of active sites being formed and consumed during the catalytic process and findings can be used to extract materials design strategies for more efficient and robust catalysts/supports. Total scattering is a promising technique for the study of structural evolutions of catalysts as well as gas-solid interactions as it can measure the long and short-range order of materials regardless of their crystallinity. Neutron total scattering in particular offers advantages for the study of catalysts under heterogeneous catalytic methane oxidation, due to the presence of light elements (C, H, O) that neutrons offer higher sensitivity to relative to x-ray or electron probes, facilitating the study of phenomena effectively "invisible" by other techniques. The synthesis method employed for $CeZrO_4$ can give rise to cubic or tetragonal crystal structures, and discerning between these structures using commonly employed x-ray techniques can be challenging due to the lack of sensitivity to subtle oxygen displacements. In this work, we use *in-situ* neutron total scattering to elucidate the role of Pd on the defect structure and stability of $CeZrO_4$ under oxidation, methane oxidation and methane reduction gas environments. Previous studies have demonstrated that exposing the catalyst to a reducing treatment, following the methane oxidation reaction, can aid in catalyst regeneration. [123, 136, 51, 137] Additionally, modern automotive engines are engineered to alternate between lean, stoichiometric, and rich gas environments to optimize fuel consumption and

to control exhaust gas. [136] Furthermore, this *in-situ* neutron total scattering study was used to commission a new quartz gas flow cell and high temperature furnace designed for the Nanoscale Ordered Materials Diffractometer instrument (NOMAD) at the Spallation Neutron Source, which enabled the collection of neutron diffraction and pair distribution function (PDF) data with improved signal to noise ratio relative to previous sample environments. Importantly, results from this *in-situ* neutron total scattering study will elucidate the influence Pd loading has on the nature and concentration of oxygen vacancies and local cation configurations in $CeZrO_4$ under methane oxidation and reduction reactions. [138]

3.3 Methods

3.3.1 Materials

Cerium (III) nitrate hexahydrate (99.5%), zirconyl (IV) nitrate (99.5%) and ethanol (99.5%) were purchased from Thermo Fisher Scientific. Metal nitrate hydrates were used to prepare sealed aqueous stock solutions immediately upon receipt from the manufacturer. Pluronic P123 (a symmetric triblock copolymer comprising poly(ethylene oxide) (PEO) and poly(propylene oxide) (PPO) in an alternating linear fashion) and tetraamminepalladium (II) chloride monohydrate (99.9%) were purchased from Sigma Aldrich.

3.3.2 Synthesis of $CeZrO_4$ and Pd-$CeZrO_4$

Mesoporous $CeZrO_4$ was synthesized using a soft templating approach via evaporation induced self-assembly (EISA). Metal nitrate precursor solutions were dissolved in ethanol, under continuous stirring, using Pluronic P123 as a block copolymer template. The solutions were allowed to evaporate in a petri dish at room temperature for 48 hours and the resulting gels were calcined in air at 600 °C for 4 hours in an oven.

Pd-$CeZrO_4$ was prepared via a traditional incipient wetness impregnation method with $Pd(NH_3)_4Cl_2$ solution to achieve 1 wt% Pd loading over $CeZrO_4$. The catalyst was dried at room temperature for 3 hours, subsequently placed in the oven to dry overnight at 120 °C and then placed in the furnace to calcine at 230 °C for 3 hours.

The samples were pressed, ground, and sieved and the fraction larger than 200 μm was retained for *in-situ* neutron total scattering measurements, to enable gas flow through the powder bed.

3.3.3 Neutron Total Scattering Measurements

Neutron powder diffraction (NPD) and atomic pair distribution function (PDF) data were collected on the NOMAD instrument (Spallation Neutron Source, Oak Ridge National Laboratory). [95] $CeZrO_4$ and Pd-$CeZrO_4$ were measured using the set-up and gas flow conditions seen in Figures 3.1 and 3.2.

A 15.97 cm long and 0.95 cm diameter custom quartz tube with a porous frit bonded 1 cm below the sample center, was designed to minimize quartz background contribution during the measurement while enabling high temperature gas flow measurements. 1 g of $CeZrO_4$ or Pd-$CeZrO_4$ sample was loaded into a specialized quartz gas flow cell, mounted on a sample stick within a vacuum furnace (with 850 °C capability) and connected to the gas-flow system. Quartz wool was placed above and below the sample bed to maintain the correct sample height in the neutron beam.

The surface of the mounted sample was cleansed of any adsorbed species by flushing with Ar for 40 minutes. The samples were oxidized in 20% O_2 in Ar at 400°C for 2 hours and the data measured under this gas flow condition is hereafter referred to as "oxidation". The temperature was ramped up to 550 °C with a 10° C per minute ramp, the sample was reacted under 2.25% CD_4, 20% O_2 in Ar at 550°C for 4 hours and the data measured under this gas flow condition is labelled "reaction".

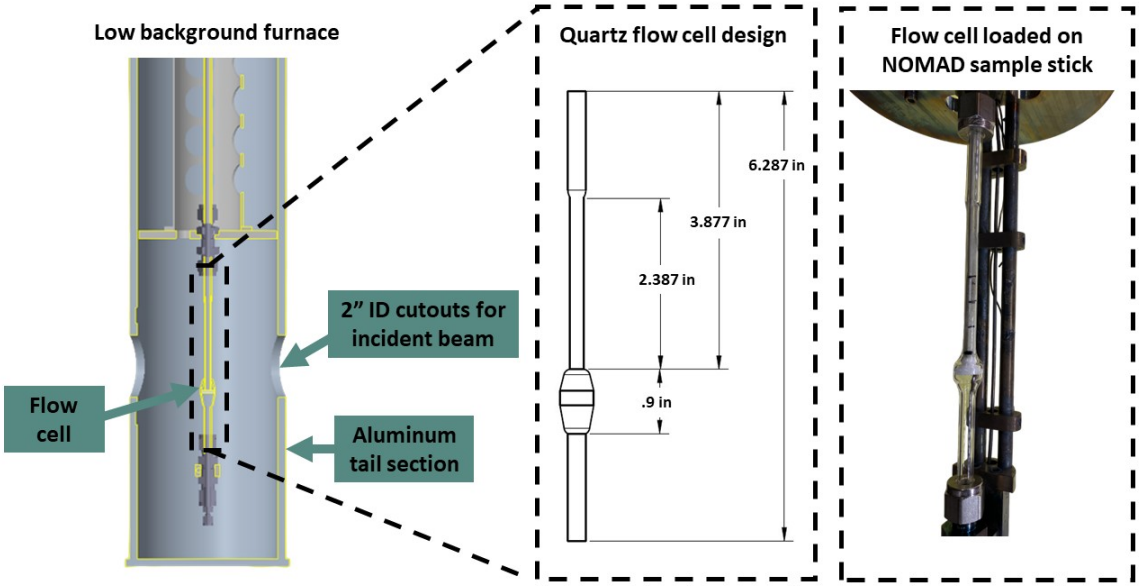


Figure 3.1: Schematic showing new low background high temperature furnace (left), dimensions of new quartz gas flow cell (center) and new quartz flow cell with Pd-$CeZrO_4$ sample loaded on NOMAD sample stick (right).

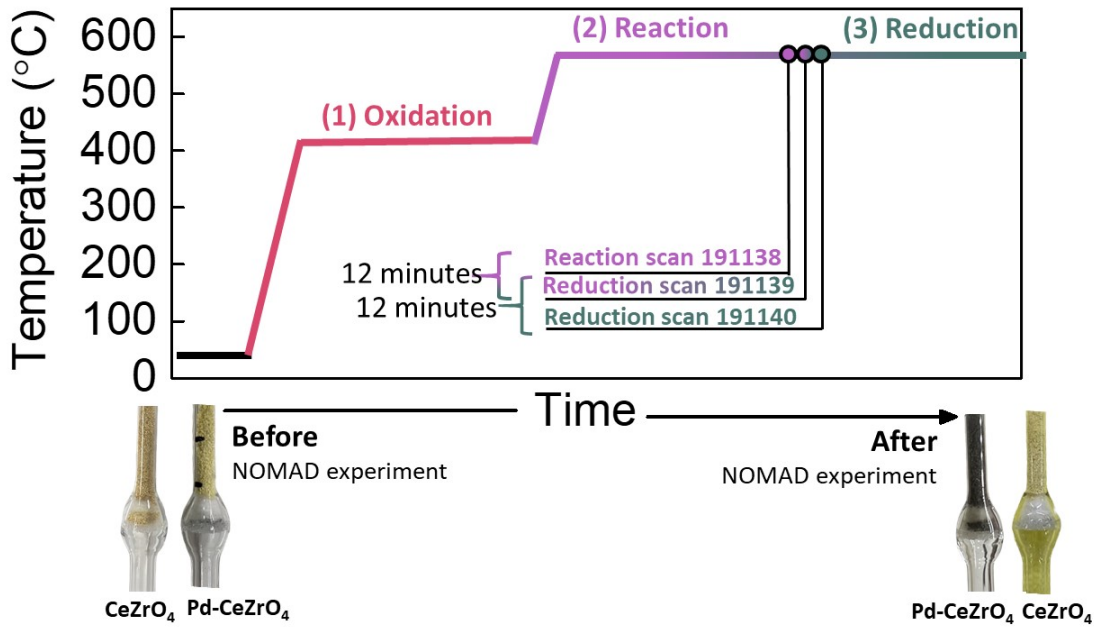


Figure 3.2: Schematic showing new low background high temperature furnace (left), dimensions of new quartz gas flow cell (center) and new quartz floe cell with Pd-$CeZrO_4$ sample loaded on NOMAD sample stick (right).

The gas flow was switched to a mixture of 2.25% CD_4 and He for 6 hours and the data measured under this gas flow condition is termed "reduction". Comparison of the series of 12 minute datasets for $CeZrO_4$ under all measurement conditions and Pd-$CeZrO_4$ under oxidation and reaction revealed that the subsets of data within each gas flow condition were approximately invariant. This demonstrates steady state reaction conditions were achieved quickly across the sample. Interestingly for the Pd-$CeZrO_4$ sample measured under reduction, *in-situ* data showed structural evolution over the course of the first 12 minutes under reduction gas flow. A measurement timeline summarizing the experimental conditions in this study is presented in Figure 3.2. As shown in the images of the quartz samples cells (bottom) of Figure 3.2, the as synthesized pale yellow $CeZrO_4$ sample appeared to be a darker shade of yellow after exposure to the sequence of gas flow environments in the NOMAD experiment while the previously pale yellow Pd-$CeZrO_4$ sample was observed to be black in color after the measurements, suggesting reduction of the sample.

The reactant gas species involved in each measurement condition and the methane oxidation reaction products were monitored using a Residual Gas Analyzer. As the m/z of methane (20) overlaps with that of doubly ionized Ar, changes in the concentration of CO_2 were used to confirm the catalytic oxidation of methane.

Temperatures for the reaction and reduction neutron total scattering measurements were chosen by performing a lab scale methane oxidation reaction at 400°C which resulted in 89% methane conversion. In this setup, the thermocouple must sit above the neutron beam to avoid parasitic scattering. A sample temperature calibration curve was generated off-line to control the temperature during the measurement using an offset. These considerations indicate additional advances in nimble and low background sample environments for *in-situ* and *operando* neutron total scattering are desirable to draw correlative conclusions between data from neutron total scattering measurements of catalytic systems and lab scale catalytic studies.

Signal from the empty quartz container was collected at 400°C and 550°C, to facilitate background subtraction from the sample data. A series of 12 minute scans were collected at each temperature and gas flow condition and the data were summed to improve statistics. Each data set was time focused, normalized, and histogrammed, and a Q_{max} of 35 $Å^{-1}$ was applied for generation of PDF data. In addition to the summed data sets, the last 12 minute data set measured under oxidation gas flow and the first two, 12 minute scans, measured under reduction flow for Pd-$CeZrO_4$ were analyzed. The results from these individual data sets are analyzed in Figure 3.8 while all other analysis is based on summed data sets to improve signal to noise ratio.

The presence of adsorbed hydrogen (e.g. as chemisorbed hydroxyls and physisorbed water) can result in an incoherent scattering signal which appears as an approximately pseudo-Voigt-like background (centered at Q = 0 $Å^{-1}$) that results in large-amplitude artefacts in the low-r region of the PDF. [97, 98] This effect is not well described analytically for TOF instruments and is generally removed in ad-hoc fashion. [97, 99] Additionally, Fourier filtering was applied during data reduction, to produce the expected limiting behavior [100] of the total scattering structure function *F(Q)* and the reduced pair distribution function *G(r)*,

$$\lim_{Q\to\infty} F(Q) = 0 \tag{3.1}$$

$$\lim_{r\to 0} G(r) = -4\pi r\rho_0. \tag{3.2}$$

3.3.4 Neutron Diffraction and PDF Analysis

The initial average structures were obtained through Rietveld refinements of neutron diffraction date using TOPAS v6 software [103]. The tetragonal fluorite phase with space group (S.G.) $P4_2/nmc$ was used as a model for all neutron diffraction data refinements, while the Pd-$CeZrO_4$ reduction data were examined using the fluorite $Fm\bar{3}m$ cubic phase. It was found during analysis that a minor

5% cubic fluorite CeO_2 phase was present in the two neutron samples. In the Rietveld analysis, the following parameters were refined: scale factor, profile parameters, unit cell parameters, background, atomic positions, isotropic atomic displacements, and oxygen site occupancies (O_{occ}). The resulting experimental pair distribution function (PDF) data were subsequently analyzed using least-squares small-box modeling in PDFgui [139]. The phase fraction and refined parameters for the impurity phases were fixed and applied as a secondary phase contribution in the neutron PDF analysis. Refinements of the locally distorted Pd-$CeZrO_4$ under reduction was tried using the tetragonal (t), fluorite and tetragonal + pyrochlore models were performed in a similar manner. [140, 141, 142]

For local structure refinements using previously reported pyrochlore (P) [143], beta $Ce_2Zr_2O_{7.5}$ phase [143], fluorite $CeZrO_4$ and K-$CeZrO_{8-x}$ [144] structural models, the oxygen occupancy was fixed while scale factors, lattice parameters, and cation and oxygen atomic displacement were refined resulting in a large number of structural parameters and overfitting.

3.3.5 Density Functional Theory Calculations

Density functional theory (DFT) calculations were carried out using the plane-wave-based Vienna Ab initio Simulation Package VASP, within the generalized gradient approximation (GGA) using the Perdew-Burke-Ernzerhof for solids (PBEsol) exchange-correlation functional in combination with the standard projector augmented wave (PAW) potential. The plane waves were expanded up to a cutoff energy of 550 eV. Brillouin zone integration was done on a $2 \times 2 \times 2$ k-point mesh grid for the single pyrochlore phase with 96 atoms. Full geometry optimizations were performed until the Hellman-Feynman forces on the atoms were relaxed below 10^{-2} eV/Å.

3.4 Results and Discussion

3.4.1 Average Structure

The measured diffraction patterns of $CeZrO_4$ and Pd-$CeZrO_4$ under the selected gas flow conditions are shown in Figure 3.3 (a). Upon comparing the diffraction patterns of $CeZrO_4$, we find that all Bragg peaks can be indexed to a $CeZrO_4$ primary phase with (S.G.) $P4_2/nmc$ (hkl indices indicated by tick marks in black). However, when transitioning from a methane oxidation to reduction gas flow environment, we observe peak shifts towards a higher diffraction angle, indicating lattice expansion. A similar, and more significant lattice expansion is observed under methane reaction gas flow in Pd-$CeZrO_4$. Furthermore, the peak [102] present at 2.24 Å under methane oxidation and reaction, disappears under methane reduction conditions for Pd-$CeZrO_4$, indicating a transition from the tetragonal $P4_2/nmc$ fluorite to cubic $Fm\bar{3}m$ fluorite phase. [140, 141, 142] As the tetragonal to cubic phase transition involves the displacement of oxygen atoms along the c-axis, the x-ray diffraction patterns appear indistinguishable due to the lack of sensitivity of x-ray probes to oxygen, a noted limitation of x-ray based characterization techniques in previous studies of $CeZrO_4$. [141] However, neutron diffraction definitively identifies the phase transition in this study.

Quantitative analysis of the diffraction patterns was performed through Rietveld refinements, with refinements for Pd-$CeZrO_4$ under oxidation, reduction at t = 0 min and reduction at t = 12 min shown in Figure 3.3 (b). The diffraction patterns of $CeZrO_4$ under all gas flow conditions and Pd-$CeZrO_4$ under oxidation and reduction at t = 0 min were successfully refined using a two phase structural model comprising of a tetragonal primary phase with space group (S.G.) $P4_2/nmc$ and secondary CeO_2 cubic phase with S.G. $Fm\bar{3}m$.

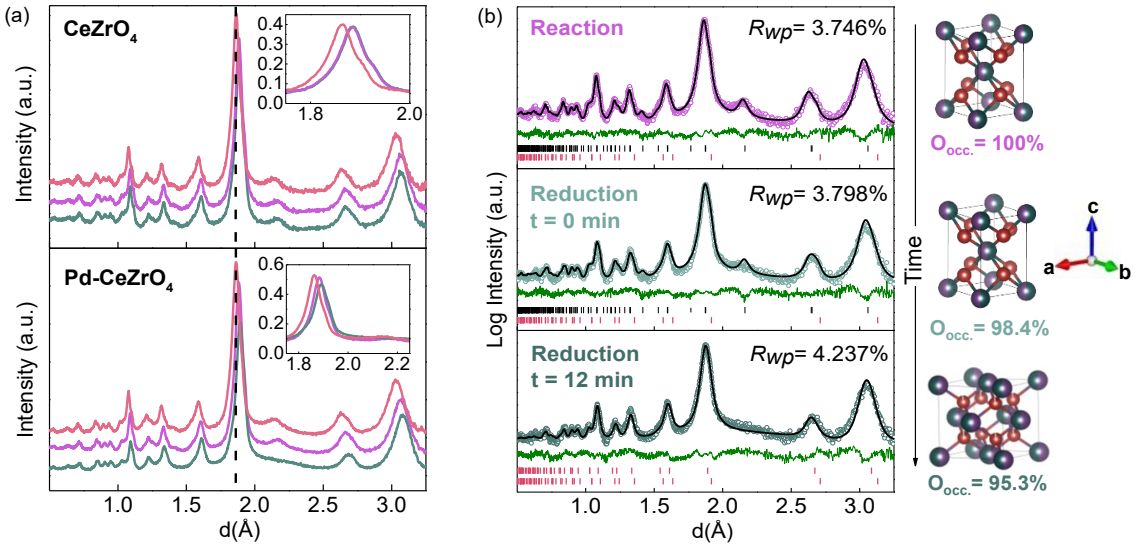


Figure 3.3: (a) Neutron diffraction patterns of $CeZrO_4$ and Pd-$CeZrO_4$ under oxidation (red line) at 400°C, methane oxidation reaction (purple line) at 550°C and methane reduction (green line) gas flow at 550°C. (b) Rietveld refinements of the neutron diffraction data of Pd-$CeZrO_4$ measured under methane oxidation reaction (top panel), methane reduction immediately upon switching gas flow environments (beginning at t = 0 min and including the first 12 minutes of data, labeled t = 0 min) (middle panel) and methane reduction gas flow beginning at t = 12 min of flow and including the subsequent 12 minutes of data, labeled t = 12 min. Measured data is shown as colored circles, structural fits are shown as black lines through the data and the difference curves in green fall below the data and fits. Pd-$CeZrO_4$ measured under methane reaction and methane reduction t = 0 min gas flow conditions were refined using two phase models comprising of a $CeZrO_4$ primary phase with (S.G.) $P4_2/nmc$ (hkl indices indicated by tick marks in black) and a secondary CeO_2 impurity phase with (S.G.) $Fm\bar{3}m$ (hkl tick marks in red). Pd-$CeZrO_4$ measured under methane reduction at t = 12 min was refined using a two phase model composed of $CeZrO_4$ and an impurity CeO_2 phases both with (S.G.) $Fm\bar{3}m$ (hkl tick marks in red). (c) Corresponding crystal structures used to refine the primary phases of Pd-$CeZrO_4$ measured under methane oxidation reaction, methane reduction at t = 0 min and methane reduction at t = 12 minutes, with corresponding refined oxygen atom occupancy shown.

However, under methane reduction conditions, Pd-$CeZrO_4$ was refined using a two phase model comprising of two cubic phases with S.G. $Fm\bar{3}m$ and distinct lattice parameters. Importantly, Pd loading appears to facilitate the phase transition from a tetragonal to cubic average structure when switching from methane reaction to reduction gas flow, as shown by the crystal structures displayed in Figure 3.3 (b), in Pd-$CeZrO_4$. [140, 141, 142] Additionally, as seen from the refined parameters from Rietveld refinements shown in Figure 3.4 the oxygen stoichiometry of $CeZrO_4$ remains stable, without the presence of oxygen defects, under all measured gas environments. Interestingly, the oxygen occupancy values of Pd-$CeZrO_4$ indicate a transition from a fully occupied oxygen sub-lattice in the tetragonal average structure under oxidation and reaction, to a cubic fluorite lattice containing ~5% oxygen vacancies under methane reduction. The formation of oxygen vacancies in Pd-$CeZrO_4$ under methane reduction suggests that Pd loading enhances the reducibility of $CeZrO_4$.

Previous literature reports have associated an increase in lattice parameter and cell volume of ceria-based mixed oxides under reducing atmospheres, with the generation of oxygen vacancies along with conversion of Ce^{4+} to Ce^{3+}, as Ce^{3+} has a larger ionic radius (1.034 Å) relative to Ce^{4+} (0.92 Å). Based on the average structure models for $CeZrO_4$ and Pd-$CeZrO_4$ under the measured gas conditions, the associated tetragonal unit cell volume was calculated as shown in Figure 3.5. Since Pd-$CeZrO_4$ has a cubic primary phase with S.G. $Fm\bar{3}m$ under methane reduction gas flow, the cubic unit cell volume was converted to a tetragonal unit cell volume ($V_{tetragonal}=V_{cubic}/2$) for comparison with the other gas flow conditions. The lattice expansion of $CeZrO_4$ displayed in Figure 3.5(a) resulting from a change in gas flow from methane oxidation to reaction is reflected by a modest increase in cell volume. A more pronounced increase in cell volume is seen in Pd-$CeZrO_4$ as a function of gas flow change from methane oxidation to reaction in Figure 3.5(b).

Samples, S.G.	R_{wp}(%)	Oz	O_{occ}	CeO_2	*a*, *c*	c/aF	Beq(Ce)	Beq(Zr)
CeZrO4, oxidation (T)	3.657	0.2188(5)	1	0.041	3.7511(7), 5.292(2)	0.9976	0.69(2)	1.64(3)
CeZrO4, reaction (T)	2.996	0.2183(5)	1	0.038	3.7547(4), 5.304(1)	0.9989	0.75(2)	1.78(2)
CeZrO4, reduction (T)	2.992	0.2182(4)	1	0.033	3.7538(5), 5.306(2)	0.9995	0.77(2)	1.81(2)
Pd-CeZrO4, oxidation (T)	2.902	0.2196(5)	1	0.056	3.7515(6), 5.288(2)	0.9967	0.64(2)	1.37(2)
Pd-CeZrO4, reaction (T)	2.703	0.2199(4)	1	0.042	3.7560(6), 5.302(2)	0.9982	0.74(2)	1.72(2)
Pd-CeZrO4, reduction (T)	2.906	0.233(2)	0.958(4)	0.063	3.781(2), 5.346(6)	0.9998	1.09(3)	3.47(5)
Pd-CeZrO4, reduction (F)	3.138	—	0.948(4)	0.064	5.3463(6)	—	1.10(3)	3.56(4)

Figure 3.4: Refined parameters from Rietveld refinements of neutron diffraction data for $CeZrO_4$ and Pd-$CeZrO_4$ under oxidation, reaction, and reduction gas flow environments. $CeZrO_4$ under all measured gas environments and Pd-$CeZrO_4$ under oxidation, reaction and reduction at t = 0 min were refined using a two phase structural model composed of S.G. $P4_2/nmc$ and a secondary CeO_2 impurity phase with $(S.G.)$ $Fm\bar{3}m$. In the tetragonal phase, O_{occ} did not vary from 1 and was thus fixed to 1. Pd-$CeZrO_4$ measured under methane reduction at t = 12 min was refined using a two-phase model composed of $CeZrO_4$ and an impurity CeO_2 phase both with $(S.G.)$ $Fm\bar{3}m$.

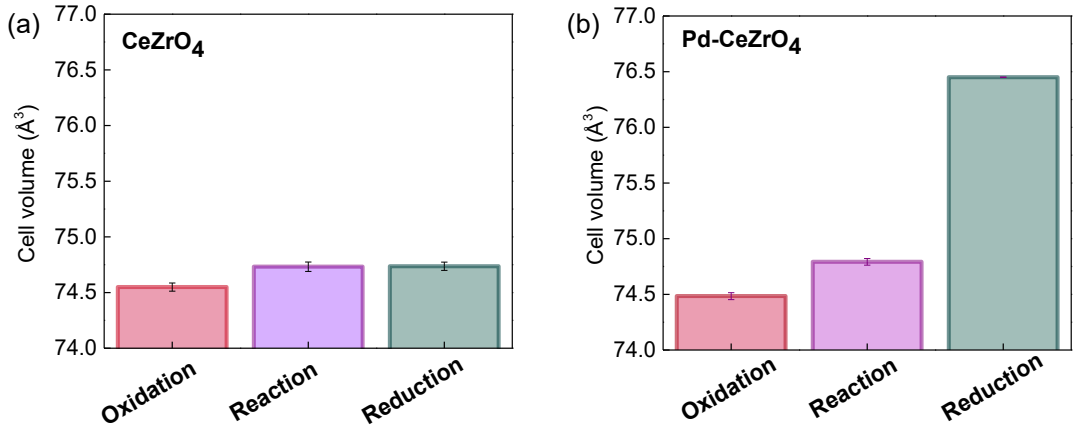


Figure 3.5: Tetragonal unit cell volume of (a) $CeZrO_4$ and (b) Pd-$CeZrO_4$ under all measured gas flow conditions calculated from Rietveld refinements of neutron diffraction data. Pd-$CeZrO_4$ has a fluorite crystal structure with (S.G.) $Fm\bar{3}m$ under methane reduction. The fluorite unit cell volume was converted to a psuedo tetragonal unit cell volume ($V_{tetragonal}$=$V_{cubic}/2$) for comparison.

Furthermore, while the cell volume of $CeZrO_4$ remains relatively unchanged upon switching from methane reaction to reduction, there is a significant increase in cell volume of Pd-$CeZrO_4$. Interestingly, while Pd-$CeZrO_4$ initially displays a slightly smaller cell volume than $CeZrO_4$ under oxidation, Pd-$CeZrO_4$ exhibits a larger cell volume, and a more pronounced increase in volume, than $CeZrO_4$ under methane reaction and reduction conditions. The more dramatic increase in cell volume of Pd-$CeZrO_4$ as a result of exposure to increasingly reducing gas flow conditions, suggests that Pd-$CeZrO_4$ has a larger concentration of oxygen vacancies and possibly more Ce^{3+} than $CeZrO_4$ and is evidence that Pd loading of $CeZrO_4$ enhances reducibility.

3.4.2 Local Structure

The average structure models from neutron diffraction refinements were applied to fit neutron PDFs of $CeZrO_4$ and Pd-$CeZrO_4$ from 1.5-30 Å, as shown in Figure 3.6 (a) and (b) respectively, to follow local structure trends evolving *in-situ* and investigate any deviations in the local and intermediate structure from the average structure. The two phase average structure model comprising of a tetragonal primary phase with S.G. $P4_2/nmc$ and a secondary CeO_2 cubic phase with S.G. $Fm\bar{3}m$, provides a reasonable fit to the PDFs for $CeZrO_4$ under all measured gas conditions and Pd-$CeZrO_4$ under oxidation and methane reaction. However, inspection of the low-r region of the PDF below 4 Å for Pd-$CeZrO_4$ measured under methane reduction indicates a significant discrepancy in the fit of the two phase cubic fluorite structural model to the measured data. Thus Pd-$CeZrO_4$ is found to evolve a distinct local structure under methane reduction gas flow. As shown in Figure 3.7, additional fits to the local atomic structure were attempted to further explore the nature of induced local structure defects, chemical short range order, or local atomic distortions for the Pd-$CeZrO_4$ data set. It was found that the tetragonal fluorite model that describes other gas flow conditions improves the fit locally, as evidenced by the lower R_{wp}, relative to the average cubic fluorite structure. This suggests the average fluorite structure arises from a super-positioning of local tetragonal motifs.

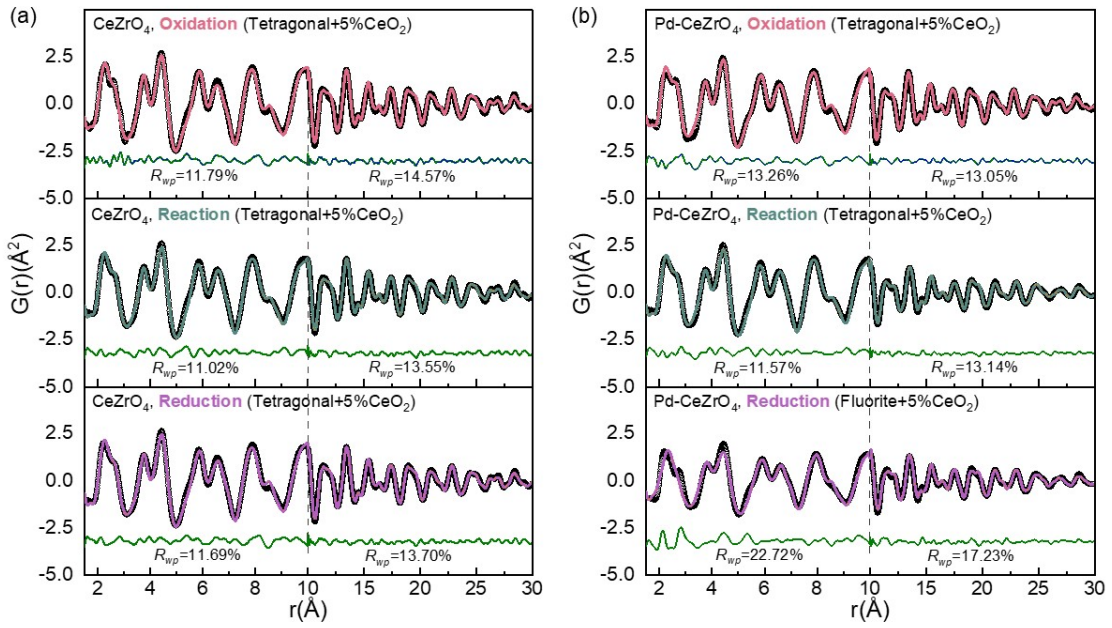


Figure 3.6: 1.5-30 Å PDF fit results for (a) $CeZrO_4$ and (b) Pd-$CeZrO_4$ under all measured gas flow conditions. $CeZrO_4$, under all measured gas conditions, and Pd-$CeZrO_4$ under oxidation and methane reaction gas flow were refined using a two phase model composed of a tetragonal $CeZrO_4$ primary phase with (S.G.) $P4_2/nmc$ and an impurity CeO_2 phase with (S.G.) $Fm\bar{3}m$. Pd-$CeZrO_4$ was refined using a two phase model with S.G. $Fm\bar{3}m$ composed of $CeZrO_4$ and an impurity CeO_2 phase. Data are shown as colored circles, fits as black lines through the data, and difference curves in green fall below the data and fits. Note that data below 10 Å is shown at enlarged scale relative to data above 10 Å.

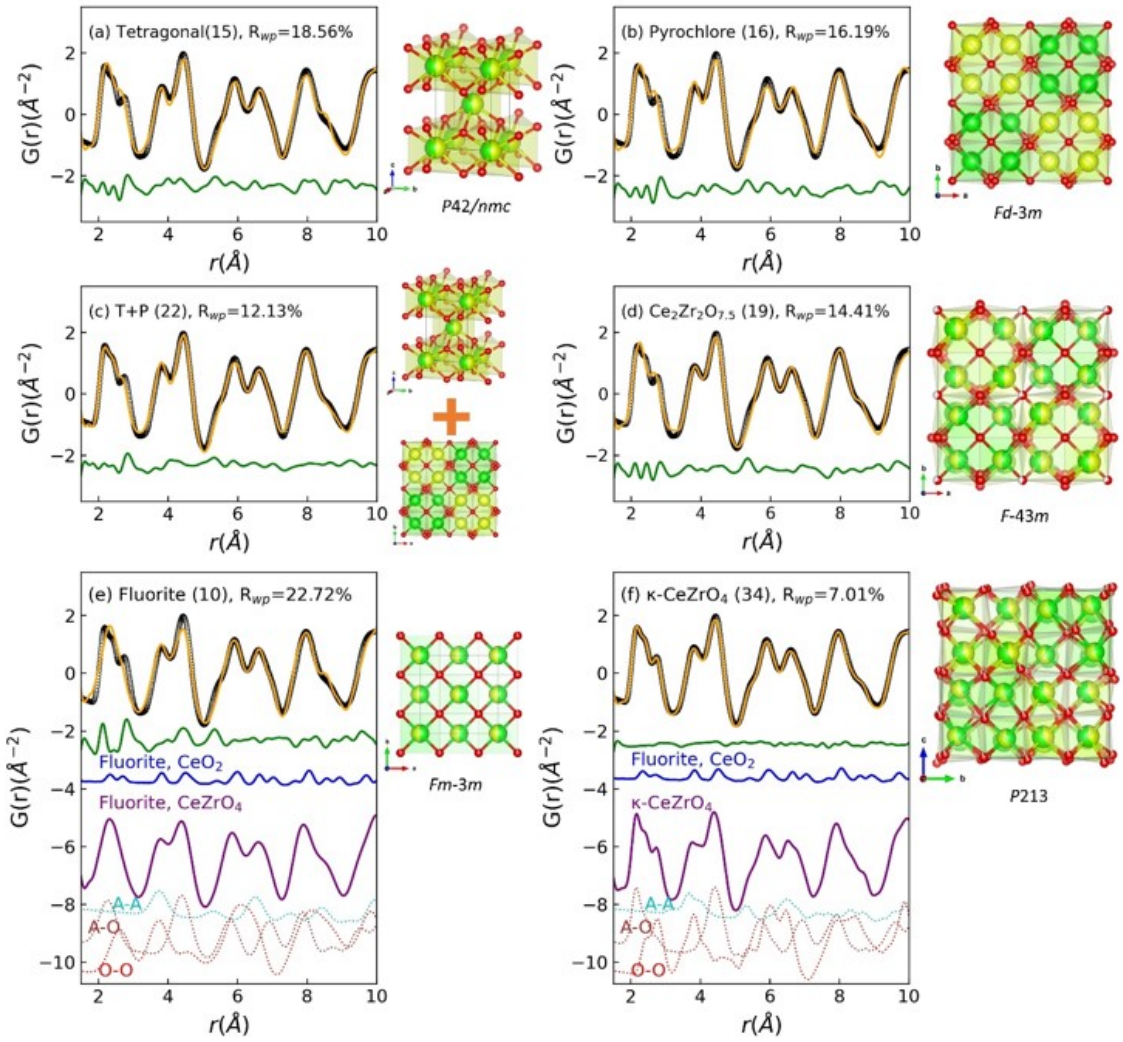


Figure 3.7: 1.5-10 Å Refinement results of PDF analysis for Pd-$CeZrO_4$ reduction data derived from various attempted structural models known to exist in $CeZrO_x$ solid solutions: (a) tetragonal (T), (b) pyrochlore (P), (c) T + P model, (d) beta $Ce_2Zr_2O_{7.5}$ phase, (e) fluorite $CeZrO_4$ and (f) K-$CeZrO_{8-x}$ phase. A 5% secondary CeO_2 cubic phase is included in all fits. In (e) and (f), a comparison of each phase contribution and partial PDFs of $CeZrO_4$ (dotted lines) are shown below the measured data. Subset figures (a), (c) and (e) show structural models where the cation sublattice is disordered and occupied on average 50/50 by Ce/Zr. Subset figures (b), (d) and (f) show structural models with varying degrees of cation ordering. (No.) indicates the total number of refined parameters in each model. Black circles and orange lines correspond to the experimental and calculated PDF data, respectively. The difference curves are presented at the bottom of each panel, and the R_{wp} values for comparison are indicated at the top right.

However, the tetragonal fluorite is still a poor description of the first few Å of the PDF. Average structure refinements indicate the formation of an increasing concentration of oxygen vacancies upon switching gas flow from methane reaction to reduction. Previous literature reports have shown that the formation of oxygen vacancies in $CeZrO_4$ can lead to ordering of the cation sub-lattice. [145, 146, 143] Subset figures (a), (c) and (e) show structural models where the cation sublattice is completely disordered and occupied on average 50/50 by Ce/Zr. The reported phases for $CeZrO_x$ solid solutions characterized by varying oxygen substoichiometry and degrees of Ce/Zr cation ordering were modeled as fits to the measured PDF data in this study as shown in subset Figure 3.7 (b), (d) and (f) corresponding to pyrochlore, beta $Ce_2Zr_2O_{7.5}$ and K-$CeZrO_{8-x}$ structures respectively.

Sasaki reported the presence of an intermediate phase, beta $Ce_2Zr_2O_{7.5}$, with a space group of $F\bar{4}3m$ which was observed during the oxidation process of pyrochlore $Ce_2Zr_2O_7$ to $Ce_2Zr_2O_{7+x}$ $(0 \leqslant x < 1)$. [143] Kishimote et al. reported the existence of a metastable K-$CeZrO_{8-x}$ phase with a space group of $P2_13$, as determined through powder x-ray diffraction studies. [146] Despite its metastable nature, the K-$CeZrO_{8-x}$ phase retained an ordered cation arrangement when compared to the fully disordered cation phase of $CeZrO_4$. The latter is characterized by a cubic fluorite structure or a metastable tetragonal fluorite t' phase with a space group of $P4_2/nmc$.[145] It is known that $Ce_2Zr_2O_{4-x}$ can undergo a structural transformation from $Ce_2Zr_2O_8$ with a fluorite structure to $Ce_2Zr_2O_7$ pyrochlore via an intermediate phase transition at $Ce_2Zr_2O_{7.5}$, under controlled oxidation/reduction conditions. This transformation is accompanied by a reduction in symmetry from $Fd\bar{3}m$ to $P2_13$ (K-$CeZrO_{8-x}$). We observed a slight improvement in the fit using a two-phase model (tetragonal and pyrochlore) compared to a single-phase model. This suggests that the real local structure is likely an intermediate between these models.

However, the intermediate $Ce_2Zr_2O_{7.5}$ phase did not accurately reproduce the experimental PDF, possibly due to the presence of a lower oxygen vacancy concentration in the real sample. The K-$CeZrO_{8-x}$ phase model in Figure 3.7

(f) appears to describe the local structure quite well, with the lowest observed R_{wp} value of 7%. However, the use of numerous refined fitting parameters and significant displacement of oxygen atoms or oxygen vacancies in the structure required to achieve this fit make it challenging to conclusively determine the presence of a K-$CeZrO_{8-x}$ local structure. The partial PDFs in Figure 3.7 (e) and (f) demonstrate that the first O-O bond peak splits into two peaks of inconsistent heights, indicating overfitting. None of attempted phases offered improved fits to the first few Å of the PDF, suggesting the induced structural changes are more complex than a simple local segregation and emphasizing the importance of accompanying theoretical work to understand the significance of local cation order/disorder and oxygen bonding environments in the incorporation of different oxygen vacancies.

The evolution of the local structure of Pd-$CeZrO_4$ was further investigated by examining the in-situ PDFs under methane oxidation reaction, methane reduction immediately upon switching gas flow environments (time = 0 minutes) and methane reduction gas flow after 12 minutes of gas equilibration as shown in Figure 3.8 (a) and (b). Interestingly, Figure 3.8 (b) shows that the *in-situ* PDF experiment tracks changes in the intensity and bond length of the Ce-O, Zr-O and O-O correlations of Pd-$CeZrO_4$ upon switching gas flow from methane reaction to reduction and as a function of time under methane reduction conditions. The correlation at ~2.5 Å under methane reaction, is typically associated with O-O pair correlations in CeO_2 based mixed oxides.

Under methane reduction, there is an evident shift in the O-O correlation towards higher r, indicating an increase in the bond length. Furthermore, the peak at ~2.2 Å which corresponds to the Ce/Zr-O bond, becomes broader upon switching to methane reduction, indicating a wider distribution of the cation-O bond lengths. As indicated by the large intensity of the difference curves below 5 Å the average structure models fail to provide an accurate description of the local oxygen and cation bonding environments.

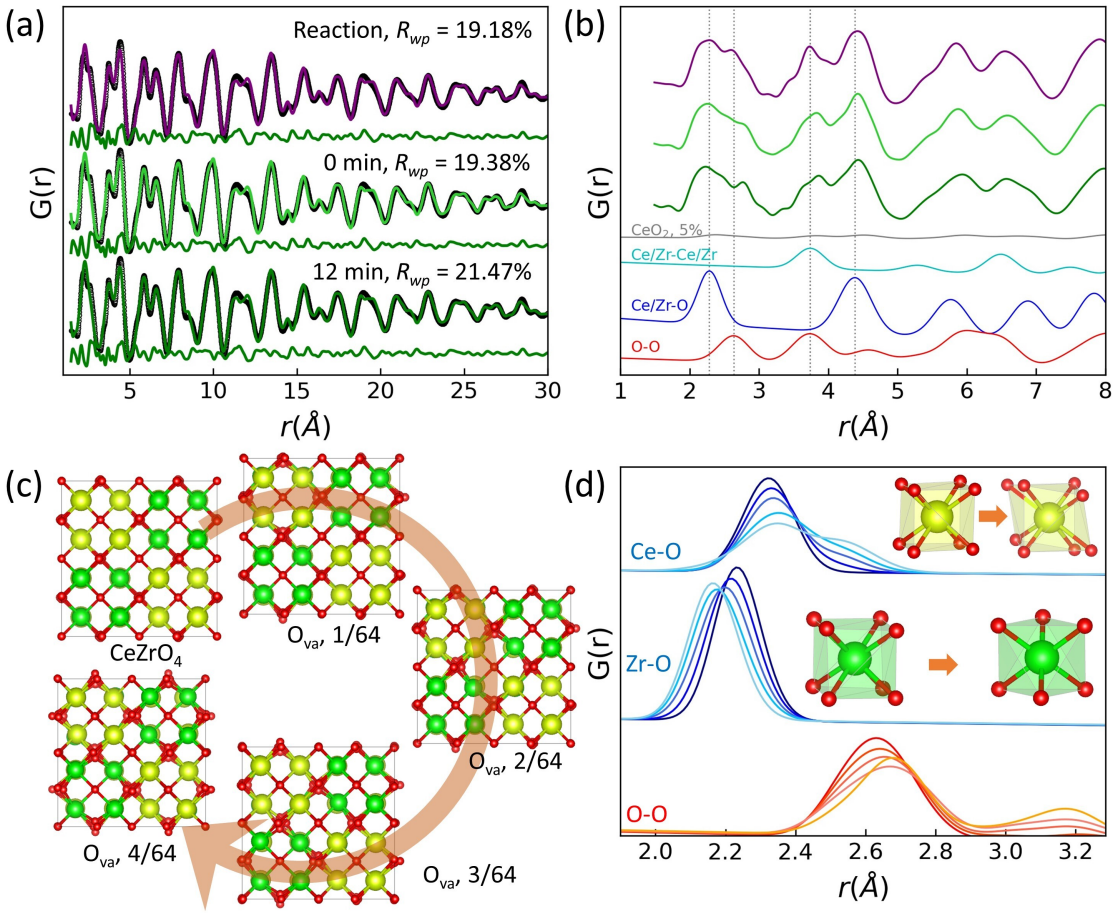


Figure 3.8: (a) 1.5-30 Å PDF fit results for Pd-$CeZrO_4$ for methane reaction (purple), reduction (t=0 min, shown in green) and reduction (t=12 min, shown in dark green) upon switching gas. Methane reaction and reduction at t=0min data was fit using a two phase structural model consisting of a $CeZrO_4$ phase with S.G. $P4_2/nmc$ and an impurity CeO_2 phase with S.G. $Fm\bar{3}m$. Methane reduction at t=12min data was refined using a a two phase cubic model with S.G. $Fm\bar{3}m$ composed of $CeZrO_4$ and an impurity CeO_2 phase. Data are shown as colored circles, fits as black lines through the data, and difference curves in green fall below the data and fits. (b) Experimental local PDFs for Pd-$CeZrO_4$ measured under methane reaction (purple), reduction (t=0 min, shown in green) and reduction (t=12 min, shown in dark green) along with simulated partial PDFs computed from a cubic $CeZrO_4$ model with S.G. $Fm\bar{3}m$. (c) Schematic illustrations depicting the structural evolutions of DFT optimization at increasing concentrations of oxygen vacancies. (d) Computed partial PDFs showing the oxygen-related atom pairs after DFT optimization, along with inset schematics highlighting the changes in Ce/Zr-O polyhedron distortions.

Thus DFT calculations were pursued to simulate varying concentrations of oxygen vacancies in $CeZrO_{4-x}$ ($x \leqslant 4/64$), which result in varying degrees of local cation ordering as shown by the crystal structures in Figure 3.8 (c). Optimized DFT calculations from exploration of these oxygen vacancy models of $CeZrO_4$ were used to calculate partial PDFs of Ce/Zr-O and O-O as shown in 3.8 (d).

It should be noted that the Ce/Zr disorder is not considered in the 96-atom fluorite structure, as the order/disorder state is not clearly established in this study. Instead, a pyrochlore Ce/Zr ordering scheme is employed, as illustrated in Figure 3.8 (c). Due to challenges in achieving energy convergence when introducing more than three oxygen vacancies, we compared the energy versus volume curves for 3/64 and 4/64 oxygen vacancies in Figure 3.9 (a) and (b), respectively.

As indicated in Figure 3.9 (c), the cell volume increases with the introduction of oxygen vacancies. This can be attributed to the conversion of Ce^{4+} to Ce^{3+}, as mentioned in the discussion of Figure 3.5. The positive formation energy values in Figure 3.9 (d) indicate that the methane reduction of $CeZrO_4$ is unlikely to occur without additional factors such as Pd loading.

For a comparative analysis, we computed the partial PDFs of Ce-O, Zr-O, and O-O with an increasing number of oxygen vacancies, as shown in Figure 3.8 (d). The Ce-O and Zr-O bond distributions exhibit distinct features upon the introduction of additional oxygen vacancies under methane reduction gas flow. When transitioning from an oxidation to reduction gas flow environment, the bond distribution in Pd-$CeZrO_4$ of the CeO_8 polyhedron changes from a single peak to a broad peak (with two short and six long bonds), while the Zr-O bond distribution experiences a shift in the peak towards the left, reflecting the transition from a ZrO_8 to a ZrO_6 polyhedron. It is worth noting that even the introduction of a single oxygen vacancy leads to significant structural changes around the local oxygen bonding environments of the two cation types.

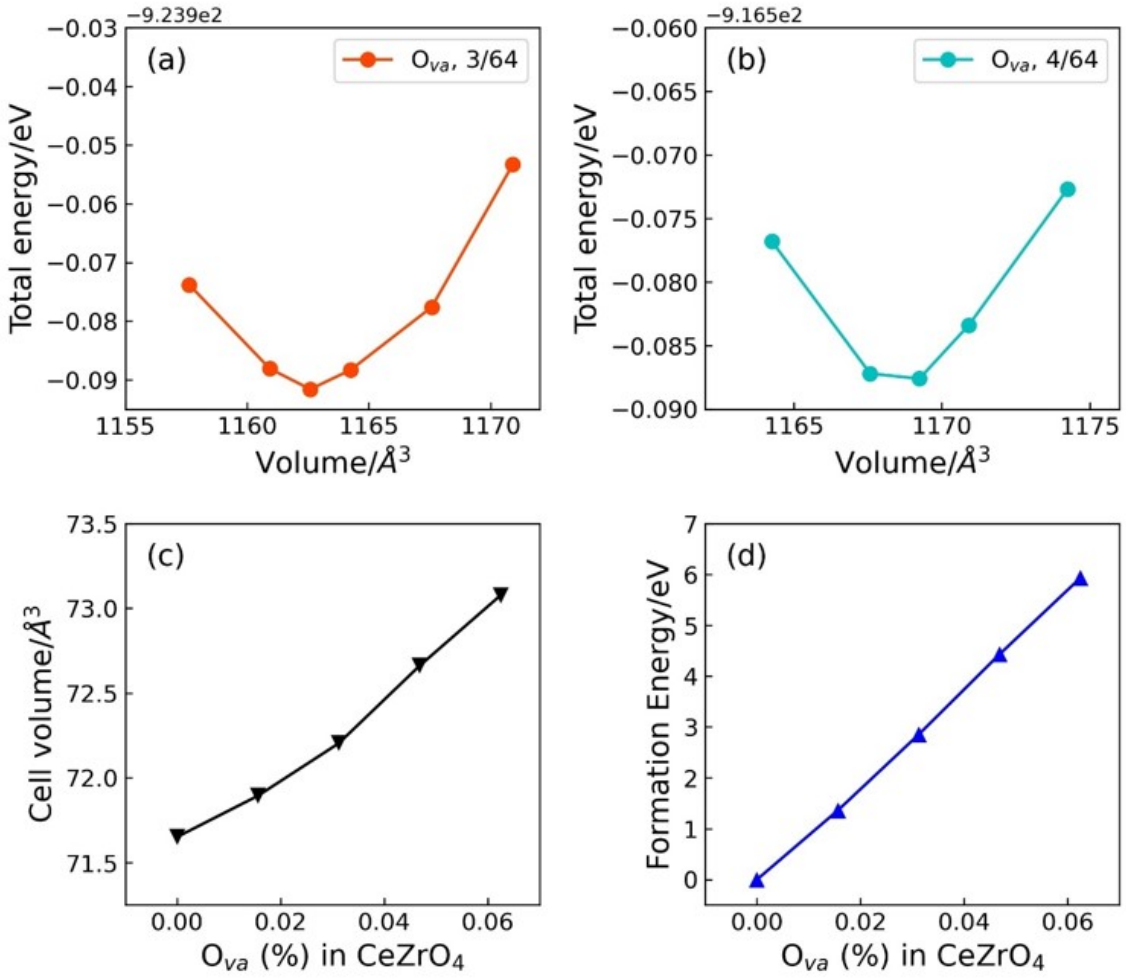


Figure 3.9: DFT optimization plots illustrating the total energy versus volume for unit cell models of $CeZrO_4$ with (a) 3/64 and (c) 4/64 oxygen vacancies. The $CeZrO_4$ models with 1/64 and 2/64 oxygen vacancies were optimized by DFT directly with cell shapes/volumes relaxed. The relationship between the cell volume (c) and the formation energy (d) in relation to the number of oxygen vacancies is depicted here.

Furthermore, we observed that as the number of oxygen vacancies increases in Pd-$CeZrO_4$ from t = 0 min to t = 12 min under methane reduction, the structural complexity more closely resembles that of the K-$CeZrO_{8-x}$ phase. Overall, the DFT calculations emphasize that the presence of oxygen vacancies has a profound impact on the local structure. While Ce/Zr are disordered under methane oxidation, the cation local environments undergo a distinct change indicative of increasing Ce/Zr distortions from t=0 min to t=12 min under methane reduction. The strong disorder in the oxygen environment and the modifications in both Ce-O and Zr-O polyhedral units pose challenges for further local structure analysis using small box modeling. However, the degree of transition from a disordered to ordered cation arrangement can be further investigated using large box Reverse Monte Carlo simulations based on DFT SQS modeling. An ordered arrangement of Ce and Zr cations has been shown to significantly enhance the oxygen storage capacity of $CeZrO_x$ solid solutions and may partly explain the enhanced reducibility observed in Pd-$CeZrO_4$ relative to $CeZrO_4$. [147, 143] It will be fascinating to observe the nature of the cation order and oxygen defects under catalytic cycling, to see if short range order or oxygen defects induced under reduction persist or revert to initial states in subsequent methane oxidation cycles.

It is important to note that while neutron total scattering provides valuable insights into the structural evolution of catalysts *in-situ* there are several challenges associated with the measurement. The quartz flow cell design necessitates the use of ~1.5 g of catalyst to position the sample in the neutron beam and obtain a reasonable signal to noise ratio. Thus the space velocity and consequently measured activity achieved during a catalytic reaction in a laboratory reactor may not be comparable to the catalytic reaction taking place during an *in-situ* neutron total scattering measurement at NOMAD.

3.5 Conclusion

In this work, we explore the effect of Pd on the average and local structure of $CeZrO_4$ under oxidation, methane oxidation reaction and methane reduction reaction conditions through an *in-situ* neutron total scattering study. A newly designed quartz gas flow cell and low background high temperature furnace were used to collect *in-situ* neutron total scattering data, under gas flow, at the NOMAD instrument at the Spallation Neutron Source and are demonstrated to offer improvements in data quality relative to the previous *in-situ* gas flow measurement set-up.

Analysis of the neutron diffraction and PDF data revealed that $CeZrO_4$ and Pd-$CeZrO_4$ share the same bulk and local tetragonal structure, with a fully occupied oxygen sublattice, under oxidation and catalytic methane oxidation reactions. This finding suggests that the structural transformation occuring in Pd-$CeZrO_4$ under catalytic methane oxidation occurs primarily through surface interfacial interactions between $CeZrO_4$ and Pd, which is challenging to resolve using a bulk characterization technique such as neutron total scattering. Forthcoming XAS analysis will provide key insights into the transformation of Pd under oxidation and catalytic methane oxidation reactions. While Pd-$CeZrO_4$ is catalytically active for the methane oxidation reaction, neat $CeZrO_4$ has a lower catalytic activity. The expected structural transformation at the surface would be minimal in comparison with Pd-$CeZrO_4$, in agreement with our findings.

While $CeZrO_4$ maintains a fully occupied oxygen sub-lattice in the local and average structure with no observed changes as a function of time under methane reduction gas flow, Pd-$CeZrO_4$ exhibits an increased concentration of oxygen vacancies over the course of the first 12 minutes under methane reduction. The formation of oxygen vacancies in Pd-$CeZrO_4$, when switching from methane reaction to reduction, is accompanied by a phase transition of Pd-$CeZrO_4$ from a tetragonal to a cubic average structure. This intriguing finding accompanies the

improved reducibility observed in Pd-$CeZrO_4$ relative to neat $CeZrO_4$, observed as a cell volume expansion associated with formation of Ce^{3+} and oxygen vacancies. Furthermore, *in-situ* neutron pair distribution function (PDF) analysis demonstrates that the disordered Ce/Zr cations in the tetragonal local structure of Pd-$CeZrO_4$ under methane oxidation reaction, exhibit a distinct change in cation local environments when transitioning to a methane reduction gas flow environment with the introduction of oxygen vacancies. The distinct local cation distortions of Ce and Zr has a significant influence on oxygen mobility and thus improves the reducibility of Pd-$CeZrO_4$ relative to neat $CeZrO_4$. This study provides fundamental insights into the role of Pd on enhancing the reducibility and methane oxidation catalytic activity of $CeZrO_4$ by increasing the concentration of oxygen vacancies and inducing distinct cation local environments.

3.6 Acknowledgements

Acknowledgement is made to the donors of the American Chemical Society Petroleum Research Fund for support of the materials synthesis efforts and the DOE Office of Science SCGSR program for access to ORNL resources used in this research. XRD measurements were completed at the Diffraction Facility at the Institute for Advanced Materials and Manufacturing at the University of Tennessee. This research used beamline BL-1B (NOMAD) at the Spallation Neutron Source, a DOE Office of Science User Facility operated by the Oak Ridge National Laboratory.

Chapter 4

Mesoporous $RE_{0.5}Ce_{0.5}O_{2-x}$ Fluorite Electrocatalysts for the Oxygen Evolution Reaction

A version of this chapter is under preparation to be submitted for publication by Sreya Paladugu, Ibrahim Munkaila Abdullahi, Sam Spinuzzi, Harish Singh, Manashi Nath*, and Katharine Page*: Paladugu, S., Munkaila, I., Spinuzzi, S., Singh, H., Nath, M. and Page, K. (2023). Binary Mesoporous Fluorites as Promising Oxygen Evolution Reaction Catalysts. In preparation.

4.1 Abstract

Developing highly active and stable electrocatalysts for the oxygen evolution reaction (OER) is key to improving the efficiency and practical application of various sustainable energy technologies including water electrolysis, CO_2 reduction and metal air batteries. Here, we use evaporation induced self-assembly (EISA) to synthesize highly porous fluorite nanocatalysts with high surface area. In this study, we demonstrate that a 50% rare earth (RE) cation substitution for Ce in the CeO_2 fluorite lattice improves OER activity and stability, by introducing oxygen vacancies into the host lattice which decreases the adsorption energy of the OH* intermediate in the OER. Among the binary fluorite compositions investigated, $Nd_2Ce_2O_7$ is shown to display the lowest OER overpotential of 243 mV achieved at a current density of 10 $mAcm^{-2}$, due to the presence of an increased concentration of oxygen vacancies and exhibits excellent cycling stability in an alkaline medium. Importantly, we demonstrate that rare-earth oxide OER electrocatalysts with high activity and stability can be achieved using the EISA synthesis route, without the incorporation of transition and noble metals.

4.2 Introduction

There is an urgent need to develop large-scale sustainable energy solutions that reduce our reliance on fossil fuels and mitigate the effects of climate change impacting our society. The oxygen evolution reaction (OER), which involves the oxidation of water to oxygen, is a fundamental half-reaction involved in

various sustainable energy technologies including water electrolysis, CO_2 reduction reaction, fuel cells and metal air batteries. [148, 149, 150, 151] A significant factor limiting the efficiency and industrial application of these technologies is the sluggish reaction kinetics of the OER; thus it is key to develop highly active and stable electrochemical catalysts for the OER.

OER catalysts with the highest reported activity thus far, consist primarily of precious metals and their oxides e.g. Ru, Ir, RuO_2, and IrO_2. [152] However, the large scale application of these precious-metal based catalysts is limited by their poor durability in alkaline media, scarcity, and high cost. The search for alternative, precious metal-free catalysts has fueled recent interests in transition metal oxides including Ni-oxides, Co-oxides, and Fe-oxides. [150, 153, 154, 155, 156] Thus far, ceria has been investigated as a co-catalyst or support for the OER, in combination with transition metals or noble metals. However, ceria based mixed oxides containing rare earth (RE) elements in place of transition or noble metal cations remain underexplored for the OER.[148]

Ceria is naturally abundant and corrosion resistant in an alkaline environment, allowing it to function as a stable electrocatalyst. Ceria has a fluorite type crystal structure and cerium atoms can dynamically and reversibly convert between 4+ and 3+ oxidation states, enabling the formation of oxygen vacancies and a defect rich structure. The two generally accepted catalytic mechanisms involved in oxide OER electrocatalysts are: (i) the adsorbate evolution mechanism (AEM) and (ii) the lattice oxygen participation mechanism (LOM). [157, 148] In both of these reaction mechanisms, the specific metal-oxygen bonding interactions at the surface of OER catalysts plays a significant role in stabilizing the oxygen-containing reaction intermediates on the catalyst surface. Tuning the oxygen vacancy structure of the catalyst and the resulting metal-oxygen bonding interactions, by introducing dopants into the host lattice, has been shown to be an effective strategy for improving the activity for OER. [148, 151] As demonstrated in previous studies, oxygen vacancies play a key role in accommodating hydroxyls, enhancing the pre-oxidation

of low oxidation species, and facilitating the deprotonation/reconstruction of OER intermediates. [158] The present work seeks to determine what impact incorporation of various single RE cations has on the OER activity of cerate fluorite electrocatalysts. Partial substitution of Ce^{4+} with (mainly) trivalent RE cations can introduce oxygen vacancies into the lattice, reduce/ potentially eliminate the need for (much more expensive) noble metal cations, and potentially promote the adsorption of oxygen-containing intermediates due to an increased concentration of oxygen vacancies. [148, 159] RE incorporation may also enhance the stability of ceria electrocatalysts relative to transition-metal incorporated ones. RE cations are not as readily oxidized/reduced (preventing or delaying surface poisoning mechanisms, reaction-induced secondary phase segregation, and particle coarsening) and their ionic radii are typically larger (potentially providing a lattice expansion effect known to facilitate transport of oxygen from the bulk to the surface). As shown in Figure 4.1 (a), when RE cations are introduced into the cubic fluorite lattice, the $Ce^{3+/4+}$ and RE^{3+} cations randomly occupy the 4*a* Wyckoff position, while the oxygen anions occupy the tetrahedral sites on position 8*c*. If there is a 50/50 balance between 3+ and 4+ cations, the oxygen positions are, on average, 7/8ths occupied; such a 'defect fluorite' system readily accommodates small increases or decreases in oxygen occupancy, the development of Frenkel defects, and other charge compensating mechanisms. Doping CeO_2 with RE^{3+} cations is known to depress the concentration of Ce^{3+} and introduce large amounts of oxygen vacancies, resulting in a stable defect-rich fluorite structure. [160, 161]

While tuning the oxygen defect structure and participating ionic radii in electrocatalysts serve as fundamental approaches to enhancing their intrinsic activity and improving their stability, catalytic activity can also be significantly influenced by morphology. Here, we use a soft templating evaporation induced self-assembly approach (EISA) to synthesize OER fluorite catalysts with high surface area, porosity and nanoarchitecture with the objectives of increasing the number of

exposed active sites and improving mass diffusion kinetics. [148] Wet chemistry-based synthesis methods such as EISA allow for intimate mixing of cations prior to calcination and can be used to achieve target phases at lower temperatures relative to solid state methods due to increased diffusion kinetics of the cations in solution. The lower calcination temperature associated with EISA also facilitates the synthesis of nano-sized particles which exhibit much larger total exposed surface areas than their bulk counterparts and an increased number of catalytically active sites. These effects are well known to improve the overall efficiency by achieving higher current densities at low overpotentials in the OER. Additionally, surface accessible porosity, which can be engineered using EISA, can improve the diffusion rates of reactants to and products from active sites, and enhance selectivity through control of secondary reactions. Furthermore, EISA is an inexpensive, highly tunable, and easily scalable synthesis approach, making it feasible for industrial manufacturing.

Fluorite samples with target composition CeO_2, $La_2Ce_2O_7$, $Pr_2Ce_2O_7$, $Nd_2Ce_2O_7$, $Tb_2Ce_2O_7$ and $Dy_2Ce_2O_7$ were synthesized using EISA to explore the role of RE cation substitution on the OER activity of fluorite nano electrocatalysts. We note that we do not control the oxygen stoichiometry in the synthesis route and thus the family may be more generally described as $RE_{0.5}Ce_{0.5}O_{4-x}$ compositions. The phase purity, crystallinity, and morphology of the samples is investigated using x-ray diffraction (XRD), Brunauer-Emmett-Teller (BET) analysis, and Scanning Electron Microscopy (SEM). Their electrocatalytic activity and stability for OER is examined in a 1M KOH electrolyte solution exploring their promise for practical application in water splitting or other technologies involving the oxygen evolution reaction.

4.3 Materials Synthesis

4.3.1 Materials

Praseodymium (III) nitrate pentahydrate (99.9%), cerium (III) nitrate hexahydrate (99.5%), terbium (III) nitrate hydrate (99.9%), lanthanum (III) nitrate hexahydrate

(98%), dysprosium (III) nitrate pentahydrate (99.9%), neodymium (III) nitrate hexahydrate (99.9%) and ethanol (99.5%) were purchased from Thermo Fisher Scientific. Pluronic P123 (a symmetric triblock co-polymer comprising poly(ethylene oxide) (PEO) and poly(propylene oxide) (PPO) in an alternating linear fashion) was purchased from Sigma Aldrich. The metal content of all metal nitrate hydrates was determined immediately upon receipt from the manufacturer and used to prepare sealed aqueous stock solutions.

Carbon cloth (CC) for the battery, fuel cell, and supercapacitor were purchased from MSE supplies, Tucson, AZ 85711 USA. Nafion (5 wt.%), and isopropanol (iPr-OH), were purchased from (Sigma–Aldrich Chemical Reagent Co., Ltd. St. Louis, MO), and potassium hydroxide (KOH) was purchased from (Fisher Scientific Pittsburgh, USA). All the reagents were used as received. The deionized (D.I.) water purified through a Millipore system was used in all experiments. The CC was washed with iPr-OH and D.I. water several times to ensure a clean surface.

4.3.2 Synthesis of Porous Binary Fluorites via Evaporation Induced Self Assembly (EISA)

Porous fluorite compositions were synthesized using a soft templating approach via evaporation induced self-assembly (EISA). Briefly, metal nitrate precursor solutions were dissolved in ethanol, under continuous stirring, using Pluronic P123 as a block co-polymer template. The solutions were allowed to evaporate in a petri dish at room temperature for 48 hours and each resulting gel was calcined in air at 600 °C for 4 hours in an oven. The following compositions were chosen to investigate the role of RE cation substitution on the electrochemical OER performance of fluorites: $La_2Ce_2O_7$, and $Pr_2Ce_2O_7$, $Nd_2Ce_2O_7$, $Tb_2Ce_2O_7$ and $Dy_2Ce_2O_7$. Additionally, the parent CeO_2 was synthesized using the same method as a reference.

4.3.3 Fabrication of the Working Electrode for OER.

All CC substrates are iPr-OH cleaned, dried, and covered with Teflon tape, leaving an exposed geometric area of 0.283 cm^2. Catalyst ink was prepared by dispersing 10.0 mg of the catalyst in 1.0 mL 0.8% Nafion in iPr-OH and ultrasonicated for 30 min. A 20 μL ink volume was pipetted out, drop-casted on the CC substrate exposed geometric area, dried at room temperature, and finally heated at 130°C in an oven for 30 min in air.

4.4 Materials Characterization and Methods

4.4.1 Structure and Morphology

Phase identification of the fluorite powder samples was performed using a Panalytical Empyrean laboratory powder x-ray diffraction (XRD) instrument and Cu Kα radiation ($\lambda = 1.5418$ Å). Rietveld refinements were performed on the XRD data using the TOPAS v6 software. [103] Data were fit to cubic fluorite and defect fluorite unit cell models with scale factor, lattice parameter a, separate isotropic atomic displacement parameters U_{iso} for O and for cations (constrained to be equivalent for Ce and RE), and Scherrer particle size L refined. The particle morphologies of the powder samples were examined using a Zeiss Auriga SEM and the chemical homogeneity of the samples was determined by performing EDS measurements on pressed pellets of the samples using a Zeiss EVO SEM equipped with energy dispersive x-Ray Spectroscopy. The BET surface area measurements were performed by loading 100 mg-150 mg of powder sample in a quartz tube and out gassing overnight at 200°C under vacuum. The surface area of the outgassed samples was then measured using a Micromeritics Gemini VII surface-area analyzer. The elemental compositions of the fluorite samples was investigated by performing x-Ray Fluorescence measurements on pressed pellets using a Malvern Panalytical Epsilon 1 EDXRF instrument with a Cu Kα source. Using a monochromatic Al

x-ray source, XPS measurements were performed using a KRATOS AXIS 165 X-ray photoelectron spectrometer (Kratos Analytical Limited, Manchester, United Kingdom). The C 1s signal at 284.5 eV was used as a reference to correct all the XPS binding energies. All XPS spectra were collected from pristine catalyst surfaces without sputtering.

4.4.2 Electrochemical Measurements

Electrochemical measurements were performed using a conventional three-electrode system connected to an IviumStat potentiostat, with the catalyst as the working electrode; graphite rod, and Ag/AgCl electrode were used as counter and reference electrodes, respectively, to measure the electrocatalytic performances. Linear sweep voltammetry (LSV) and cyclic voltammetry (CV) were used to study the OER catalytic performance and cycling stability. All activity data were iR-corrected and measured through electrochemical impedance studies to reduce uncompensated solution resistance. All potentials measured were calibrated to RHE using Equation S4.1. All electrolytes were saturated by N2 (for OER) bubbles before and during the experiments.

The steady-state performance and durability of all the electrocatalysts in OER for long-term chronoamperometric stability in the alkaline electrolyte of 1 M KOH solution were carried out in two forms: (i) At a constant current density of 10 $mAcm^{-2}$ for 16 h for all the binary fluorite series (ii) At various current densities between 5 – 15 $mAcm^{-2}$ as a multistep study, carried out for $Nd_2Ce_2O_7$ and $Dy_2Ce_2O_7$ in N_2-saturated 1.0 M KOH electrolyte at room temperature.

The Tafel slope, an important parameter to explain the electrokinetic activity of these thin film catalysts for OER and HER processes, was estimated from the Tafel plot. The Tafel equation is given as the dependence of overpotential η on the current density j as shown in Equation S4.2.

The EIS experiments were performed within the $10^5 - 10^{-2}$ Hz frequency range, at an AC signal amplitude of 10 mV, to study the electrode kinetics and estimate the

electrolyte resistance (Rs) and charge transfer resistance at the electrode (catalyst)-electrolyte interface (R_{ct}). The Nyquist plots were collected in N_2-saturated 1.0 M KOH at an applied potential of 0.45 V vs. Ag|AgCl (KCl saturated). Turnover frequency, mass activity, electrochemically active surface area and roughness factor of the electrocatalysts were calculated using Equations S4.3-S4.7 respectively.

4.4.3 Density Functional Theory (DFT)

Density Functional Theory (DFT) calculations were performed using the Vienna ab-initio Simulation Package (VASP). To determine the electron exchange-correlation, the generalized gradient approximation (GGA) was applied to the Perdew-Burke-Ernzerhof (PBE) function scheme. The plane-wave basis set's kinetic cutoff energy was set at 520 eV. The lattice vectors and all atomic positions were optimized by the conjugate gradient algorithm. Geometries were refined until the threshold force was smaller than 0.01 eV/Å and the total energy change was less than 1×10^{-5}eV. The slab models have used the (1 0 0) surface of $Nd_2Ce_2O_7$ and CeO_2, and a 10 Å vacuum in the *c*-direction was added to avoid periodic boundary interaction. A Monkhorst-Pack scheme K-point grid was set to $9 \times 9 \times 1$ during surface relaxation.

4.5 Results and Discussion

4.5.1 Phase purity and sample morphology

As seen in Figure 4.1 (b), Rietveld refinements were performed on powder x-ray diffraction (XRD) data to determine the average crystal structure and phase purity of the fluorite samples prepared by calcination at 600°C. XRD patterns of all samples display broad peaks, indicative of the highly nanocrystalline nature of samples produced using the low temperature EISA synthesis route. Interestingly, incorporation of RE^{3+} cations in CeO_2 leads to a clear broadening of diffraction peaks, suggesting a decrease in crystallinity or particle size.

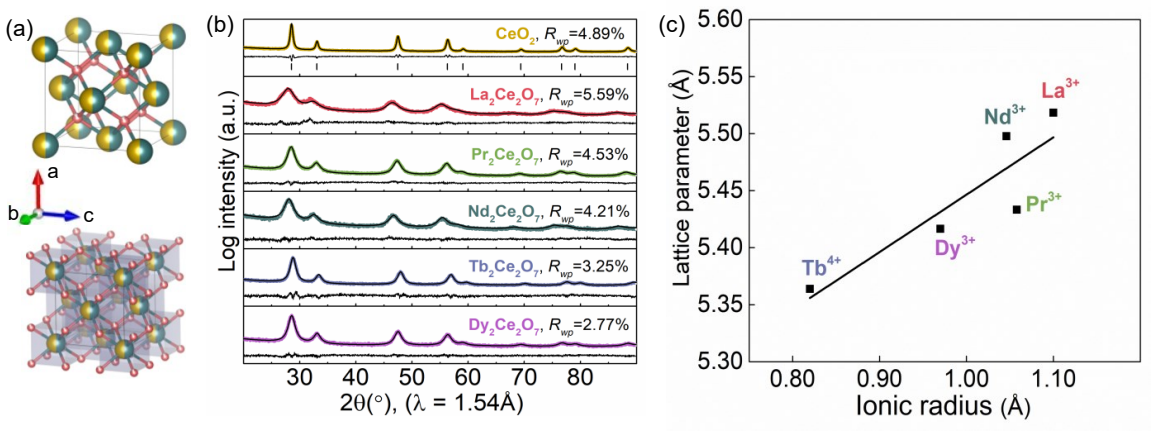


Figure 4.1: (a) Salient features of the $RE_{0.5}M_{0.5}O_{2-x}$ rare earth fluorite oxide structure family. When the 4+ fluorite metal M site is substituted with mainly trivalent RE (3+) species, charge compensation occurs through point defects on the oxygen sublattice. The unit cell on the top depicts a system where cation sites are occupied, on average, with equal parts of a RE ion and Ce ion. The defect-fluorite can be written as $RE_{0.5}Ce_{0.5}O_{2-x}$. In the unit cell on the bottom, the VIII-fold cation coordination polyhedra are depicted as light purple cubes with O atoms at the vertices. (b) Rietveld refinements of X-ray powder diffraction data of the fluorite samples. Measured data are shown as colored circles, structure model fits as a black line through the data, and the difference curves in black fall below the data and fits. CeO_2 was refined using a cubic fluorite structure as indicated by the hkl tick marks in black. The binary fluorites in the series were refined using a defect fluorite structure(with 50% RE and 50% Ce on each M site and 7/8ths of O sites occupied). (c) Variation in lattice parameters from Rietveld refinements of the binary fluorite samples, as a function of ionic radius of the RE^{3+} cations in assumed VII-fold coordination with oxygen.

Rietveld refinement of the CeO_2 sample was performed successfully using the canonical ceria fluorite unit cell model described with space group (S.G.) $Fm\bar{3}m$, where the Ce cations occupy the face-centered Wyckoff position 4*a* and oxygen anions occupy the tetrahedral 8*c* position. [68, 101] All fluorite samples containing RE cations display a single phase defect fluorite structure as shown in Figure 4.1 (a), also indexed to space group $Fm\bar{3}m$, but with RE^{3+} randomly occupying half the 4*a* sites and oxygen anions occupying an assumed 7/8ths of 8*c* sites. The addition of RE^{3+} cations to ceria suppresses the formation of Ce^{3+} and promotes the formation of oxygen vacancies due to the need for charge compensation. [160]

Extracted parameters from Rietveld refinement provide further structural insights into the effects of RE incorporation in CeO_2. In an ideal fluorite structure, Ce^{4+} cations are VIII-fold coordinated with oxygen; however, introducing (mainly) RE^{3+} cations into the fluorite lattice results in a change in average cation coordination from VIII-fold to VII-fold. The ionic radii for VII-fold coordination can be estimated as an average of ionic radii for VI and VIII-fold coordination. As seen in Table 4.1 and Figure 4.1 (c), inclusion of RE^{3+} cations in CeO_2 generally results in a lattice expansion, increasing with an increase in average ionic radius. This is due to the larger ionic radius of La^{3+} (1.1 Å), Pr^{3+} (1.06 Å), Nd^{3+} (1.05 Å), and Dy^{3+} (0.97 Å) relative to Ce^{4+} (0.92 Å) in VII-fold coordination.[162, 163, 164]. It is noted that Ce^{3+} in VII-fold coordination has a larger ionic radius (1.07 Å) relative to Ce^{4+}. As a noted exception to the trend, Tb inclusion does not increase the lattice volume of the fluorite structure. Tb^{4+} has ionic radii of 0.76 Å in VI-fold coordination and 0.88 Å in VIII-fold coordination, while Tb^{3+} has an ionic radius of 0.98 Å in VII-fold coordination. The valence states of the fluorite cations will be discussed in further detail in connection with X-ray photoelectron spectroscopy results. Interestingly, samples containing RE cations display a clear decrease in average crystallite size refined via XRD analysis (<10 nm crystalline correlation length) relative to CeO_2 (~20 nm). The average crystalline correlation lengths are found to be much smaller than external particle morphologies discussed in

the following section, revealing that the particles are highly disordered and/or contain many nano-sized grains. It is noted that substitution of Ce^{4+} with larger (or smaller) RE cations is expected to induce lattice disorder, and fluorite compositions incorporating larger RE cations (La, Pr, and Nd) generally display more peak broadening (less crystallinity) than those incorporating smaller RE cations (Tb and Dy) in our series. High lattice disorder is additionally suggested by the high refined atomic displacement parameters in the reported Rietveld refinement results in Table 4.1.

The effectiveness of a catalyst is largely dependent on accessible surface area, which can be determined through examination of particle morphology. SEM was used to study the morphology of the fluorite sample series; all samples were found to be highly heterogeneous, with a diverse range of particle sizes. In particular, micrometer scale porous flakes and spherical nanoparticle agglomerates are distinctly displayed as shown by representative SEM images of $Nd_2Ce_2O_7$ in SI Figure S4.1 (a) and (b). Similar observations of the coexistence of micrometer sized flakes and spherical nanoparticles were reported in fluorite structured materials made via a solution combustion method by Cong et al. [165] Surface area values for the sample series measured using BET are displayed in Table 4.1, ranging between $\sim 50 m^2 g^{-1}$ and $\sim 90 m^2 g^{-1}$ across the series. The higher attained surface areas at 600°C of RE containing samples may be related to the higher decomposition temperatures of RE nitrates relative to Ce nitrate leading to possible delayed nucleation and growth from solution. [166]

Energy Dispersive Spectroscopy (EDS) measurements were performed on all RE^{3+} containing samples to investigate the formation of a solid solution. Elemental mapping confirmed the homogeneous distribution of all elements present at the micron scale. Spectra were collected for various particle morphologies across sample locations to confirm that the different morphologies possess the same chemical composition and distribution. Representative EDS elemental mapping results for $Nd_2Ce_2O_7$ are shown in SI Figure S4.1 (c) and (d).

Table 4.1: Lattice parameter a, isotropic atomic displacement parameters U_{iso}s, average crystalline correlation length L, and resulting goodness of fit R_{wp} resulting from XRD Rietveld refinements of the fluorite sample series data. Measured BET surface area (SA) is also shown for the samples.

	CeO_2	$La_2Ce_2O_7$	$Pr_2Ce_2O_7$	$Nd_2Ce_2O_7$	$Tb_2Ce_2O_7$	$Dy_2Ce_2O_7$
a (Å)	5.41300(6)	5.5180(6)	5.4330(2)	5.4980(4)	5.3640(2)	5.4160(3)
B_{eq}(Ce/RE) (Å^2)	1	0.10(2)	0.20(1)	0.23(1)	0.67(1)	1.33(1)
B_{eq}(O) (Å^2)	1	3.7(1)	0.99(6)	2.8(1)	0.89(5)	2.53(7)
L (nm)	18.89(2)	3.48(1)	5.88(1)	4.64(1)	7.75(1)	6.67(1)
R_{wp}	4.89	5.51	4.53	4.21	3.25	2.77
BET SA (m^2g^{-1})	122.44	52.11	87.67	60.92	78.61	69.78

Measured atomic ratios of RE cations to Ce from XRF measurements are displayed in SI Table S4.1 and were found to closely resemble the target stoichiometry with minor deviation.

X-ray photoelectron spectroscopy (XPS) was used to determine the valence states of the elemental constituents present on the surface of the fluorite catalysts. As seen in SI Figure S4.3, the high-resolution Ce 3d spectra of CeO_2 shows six peaks with multiplet splitting. The peaks were observed at 882.1, 888.4, and 897.9 eV for $3d_{5/2}$ and at 990.5, 906.8, and 916.3 eV for $3d_{3/2}$, confirming the presence of both Ce (III) and Ce (IV) commonly observed in ceria and ceria based mixed oxides. [167, 168, 2]

The high-resolution La 3d spectrum of $La_2Ce_2O_7$ shown in SI Figure S4.4 displayed doublet splitting, further deconvoluted into four peaks (two per doublet). The peaks observed at 834.5 and 851.4 eV correspond to the spin-orbit $3d_{5/2}$ and $3d_{3/2}$, respectively, while the peaks at 838.3 and 855.6 eV were identified as satellite peaks associated with $3d_{5/2}$ and $3d_{3/2}$, respectively. [169]

SI Figure S4.5 shows the high-resolution Pr 3d spectrum of Pr in $Pr_2Ce_2O_7$ with two doublets at 932.8 and 953.4 eV, and satellites at 928.4 and 984.2 eV, indicating the presence of the Pr (III) oxidation state. This observation aligns with the preferential trivalent state commonly observed for most RE-ions. [170] Additionally, the satellites at lower binding energy are attributed to the well-known $4f_3$ final state. [171, 172]

The presence and bonding state of Nd in $Nd_2Ce_2O_7$ was confirmed from the high-resolution Nd 3d spectra shown in SI Figure S4.6, which displayed two doublets at 977.8 and 982.3 eV, corresponding to a satellite and Nd (VI) of $3d_{5/2}$, as well as at 1000.1 and 1004.7 eV, corresponding to a satellite and Nd (III) of $3d_{3/2}$. [173, 174] The 4d spectra (SI Figure S4.6 (c)) exhibited 121.1 and 124.3 eV peaks associated with a satellite and 4d in oxides. [175]

XPS analysis of $Tb_2Ce_2O_7$ from high-resolution Tb 3d spectrum (SI Figure S4.7 (b)), confirmed the presence of Tb (IV) as indicated by the observed characteristic

doublet peaks of $3d_{5/2}$ and $3d_{3/2}$, along with their corresponding satellites at 1241.0, 1276.0, 1251.4, and 1287.0 eV, respectively. These results were consistent with the findings reported in the literature on RE oxides. [176, 177]

As shown in SI Figure S4.8, the Dy 3d spectrum revealed doublet peaks corresponding to spin-orbit splitting at 1296.2 and 1334.6 eV for Dy (III) arising from $3d_{3/2}$ and $3d_{5/2}$, respectively. [178, 179] Additionally, a satellite peak at 1303.9 eV was attributed to the Dy (IV) $3d_{5/2}$ components, indicating the presence of mixed Dy-ion states on the surfaces commonly seen in its oxides. [179]

The presence of oxygen vacancies in oxide based electrocatalysts can strongly influence the kinetics of the OER by affecting the binding strengths of oxygen-containing intermediates, such as MOOH* and MOH* (M = metal cation(s)), with the catalyst surface. [180] Thus, the concentration of oxygen vacancies in the fluorite catalysts was investigated by analyzing the high-resolution O 1s XPS spectra for all samples in the series. As seen in Figure 4.2, the O 1s XPS spectra for all catalysts were deconvoluted into two main peak components: oxygen vacancy (O_V) and lattice oxygen (O_L). The O_L binding peak at approximately 528.8 eV in the O 1s XPS spectra of each catalyst is associated with a typical metal-oxygen bond of the lattice oxygen. [181] The peak at 530.9 eV corresponds to loosely absorbed oxygen species associated with oxygen vacancies. The O_V peak at 531.5 eV was attributed to the presence of surface chemisorbed oxygen associated with defects (oxygen vacancies).[181, 182] The proportion of surface oxygen vacancies in the catalysts was estimated by calculating the ratio of the O_V/O_L peak areas, with higher ratios indicating a larger amount of surface oxygen vacancies. [170] All the binary fluorite compositions exhibit an increase in oxygen vacancy concentration relative to CeO_2, to compensate for the extra positive charge introduced by substitution of Ce^{4+} with primarily RE^{3+} cations. Interestingly, $Nd_2Ce_2O_7$ displays the highest concentration of oxygen vacancies among all binary fluorites in the series.

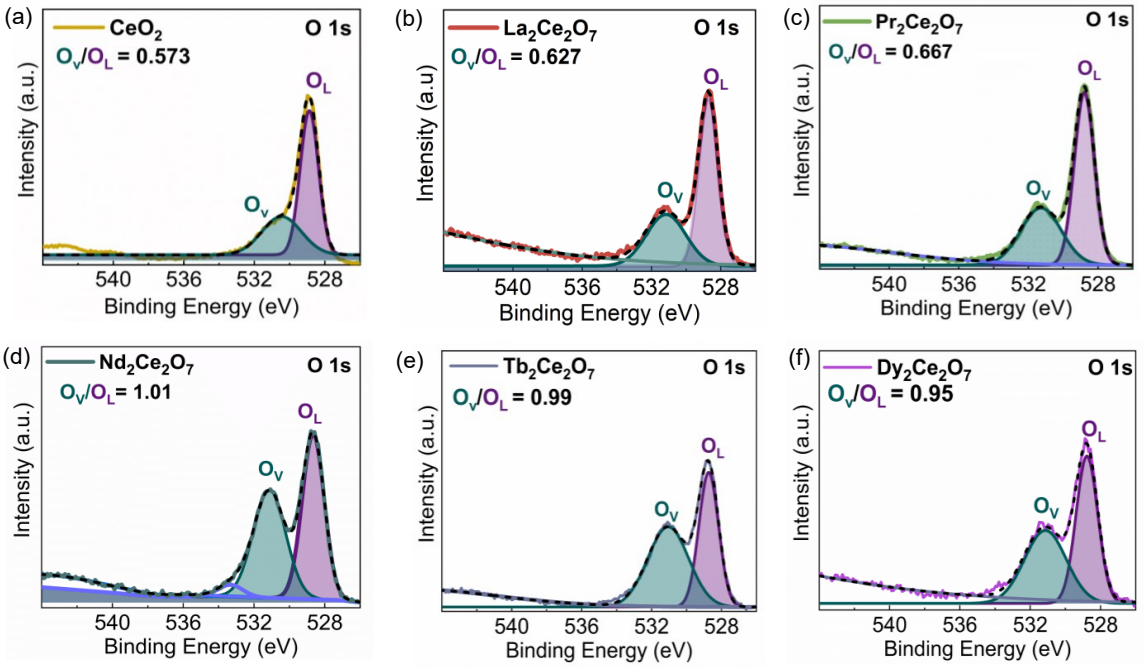


Figure 4.2: O 1s core level binding energy spectra of (a) CeO2; (b) $La_2Ce_2O_7$; (c) $Pr_2Ce_2O_7$; (d) $Nd_2Ce_2O_7$; (e) $Tb_2Ce_2O_7$ and (f) $Dy_2Ce_2O_7$ catalysts. The area ratios of vacancy-related (O_v, green) and lattice-related (O_L, purple) are provided.

While Tb and Dy O_V/O_L values are close to that of Nd, they will likely have fewer overall charge compensating oxygen vacancies, due to the incorporation of Tb^{4+} and, to a lesser extent, Dy^{4+}.These two factors suggest the potential for $Nd_2Ce_2O_7$ as an efficient electrocatalyst for OER. Oxygen vacancies facilitate the adsorption of hydroxyl intermediates and initiate the reconstruction of defective surfaces under an applied potential [169, 183], resulting in improved OER performance. Achieving a high concentration of oxygen vacancies is crucial to enhancing solid-to-charge carrier (STCH) performance, which is a key factor in determining electrochemical activity.[184] The interaction and repulsion between oxygen vacancies[185, 186] arises from surplus electrons that remain in the lattice upon vacancy formation, resulting in a higher abundance of extra charge carriers. The excess electrons and the accompanying local bond distortion resulting from an oxygen vacancy are referred to as oxygen vacancy polarons.[185, 186]

Residual carbon was detected in the fluorite series via XPS. The C 1s spectra of all fluorite samples in the series exhibit a sharp asymmetric peak at 285.0 eV, ascribed to amorphous carbon present in the form of C-C/C-H.[187] The peak at 288.8 eV is attributed to incomplete oxidation of carbon species: O–C–O/O–C=O . [188] The amount of residual carbon in all fluorite compositions was determined to be similar based on FTIR measurements and is unlikely to contribute to observed differences in OER performance.

4.5.2 Electrocatalytic performance for the OER

The electrocatalytic performance of the as synthesized binary fluorites was assessed for the OER in a 1 M KOH alkaline solution, using a three-electrode system. Linear sweep voltammetry (LSV) was employed to obtain OER polarization plots at a scan rate of 10 mV/s and compare the performance of the binary fluorite catalysts as seen in Figure 4.3 (a).

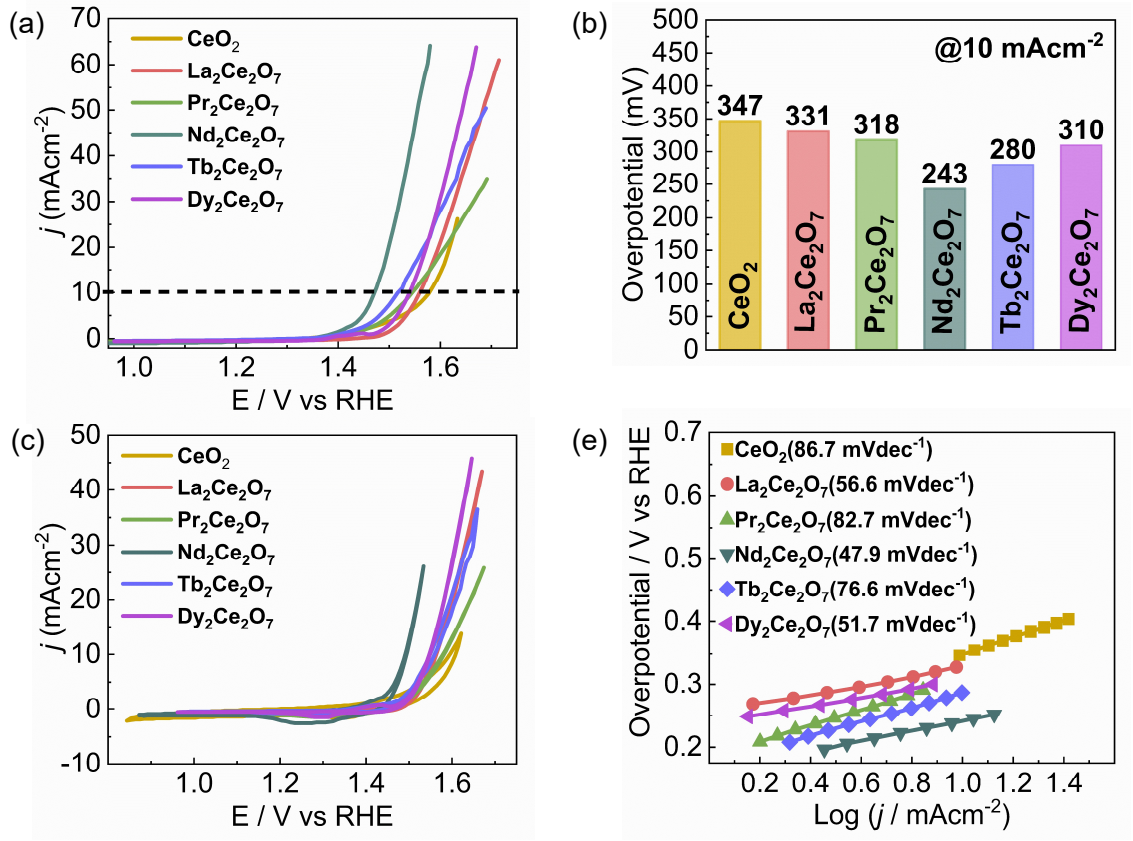


Figure 4.3: Electrocatalytic performance of CeO_2, $La_2Ce_2O_7$, $Pr_2Ce_2O_7$, $Nd_2Ce_2O_7$, $Tb_2Ce_2O_7$, and $Dy_2Ce_2O_7$ catalysts (a) LSVs; (b) Overpotential at current density of 10 $mAcm^{-2}$; (c) Cyclic voltammograms; (d) Tafel plots. All electrocatalysis data are measured in N_2 saturated 1 M KOH at a 10 mV s^{-1} scan rate.

As evidenced by the LSVs, $Nd_2Ce_2O_7$ exhibited a significantly lower overpotential of 243 mV at a current density of 10 $mAcm^{-2}$, indicating higher catalytic activity as compared to $La_2Ce_2O_7$ (overpotential of 331 mV), $Pr_2Ce_2O_7$ (overpotential of 318 mV), $Tb_2Ce_2O_7$ (overpotential of 280 mV), $Dy_2Ce_2O_7$ (overpotential of 310 mV) and CeO_2 (overpotential of 347 mV) (Figure 4.3 (b)). The intrinsic catalytic activity of the catalysts ranging from highest to lowest can be ranked as follows: $Nd_2Ce_2O_7$ > $Tb_2Ce_2O_7$ > $Dy_2Ce_2O_7$ > $Pr_2Ce_2O_7$ > $La_2Ce_2O_7$ > CeO_2, suggesting that $Nd_2Ce_2O_7$ has the highest activity in the series. Notably the CeO_2 catalyst, synthesized using a soft templating approach in this study, demonstrated an overpotential of 347 mV, surpassing other reported neat CeO_2 OER electrocatalysts in the literature. [3, 1, 4] This suggests that soft templating via evaporation-induced self-assembly is a promising method for the synthesis of efficient electrocatalysts for the OER. Furthermore, all binary fluorite compositions exhibit a lower overpotential than neat CeO_2, presumably due to the increase in oxygen vacancy concentration, enhanced oxygen mobility from lattice disorder or expansion effects, and electronic perturbation effects resulting from RE cation incorporation into the fluorite lattice.

Cyclic voltammetry (CV) of all samples revealed pre-oxidation peaks associated with the oxidation of the active metal site (Figure 4.3 (c)). The pre-oxidation peaks for $Nd_2Ce_2O_7$, $Tb_2Ce_2O_7$, $Dy_2Ce_2O_7$, $Pr_2Ce_2O_7$, $La_2Ce_2O_7$ and CeO_2 occurred at 1.35, 1.43, 1.39, 1.40 and 1.38 V vs. RHE, respectively, at a scan rate of 10 mVs^{-1}, primarily originating from the contributions of Ce (III)/Ce (IV). This effect becomes more pronounced when varying the scan rates. The shift in oxidation peak potential relative to the parent CeO_2 indicates the influence of electronic perturbation resulting from incorporating a RE-element in the binary fluorites. Tafel plots derived from LSV curves were used to analyze the OER kinetics of the electrocatalyst. As shown in Figure 4.3 (d), $Nd_2Ce_2O_7$ exhibited the smallest Tafel slope of 43.1 mV dec^{-1}, indicating faster electrocatalytic kinetics for OER. Interestingly, the Tafel slopes for $Dy_2Ce_2O_7$ (51.7 mV dec^{-1}) and $La_2Ce_2O_7$ (56.6 mV dec^{-1}) were observed to be smaller than that of $Tb_2Ce_2O_7$ (76.6 mV dec^{-1}).

Although $Tb_2Ce_2O_7$ is more catalytically active, it has slower electrokinetics than $Dy_2Ce_2O_7$ and $La_2Ce_2O_7$. Therefore, the electrokinetic activity of the fluorite series, as determined by the Tafel slope, follows the order $Nd_2Ce_2O_7$ (47.9 mV dec^{-1}) > $Dy_2Ce_2O_7$ (51.7 mV dec^{-1}) > $La_2Ce_2O_7$ (56.6 mV dec^{-1}) > $Tb_2Ce_2O_7$ (76.6 mV dec^{-1}) > $Pr_2Ce_2O_7$ (82.2 mV dec^{-1}) > CeO_2 (86.7 mV dec^{-1}). Importantly, a 50% rare earth (RE) cation substitution for Ce in the CeO_2 fluorite lattice enhances the electrokinetics of the OER, in addition to the activity. The binary fluorites reported in this study display improved OER performance compared to previously reported CeO_2-based electrocatalysts. [2, 186, 1, 4, 189, 129, 190, 191]

To further evaluate the catalytic performance for OER, the mass activities and turnover frequency (TOF) at an overpotential of 350 mV were calculated as presented in Figures 4.4 (a) and (b) respectively. Among all fluorite catalysts, $Nd_2Ce_2O_7$ demonstrated the highest OER activity, exhibiting a mass activity of 36.0 Ag^{-1} and a TOF of 0.0643 s^{-1}. $Tb_2Ce_2O_7$ and $Dy_2Ce_2O_7$ showed very similar performance with the same mass activity of 14.56 Ag^{-1} and a TOF of 0.0268 and 0.0271 s^{-1}, respectively. The superior OER activity of the $Nd_2Ce_2O_7$ catalyst can tentatively be attributed to the electronic structure perturbation resulting from the incorporation of Nd and an increased number of catalytically active sites originating from higher concentration of oxygen vacancies. [192]

Electrochemical impedance spectroscopy (EIS) analysis revealed that electrical resistivity influences the OER activity. EIS spectra of the fluorite series revealed semicircular curves, indicating a combination of electron transfer and double-layer charging processes. The Nyquist plots generated at 0.45 V vs. RHE are shown in Figure 4.4 (c).An equivalent circuit (inset in Figure 4.4 (c)) consisting of electrolyte resistance (R_s), charge transfer resistance (R_{ct}), constant phase element (CPE), and Warburg element (W) were used for evaluation (Figure S4.2). $Nd_2Ce_2O_7$ exhibited the lowest R_{ct} of 7.95 Ω at a potential of 1.45 V vs. RHE, followed by $Tb_2Ce_2O_7$ with an R_{ct} of 10.10 Ω. CeO_2 displayed the largest resistance of 18.1 Ω.

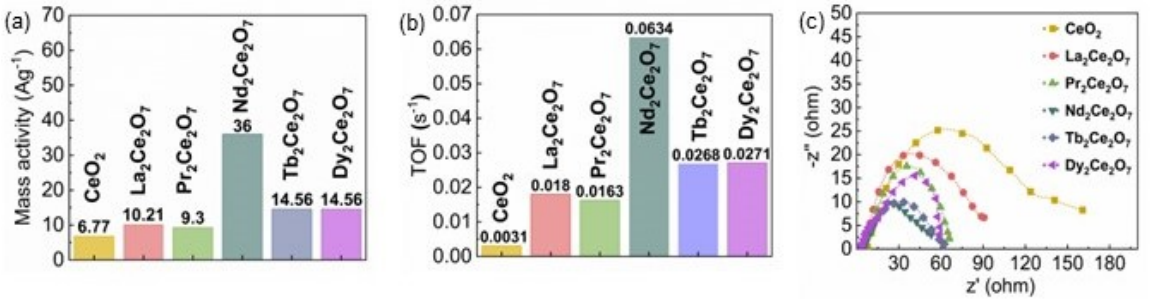


Figure 4.4: Electrocatalytic performance of CeO_2 (mustard), $La_2Ce_2O_7$ (pink), $Pr_2Ce_2O_7$ (green), $Nd_2Ce_2O_7$ (blue-green), $Tb_2Ce_2O_7$ (blue), and $Dy_2Ce_2O_7$ (violet) catalysts (a) Mass activity of different catalysts; (b) Turnover frequency (TOF) and (c) Nyquist plots in the AC frequency range between 100 kHz and 0.1 Hz at 0.45 V.

A lower R_{ct} indicates faster charge transfer kinetics between the electrocatalyst surface and the electrolyte solution during OER. The observed trend in the R_{ct} of the fluorite samples aligns with the trend observed in overpotential. In general, the use of polymer binders for improved catalyst-substrate adhesion resulted in a decrease in the conductivity of all catalysts during OER.

To elucidate differences in charge density of adsorbed OH across the fluorite sample series, density functional theory (DFT) calculations were performed. Slab models of the (100) crystal facet of the fluorites were constructed as shown by a representative crystal structure of $Nd_2Ce_2O_7$ in Figure 4.5 (a) and the differential charge densities of the adsorbed OH group on the RE cation sites were calculated as seen in Figure 4.5 (b). According to the integrated charge density difference, the Nd/Ce-OH layer is surrounded by an apparent electron accumulation at Nd or Ce atoms (sky-blue region) and an electron reduction at O atoms (yellow region), leading to new electronic states at the Nd/Ce-OH heterointerface. The largest electron cloud, depicted in Figure 4.5 (a), indicates a high rate of electron transfer and robust contact between OH^* and the Nd on the catalyst surface; this is supported by the value of the adsorption energy of OH^- on Nd in $Nd_2Ce_2O_7$, which is negative (-2.68 eV) and has the smallest OH^- adsorption energy among all the fluorites investigated in this study. The smallest OH^- adsorption energy of $Nd_2Ce_2O_7$ accelerates the kinetics of the OER. It is noted that all $RE_2Ce_2O_7$ compositions studied here had smaller OH^- adsorption energy relative to the CeO_2 surface. Qualitatively, the trends in smaller adsorption energies matches the trend in smaller overpotentials for OER in the series.

To determine the role of morphology in enhancing the OER performance of the fluorite series, trends in the electrochemically active surface areas (ECSAs) of the catalysts was plotted against OER activity. ECSAs were determined by evaluating the specific electrochemical double-layer capacitance (Cdl) through CV measurements at various scan rates (2.5-50 mV s^{-1}) (SI Figures S4.8-S4.13).

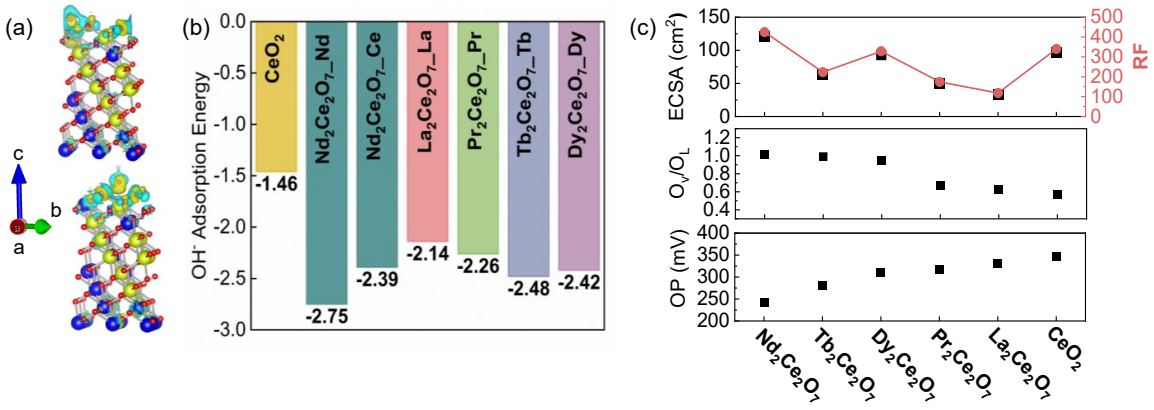


Figure 4.5: (a) Slab models of the (100) surface of $Nd_2Ce_2O_7$ used to calculate differential charge densities of adsorbed OH on Nd (top) and Ce (bottom) sites; (b) OH adsorption energy of the fluorite sample series calculated using the DFT VASP package; (c) Comparison of the trends in ECSA, area ratios of vacancy-related (O_V) and lattice-related (O_L) oxygen calculated from the O1s core level binding spectra from XPS measurements and overpotential at current density of 10 $mAcm^{-2}$ for the fluorite series.

The ECSA and roughness factor were computed and are presented in Figure 4.5 (c). $Nd_2Ce_2O_7$ was found to have the largest ECSA, likely due to the highly nanocrystalline nature of the sample, in corroboration with the broad diffraction peaks observed by XRD. Although CeO_2 exhibits higher ECSA than the other binary fluorites, it showed the lowest OER activity. Furthermore, an increase in ECSA does not directly correlate with a decrease in overpotential across the fluorite series suggesting that ECSA is not the sole factor influencing OER activity. Generally, for highly active catalysts, such as $Nd_2Ce_2O_7$, the larger ECSA observed translates to more exposed electrochemically active sites, facilitating electrolyte infiltration and surface interaction with the active sites of the electrocatalyst. [193] This leads to a high OER activity without hindrance from mass transfer limitations in the electrolyte. [194] A larger ECSA value also leads to higher surface roughness (RF), which is another parameter examined and can affect catalytic activity.

Interestingly, upon comparing trends in OER overpotential of the fluorite series with their corresponding ratio of the O_V/O_L peak areas from the O1s XPS spectra, we observe a clear trend suggesting that an increase in concentration of oxygen vacancies leads to a decrease in overpotential. Surface-enriched oxygen vacancies play a key role in accommodating hydroxyls, enhancing the pre-oxidation of low oxidation species, and facilitating the deprotonation/reconstruction of intermediates. [158] Additionally, achieving a higher valence state via coordination expansion is crucial in forming the initial active M-OOH* species for the oxygen evolution reaction (OER). [195] Since the exposed RE-sites exhibit improved electrophilicity, hydroxyl adsorption onto the Ce-active sites can be facilitated by oxygen vacancies (OV), leading to adsorbed M-OH* intermediate species. Subsequently, this process triggers the deprotonation step at a minimal potential, forming active oxygen species (RE-OOH*) on the catalyst surface. This rationalizes the observed enhancement in OER activity across the fluorite series.

To investigate the pre-oxidation behavior of the catalysts during OER, cyclic voltammetry (CV) was employed. The CV plots reveal that the pre-oxidation

peak of the catalyst becomes more pronounced at higher scan rates (SI Figures S4.14-S4.19). $La_2Ce_2O_7$, $Nd_2Ce_2O_7$, and CeO_2 demonstrate one reduction and one oxidation peak at all scan rates. Their oxidation peak shifts slightly towards a higher potential and their reduction peak towards a lower potential with increasing scan rate. This indicates that they have similar redox processes (involving Ce). In contrast, $Pr_2Ce_2O_7$ and $Tb_2Ce_2O_7$ show two distinct reduction peaks and two overlapping oxidation peaks, with the reduction peaks more obviously identified, as shown in Figures S4.5 and S4.17, suggesting that both Ce in combination with Pr/Tb are involved in a unique redox process for these binary fluorite systems. Similarly, $Dy_2Ce_2O_7$ shows two overlapping reductions and two distinct oxidation peaks, where the oxidation peaks are more obviously recognized, as shown in Figure S18. Similarly, this suggests that Ce and Dy are both involved in this composition's pre-oxidation process. Overall, this indicates that Ce ions may serve as the main active site while the other RE cations play differing roles in modulating catalyst electronic and structural configuration, thereby significantly enhancing electrocatalytic performance in OER. The electrochemical parameters for the fluorite electrocatalysts are compared in Table 4.2.

4.5.3 OER Electrocatalytic Stability

The stabilities of the overall best performing catalyst ($Nd_2Ce_2O_7$) and the catalyst with the second highest electrokinetic activity, $Dy_2Ce_2O_7$, were evaluated by multistep chronopotentiometry at various currents ranging from 5 mA to 25 mA (Figure 4.6). The results demonstrate the remarkable stability of the fluorite series over extended periods and their ability to withstand varying currents without rapid degradation. Additionally, the long-term durability of all the catalysts was investigated by subjecting them to constant potential measurements for 16 hours (SI Figure S4.21).

Table 4.2: Electrocatalytic performance of fluorite catalysts in the series.

	CeO_2	$La_2Ce_2O_7$	$Pr_2Ce_2O_7$	$Nd_2Ce_2O_7$	$Tb_2Ce_2O_7$	$Dy_2Ce_2O_7$
Onset potential (V)	1.52	1.49	1.47	1.42	1.44	1.48
Overpotential@10 $mAcm^{-2}(mV)$	347	331	318	243	280	310
$Ce^{3+} \rightarrow Ce^{4+}$ oxidation peak potential (V)	1.38	1.43	1.41	1.35	1.39	1.4
TOF (s^{-1})	0.0031	0.018	0.0163	0.0634	0.0268	0.0271
Mass activity $\left(Ag^{-1}\right)$	6.77	10.21	9.3	36	14.56	14.56
Tafel slope $\left(mVdec^{-1}\right)$	86.7	56.6	82.2	47.9	76.6	51.7
ECSA $\left(cm^2\right)$	96.2	33.4	49.4	120.4	63.2	93
RF	339.8	118.1	174.3	425.5	223.2	328.6

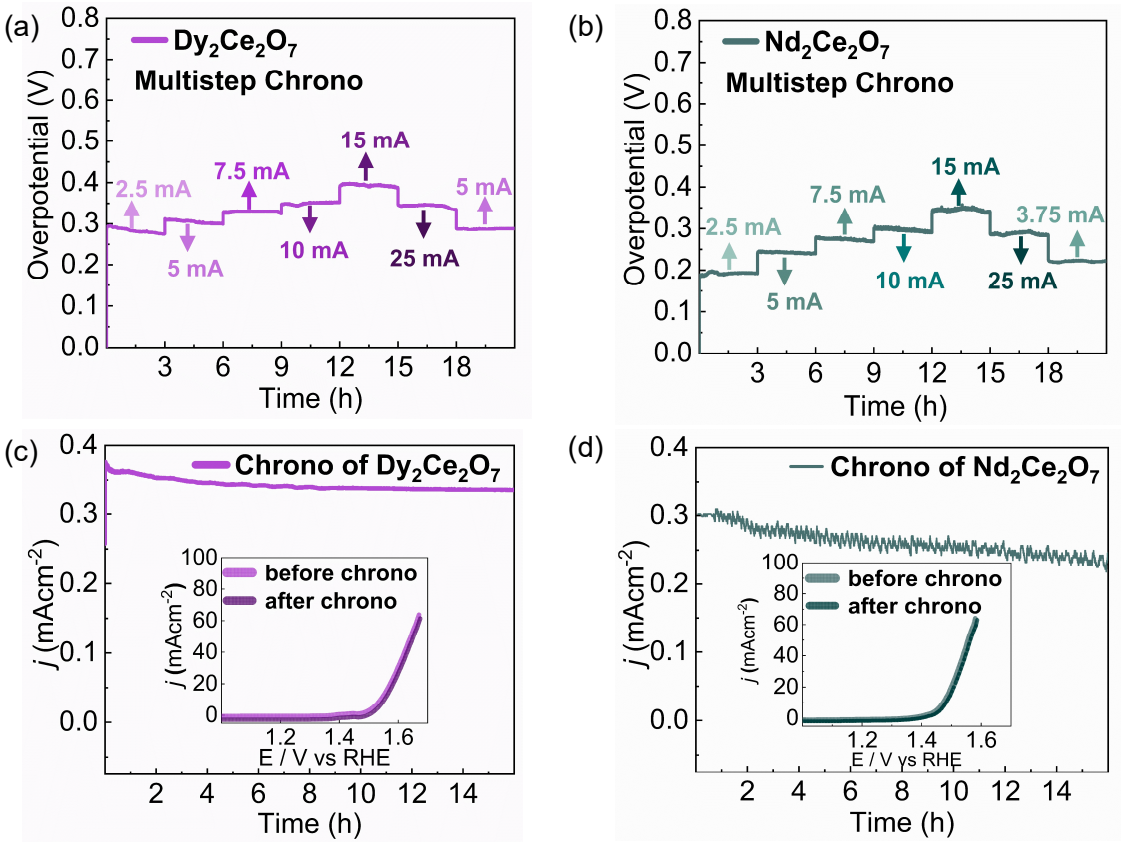


Figure 4.6: (a) Multistep chronopotentiometry study at various currents for (a) $Dy_2Ce_2O_7$; (b) $Nd_2Ce_2O_7$. Chronopotentiometry stability at a constant current of 10 mA (c) $Dy_2Ce_2O_7$; (d) $Nd_2Ce_2O_7$.

The fluorite electrocatalysts exhibited robust catalytic stability over 16 hours under uninterrupted OER conditions at a constant current of 10 mA, as demonstrated by the long-term chronopotentiometry stability test (Figure 4.6 and SI Figure S4.21). No significant deterioration or observable changes in the OER polarization plots of $Dy_2Ce_2O_7$ and $Nd_2Ce_2O_7$ were observed before and after the stability study, indicating excellent mass transfer properties and mechanical ruggedness of the electrode, as depicted in the inset of Figure 4.6 (c,d).

Additionally, XPS analysis (SI Figure S4.22-4.27) reveals no notable alterations in the surface electronic states and elemental compositions of the catalysts before and after the stability measurements, indicating that the integrity of the catalysts remains intact. However, in the O1s spectra of the fluorite samples, additional peaks are observed, indicating the adsorption of OH^* species on the surface after activity. This suggests that OH^- adsorption occurs during catalyst activation and is attributed to physisorption. Furthermore, the C 1s spectra show additional peaks at 295.6 eV which is assigned to aromatic -C=O, while the peaks at 292.9 and 291.5 eV are attributed to an aromatic shake-up, and 283.9 eV corresponds to sp2 and sp3-hybridized carbon (C=C/C–C). [196] The new carbon species observed post OER arise from surface contamination and oxidation products resulting from the reaction, as previously described in literature. [197] Overall, fluorite catalysts synthesized using the EISA approach are found to have decent stability, with no apparent signs of degradation, indicating their promise to deliver the robustness and longevity needed for OER applications.

The remarkable catalytic performance of the $Nd_2Ce_2O_7$ catalyst can primarily be attributed to the improvements in charge and mass transfer achieved through our unique electrode design. The presence of abundant oxygen vacancy defects in the $Nd_2Ce_2O_7$ phase enhances the electrokinetics of the OER process. In addition, incorporating RE-element within the CeO_2 structure provides a favorable modification of the electronic structure. Furthermore, the porous, nanostructured nature of the catalyst plays a significant role in minimizing the contact region

between bubbles and the electrode, facilitating efficient bubble release and reactant transfer. The high surface area to volume ratio of the nanocatalyst and the lattice expansion resulting from incorporating Nd, increase the number of active sites and enhance electron transport conductivity from the catalyst's surface. It will be of great interest to explore whether there is an optimal substitution level of Nd for Ce in the $Nd_xCe_{1-x}O_{2-x}$ solid solution series and whether incorporation of multiple REs in $RE_xCe_{1-x}O_{2-x}$ fluorites will further enhance activity or stability for OER electrocatalysis.

4.6 Conclusion

In this work, EISA was demonstrated as a promising, inexpensive and scalable route to synthesize OER catalysts with high surface area and mesoporosity, belonging to the cerate fluorite class of materials. Although CeO_2 in this study appeared to have the highest overpotential and consequently, the least activity towards OER, its activity is higher than the pristine CeO_2 systems reported in the literature.

The substitution of 50% RE cations for Ce in the CeO_2 fluorite lattice was found to enhance OER activity and stability. Incorporating a RE cation into the host CeO_2 lattice is shown to significantly enhance the OER performance in a 1M KOH electrolyte solution compared to pristine CeO_2. Furthermore, all binary fluorite compositions demonstrate stability in an alkaline medium over long periods of operation at a constant potential. Among the RE binary fluorite samples investigated, $Nd_2Ce_2O_7$ demonstrated the highest OER activity exhibiting a low overpotential of 243 mV at a current density of 10 mA cm^{-2} with a low Tafel slope of 47.9 $mVdec^{-1}$, high TOF of 0.0634 s^{-1}, and high mass activity of 36 Ag^{-1} respectively. Additionally, $Nd_2Ce_2O_7$ displayed promising long-term durability in an alkaline medium. This high OER activity can be attributed to the electronic redistribution and the introduction of a large concentration of oxygen vacancies, induced by incorporating Nd cations into the CeO_2 host fluorite lattice. This study provides valuable insights into using RE-element substitution to tailor the structure

and electronic properties of the fluorite class of materials, enabling the development of highly active and stable electrocatalysts. Importantly, we demonstrate that rare-earth oxide OER catalysts with high activity and stability can be achieved using the low cost EISA synthesis route, without the incorporation of transition and noble metals.

4.7 Acknowledgements

Acknowledgement is made to the donors of the American Chemical Society Petroleum Research Fund for support of the materials synthesis efforts in this research. XRD measurements were completed at the Diffraction Facility at the Institute for Advanced Materials and Manufacturing at the University of Tennessee. This research used beamline BL-1B (NOMAD) at the Spallation Neutron Source, a DOE Office of Science User Facility operated by the Oak Ridge National Laboratory.

Appendix

Supplemental Information (SI)

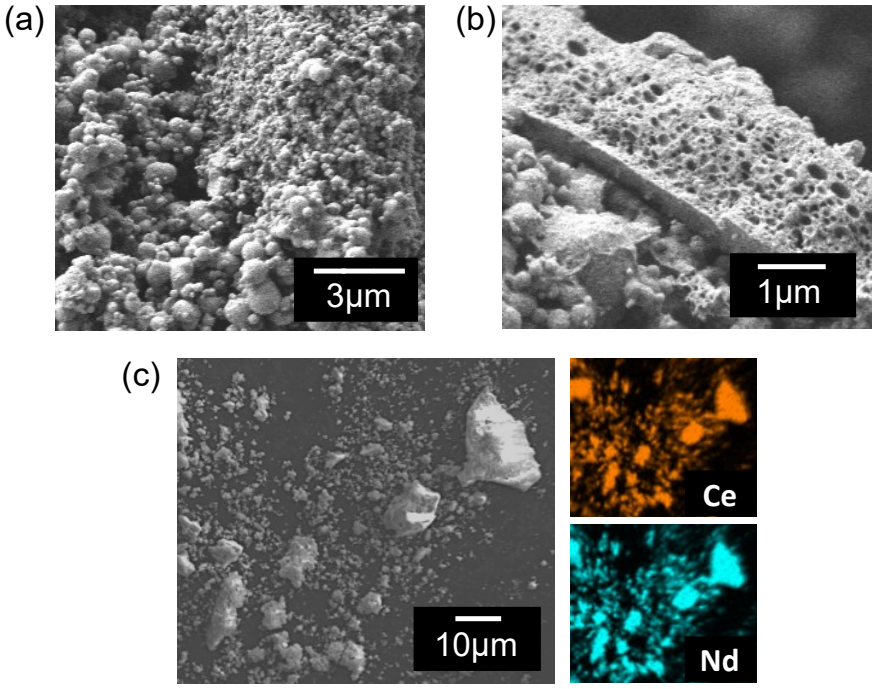


Figure S4.1: Scanning electron microscopy images showing the heterogeneous morphology of $Nd_2Ce_2O_7$ calcined at 600°C including (a) spherical nanoparticles and (b) porous flakes. (c) Elemental Dispersive microscopy image of $Nd_2Ce_2O_7$ calcined at 600°C with elemental mapping shown to the right.

Table S4.1: Chemical composition results from X-ray Fluorescence (XRF) of binary fluorites.

$Tb_2Ce_2O_7$		
Element	Wt% XRF	Target Wt %
Ceria	43.97	46.85
Terbium	56.03	53.15
$La_2Ce_2O_7$		
Element	Wt% XRF	Target Wt %
Ceria	52.59	50.22
Lanthanum	47.41	49.78
$Pr_2Ce_2O_7$		
Element	Wt% XRF	Target Wt %
Ceria	51.10	49.86
Praseodymium	48.90	50.14
$Dy_2Ce_2O_7$		
Element	Wt% XRF	Target Wt %
Ceria	46.00	46.30
Praseodymium	54.00	53.70
$Nd_2Ce_2O_7$		
Element	Wt% XRF	Target Wt %
Ceria	43.49	49.27
Praseodymium	56.51	50.73

Electrochemical Measurements

Electrochemical measurements were performed using a conventional three-electrode system connected to an IviumStat potentiostat, with the fluorite catalyst as the working electrode, while graphite rod and Ag/AgCl electrode were used as counter electrode and reference electrodes respectively, to measure the electrocatalytic performances. Linear sweep voltammetry (LSV), and cyclic voltammetry (CV) and were carried out to study the OER catalytic performance and cycling stability. In order to reduce uncompensated solution resistance, all activity data were iR corrected, which was measured through electrochemical impedance studies.

All potentials measured were calibrated to RHE using the following Equation S4.1:

$$E_{(RHE)} = E_{(Ag/AgCl)} + 0.197V + 0.059 \times pH \tag{4.1}$$

All electrolytes were saturated by oxygen (for OER) bubbles before and during the experiments.

The steady-state performance and durability of all the electrocatalysts in OER for long-term chronoamperometric stability in an alkaline electrolyte of 1 M KOH solution was carried out in two forms: (a) At constant current density of 20 mA cm^{-2} for 16 h, (b) at various current densities between 5 – 30 mA cm^{-2} as multistep study, in N_2-saturated 1.0 M KOH at room temperature.

The Tafel slope, an important parameter to explain the electrokinetic activity of these catalysts for OER processes, was estimated from a Tafel plot. The Tafel equation is given as the dependence of overpotential η on the current density j as shown in Equation S4.2

$$\eta = \alpha + \frac{2.3RT}{\alpha nF} \log j \tag{4.2}$$

where α is the transfer coefficient, n is the number of electrons involved in the reaction, and F is the Faraday constant. The Tafel slope is given by $\frac{2.3RT}{\alpha nF}$. The Tafel plots in this work were calculated from the reverse scan of CV collected at a scan rate of 2 mV s^{-1} in a non-stirred N_2-saturated 1.0 M KOH solution.

The Electrochemical Impedance Spectroscopy (EIS) experiments were performed within $10^5 - 10^{-2}$ Hz frequency range, at an AC signal amplitude of 10 mV, to study the electrode kinetics and estimate the electrolyte resistance (Rs), and charge transfer resistance at the electrode (catalyst)-electrolyte interface (R_{ct}). The Nyquist plots were collected in N_2-saturated 1.0 M KOH at an applied potential of 0.55 V vs. Ag|AgCl (KCl saturated).

Turnover frequency (TOF) for the electrocatalysts was calculated from Equation S4.3:

$$TOF = \frac{j \times A}{4 \times m \times F} \tag{4.3}$$

where j is the current density in mA cm^{-2} at a given overpotential (e.g., $\eta = 0.31$ V), A is the surface area of the electrode (0.283 cm^2), F is the Faraday constant (a value of 96485 C mol^{-1}, and m is moles of catalyst on the electrode.

Mass activity (A g^{-1}) is the current density per unit mass of the active catalyst at a given overpotential. This is calculated from catalyst loading m and the measured current density j (mA cm^{-2}) of the catalyst, at $\eta = 0.31$ V, calculated from Equation S4.4.

$$\text{Mass activity} = \frac{j}{m} \tag{4.4}$$

The electrochemically active surface area (ECSA) of the catalyst was estimated by measuring the electrochemical double-layer capacitance (C_{DL}) at different scan rates in the non-Faradaic region. It was assumed that current obtained in the non-Faradaic region is caused by double-layer charging instead of electrochemical reactions or charge transfer. The double-layer current (i_{DL}) was obtained by

performing cyclic voltammograms (CVs) with various scan rates in a non-stirred N_2 saturated 1.0 M KOH solution. The ratio of double-layer current (i_{DL}) and the scan rate (V) of CV yielded the specific electrochemical double-layer capacitance (C_{DL}) = averaging of cathodic and anodic slopes absolute values obtained from the CV plot in the non-faradaic region as described in Figure S4.5.

$$i_{DL} = C_{DL} \times \mathrm{v} \tag{4.5}$$

The ECSA of the catalyst was calculated using Equation S4.6 where C_s is the specific capacitance as reported in alkaline solution to be between 0.022 and 0.130 mF cm^{-2} in alkaline solution [198]. In this study, we assumed the value of

$$\mathrm{C_s} = 30\,\mu\mathrm{Fcm}^{-2} \tag{4.6}$$

based on previously reported OER catalysts in alkaline medium. [198, 199]

$$ECSA = C_{DL}/C_s \tag{4.7}$$

Roughness factor (RF) is another important parameter that defines catalyst surface roughness and can influence observed catalytic properties. Roughness factor (RF) is estimated as the ratio of ECSA and the geometric electrode area of 0.283 cm^2.

$$RF = ECSA/SA \tag{4.8}$$

Parameters	CeO_2	$La_2Ce_2O_7$	$Pr_2Ce_2O_7$	$Nd_2Ce_2O_7$	$Tb_2Ce_2O_7$	$Dy_2Ce_2O_7$
R_s/ohm	7.83	5.73	4.72	3.54	4.72	3.85
R_{ct}/ohm	18.10	14.31	13.83	7.95	10.10	11.69
CPE/F	4.174×10^{-4}	3.91×10^{-3}	1.71×10^{-3}	5.82×10^{-2}	1.71×10^{-3}	3.91×10^{-3}
$W_1/s^{(1/2)/ohm}$	-	4.73×10^{1}	2.72×10^{1}	-	2.41×10^{1}	1.31×10^{1}

Figure S4.2: Parameters of equivalent circuit obtained from fitting of electrochemical impedance spectroscopy (EIS) experimental data.

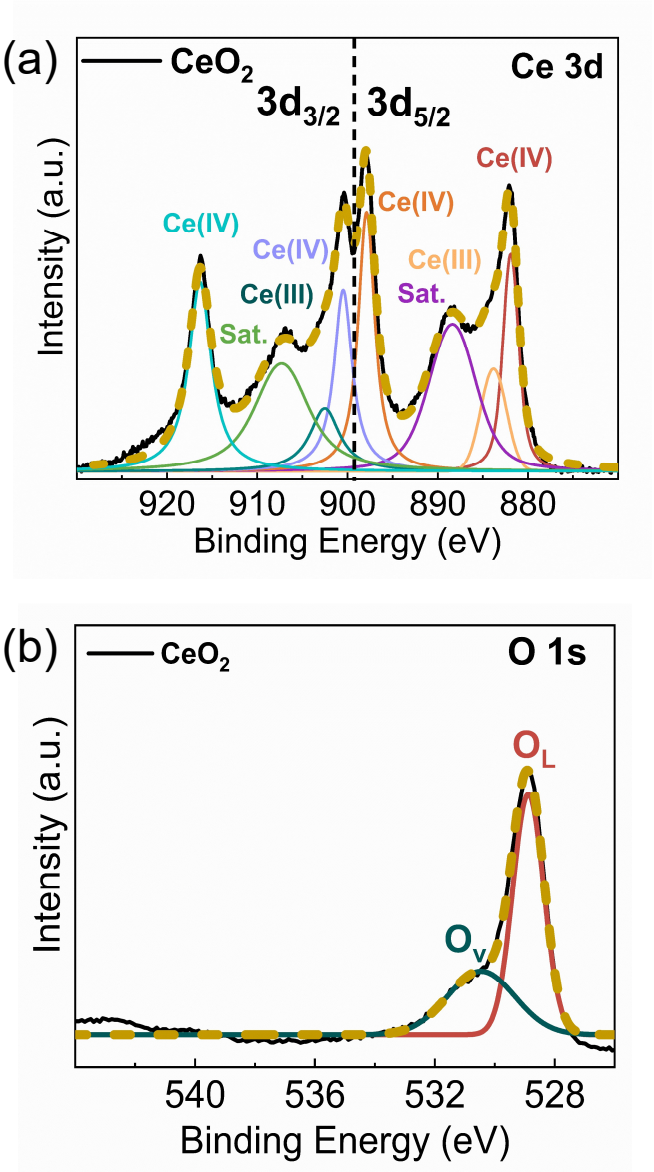


Figure S4.3: High resolution XPS spectra of CeO_2 (a) Ce 3d; (b) O 1s.

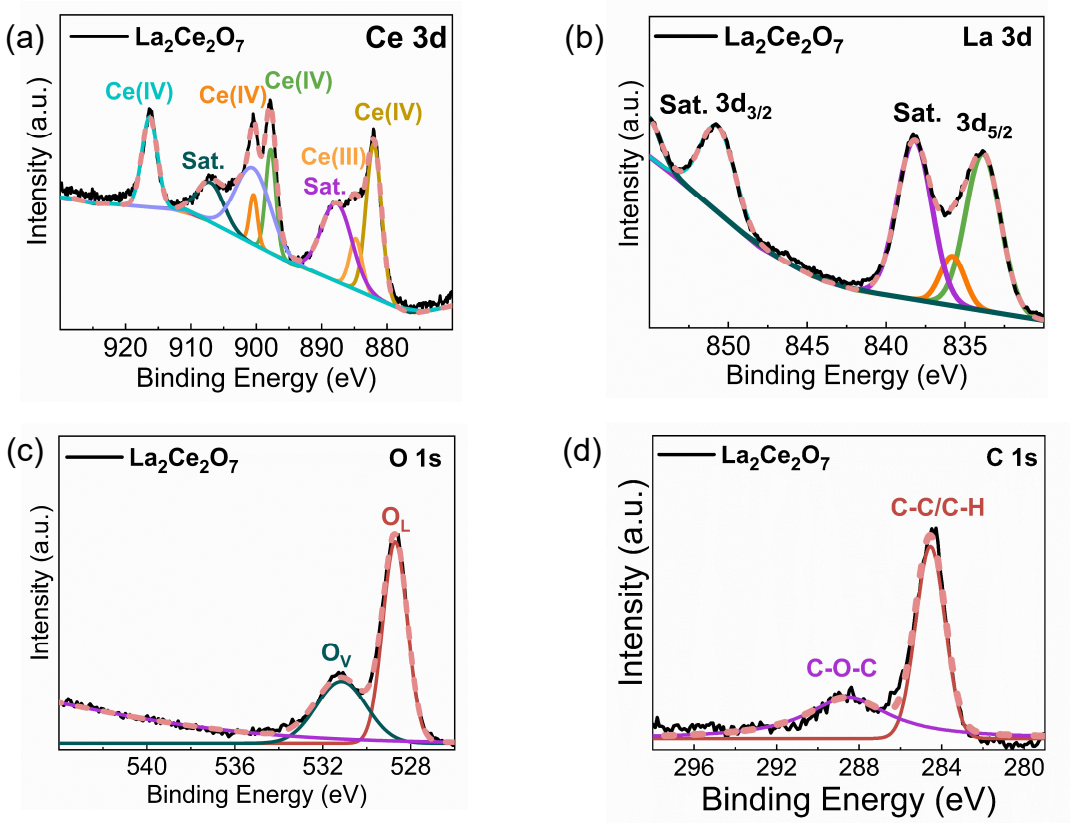


Figure S4.4: High resolution XPS spectra of $La_2Ce_2O_7$ (a) Ce 3d; (b) La 3d; (c) O 1s; (d) C 1s.

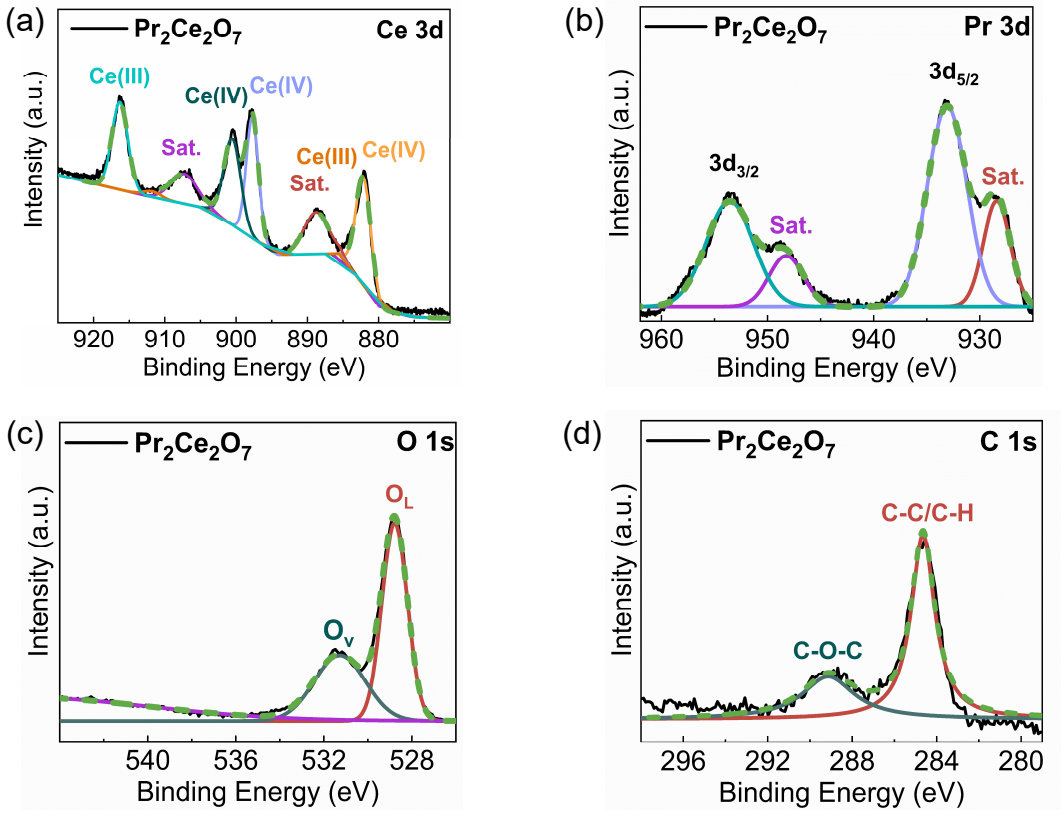


Figure S4.5: High resolution XPS spectra of $Pr_2Ce_2O_7$ (a) Ce 3d; (b) Pr 3d; (c) O 1s; (d) C 1s.

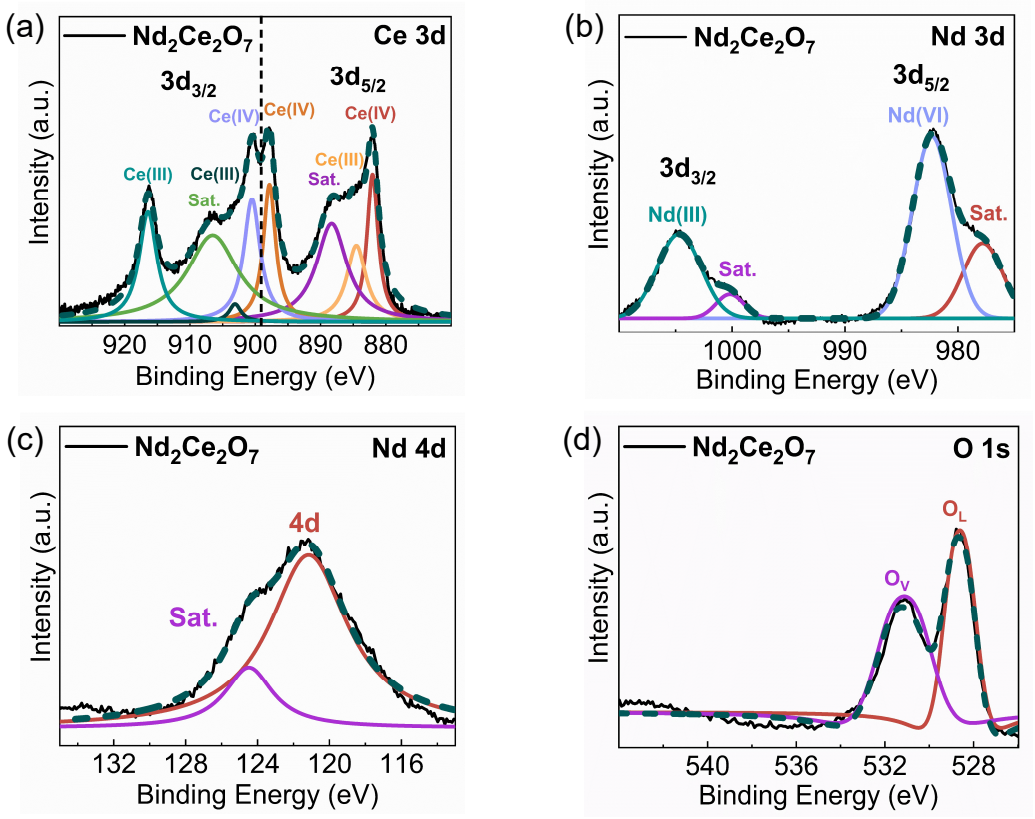


Figure S4.6: High resolution XPS spectra of $Nd_2Ce_2O_7$ (a) Ce 3d; (b) Nd 3d; (c) Nd 4d; (d) O 1s.

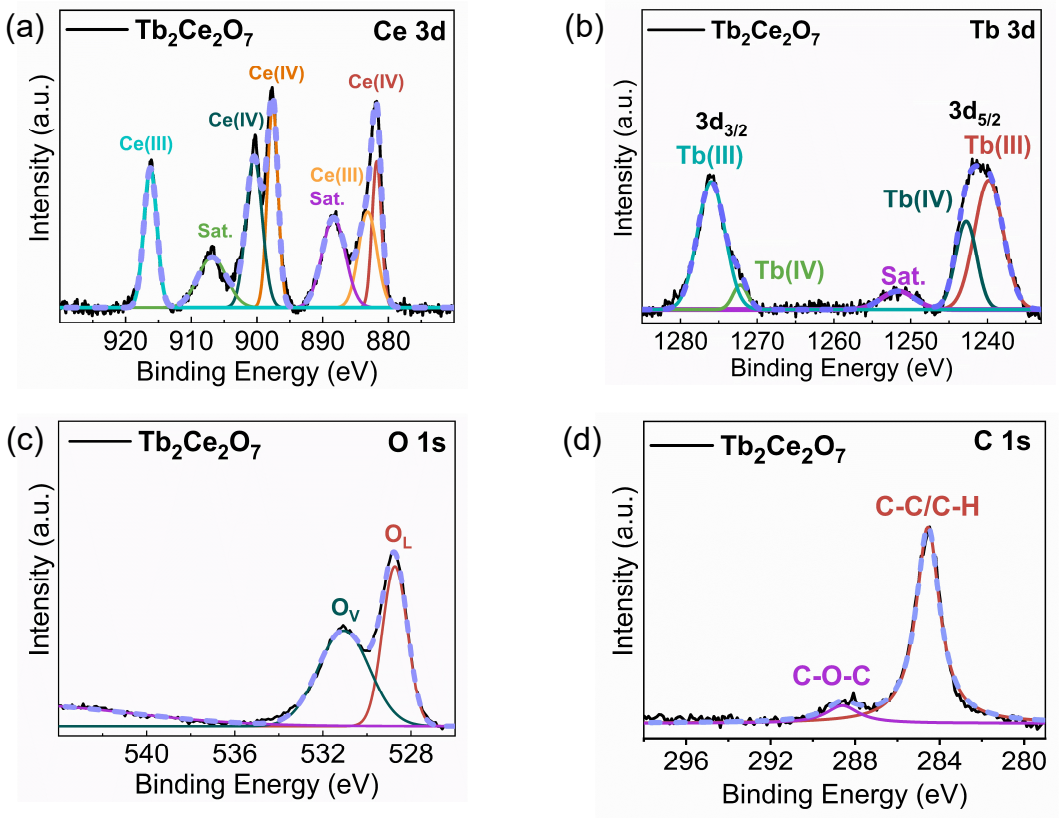


Figure S4.7: High resolution XPS spectra of $Tb_2Ce_2O_7$ (a) Ce 3d; (b) Tb 3d; (c) O 1s; (d) C 1s.

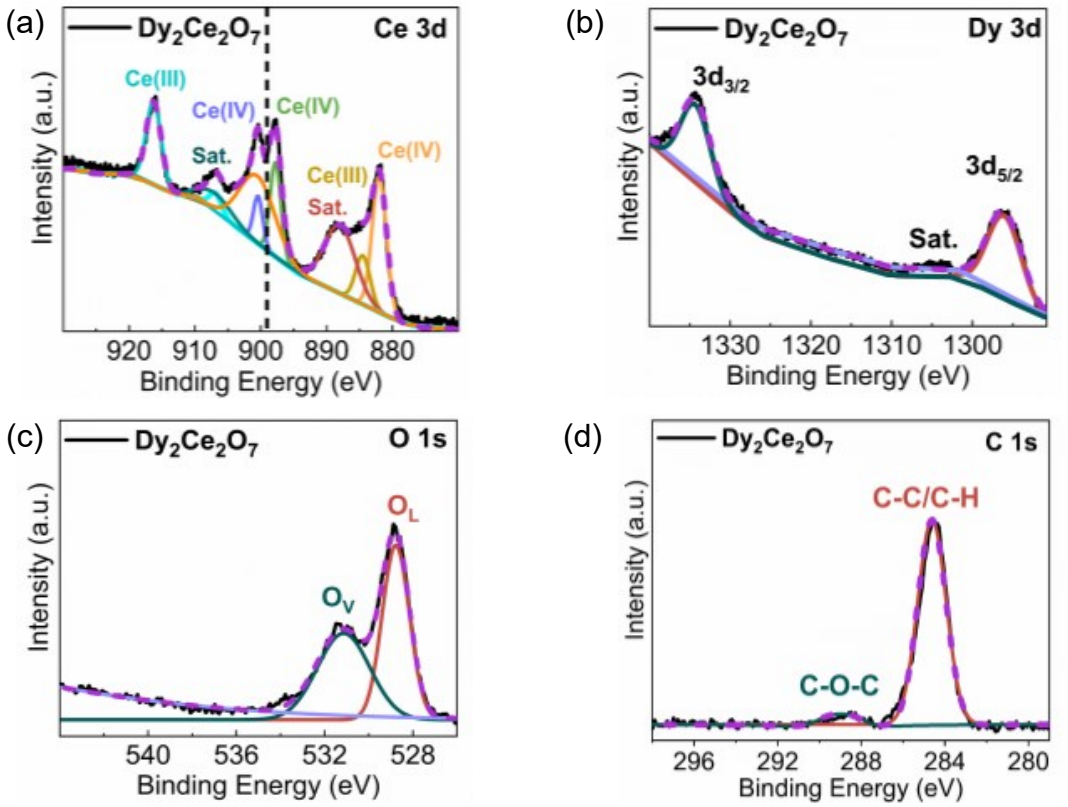


Figure S4.8: High resolution XPS spectra of $Dy_2Ce_2O_7$ (a) Ce 3d; (b) Dy 3d; (c) O 1s; (d) C 1s.

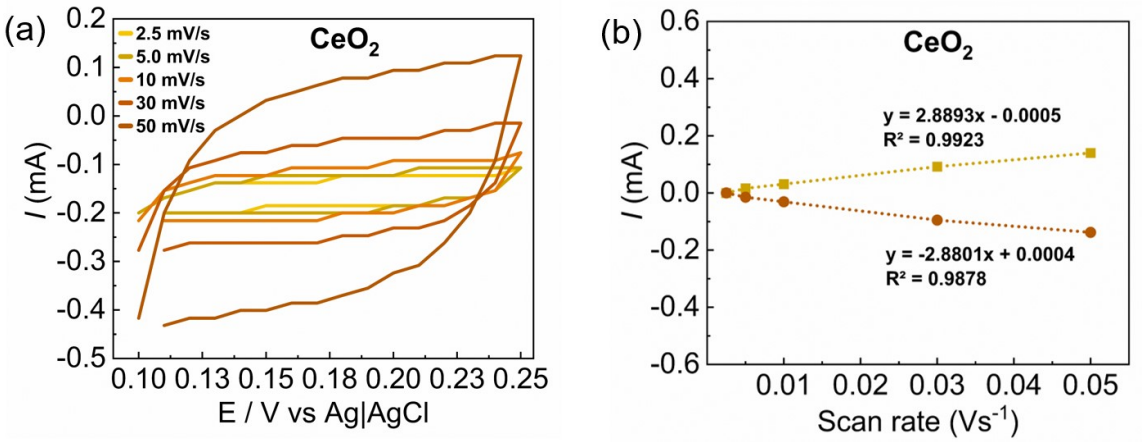


Figure S4.9: (a) Cyclic voltammograms measured at different scan rates for CeO_2; (b) Plots of anodic and cathodic currents measured as a function of different scan rates for CeO_2 in N_2 saturated 1 M KOH at a scan rate of 10 mV s^{-1}.

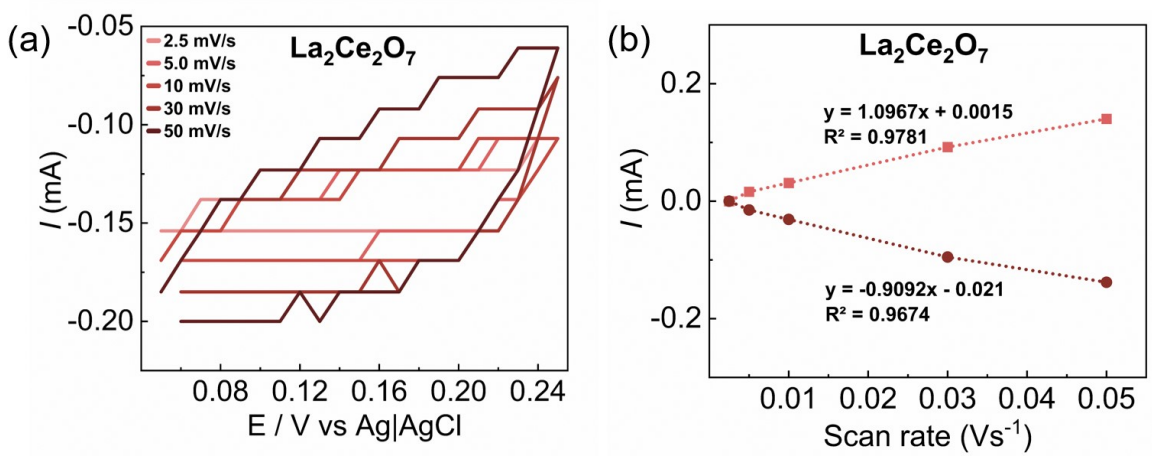


Figure S4.10: (a) Cyclic voltammograms measured at different scan rates for $La_2Ce_2O_7$; (b) Plots of anodic and cathodic currents measured as a function of different scan rates for $La_2Ce_2O_7$ in N_2 saturated 1 M KOH at a scan rate of 10 mV s^{-1}.

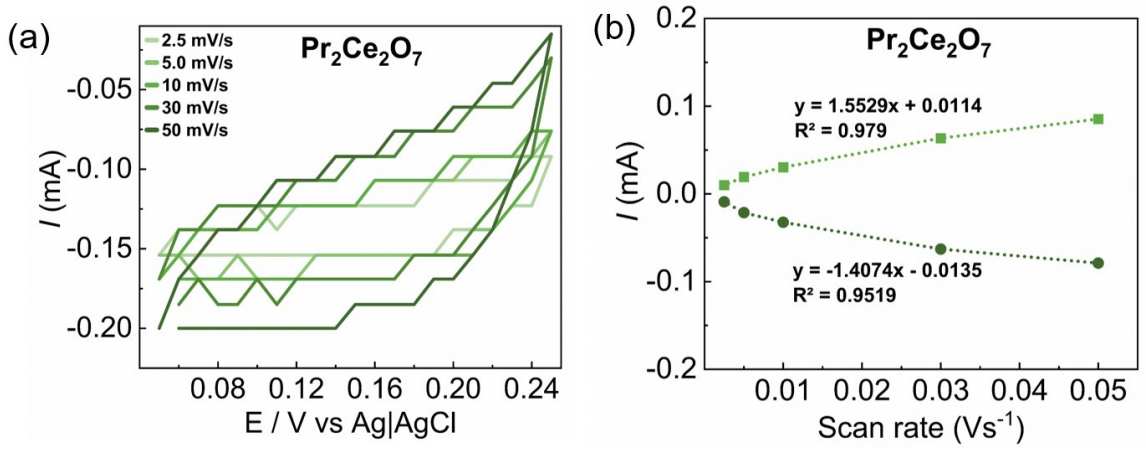


Figure S4.11: (a) Cyclic voltammograms measured at different scan rates for $Pr_2Ce_2O_7$; (b) Plots of anodic and cathodic currents measured as a function of different scan rates for $Pr_2Ce_2O_7$ in N_2 saturated 1 M KOH at a scan rate of 10 mV s^{-1}.

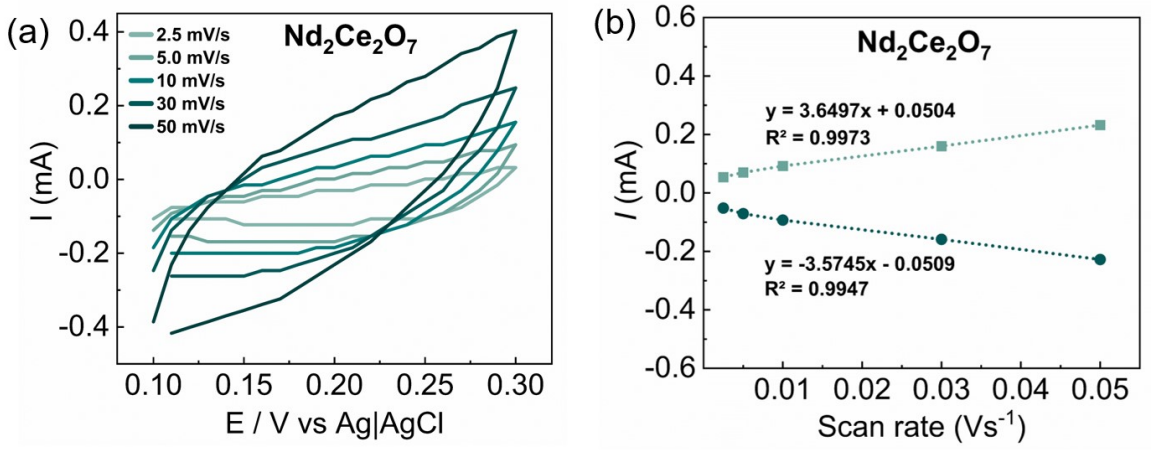


Figure S4.12: (a) Cyclic voltammograms measured at different scan rates for $Nd_2Ce_2O_7$; (b) Plots of anodic and cathodic currents measured as a function of different scan rates for $Nd_2Ce_2O_7$ in N_2 saturated 1 M KOH at a scan rate of 10 mV s^{-1}.

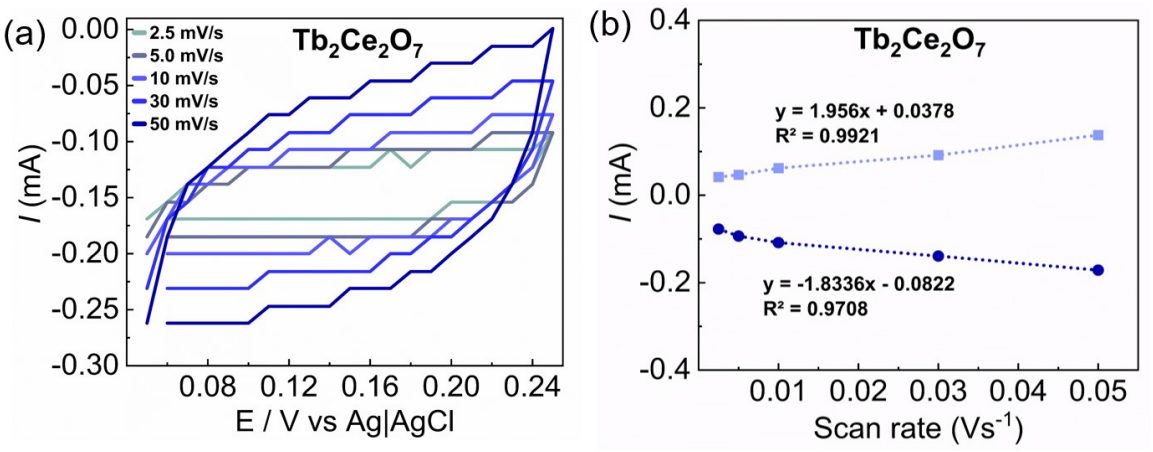


Figure S4.13: (a) Cyclic voltammograms measured at different scan rates for $Tb_2Ce_2O_7$; (b) Plots of anodic and cathodic currents measured as a function of different scan rates for $Tb_2Ce_2O_7$ in N_2 saturated 1 M KOH at a scan rate of 10 mV s^{-1}.

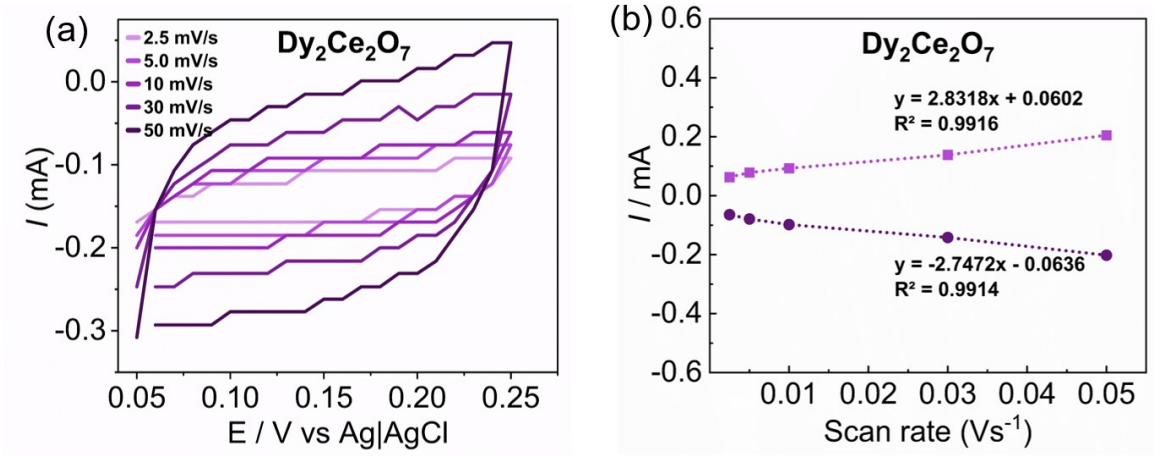


Figure S4.14: (a) Cyclic voltammograms measured at different scan rates for $Dy_2Ce_2O_7$; (b) Plots of anodic and cathodic currents measured as a function of different scan rates for $Dy_2Ce_2O_7$ in N_2 saturated 1 M KOH at a scan rate of 10 mV s^{-1}.

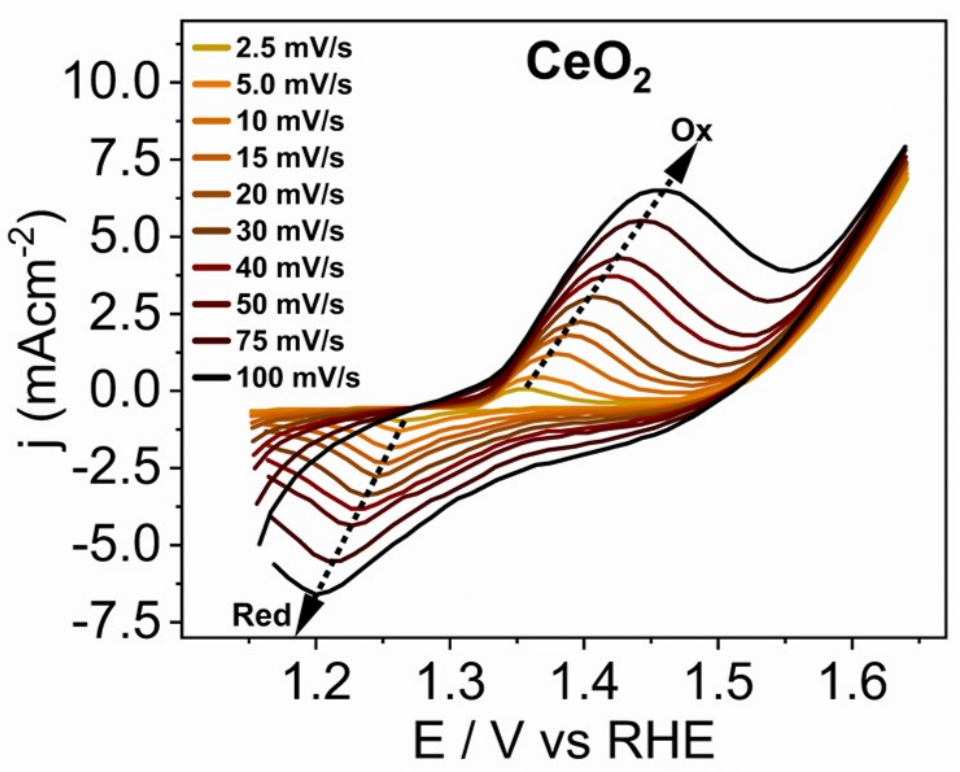


Figure S4.15: Electrocatalytic performance of CeO_2: Cyclic voltammograms measured in N_2 saturated 1 M KOH at different scan rates.

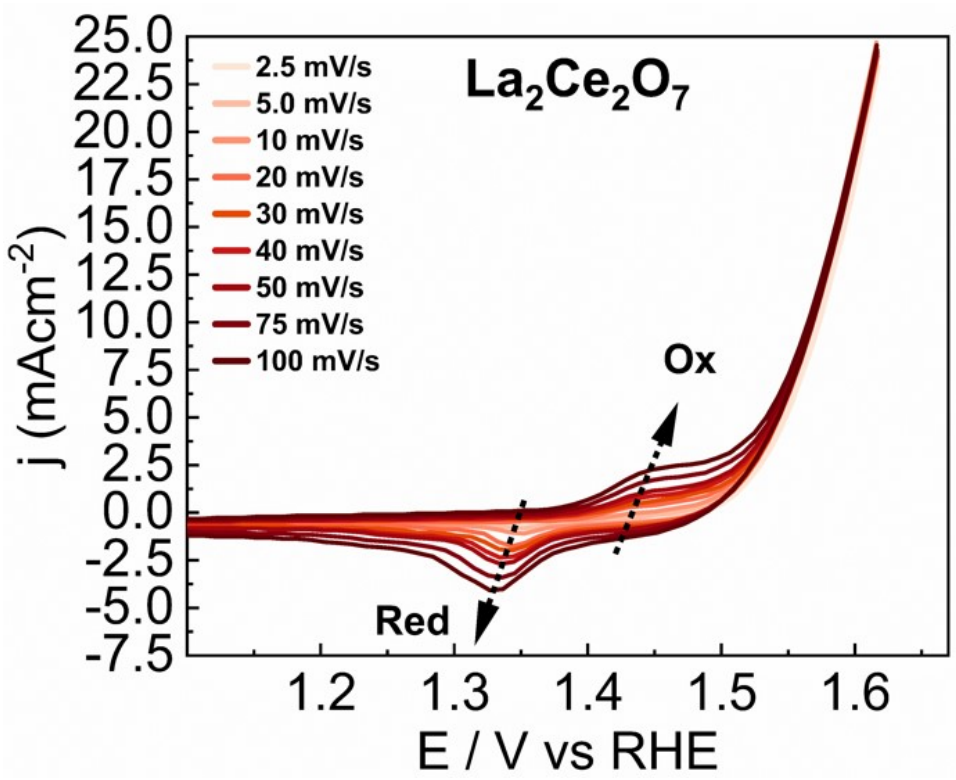


Figure S4.16: Electrocatalytic performance of $La_2Ce_2O_7$: Cyclic voltammograms measured in N_2 saturated 1 M KOH at different scan rates.

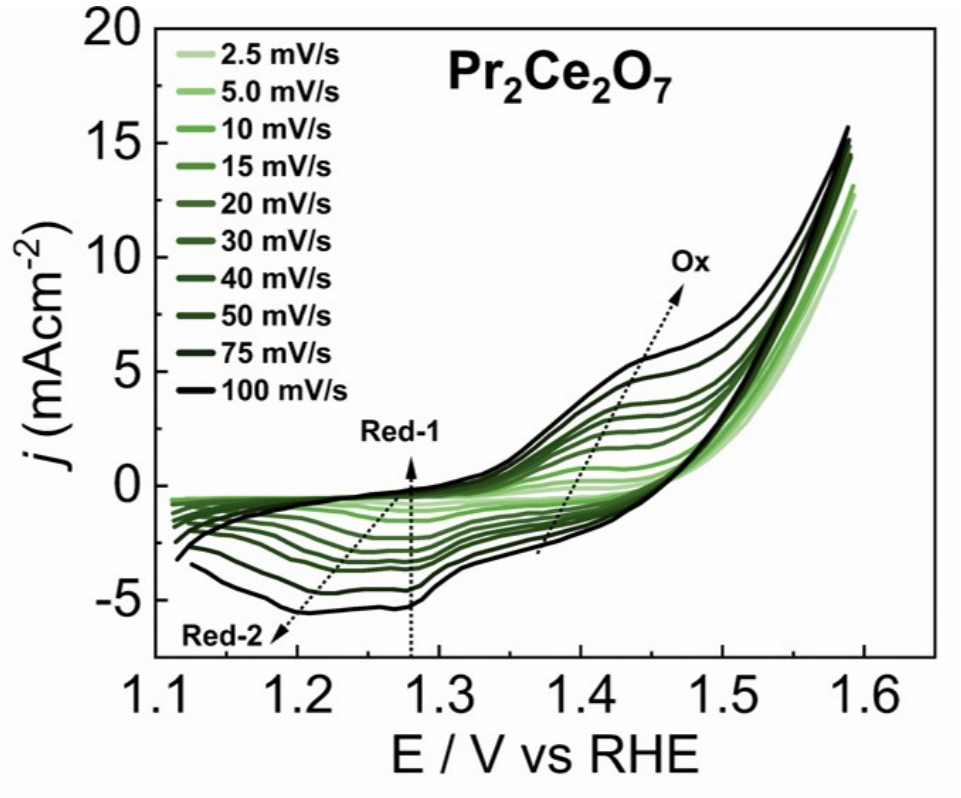


Figure S4.17: Electrocatalytic performance of $Pr_2Ce_2O_7$: Cyclic voltammograms measured in N_2 saturated 1 M KOH at different scan rates.

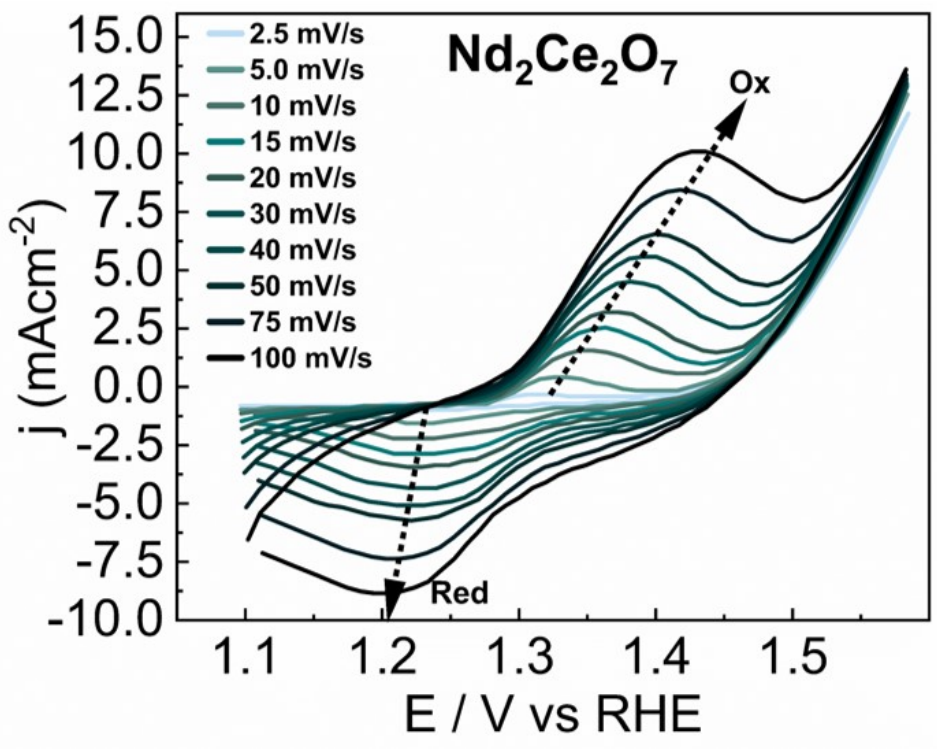


Figure S4.18: Electrocatalytic performance of $Nd_2Ce_2O_7$: Cyclic voltammograms measured in N_2 saturated 1 M KOH at different scan rates.

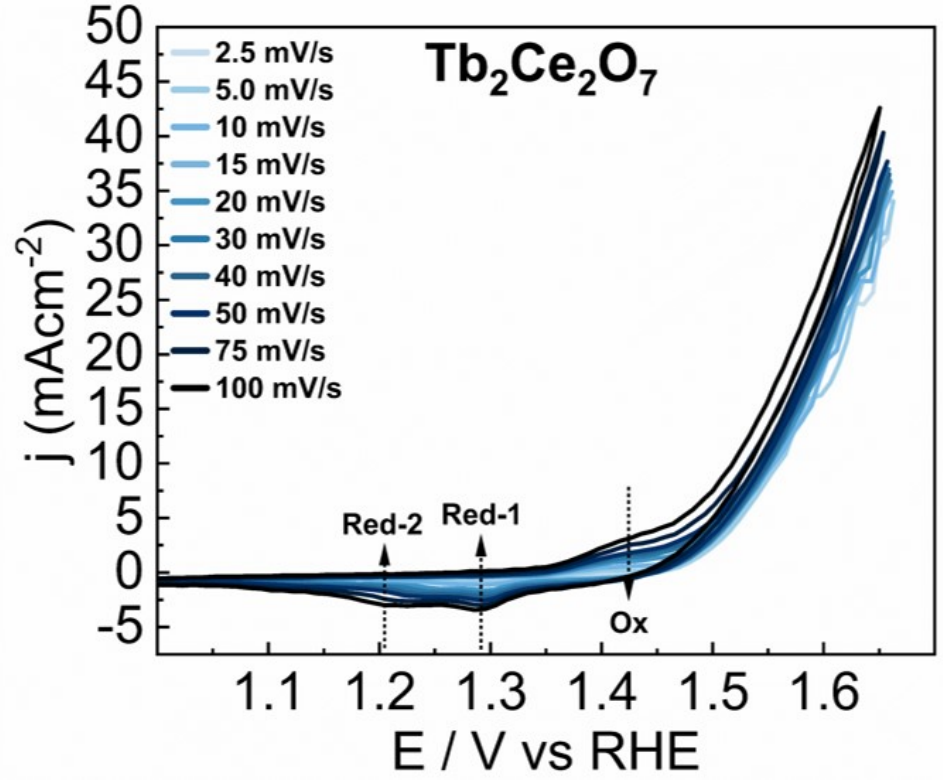


Figure S4.19: Electrocatalytic performance of $Tb_2Ce_2O_7$: Cyclic voltammograms measured in N_2 saturated 1 M KOH at different scan rates.

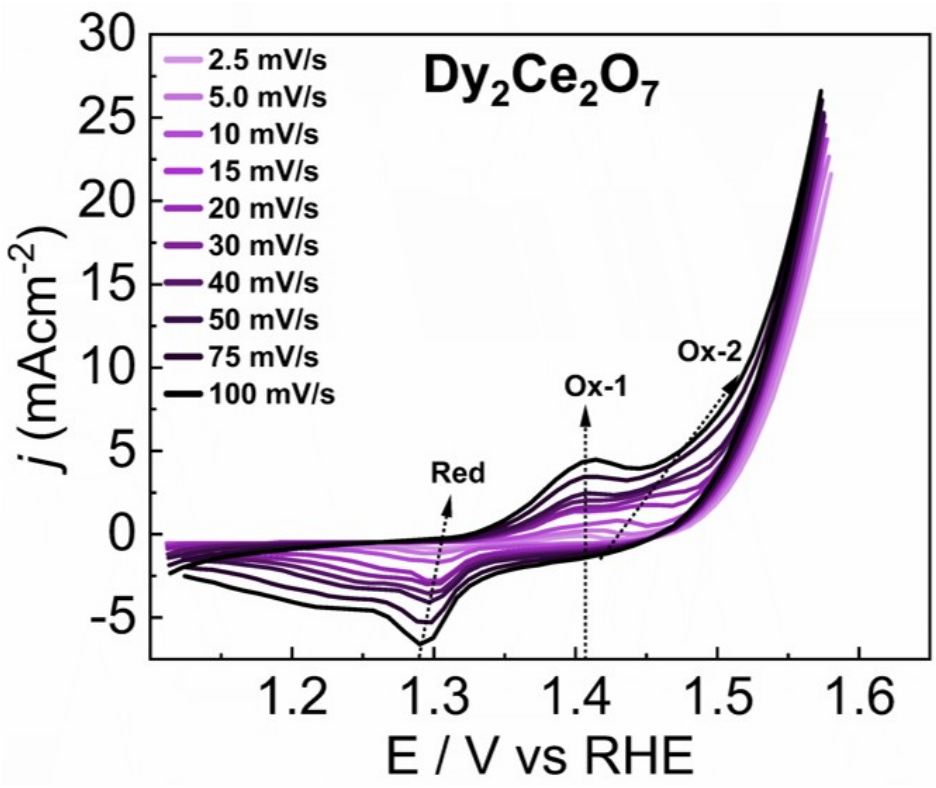


Figure S4.20: Electrocatalytic performance of $Dy_2Ce_2O_7$: Cyclic voltammograms measured in N_2 saturated 1 M KOH at different scan rates.

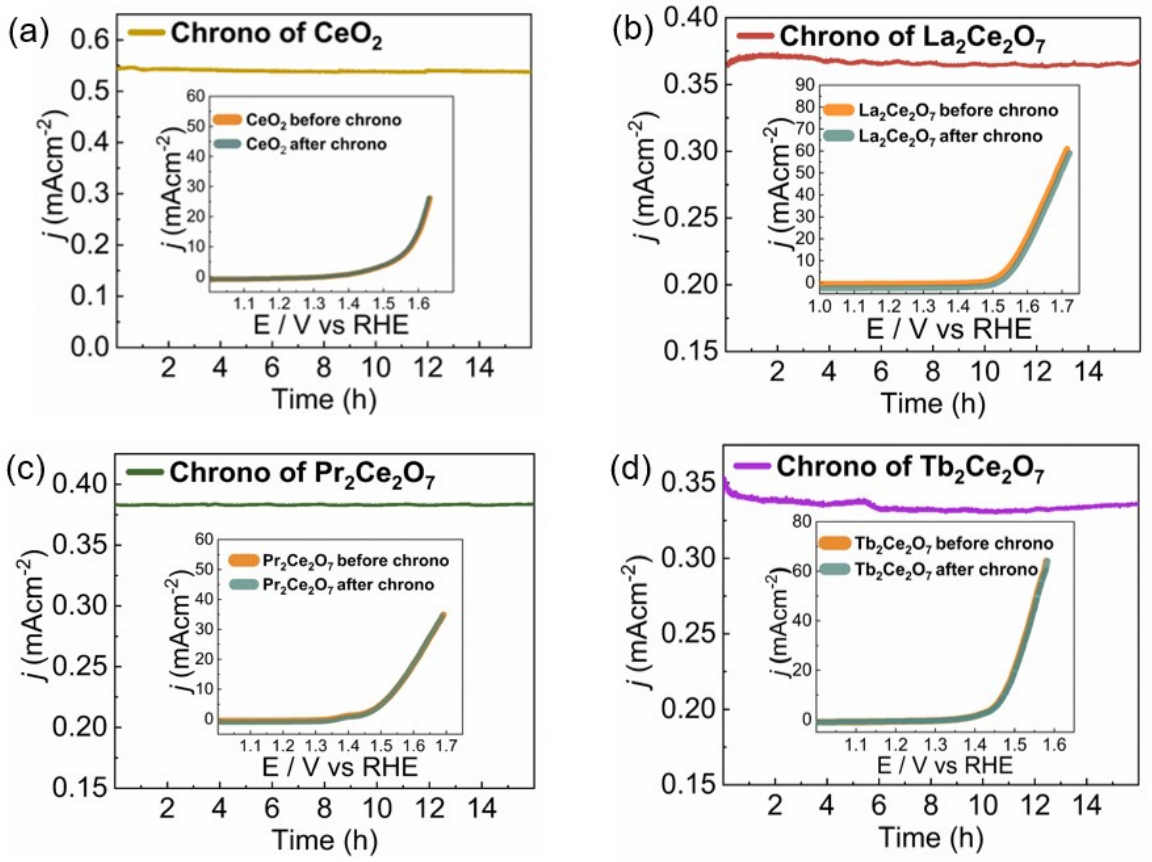


Figure S4.21: Electrocatalytic chronopotentiometry stability at constant current of 10 mA (a) CeO_2; (b) $La_2Ce_2O_7$; (c) $Pr_2Ce_2O_7$; (d) $Tb_2Ce_2O_7$; measured in N_2 saturated 1 M KOH after 16h chronoamperometry.

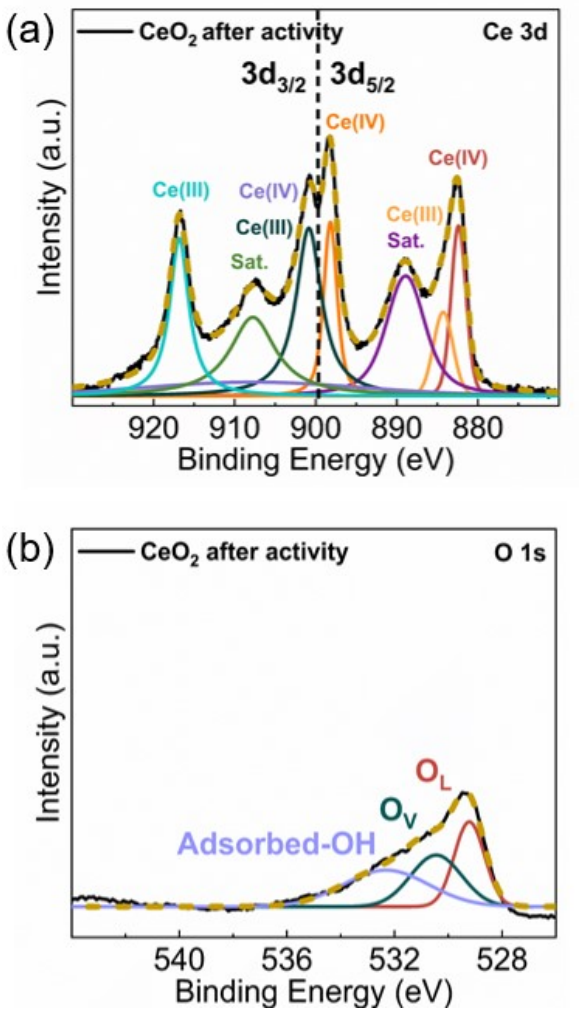


Figure S4.22: High resolution XPS spectra of CeO_2 after activity (a) Ce 3d; (b) O 1s.

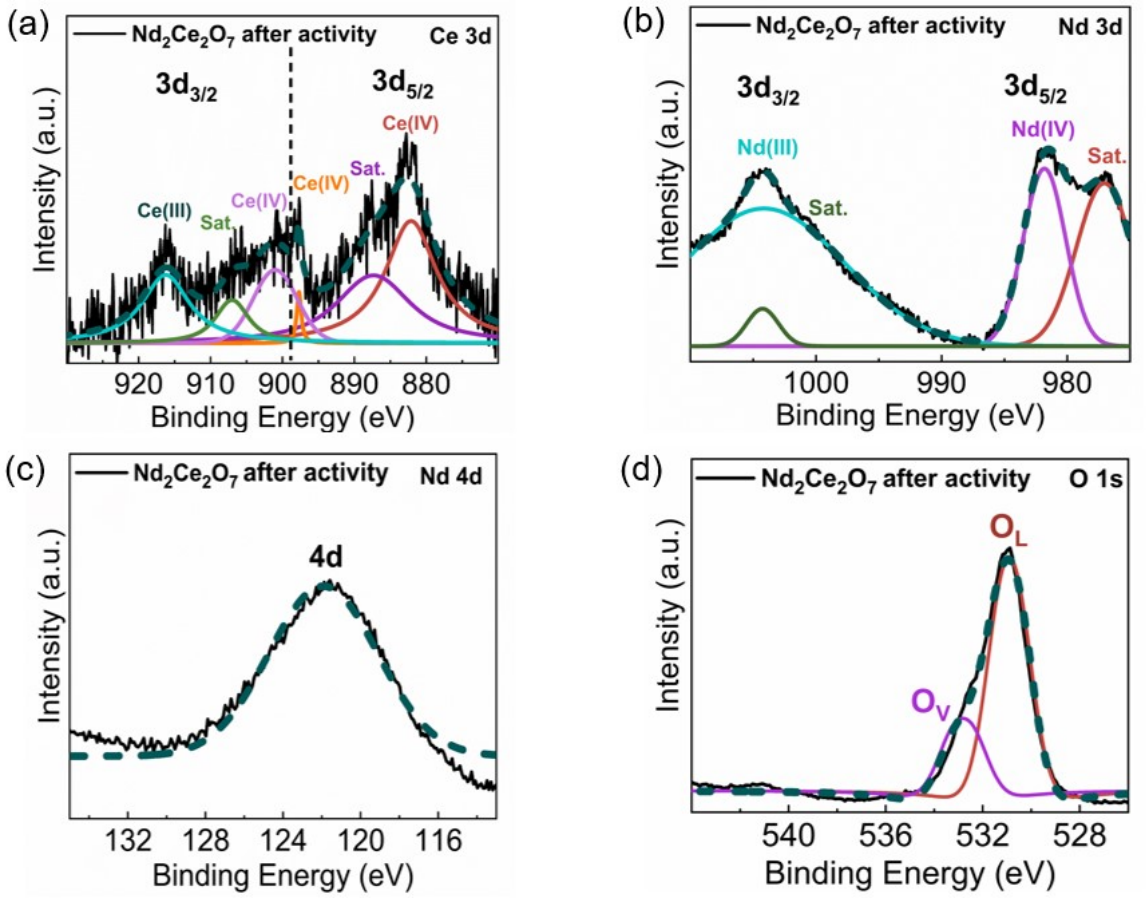


Figure S4.23: High resolution XPS spectra of $Nd_2Ce_2O_7$ after activity (a) Ce 3d; (b) Nd 3d; (c) Nd 4d; (d) O 1s.

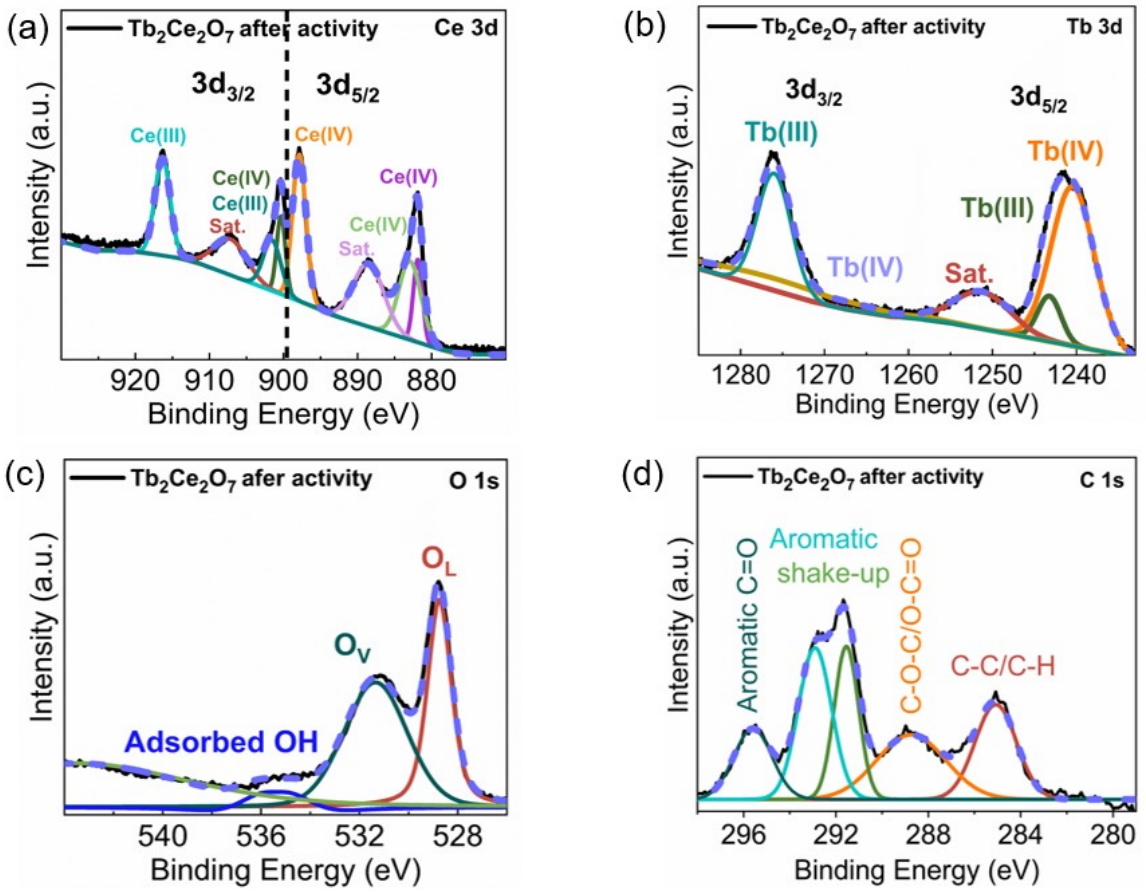


Figure S4.24: High resolution XPS spectra of $Tb_2Ce_2O_7$ after activity (a) Ce 3d; (b) Tb 3d; (c) O 1s; (d) C 1s.

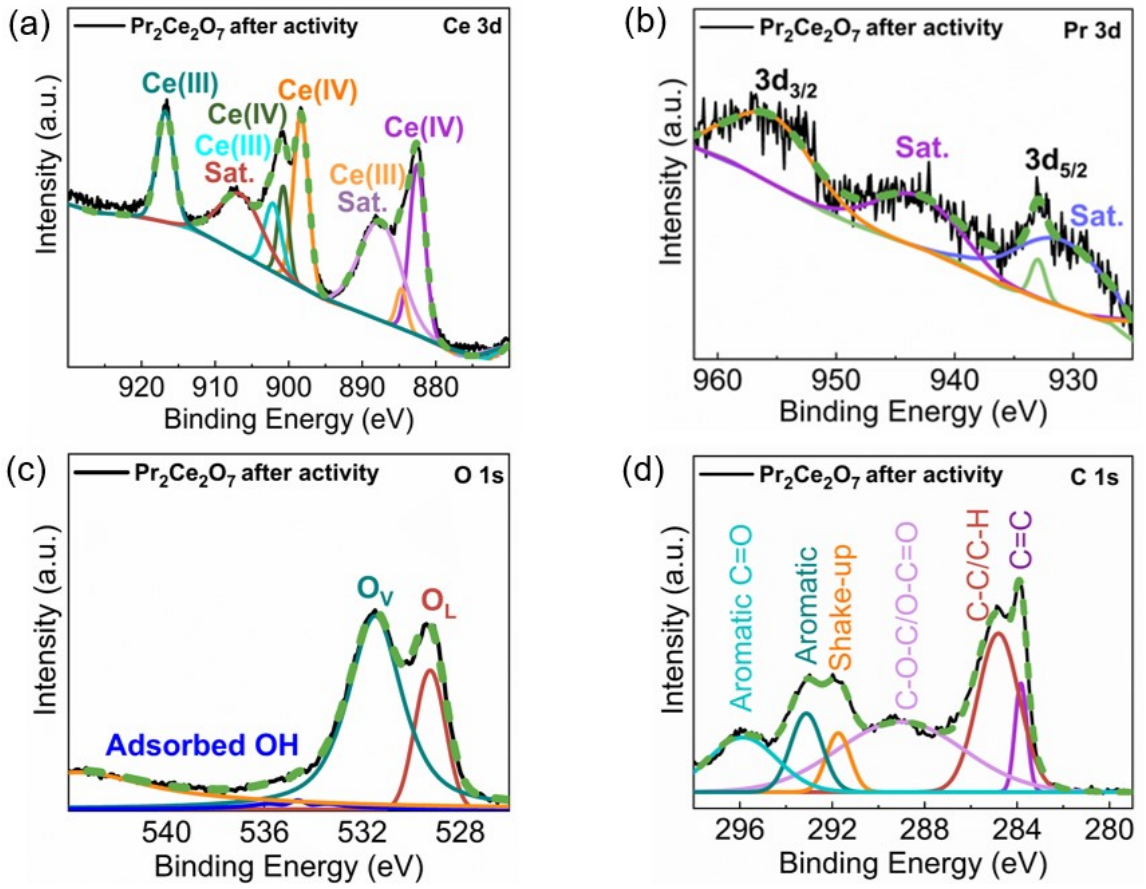


Figure S4.25: High resolution XPS spectra of $Pr_2Ce_2O_7$ after activity (a) Ce 3d; (b) Pr 3d; (c) O 1s; (d) C 1s.

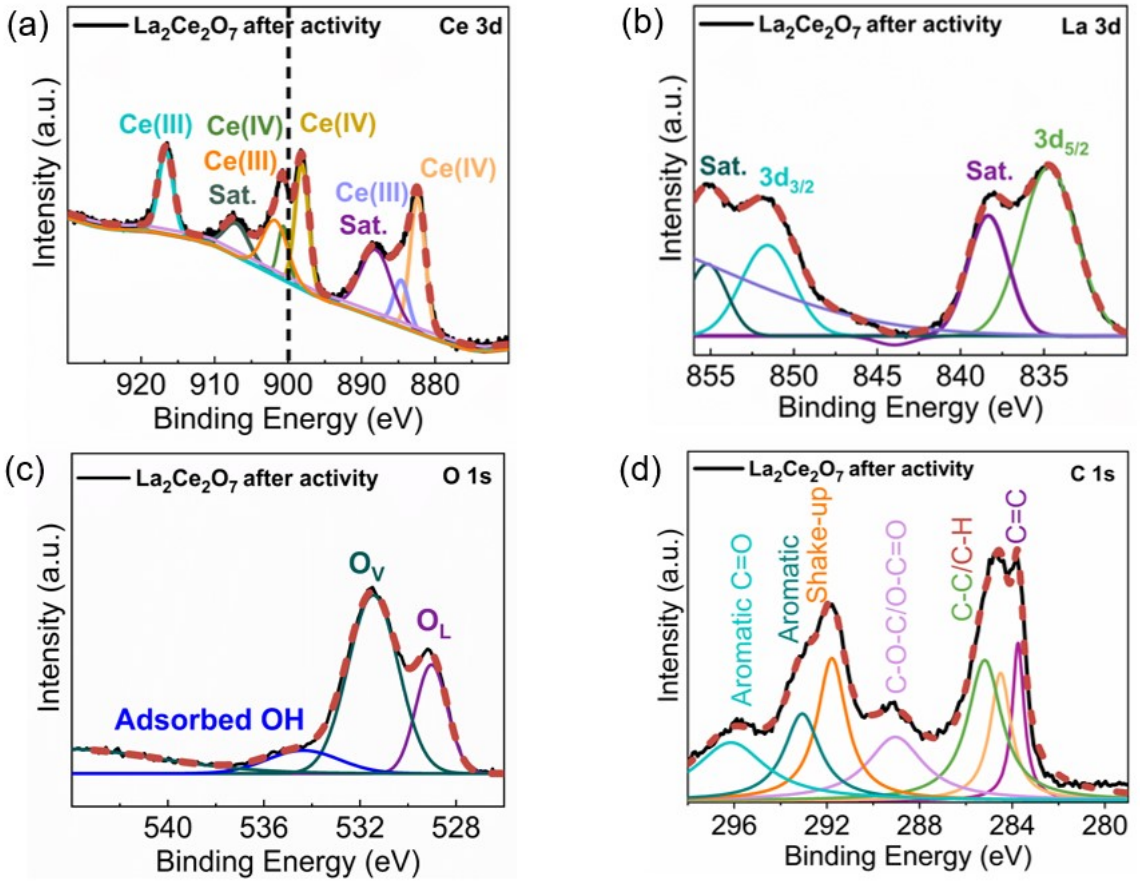


Figure S4.26: High resolution XPS spectra of $La_2Ce_2O_7$ after activity (a) Ce 3d; (b) La 3d; (c) O 1s; (d) C 1s.

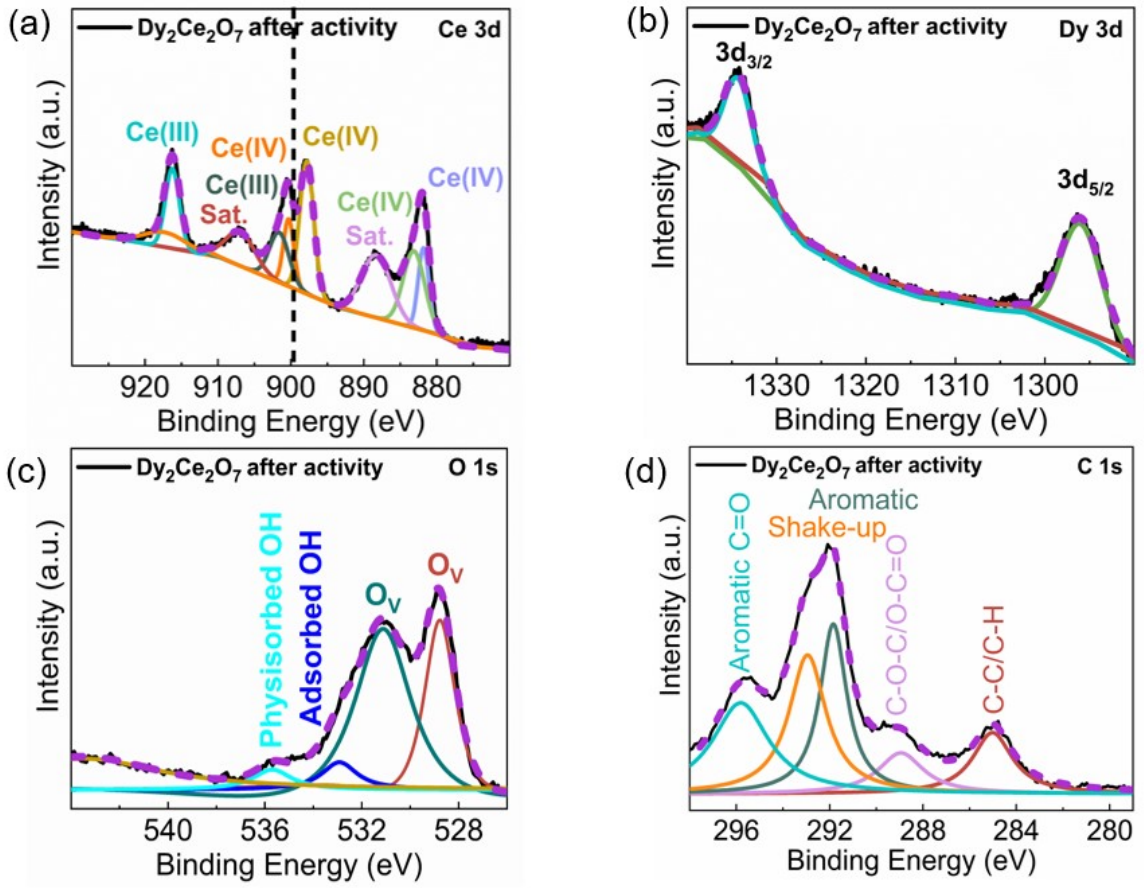


Figure S4.27: High resolution XPS spectra of $Dy_2Ce_2O_7$ after activity (a) Ce 3d; (b) Dy 3d; (c) O 1s; (d) C 1s.

Chapter 5

Tailored $(La_{0.2}Pr_{0.2}Nd_{0.2}Tb_{0.2}Dy_{0.2})_2Ce_2O_7$ as a Highly Active and Stable Nanocatalyst for the Oxygen Evolution Reaction

A version of this chapter was submitted and is under revision for publication by Sreya Paladugu, Ibrahim Munkaila Abdullahi, Palani Jothi, Manashi Nath*, and Katharine Page*: Paladugu, S., Munkaila, I., Jothi, P.,Nath, M and Page, K. (2023). Tailored $(La_{0.2}Pr_{0.2}Nd_{0.2}Tb_{0.2}Dy_{0.2})_2Ce_2O_7$ as a Highly Active and Stable Nanocatalyst for the Oxygen Evolution Reaction. In revision.

5.1 Abstract

Designing highly active and robust catalysts for the oxygen evolution reaction is key to improving the overall efficiency of the water splitting reaction. We have previously demonstrated that evaporation induced self-assembly (EISA) can be used to synthesize highly porous and high surface area cerate-based fluorite nanocatalysts, and that substitution of Ce with 50% rare earth (RE) cations significantly improves electrocatalyst activity. Herein we further explore the defect structure of the best performing nanocatalyst in the series, $Nd_2Ce_2O_7$, with a combination of neutron diffraction and neutron pair distribution function analysis. It is found that Nd^{3+} cation substitution for Ce in the CeO_2 fluorite lattice introduces higher levels of oxygen Frenkel defects and induces a partially reduced $RE_{1.5}Ce_{1.5}O_{5+x}$ phase with oxygen vacancy ordering. Significantly, it is demonstrated that the concentration of oxygen Frenkel defects and improved electrocatalytic activity can be further enhanced by increasing the compositional complexity (number of RE cations involved) in the substitution. The resulting novel compositionally-complex fluorite– $(La_{0.2}Pr_{0.2}Nd_{0.2}Tb_{0.2}Dy_{0.2})_2Ce_2O_7$ is shown to display a low OER overpotential of 210 mV at a current density of 10 $mAcm^{-2}$ in 1M KOH, and excellent cycling stability. We suggest that increasing the compositional complexity of fluorite nanocatalysts expands our ability to tailor catalyst design.

5.2 Introduction

Electrochemical water splitting has been proposed as a sustainable approach to store electricity generated from intermittent renewable energy sources in the form of hydrogen fuel and reduce our reliance on fossil fuels. [200, 129, 201, 202] Water splitting is composed of two half reactions: the oxygen evolution reaction (OER) and the hydrogen evolution reaction, which occur at the anode and cathode respectively. [148, 149, 203, 201] The overall efficiency and large scale industrialization of the water splitting reaction is limited by the sluggish kinetics of the four electron-proton transfer process involved in OER.[204, 151, 205] Thus far, the benchmark electrocatalysts used to reduce the overpotential required for the OER have primarily comprised of precious metals and their oxides (Ru, Ir, RuO_2, and IrO_2). [206, 152] Despite their high activity, the scarcity, high cost and instability of precious metal based oxides presents major drawbacks. In this context, contemporary research efforts have been directed towards the development of alternate highly active precious metal-free electrocatalysts for the OER.

Ceria based mixed oxides have shown promise for electrocatalysis applications, owing to ceria's abundance in natural reserves, excellent reduction and oxidation (redox) properties, and mechanical stability and corrosion resistance in alkaline environments. [148] The desirable redox properties of ceria arise from its ability to dynamically and reversibly convert between Ce(III) and Ce(IV), enabling the formation of oxygen vacancies and a defect rich structure. [71, 160, 207] Previous studies have demonstrated that introducing dopants into the host lattice of ceria is an effective materials design strategy to tune the electronic and defect structure of ceria, leading to favorable adsorption sites for reaction intermediates and enhanced OER activity. [148]

In Chapter 4, it was demonstrated that cerate-based OER catalysts with high activity and stability can be achieved using the EISA synthesis route. Furthermore, the work revealed that 50% substitution of any one of the RE cations La, Pr,

Nd, Tb, or Dy for Ce improved the electrocatalytic activity relative to a CeO_2 composition prepared by the same method. Among the rare earth cerate oxides examined, $Nd_2Ce_2O_7$ achieved the best activity (OER overpotential of 243 mV at a current density of 10 $mAcm^{-2}$), and displayed modest stability under cycling in an alkaline medium. Crystal structure analysis, X-ray Photoelectron Spectroscopy (XPS) studies, and supporting Density Functional Theory (DFT) calculations across the series suggest the increased activity can be linked to large concentrations of oxygen vacancies and a redistribution of electronic structure in the host lattice. Oxygen vacancies have been shown to increase adsorption of oxygen-containing intermediates in the OER and enhance catalytic activity. [208, 209, 210] There are two generally accepted mechanisms via which the OER proceeds: the adsorbate evolution mechanism and the lattice oxygen participation mechanism. [180] The kinetics of both of these mechanisms is influenced by the oxygen vacancy structure and the resulting binding strengths of the oxygen-containing intermediates such as MOOH* and MOH* (M = metal cation(s)) with the catalyst surface. [180] Investigation into the nature and extent of oxygen vacancies present in EISA derived $Nd_2Ce_2O_7$ relative to CeO_2 is therefore of great interest.

Compositionally complex oxides (CCOs) are a class of multi-component oxides comprised of multiple cations on at least one distinct crystallographic lattice site. CCO is a more general class than the related High Entropy Oxides or Entropy Stabilized Oxides. [211] Although there is much debate about the precise definition of CCOs in the research community, CCOs are loosely defined as having a mixing configurational entropy of 1-1.5R (with R being the ideal gas constant) on at least one cation lattice site. [212, 213] CCOs have attracted interest as promising OER catalysts due to observed instances of improved catalytic activity, lower overpotentials and longer-term stability compared to end-member compositions. [214, 215] The improved OER activity of CCOs has been attributed to entropy stabilization and the synergistic effect of incorporating various catalytically active metal elements. [159] Additionally, the CCO platform can be used to introduce

more structural defects and oxygen vacancies than known endmember oxide systems. [148, 159]

In this work, we examine the effect of introducing Nd and multiple rare earth cations into the fluorite type host lattice of ceria on the nature and extent of oxygen vacancy structure, and intrinsic OER activity of the electrocatalyst. We use the CCO concept to design a new compositionally complex fluorite nanostructure within the class $RE_{0.5}M_{0.5}O_{2-x}$, where RE represents rare earth cations and M is cerium (Ce). Ceria, which has a fluorite type crystal structure, has been investigated as a co-catalyst or support for the OER, in combination with transition metals or noble metals. [148, 216, 217, 218] In Chapter 4, we showed that partial substitution of Ce^{4+} with (mainly) trivalent RE cations can introduce oxygen vacancies into the lattice, reduce/ potentially eliminate the need for noble metal cations, and potentially promote the adsorption of oxygen containing intermediates in the OER such as MOOH* and MOH*. As shown in Figure 5.1, when RE cations are introduced into the fluorite lattice, the $Ce^{3+/4+}$ and RE cations randomly occupy the 4*a* Wyckoff position, while the oxygen anions occupy 7/8ths of the tetrahedral sites on position 8*c*. Doping CeO_2 with (mainly) lower valent RE^{3+} cations such as Pr, Nd, Dy and La is known to depress the concentration of Ce^{3+} and introduce large amounts of oxygen vacancies resulting in a defect fluorite structure. [160, 207, 175, 173, 174, 178]

Here, we again use a soft templating evaporation induced self-assembly approach (EISA) to synthesize OER fluorite catalysts with high surface area, porosity/nanoarchitecture, and varying degrees of compositional complexity, with the objective of increasing the number of exposed active sites and improving mass diffusion kinetics. [148] Furthermore, EISA is an inexpensive, highly tunable, and easily scalable synthesis approach, making it feasible for industrial manufacturing.

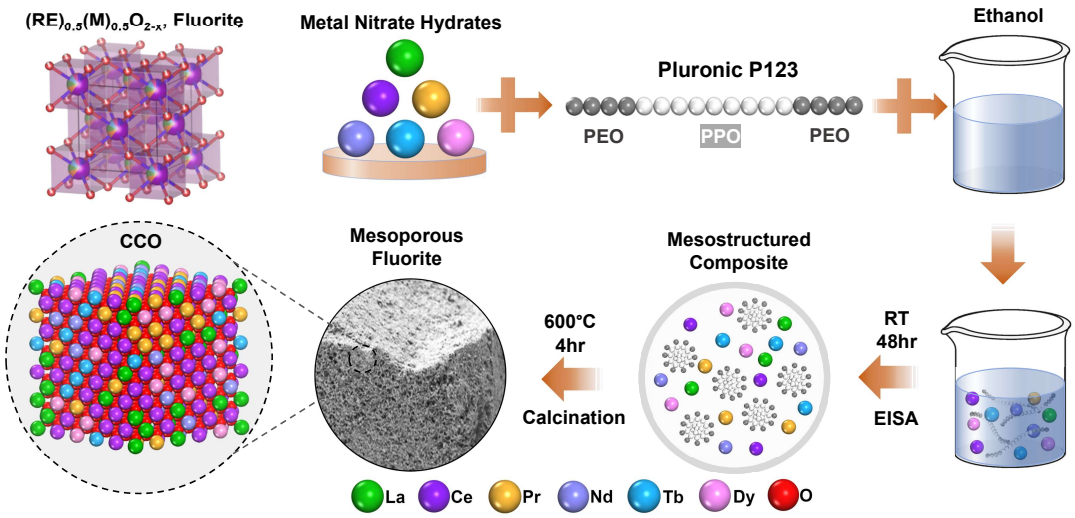


Figure 5.1: Synthesis schematic of mesoporous fluorite catalysts using a soft templating strategy via Evaporation Induced Self Assembly (EISA); calcination temperatures between 400°C and 1000°C are used in this work. The fluorite unit cell is shown on the top left with VIII-fold cation coordination polyhedron depicted as purple cubes with red O atoms at the vertices. The cation sites are occupied, on average, with equal parts of 5 RE ions and 1 M ion. When the fluorite A site is doped with a trivalent (+3) species, a multivalent cation like Ce is reduced from a +4 to a +3 state, and charge compensation occurs through point defects on the oxygen lattice sites resulting in a defect fluorite structure where Ce is VII-fold coordinated with oxygen. The CCO with a defect-fluorite structure can be written as $RE_{0.5}M_{0.5}O_{2-x}$.

Using the EISA approach, fluorite samples with nominal compositions: CeO_2, $Nd_2Ce_2O_7$ and $(La_{0.2}Pr_{0.2}Nd_{0.2}Tb_{0.2}Dy_{0.2})_2Ce_2O_7$ (hereafter referred to as $RE_2Ce_2O_7$) were synthesized at various calcination temperatures to find optimized reaction conditions and determine the effect of incorporating a single RE cation and multiple RE cations in a compositionally complex configuration on the OER activity of fluorite nano electrocatalysts. The phase purity and morphology of the samples are examined with X-ray diffraction, Brunauer-Emmett-Teller (BET) and Scanning Electron Microscopy (SEM) studies. X-ray Photoelectron Spectroscopy (XPS) is used to determine surface valence states. Raman spectroscopy and neutron total scattering analysis are applied to study the nature and correlation length scale of oxygen vacancies in the series. Linear sweep voltammetry (LSV) measurements and chronoamperometry stability measurements are performed in alkaline solution to examine electrocatalytic activity and stability and link structure-property effects with the extent of compositional substitution.

5.3 Materials Synthesis

5.3.1 Materials

Praseodymium (III) nitrate pentahydrate (99.9%), cerium (III) nitrate hexahydrate (99.5%), terbium (III) nitrate hydrate (99.9%), lanthanum (III) nitrate hexahydrate (98%), dysprosium (III) nitrate pentahydrate (99.9%), neodymium (III) nitrate hexahydrate (99.9%) and ethanol (99.5%) were purchased from Thermo Fisher Scientific. Pluronic P123 (a symmetric triblock copolymer comprising poly(ethylene oxide) (PEO) and poly(propylene oxide) (PPO) in an alternating linear fashion) was purchased from Sigma Aldrich. All metal nitrates were used to prepare sealed aqueous stock solutions immediately upon receipt from the manufacturer.

Carbon cloth (CC) for the battery, fuel cell and supercapacitor was purchased from MSE supplies. Nafion (5%) and isopropanol (iPr-OH), were purchased from Sigma–Aldrich and sodium hydroxide was purchased from Fisher Scientific and

these reagents were used as received. Deionized (D.I) water purified through a Millipore system was used in all experiments. The CC was washed with iPr-OH and D.I. water several times to ensure the surface was clean before use.

5.3.2 Synthesis of Mesoporous Fluorites via Evaporation Induced Self Assembly (EISA)

Mesoporous fluorite compositions were synthesized using a soft templating approach via evaporation induced self-assembly, as illustrated in Figure 5.1. Briefly, metal nitrate precursor solutions were dissolved in ethanol, under continuous stirring, using Pluronic P123 as a block copolymer template. The solutions were allowed to evaporate in a petri dish at room temperature for 48 hours and the resulting gels were calcined in air at 400°C, 600°C, 800°C or 1000°C for 4 hours in an oven. The following compositions were chosen to investigate the role of RE cations and compositional complexity on the electrochemical OER performance of fluorites: $(La_{0.2}Pr_{0.2}Nd_{0.2}Tb_{0.2}Dy_{0.2})_2Ce_2O_7$, $Nd_2Ce_2O_7$ and CeO_2. $(La_{0.2}Pr_{0.2}Nd_{0.2}Tb_{0.2}Dy_{0.2})_2Ce_2O_7$ is referred to as $RE_2Ce_2O_7$ in this study.

5.3.3 Fabrication of the Working Electrode for OER

All carbon cloth substrates were cleaned using iPr-OH, dried and covered with Teflon tape, leaving an exposed geometric area of 0.283 cm^2. Catalyst ink was prepared by dispersing 10.0 mg of the catalyst in 1.0 mL 0.8% Nafion in iPr-OH and ultrasonicated for 30 min. A 20 μL volume of the ink was dropcasted on the exposed area of the CC substrate, dried at room temperature, and finally heated at 130°C in an oven for 30 min in air to obtain the working electrode.

5.4 Materials Characterization and Methods

5.4.1 Structure and Morphology

Phase identification of the as synthesized fluorite powder samples was performed using a Panalytical Empyrean laboratory powder X-ray diffraction (XRD) instrument with Cu Kα radiation (λ = 1.5418 Å). Rietveld refinements were performed on the XRD data using the TOPAS v6 software.[103] Data were fit to a tetragonal unit cell model with S.G. $P4_2/nmc$ for CeO_2 and a cubic defect fluorite unit cell model with S.G. $Fm\bar{3}m$ for $Nd_2Ce_2O_7$ and $RE_2Ce_2O_7$. Lattice parameter(s), isotropic atomic displacement parameters and Scherrer particle size parameters were refined. $Nd_2Ce_2O_7$ calcined at 1000°C was fit to a cubic C-type (bixbyite) structure and refined similarly. The chemical homogeneity of the samples was investigated by performing EDS measurements on pressed pellets of the fluorite CCOs using a Zeiss EVO SEM equipped with energy dispersive X-Ray Spectroscopy. BET surface area measurements were performed by loading 100 mg - 150 mg of powder sample in a glass tube and out gassing overnight at 200°C in vacuum. The outgassed samples were then measured using a Micromeritics Gemini VII surface-area analyzer. XPS measurements were performed using a KRATOS AXIS 165 X-ray photoelectron spectrometer (Kratos Analytical Limited, Manchester, United Kingdom) using a monochromatic Al X-ray source. The C 1s signal at 284.5 eV was used as a reference to correct all the XPS binding energies. Neutron powder diffraction (NPD) and atomic pair distribution function (PDF) data were collected at 300 K on the Nanoscale Ordered Materials Diffractometer (NOMAD) at the Spallation Neutron Source (SNS) at Oak Ridge National Laboratory (ORNL).[95] 100 mg of each sample was loaded into a 3 mm diameter quartz capillary, placed in a temperature controlled Ar cryostream, and data were collected for 1 h. Signals from the empty quartz capillary and instrument were collected to facilitate background subtraction from the sample data. Data reduction was completed using

the Advanced Diffraction Environment (ADDIE) suite and a Q_{max} of 25 $Å^{-1}$ and a Lorch filter was applied for PDF generation.[219] The data was corrected for detector deadtime, absorption, and multiple scattering effects, and subsequently normalized by the incident flux and total scattering cross section of the sample. Rietveld refinements of the neutron diffraction data were performed using TOPAS v6 software [103] and PDF analysis was completed using the PDFgui software package. [139] Rietveld refinement of TOF neutron diffraction data for CeO_2 was performed using S.G. $P4_2/nmc$ while $Nd_2Ce_2O_7$ and $RE_2Ce_2O_7$ were refined using a two phase structural model comprising of a primary phase with S.G. $Fm\bar{3}m$ containing oxygen Frenkel defects and a secondary phase with S.G. $Pnn2$ containing oxygen vacancy ordering. For all samples, lattice parameter(s), isotropic atomic displacement and oxygen occupancy were refined. The same average structure models for $Nd_2Ce_2O_7$ and $RE_2Ce_2O_7$ were applied to PDF analysis and most parameters were fixed, while lattice parameter a was refined. PDF analysis for CeO_2 was performed using a two phase structural model comprising of a primary phase with S.G. $P4_2/nmc$ containing oxygen Frenkel defects and a secondary phase with S.G. $Pnn2$ containing oxygen vacancy ordering. Lattice parameters, isotropic atomic displacement and oxygen occupancy were refined. XPS measurements were performed using a KRATOS AXIS 165 x-ray photoelectron spectrometer. The C1s signal at 285.4 eV was used as a reference to correct all the XPS binding energies. All XPS spectra were collected from pristine catalyst surfaces without sputtering. The Raman spectra of the catalyst were recorded with LabRam ARAMIS (HORIBA Jobin-Yvon Raman spectrometer equipped with a CCD detector) in the Raman shift range between 50 cm^{-1} to 1800 cm^{-1}, 1200 lines mm^{-1} grating, HeNe laser 632.8 nm excitation with a nominal output power of 100mW, 0.95 cm^{-1}/pixel spectral dispersion, 10% of laser power, 10x objective, 0.25 numerical aperture, 100 μm slit, 200 μm hole, 30 seconds exposure time, and 10x accumulations for each sample acquisition. [220]

5.4.2 Electrochemical Measurements

Electrochemical measurements were performed using a conventional three-electrode system connected to an IviumStat potentiostat, with the fluorite catalyst as the working electrode, while graphite rod and Ag/AgCl electrode were used as counter electrode and reference electrodes respectively, to measure the electrocatalytic performances. Linear sweep voltammetry (LSV), and cyclic voltammetry (CV) were carried out to study the OER catalytic performance and cycling stability. In order to reduce uncompensated solution resistance, all activity data were iR corrected, which was measured through electrochemical impedance studies. All potentials measured were calibrated to a reversible hydrogen electrode (RHE) using SI Equation S4.1 from Chapter 4. All electrolytes were saturated by oxygen (for OER) bubbles before and during the experiments.

The steady-state performance and durability of all the electrocatalysts in OER for long-term chronoamperometric stability in an alkaline electrolyte of 1 M KOH solution was carried out in two forms: (a) at constant current density of 20 mA cm^{-2} for 16 h, (b) for $RE_2Ce_2O_7$, various current densities between 5 – 30 mA cm^{-2} as multistep study, in N_2-saturated 1.0 M KOH at room temperature.

The Tafel slope, which is an important parameter to explain the electrokinetic activity of these catalysts for OER and HER processes, was estimated from a Tafel plot with the equation shown in SI Equation S4.2 from Chapter 4.

The Electrochemical Impedance Spectroscopy (EIS) experiments were performed within $10^5 - 10^{-2}$ Hz frequency range, at an AC signal amplitude of 10 mV, to study the electrode kinetics and estimate the electrolyte resistance (Rs), and charge transfer resistance at the electrode (catalyst)-electrolyte interface (R_{ct}). The Nyquist plots were collected in N_2-saturated 1.0 M KOH at an applied potential of 0.55 V vs. Ag|AgCl (KCl saturated).

Turnover frequency (TOF), mass activity, electrochemically active surface area (ECSA) and roughness factor (RF), which are parameters used to evaluate the

electrocatalytic performance of catalysts for the OER, were determined for the fluorite samples as described in the Supplemental Information section of Chapter 4.

5.5 Results and Discussion

5.5.1 Structure and Morphology

CeO_2, $Nd_2Ce_2O_7$ and $RE_2Ce_2O_7$ were synthesized using EISA as detailed in Section 4.2.1 and illustrated in Figure 5.1, at 400°C, 600°C, 800°C and 1000°C to find the optimal calcination temperature for the OER. The structure of the samples was investigated using powder X-ray diffraction (XRD) as shown in Figure 5.2 and the morphology and sample homogeneity was determined using Scanning Electron Microcopy (SEM) and Energy Dispersive X-ray Spectroscopy (EDS) as seen in Figure 5.2 f and i.

XRD was performed to determine the phase purity and crystallinity of the samples with increasing calcination temperature, as seen in Figure 5.2 (a), (d) and (g). XRD patterns of all samples as prepared at 400°C, display peak broadening indicative of the highly nanocrystalline nature of samples produced using the low temperature EISA synthesis route. Interestingly, samples containing RE cations appear less crystalline than those with CeO_2 composition, at all calcination temperatures. As the calcination temperature increases, the Bragg peaks become progressively narrower, indicating enhanced crystallinity, which can be attributed to particle growth. It is notable that at 800°C and 1000°C, $RE_2Ce_2O_7$ displays the most significantly broadened diffraction peaks possibly due to greater intrinsic disorder and/or smaller crystalline grain size resulting from sluggish diffusion kinetics.

CeO_2 was found to form an average tetragonal structure while $RE_2Ce_2O_7$ samples form an average cubic fluorite structure at all calcination temperatures, with no evidence of secondary phases. $Nd_2Ce_2O_7$ was found to form an average cubic fluorite structure up to calcination temperatures of 800 °C.

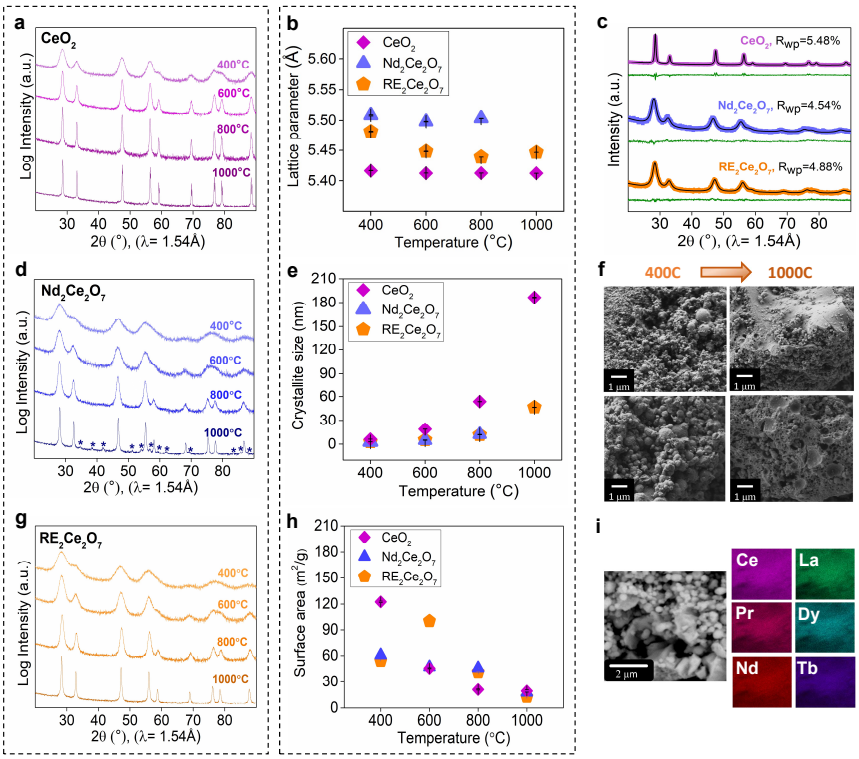


Figure 5.2: XRD patterns of CeO_2, $Nd_2Ce_2O_7$ and $RE_2Ce_2O_7$ shown in (a),(d) and (g) respectively, prepared by calcination at 400°C, 600°C, 800°C and 1000°C (from top to bottom of each panel). The XRD pattern of $Nd_2Ce_2O_7$ calcined at 1000°C shows the formation of superstructure peaks as indicated by the blue stars. Refined values from Rietveld refinements of data for CeO_2, $Nd_2Ce_2O_7$ and $RE_2Ce_2O_7$ are shown for (b) lattice parameter, (e) crystallite size and (h) BET surface area. Rietveld refinement results of XRD data of samples prepared by calcination at 600°C are shown in (c), where the data was fit to a tetragonal phase with S.G. $P4_2/nmc$ for CeO_2 and a cubic phase with S.G. $Fm\bar{3}m$ for $Nd_2Ce_2O_7$ and $RE_2Ce_2O_7$. Measured data are shown as colored circles, structural model fits as a black line through the data, and the difference curves in green fall below the data and fits. (f) Scanning Electron Microscopy (SEM) images of $RE_2Ce_2O_7$ prepared by calcination at 400°C for 4 hours (shown in the column on the left) and 1000°C for 4 hours (shown in the column on the right). (i) SEM image (left) and corresponding EDS spectra maps (right, in color) for $RE_2Ce_2O_7$ prepared by calcination at 400°C for 4 hours. A region displaying heterogeneous morphology (larger flakes and smaller spheres) was intentionally selected.

At 1000 °C, the formation of superstructure peaks is observed, indicated by the blue stars in Figure 5.2 (d). Rietveld refinement of the CeO_2 sample was performed successfully using a tetragonal unit cell model described with space group (S.G.) $P4_2/nmc$. In the tetragonal structure, the Ce ions occupy the 4f Wyckoff position at the center of the oxygen octahedra, while the oxygen ions occupy the 8c Wyckoff position at the vertices of the octahedra and are coordinated by four Ce ions in a square planar arrangement. The average structure of $Nd_2Ce_2O_7$ up to 800°C and $RE_2Ce_2O_7$ at all calcination temperatures, was modeled successfully with a single phase defect fluorite structure, indexed to space group (S.G.) $Fm\bar{3}m$, with RE and Ce cations randomly occupying 4*a* sites and oxygen anions occupying 7/8ths of 8*c* sites. [68, 101] Representative Rietveld refinement results for the samples calcined at 600°C are shown in Figure 5.2 (c). Interestingly, the inclusion of RE cations in the CeO_2 lattice results in the formation of a higher symmetry cubic structure rather than a tetragonal structure.

The $Nd_2Ce_2O_7$ sample calcined at 1000°C forms a cubic C-type (bixbyite) structure with space group $Ia\bar{3}$ as shown by the Rietveld refinement in SI Figure S5.1. The presence of this cubic C-type structure in rare-earth containing cerates has been widely reported in literature. [160, 221, 222, 161, 223, 224] The C-type structure is related to the fluorite structure but exhibits oxygen vacancy ordering resulting from the selective removal of 25% of the oxygen anions. [221, 224] Whereas the cations in the fluorite structure are 8-fold coordinated with oxygen, the cations in the C-type structure are 6-fold coordinated and occupy the 8*b* and 24*d* Wyckoff sites with the O anions occupying the 48*e* sites. Interestingly, while the $Nd_2Ce_2O_7$ sample calcined at 1000°C displays a C-type structure, the $RE_2Ce_2O_7$ sample retains a defect fluorite structure at all calcination temperatures. It appears that the incorporation of five RE cations into the defect fluorite phase has inhibited the formation of the C-type structure, potentially making it a more stable catalyst than $Nd_2Ce_2O_7$.

Extracted parameters from Rietveld refinement provide further insights into structural trends across the series. As seen in Figure 5.2 (b), inclusion of RE^{3+} cations results in a lattice expansion. In an ideal fluorite structure, Ce^{4+} cations are VIII-fold coordinated with oxygen; however, introducing (mainly) RE^{3+} cations into the fluorite lattice results in oxygen vacancies and a change in average cation coordination from VIII-fold to VII-fold. The increase in lattice parameter upon inclusion of RE^{3+} cations is due to the larger ionic radius of La^{3+} (1.1 Å), Nd^{3+} (1.046 Å), Pr^{3+} (1.058 Å), Tb^{3+} (0.98 Å) and Dy^{3+} (0.97 Å) relative to Ce^{4+} (0.92 Å) in VII-fold coordination. The ionic radii for VII-fold coordination were calculated as an average of ionic radii for VI and VIII fold coordination. [162, 163, 164] Tb, Dy and Pr are known to form mixed 3+ and 4+ valence states. [224, 160, 225, 224]

No significant changes were observed in lattice parameter with increasing calcination temperature, suggesting that oxygen stoichiometry remains consistent with increased calcination temperature (lattice expansion is a noted side effect of oxygen sub-stoichiometry in ceria and related compounds). [226, 106, 227] The thermal stability of the fluorite samples with increasing calcination temperature was explored by extracting trends in crystallite size, shown in Figure 5.2 (e). Interestingly, samples containing RE cations display less dramatic crystallite size growth than CeO_2 samples with an increase in calcination temperature. Samples with 1 RE constituent cation exhibit similar crystallite size growth behavior compared to those with 5 RE constituent cations.

In addition to the structure of a catalyst, surface area and morphology are important parameters that can significantly influence catalytic activity by affecting accessibility to active sites, the number of exposed active sites and mass transfer limitations. Thus, BET was used to measure the surface areas of the sample series as displayed in Figure 5.2 (h). BET surface areas of the samples were found to be highly dependent on composition and calcination temperature. Typically, in nano oxide catalysts, increasing calcination temperature leads to particle size

growth/coarsening and a corresponding decrease in BET surface area. Interestingly, the CCO composition in the series shows an anomalous increase in surface area when the calcination temperature of the sample is increased from 400°C to 600°C, followed by a decrease in surface area at calcination temperatures beyond 600°C. Other compositions show a decrease in surface area with increasing calcination temperature. The calcination series was repeated multiple times for each composition, and the trends were reproducible.

To further elucidate the surface area trends observed, the morphology of the $RE_2Ce_2O_7$ sample was studied as a function of increasing calcination temperature. As seen in Figure 5.2 (f) the sample was found to be highly heterogeneous, with a large particle size distribution and the presence of at least two distinct morphologies: (i) micrometer scale porous flakes and (ii) spherical nanoparticle agglomerates, similar to CCO morphologies reported by Cong et al. [165] With increasing calcination temperature, Ostwald ripening occurs resulting in larger but fewer spherical nanoparticles and an overall decrease in BET surface area. At higher calcination temperatures, the morphology is dominated by micrometer sized flakes with smaller, and more closed (less accessible) pores. The same overall trends in morphology as a function of increasing calcination temperature were observed in $Nd_2Ce_2O_7$ and CeO_2. However, the distinct BET surface area trends of $RE_2Ce_2O_7$, $Nd_2Ce_2O_7$ and CeO_2 suggests that the greater compositional complexity and more sluggish diffusion in the CCO sample may give rise to complex morphology/growth patterns that can potentially be further optimized with thermal processing.

EDS measurements were performed on the $RE_2Ce_2O_7$ sample to investigate the formation of a solid solution. Elemental mapping, shown in Figure 5.2 (i) confirmed the homogeneous distribution of all elements present (La, Pr, Dy, Tb, Nd, Ce and O) at the micron scale. Spectra were collected for various particle morphologies across sample locations to confirm that the different morphologies possess the same chemical composition and distribution. Atomic ratios of RE cations to Ce as measured using EDS and X-ray Fluorescence (XRF) are displayed in SI Table S5.1.

While several atomic percent error can be encountered with these methods, the analysis overall indicates compositions were found to closely resemble the target stoichiometry with minor deviation.

5.5.2 Defect Chemistry

Oxygen vacancies have been shown to increase adsorption of oxygen containing intermediates in the OER and enhance catalytic activity. [208, 209, 210] The effects of introducing rare earth cations on the defect chemistry of the fluorite catalyst series were evaluated as shown in Figure 5.3 using Raman spectroscopy (a, d and g), neutron total scattering (b, e and h), and X-ray photoelectron spectroscopy (XPS) (c, f and i).

Raman spectroscopy was used to characterize the defect modes present in the sample series. As seen in Figure 5.3 (a), the Raman spectra of CeO_2 prepared by calcination at various temperatures shows a single Raman peak at 463 cm^{-1}. This peak can be ascribed to the first-order mode of F2g and corresponds to the $Ce-O$ symmetric stretching of the CeO_8 vibrational unit in CeO_2. [79, 228] An increase in the calcination temperature is accompanied by a decrease in the bandwidth of the first order mode of F2g with peak at 463 cm^{-1}. Such an observation has been attributed to an increase in particle size in previous literature reports. [79, 228]

As shown in Figures 5.3 (d) and (g), $Nd_2Ce_2O_7$ and $RE_2Ce_2O_7$ exhibit D-band peaks at 580 cm^{-1} Raman shift. The D-band for $Nd_2Ce_2O_7$ samples calcined at 400°C and 600°C is split into D1 centered at 558 cm^{-1} and D2 centered around 607 cm^{-1}. The D band splitting is influenced by the concentration of Nd^{3+} as well as calcination temperature. An increase in the calcination temperature leads to a blue-shift of the D-band in $RE_2Ce_2O_7$ and $Nd_2Ce_2O_7$. This shift is more obvious in $Nd_2Ce_2O_7$ indicating a higher degree of local distortion in the lattice, perhaps due to its slightly expanded lattice. [229]

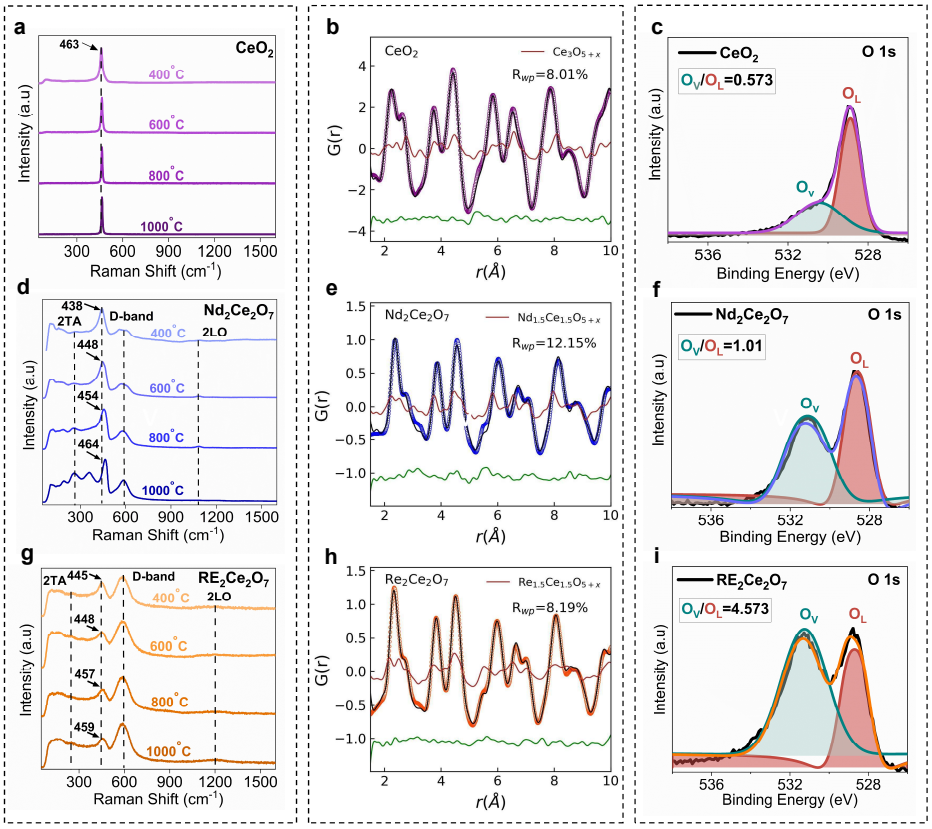


Figure 5.3: Raman, neutron PDF and XPS results for fluorite catalysts prepared by calcination at 600°C where the top row represents CeO_2, the middle row shows $Nd_2Ce_2O_7$ and the bottom row represents $RE_2Ce_2O_7$. Raman spectra (λ_{ex} = 632.8 nm) are shown in the panel on the left as (a), (d) and (g). Preliminary 2-10 Å neutron PDF refinements using a two phase model comprising of Frenkel-type defects with S.G. $Fm\bar{3}m$ and $Pnn2$- type Ce_3O_{5+x} for CeO_2, $Nd_{1.5}Ce_{1.5}O_{5+x}$ for $Nd_2Ce_2O_7$ and $RE_{1.5}Ce_{1.5}O_{5+x}$ for $RE_2Ce_2O_7$ are shown in the panel in the middle as (b), (e) and (h). High resolution XPS O 1s core level binding energy spectra are shown in the panel on the right in (c), (f) and (i) where the area ratios of vacancy-related (O_V ,green) and lattice-related (O_L , red) oxygen are computed.

The Raman spectra of both samples show a defect-induced Raman D-band and a second-order transverse acoustic (2TA) mode at 580 and 253 cm^{-1} which arise from the presence of oxygen vacancies and single or multiple RE dopant cations. [1] The highly pronounced D-band observed in $RE_2Ce_2O_7$ compared to $Nd_2Ce_2O_7$ comes from the defects-induced by multiple RE metal doping. Similar Raman spectra have been reported in metal doped ceria oxides. [79, 229, 230] Furthermore, a very small overtone peak of longitudinal optic (LO) mode at 2 LO (1080 cm^{-1}) was observed, characteristic of relaxation of multi-phonon by Raman resonance effect. However, the LO mode is less sensitive to defects relative to the D-band.

Based on Raman Spectroscopy analysis $RE_2Ce_2O_7$ is found to display the highest amount of defect concentration relative to the other fluorite compositions in the series, as indicated by the intensities of the D-band. Additionally, $RE_2Ce_2O_7$ calcined at 600°C displays the highest surface area, and trends in lattice parameter and crystallite size with higher calcination temperature indicate that the composition displays improved thermal stablility relative to CeO_2. As $RE_2Ce_2O_7$ calcined at 600°C presents promise as an OER catalyst, all compositions calcined at 600°C were investigated further to determine the role of RE cations on OER catalytic performance.

To probe the nature of oxygen vacancies in both the average and local structure of the fluorite series, neutron total scattering analysis (Bragg diffraction, pair distribution function) was employed. Neutron diffraction and PDF have previously shown great sensitivity to the nature and length scale of oxygen vacancy correlations in catalysts [231, 60, 209], being more sensitive probes of oxygen atoms relative to X-ray techniques. Rietveld refinements were performed on the neutron diffraction data for the fluorite samples calcined at 600°C as shown in SI Figure S5.2. Rietveld refinements revealed that CeO_2 exhibits a tetragonal average structure with S.G. $P4_2/nmc$. $Nd_2Ce_2O_7$ was successfully fit to a two phase structural model comprising of a primary cubic phase with S.G. $Fm\bar{3}m$ containing oxygen Frenkel defects and a secondary oxygen vacancy ordered $Nd_{1.5}Ce_{1.5}O_{5+x}$ (1/6th

oxygen vacancy) phase with orthorhombic S.G. *Pnn*2 which has been previously observed in CeO_2 nanorods.[231] $RE_2Ce_2O_7$ was fit using the same two phase model as $Nd_2Ce_2O_7$ but with the stoichiometry- $RE_{1.5}Ce_{1.5}O_{5+x}$ (where RE = La, Nd, Tb, Dy and Pr) in the secondary phase. Oxygen occupancy values vary across the models in these preliminary fits and warrant further investigation, Attempts to fit CeO_2 using this two phase structural model led to a worse quality of fit as indicated by a higher R_{wp} value, despite the inclusion of additional refinable parameters. Nonetheless, a higher concentration of oxygen defects in $RE_2Ce_2O_7$ compared to $Nd_2Ce_2O_7$ is corroborated by Raman spectroscopy analysis, which reveals a stronger intensity of the defect-induced Raman D-band in $RE_2Ce_2O_7$. It is worth nothing that the actual oxygen defect patterns in $Nd_2Ce_2O_7$ and $RE_2Ce_2O_7$ are likely to be a complex combination of multiple oxygen defect structures known to form in CeO_2 based oxides. [231, 111]

Additionally, the presence of oxygen vacancies in the local structure of the samples was investigated by applying the average structure models from neutron diffraction to refinements of the neutron pair distribution functions (PDF) from 1.5-10 Å. Various single and two phase structural models were explored during refinements, including the Frenkel type defect structure and C-type bixbyite structure. PDF analysis of CeO_2, $Nd_2Ce_2O_7$ and $RE_2Ce_2O_7$ are shown in Figure 5.3 (b), (e) and (h) respectively. CeO_2 was successfully refined based on a two-phase structural model, consisting of a primary phase with S.G. $P4_2/nmc$ containing oxygen Frenkel defects and a secondary oxygen vacancy ordered Ce_3O_{5+x} (1/6th oxygen vacancy) phase with orthorhombic S.G. *Pnn*2. Although the inclusion of the Ce_3O_{5+x} phase does not enhance the overall fit quality of the average structure of CeO_2 in neutron diffraction refinements, it notably improves the fit quality of the local structure as evidenced by the decrease in R_{wp} from 14.4% to 8%. This finding suggests the existence of a limited coherence length for the partially reduced Ce_3O_{5+x} phase within CeO_2. The correlation length scale of oxygen vacancies

has been shown to strongly influence the redox properties and resulting catalytic performance of ceria-based mixed oxides [60] and OER catalysts in general[209].

$Nd_2Ce_2O_7$ and $RE_2Ce_2O_7$ were refined using the same two-phase structural model applied to neutron diffraction refinements, with a primary S.G. $Fm\bar{3}m$ phase containing oxygen Frenkel defects and secondary Nd/$RE_{1.5}Ce_{1.5}O_{5+x}$ phase with S.G. $Pnn2$. Consistent with neutron diffraction refinements, preliminary PDF analysis indicates the presence of a larger concentration of oxygen Frenkel defects in the local structure of $RE_2Ce_2O_7$ in comparison with $Nd_2Ce_2O_7$. Interestingly, a more prominent peak shoulder around 3 Å was observed in $Nd_2Ce_2O_7$ in contrast to $RE_2Ce_2O_7$, which could potentially be attributed to the O-O pair from the partially reduced Nd/$RE_{1.5}Ce_{1.5}O_{5+x}$ phase.[231] This finding suggests that the $RE_{1.5}Ce_{1.5}O_{5+x}$ phase in $RE_2Ce_2O_7$ is more reduced and contains more oxygen vacancies compared to the $Nd_{1.5}Ce_{1.5}O_{5+x}$ phase in $Nd_2Ce_2O_7$.

XPS was used to further examine the variation in oxygen defect chemistry of these samples and determine the valence states of the elemental constituents present on the surface of the fluorite catalysts. The wide scan survey spectra of all the samples in the series confirmed the coexistence of their respective constituent elements on their surfaces (SI Figure S5.3). The high- resolution La 3d spectrum of $RE_2Ce_2O_7$ shown in SI Figure S5.4 (a), exhibits regular doublet splitting which is further deconvoluted into four peaks (two peaks per doublet). The peaks at 834.5 eV and 851.4 eV, correspond to spin orbital $3d_{5/2}$ and $3d_{3/2}$ respectively, while the peaks at 838.3 eV and 855.6 eV, are satellite peaks ascribed to $3d_{5/2}$ and $3d_{3/2}$ respectively. [169] These peaks correspond to La–O_2 as supported by previous reports.[232]

The high- resolution Ce 3d spectra of $RE_2Ce_2O_7$, $Nd_2Ce_2O_7$ and CeO_2 are highly comparable (SI Figures S5.4 (b), S5.5 (a) and S5.6 (a) respectively) and all exhibit multiplet splitting, comprising six identical peaks at 882.1 eV, 888.4 eV and 897.9 eV for $3d_{5/2}$ and 990.5 eV, 906.8 eV and 916.3 eV for $3_d3/2$. These peaks confirm the presence of Ce(III) and Ce(IV) oxidation states in all the fluorite samples. [233, 234,

2] The high-resolution Pr 3d spectrum of $RE_2Ce_2O_7$ (SI Figure S5.4 (c)) shows two doublets corresponding to $3d_{5/2}$ and $3d_{3/2}$ at 932.8 eV and 953.4 eV with satellites at 928.4 eV and 984.2 eV respectively, indicating the presence Pr(III), in agreement with the preferential trivalent state of most RE-ions. [175] The observed satellites at a slightly lower binding energy are ascribed to the well-probed 4f3 final state. [171, 172] The presence of Nd was confirmed in both $RE_2Ce_2O_7$ and $Nd_2Ce_2O_7$ from the high resolution Nd 3d spectra (SI Figures S5.4 (d), S5.6 (b)). The spectra show two doublets at 977.8 eV and 982.3 eV corresponding to a satellite and Nd(VI) of $3d_{5/2}$, and satellites at 1000.1 and 1004.7 eV corresponding to Nd(III) of $3d_{3/2}$ [173, 174]. The 4d spectra of $RE_2Ce_2O_7$ and $Nd_2Ce_2O_7$ shown in SI Figures S5.4 (e) and S5.6 (c) display peaks at 121.1 eV and 124.3 eV corresponding to a satellite and 4d. [175] The presence of Tb in the high-resolution Tb 3d spectrum of $RE_2Ce_2O_7$ (SI Figure S5.4 (f)) was confirmed by the presence of two characteristic doublet peaks for 3d5/2 and 3d3/2 and their corresponding satellites at 1241.0 eV, 1276.0 eV, 1251.4 eV and 1287.0 eV respectively. These characteristic peaks indicate the presence of Tb(IV) in agreement with literature reports. [176, 235] Dy 3d spectrum of the $RE_2Ce_2O_7$ (SI Figure S5.4 (g)) shows doublet peaks due to the spin−orbit splitting at 1296.4 eV, and 1334.4 eV corresponding to Dy(III) of $3d_{3/2}$ and $3d_{5/2}$ respectively. [178, 236] The satellite peak at 1303.9 eV is assigned to Dy(IV) $3d_{5/2}$ components, indicating the presence of mixed Dy ion states on the surface. [236]

As seen in Figure 5.3 (c), (f) and (i), the high-resolution O 1s XPS spectra for all fluorite samples were deconvoluted into two main peak components: oxygen vacancies (O_V), and lattice oxygen (O_L). The peak at 530.9 eV corresponds to a loosely absorbed oxygen species (correlated to oxygen vacancies). The O_L binding peak at 528.8 eV for each sample was associated with typical metal-oxygen bonding of lattice oxygen, [181] while O_V peak at 531.5 eV was attributed to the presence of surface chemisorbed oxygen associated with defects (oxygen vacancies). [181, 182] The area ratio of O_V/O_L has been employed as a metric for estimating the proportion of surface oxygen vacancies, with higher ratios suggesting larger amounts of surface

oxygen vacancies. [237] The larger concentration of surface oxygen vacancies in $RE_2Ce_2O_7$ facilitates the pre-oxidation of RE sites, increases hydroxyl adsorption and promotes the reconstruction of the defective surface with applied potential, [169, 183] consequently improving OER performance.

5.5.3 Catalytic Performance for the Oxygen-Evolution Reaction

The electrocatalytic behavior of the fluorite samples for the OER was studied using a three-electrode system, in a 1 M KOH alkaline solution. Fluorite samples synthesized at different calcination temperatures were tested to determine their catalytic activity towards OER. Among all compositions, samples calcined at 600°C showed optimal catalytic activity and hence these samples were pursued for further study. Polarization plots obtained from linear sweep voltammetry (LSV) of CeO_2, $Nd_2Ce_2O_7$ and $RE_2Ce_2O_7$ synthesized at 600°C, measured using a scan rate of 10 mV s^{-1}, are shown in Figure 5.4 (a).

$RE_2Ce_2O_7$ demonstrated an exceptionally low overpotential of 210 mV attained at a current density of 10 mV s^{-2} and exhibited higher catalytic activity than the $Nd_2Ce_2O_7$ and CeO_2 samples, which showed overpotentials of 243 mV, and 347 mV respectively (Figure 5.4 (b)). The intrinsic OER activity of these catalysts can be ranked as follows ranging from highest to lowest activity: $RE_2Ce_2O_7$ > $Nd_2Ce_2O_7$ > CeO_2. Consequently, $RE_2Ce_2O_7$ is determined to be the best electrocatalyst in this series as it displays the highest intrinsic catalytic activity. As mentioned in Chapter 4, it is important to note that the overpotential observed for the CeO_2 (347 mV) sample synthesized using EISA in this study, outperforms pristine CeO_2 OER electrocatalysts previously reported in literature [1, 3, 4] (relative comparison shown in SI Figure S5.7). This suggests that EISA is a promising synthesis route for producing highly active OER catalysts relative to other synthesis approaches.

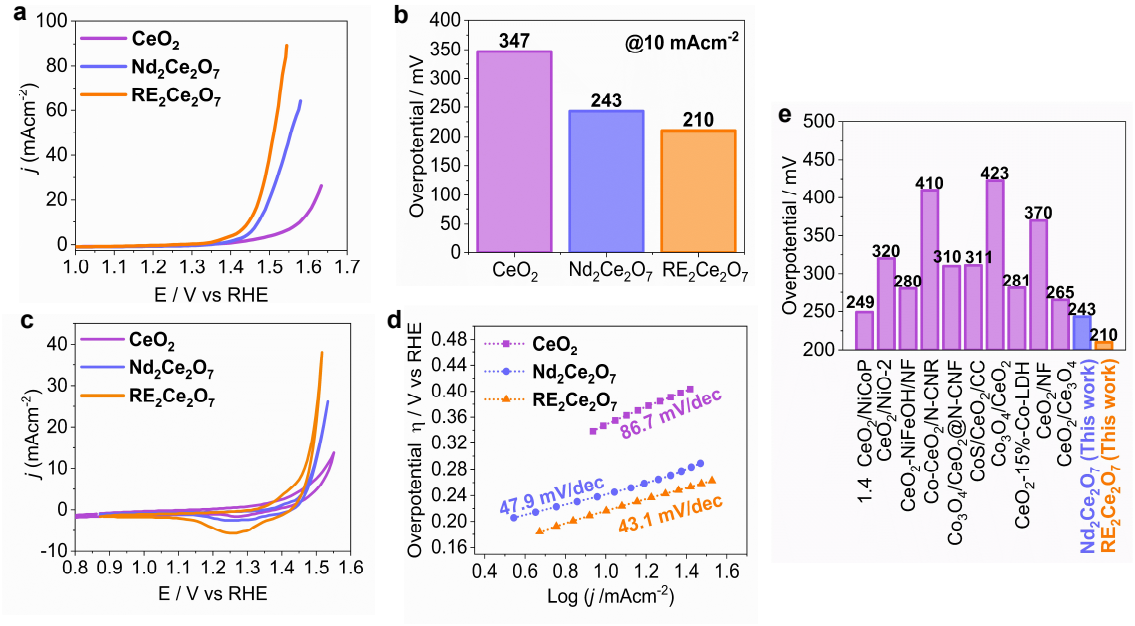


Figure 5.4: Electrocatalytic performance of CeO_2 (purple), $Nd_2Ce_2O_7$ (blue) and $RE_2Ce_2O_7$ (purple) calcined at 600°C: (a) LSVs measured in N_2 saturated 1 M KOH at a scan rate of 10 mV s^{-1}, (b) overpotential at a current density of 10 mA cm^{-2}, (c) cyclic voltammograms measured in N_2 saturated 1 M KOH at a scan rate of 10 mV s^{-1}, (d) Tafel plots and (e) overpotential benchmark at 10 mA cm^{-2} for recent reports on CeO_2 –based catalysts compared to $RE_2Ce_2O_7$. [1, 2, 3, 4, 5, 6, 7, 8, 9]

Cyclic voltammetry (CV) of all samples exhibit pre-oxidation peaks indicating oxidation of the active metal sites (Figure S7). $RE_2Ce_2O_7$, $Nd_2Ce_2O_7$ and CeO_2 show pre-oxidation peaks at 1.433, 1.349 and 1.381 V vs RHE at 10 mV/s scan rate respectively arising from Ce(III)/Ce(IV) contributions. The pre-oxidation peaks are more pronounced with variations in scan rate. The shift in the oxidation peak potential of $RE_2Ce_2O_7$ and $Nd_2Ce_2O_7$, relative to CeO_2, indicates the electronic perturbation effect resulting from the addition of a single/ multiple RE cation(s). The Tafel plots generated from LSV curves, were employed to evaluate the OER kinetics of the electrocatalysts. As displayed in Figure 5.4 (d), $RE_2Ce_2O_7$ achieved the smallest Tafel slope of 43.1 mV dec^{-1}, demonstrating that it has the fastest electrocatalytic kinetics for OER. Tafel slopes for $Nd_2Ce_2O_7$ and CeO_2 were observed to be 49.9 mV dec^{-1} and 86.7 mV dec^{-1} respectively. Thus, the electrokinetic activity of the catalysts based on the Tafel slope, follows the order $RE_2Ce_2O_7$ (43.1 mV dec^{-1}) > $Nd_2Ce_2O_7$ (49.9 mV dec^{-1}) > CeO_2 (86.7 mV dec^{-1}). The OER performance of $RE_2Ce_2O_7$ and $Nd_2Ce_2O_7$ reported herein outperform previously reported CeO_2-based electrocatalysts, some of which are summarized as shown in Figure 5.4(e), demonstrating that RE incorporation can enhance the performance of fluorite OER electrocatalysts. [1, 2, 3, 4, 5, 6, 7, 8, 9] The computed mass activities and turn over frequency (TOF) (at η = 310 mV) are additional parameters employed to probe catalytic OER performance (Figure 5.5 (a), 5.5 (b)).

The $RE_2Ce_2O_7$ catalyst demonstrates the best OER activity as it exhibits the highest mass activity and TOF of 47.1 A g^{-1} and 0.0841 s^{-1} respectively. The second-best performance was displayed by $Nd_2Ce_2O_7$ with a mass activity of 23.3 A g^{-1} and TOF of 0.0841 s^{-1}, while CeO_2 showed the weakest performance in this sample series towards OER. The superior intrinsic catalytic activity of $RE_2Ce_2O_7$ relative to the other fluorite catalysts may be explained by the increased number of catalytically active sites, the increase in electronic structure perturbation and oxygen vacancy formation resulting from incorporation of multiple RE cations. [192] To further elucidate the observed enhancement in OER performance resulting

from RE incorporation in fluorite catalysts, the electrochemically active surface areas (ECSAs) of the catalysts was determined from specific electrochemical double-layer capacitance (Cdl) by carrying out CV within a region of non-Faradaic current at varying scan rates (2.5–50 mV s^{-1}) shown in (SI Figures S5.9-5.11).

The ECSA and roughness factor were computed (SI Equations S4.7, S4.8 from Chapter 4) as shown in Figure 5.5 (c). $RE_2Ce_2O_7$ exhibited the largest ECSA, likely due to its highly nanocrystalline nature as evidenced by XRD and SEM analysis. CeO_2 presented the lowest ECSA due to its more crystalline morphology. The largest ECSA and highest activity of the $RE_2Ce_2O_7$ sample relative to the other fluorite samples emphasizes the role of morphology on OER activity. This large ECSA translates to a larger number of exposed electrochemically active sites, facilitating electrolyte infiltration and surface interaction with the electrocatalyst, [231] consequently, leading to exceptional activity toward OER with no hinderance of mass transfer in the electrolyte. [194]

Electrochemical impedance spectroscopy (EIS) analysis reveals the influence of electrical resistivity on OER activity. The EIS spectra of the samples show semicircular curves, indicating electron transfer coupled with the double-layer charging process. The generated Nyquist plots evaluated at 0.55 V vs RHE are shown in Figure 5.5 (d). The equivalent circuit, shown in the inset, was comprised of the electrolyte resistance (R_s), charge transfer resistance (R_{ct}), and constant phase element (CPE) (Table S9). All samples displayed a decrease in conductivity due to reduced interfacial contact from the use of polymer binders to adhere the catalysts to the substrate. However, $RE_2Ce_2O_7$ was found to have the least charge-transfer resistance (R_{ct}) of 3.02 Ω at a potential of 1.55 V (vs RHE), while $Nd_2Ce_2O_7$ and CeO_2 showed a resistance of 7.95 Ω and 18.10 Ω respectively. Thus $RE_2Ce_2O_7$ demonstrates the fastest charge transfer electrokinetics between the electrocatalyst surface and electrolyte solution in the OER.

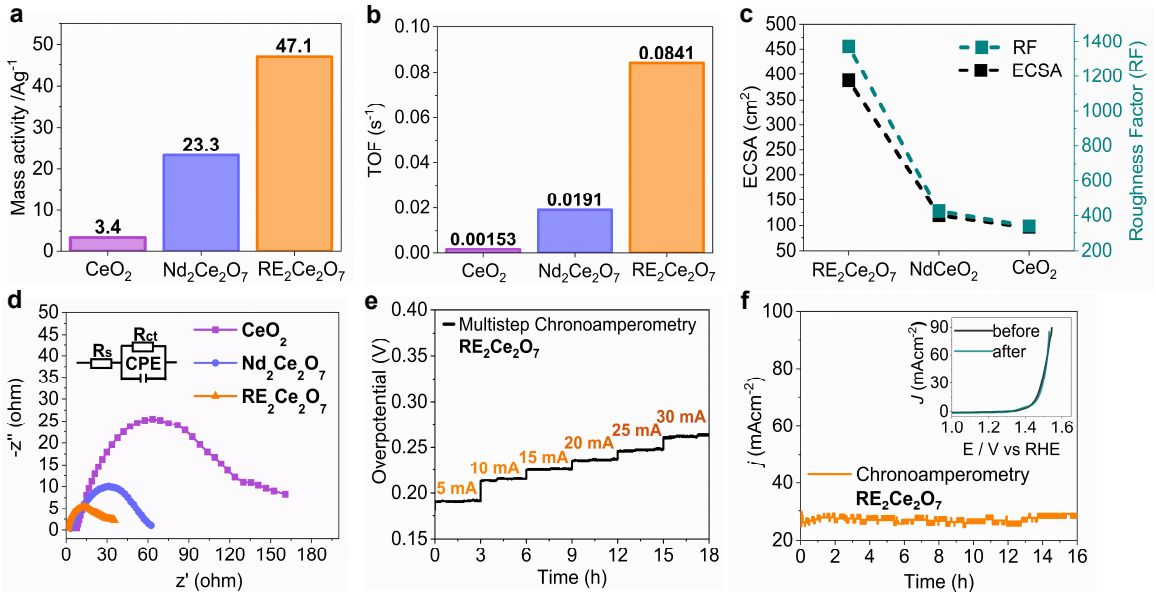


Figure 5.5: Electrocatalytic performance of CeO_2 (purple), $Nd_2Ce_2O_7$ (blue) and $RE_2Ce_2O_7$ (orange) calcined at 600°C: (a) mass activity, (b) turnover frequency (TOF), (c) electrochemically active surface area (ECSA) shown in black and roughness factor (RF) shown in green and (d) Nyquist plots in the AC frequency range between 100 kHz and 0.1 Hz at 0.55 V; (e) multistep chronoamperometry study of $RE_2Ce_2O_7$ at various current densities and (f) chronoamperometric stability of $RE_2Ce_2O_7$ at 0.46 V, where the inset displays OER polarization plots of $RE_2Ce_2O_7$ before and after chronoamperometry.

The multistep stability performance of the best catalyst, $RE_2Ce_2O_7$, was measured at different currents (5-30 mA) (Figure 5.5(e)), and can be compared to that of $Nd_2Ce_2O_7$ and $Dy_2Ce_2O_7$ presented in Chapter 4. Additionally, the long-term durability of all the catalysts was measured at a constant potential, maintained for 16 h (Figure 5.5(f), SI Figure S5.12). The results indicate the robustness of $RE_2Ce_2O_7$ both for long term stability and at varying currents at multiple stages, with no rapid degradation of the catalyst. In addition, $Nd_2Ce_2O_7$ and CeO_2 show decent stability with no clear degradation, suggesting their robustness for the OER. Achieving a higher valence state is an essential step to initiating the formation of active $M-OOH^*$ species for OER. [238] Surface oxygen vacancies are known to accommodate hydroxyls, consequently enhancing pre-oxidation of low oxidation species, and enabling deprotonation/reconstruction of intermediate species. [158] As exposed RE sites exhibit improved electrophilicity, hydroxyl adsorption onto Ce active sites can be facilitated by oxygen vacancies (V_O) to generate adsorbed $M-OH^*$ intermediate species and thereafter instigate the deprotonation step at a minimal potential to generate active oxygen species ($RE-OOH^*$) on the catalyst surface, which justifies the observed enhancement in OER activity.

To examine the behavior of catalysts pre-oxidation during OER, CV was employed. During OER, the pre-oxidation peak of the catalyst as demonstrated by the CV plots becomes more pronounced at higher scan rates (SI Figure S5.8). $Nd_2Ce_2O_7$ and CeO_2 exhibit one oxidation and one reduction peak at all scan rates. With varying scan rate from 2.5-100 mV/s, both $Nd_2Ce_2O_7$ and CeO_2, show a shift in oxidation peak to a higher potential and a shift in reduction peak to a lower potential. This suggests that the redox processes in $Nd_2Ce_2O_7$ are similar to those in CeO_2. However, $RE_2Ce_2O_7$ exhibits two distinct reduction peaks and one oxidation peak shoulder, suggesting a unique redox process for the CCO catalyst. The difference in redox behavior of $RE_2Ce_2O_7$ can be attributed to the pre-oxidation of Ce and other RE metal ions present in this composition. Ce ions may be the main active site while other ions play a supporting role in

modulating its electronic/structural configuration, thereby significantly boosting its electrocatalytic performance towards OER. The electrochemical OER parameters of CeO_2, $Nd_2Ce_2O_7$ and $RE_2Ce_2O_7$ electrocatalysts are compared in Table 5.1. $RE_2Ce_2O_7$ shows the lowest overpotential and Tafel slope, indicating the best activity. Furthermore, the obtained TOF, mass activity and ECSA for $RE_2Ce_2O_7$ were highest among the fluorite sample series, further corroborating its exceptional performance. Higher ECSA value generally indicates larger electrochemically active surface area which improves electrolyte/active sites interaction, leading to better catalytic performance for OER. Large ECSA value results in high surface roughness (RF), which is another parameter examined, that affects catalytic activity.

It is our understanding that the exceptional catalytic performance of our novel $RE_2Ce_2O_7$ catalyst can primarily be attributed to improvements in charge and mass transfer. The abundant oxygen vacancy defects in $RE_2Ce_2O_7$ enhances the OER electrokinetics, while the incorporation of RE elements into the CeO_2 lattice provides suitable electronic structure. Furthermore, the mesoporous and nanostructured nature of the $RE_2Ce_2O_7$ sample substantially minimizes the bubbles/electrode contact region, which facilitates the bubble release and reactant transfer. In addition, the lattice expansion and local atomic disorder resulting from RE incorporation increases the number of active sites as well as electron transport conductivity from the surface of the catalyst.

The chronoamperometric stability of CeO_2, $Nd_2Ce_2O_7$ and $RE_2Ce_2O_7$ for 16h (SI Figure S5.12, Figure 5.5 (f)) indicate robust catalytic stability with no significant deterioration under uninterrupted OER conditions at constant potentials of 1.46, 1.52 and 1.65 V respectively. The OER polarization plot of $RE_2Ce_2O_7$ before and after the stability study shows no observable changes as displayed by the inset in Figure 5.5 (f), demonstrating the excellent mass transfer property and mechanical ruggedness of the $RE_2Ce_2O_7$ electrode in an alkaline environment. Following stability measurements, analysis of the catalyst surface using Raman revealed no new phase formation on the catalyst surface as seen in SI Figure S5.13.

Table 5.1: Catalytic performance of fluorite catalysts.

	CeO_2	$Nd_2Ce_2O_7$	$RE_2Ce_2O_7$
Onset potential (V)	1.52	1.41	1.38
Overpotential @ 10 mA cm^{-2} (mV)	347	243	210
$Ce^{3+} \rightarrow Ce^{4+}$ oxidation peak potential (V)	1.38	1.35	1.43
TOF (s^{-1})	0.0015	0.0191	0.0841
Mass Activity (Ag^{-1})	3.43	23.26	47.09
Tafel slope (mV $deccm^{-1}$)	86.7	47.9	43.1
ECSA (cm^2)	96	120	388
RF	340	425	1372

Furthermore, XPS analysis of all samples after carrying out stability measurements are shown in SI Figures S5.14–S5.16. XPS results show no significant changes in surface electronic states of the elemental compositions of the catalysts before and after stability measurement for all samples indicating that the integrity of the catalysts is retained. In addition, the O1s spectrum of $RE_2Ce_2O_7$ (SI Figure S5.14 (h)) shows the presence of both chemically and physically adsorbed OH after activity, demonstrating the quick adsorption of OH on the surface, consistent with its characteristic large surface area and high concentration of oxygen vacancies and active sites.

5.6 Conclusion

In this work, EISA derived CeO_2, $Nd_2Ce_2O_7$, and CCO $RE_2Ce_2O_7$ high surface area nanocatalysts are studied to understand the impact of calcination temperature and extent of compositional complexity on OER electrocatalytic activity and stability. Among the various calcination temperatures investigated, fluorite compositions calcined at 600°C were found to exhibit the optimal catalytic activity for the OER. CCO $RE_2Ce_2O_7$ synthesized at 600°C outperforms some of the best OER catalysts including RuO_2, IrO_2 and NiO_x. [239] Additionally, chronoamperometry stability measurements in an alkaline environment reveal that $RE_2Ce_2O_7$ displays long term stability with no evidence of degradation.

A combination of long range and short range structural probes reveals the inclusion of mainly RE^{3+} cations in the fluorite lattice results in the formation of Frenkel defects and a partially reduced defect phase with local and long-range oxygen vacancy ordering ($RE_{1.5}Ce_{1.5}O_{5+x}$) to maintain charge balance. While inclusion of Nd (a single RE^{3+} cation) was found to induce these effects and improve OER activity, the compositionally complex $RE_2Ce_2O_7$ catalyst displayed the highest extent of vacancy ordering and best OER activity. The superior intrinsic catalytic activity of $RE_2Ce_2O_7$ relative to the other fluorite catalysts in this series (reported in Chapter 4 and studied in more detail for the case of Nd in this Chapter),

may be attributed to an increase in: (i) number of catalytically active sites, (ii) electronic structure perturbation and (iii) concentration of oxygen Frenkel defects and partially reduced $RE_{1.5}Ce_{1.5}O_{5+x}$ defect phase resulting from the incorporation of multiple RE cations. The larger concentration of surface oxygen vacancies in $RE_2Ce_2O_7$ facilitates the pre-oxidation of RE sites, increases hydroxyl adsorption and promotes the reconstruction of the defective surface with applied potential. In addition to an improvement in intrinsic catalytic activity, the large surface area resulting from the nanoarchitecture of the $RE_2Ce_2O_7$ catalyst plays a key role in improving OER activity by increasing the number of exposed electrochemically active sites, facilitating electrolyte infiltration and surface interaction with the electrocatalyst. Overall, this work demonstrates that a CCO configuration expands abilities to tailor fluorite nanocatalysts.

5.7 Acknowledgements

Acknowledgement is made to the donors of the American Chemical Society Petroleum Research Fund for support of the materials synthesis efforts in this research. XRD measurements were completed at the Diffraction Facility at the Institute for Advanced Materials and Manufacturing at the University of Tennessee. This research used beamline BL-1B (NOMAD) at the Spallation Neutron Source, a DOE Office of Science User Facility operated by the Oak Ridge National Laboratory.

Appendix

Supplemental Information (SI)

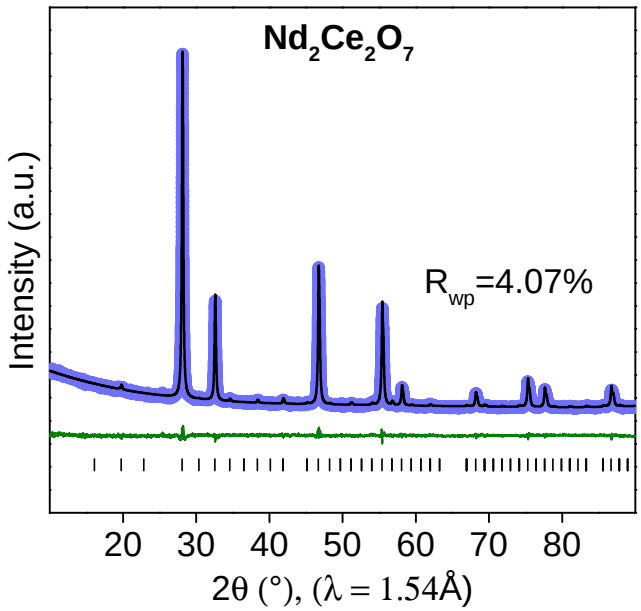


Figure S5.1: Rietveld refinement of powder XRD data of $Nd_2Ce_2O_7$, calcined at 1000°C, using a cubic C-type (bixbyite) structure with space group $Ia\bar{3}$.

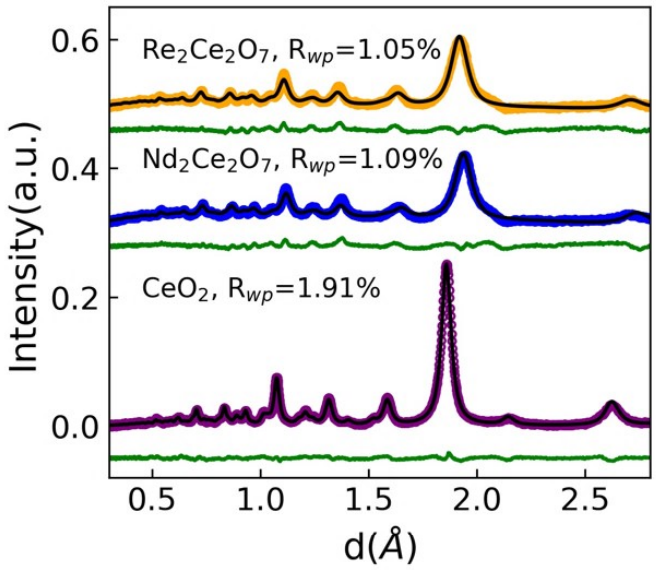


Figure S5.2: Rietveld refinements of neutron diffraction data of $RE_2Ce_2O_7$, $Nd_2Ce_2O_7$ and CeO_2 (from top to bottom) calcined at 600°C. CeO_2 was fit using a tetragonal structure model with S.G. $P4_2/nmc$. $RE_2Ce_2O_7$ and $Nd_2Ce_2O_7$ were fit using a two phase structure model comprising of a primary cubic phase with S.G. $Fm\bar{3}m$ and a secondary oxygen vacancy ordered phase with orthorhombic S.G. $Pnn2$. The secondary phase has a stoichiometry of $RE_{1.5}Ce_{1.5}O_{5+x}$ in the case of $RE_2Ce_2O_7$ and $Nd_{1.5}Ce_{1.5}O_{5+x}$ for $Nd_2Ce_2O_7$.

Table S5.1: Chemical composition results from Energy Dispersive X-ray Spectroscopy (EDS) elemental mapping and X-ray Fluorescence (XRF) of $RE_2Ce_2O_7$ prepared by calcination at 600°C for 4 hours.

$RE_2Ce_2O_7$			
Element	Wt% EDS	Wt% XRF	Target Wt%
Ce	48.96	48.17	48.45
La	10.12	8.66	9.61
Pr	10.08	7.16	9.74
Nd	10.27	10.35	9.97
Dy	10.22	12.27	11.24
Tb	10.34	13.4	10.99

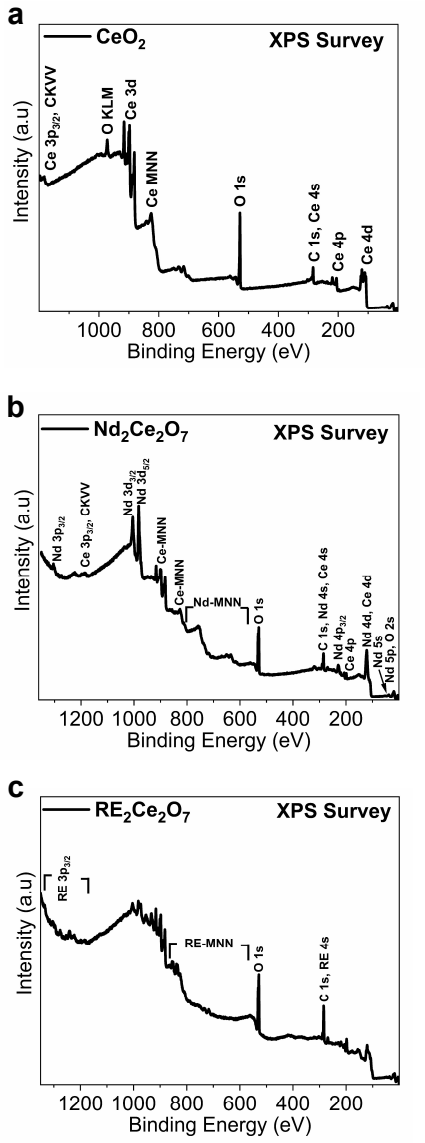


Figure S5.3: Wide-scan survey XPS spectra of (a) CeO_2, (b) $Nd_2Ce_2O_7$ and (c) $RE_2Ce_2O_7$. The C 1s spectra were deconvoluted with the peak at 284.9 eV corresponding to a Sp^3-C bond, and the peak at 288.8 eV corresponding to a C-O bond of ether, or carbonyl functional groups, and the peak at 292.1 and 295.7 eV corresponding to C=O bond of carbonyl groups. [10, 11, 12]

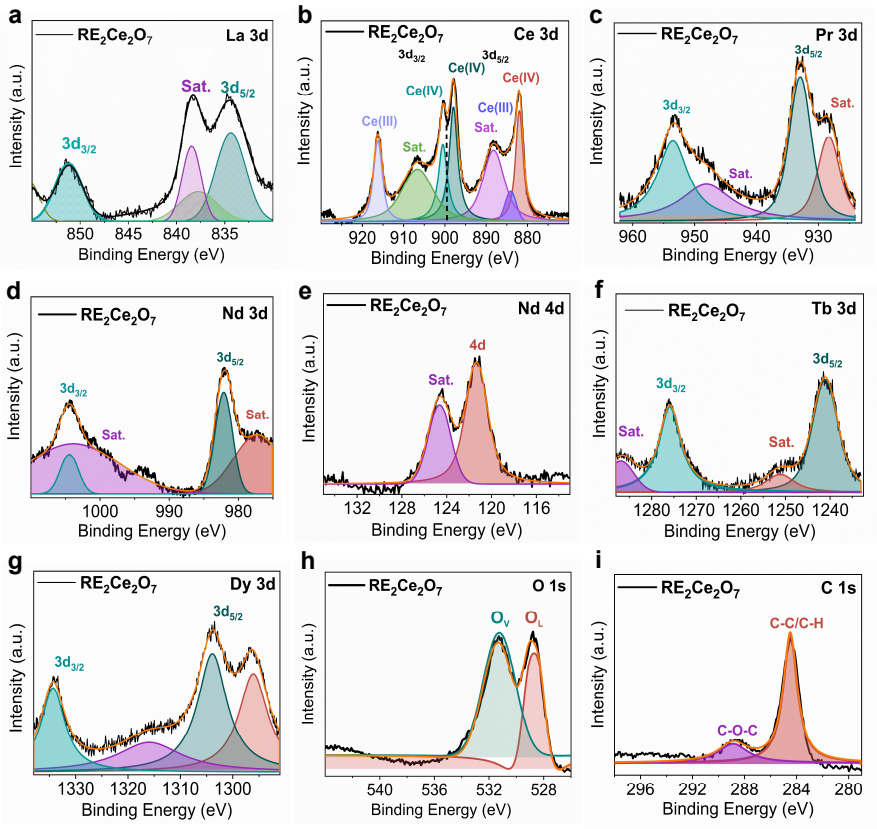


Figure S5.4: High resolution XPS spectra of $RE_2Ce_2O_7$: (a) La 3d; (b)Ce 3d; (c) Pr 4d; (d) Nd 3d; (e)Nd 4d; (f) Tb 3d; (g) Dy 3d; (h) O 1s; (h) C 1s.

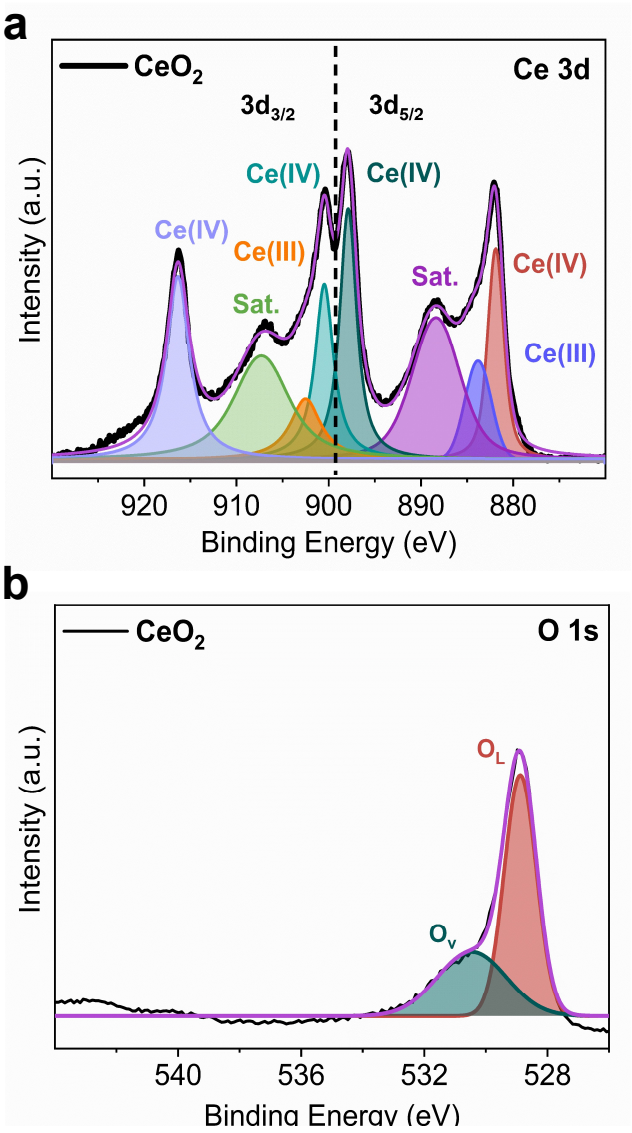


Figure S5.5: High resolution XPS spectra of CeO_2: (a) Ce 3d and (b) O 1s.

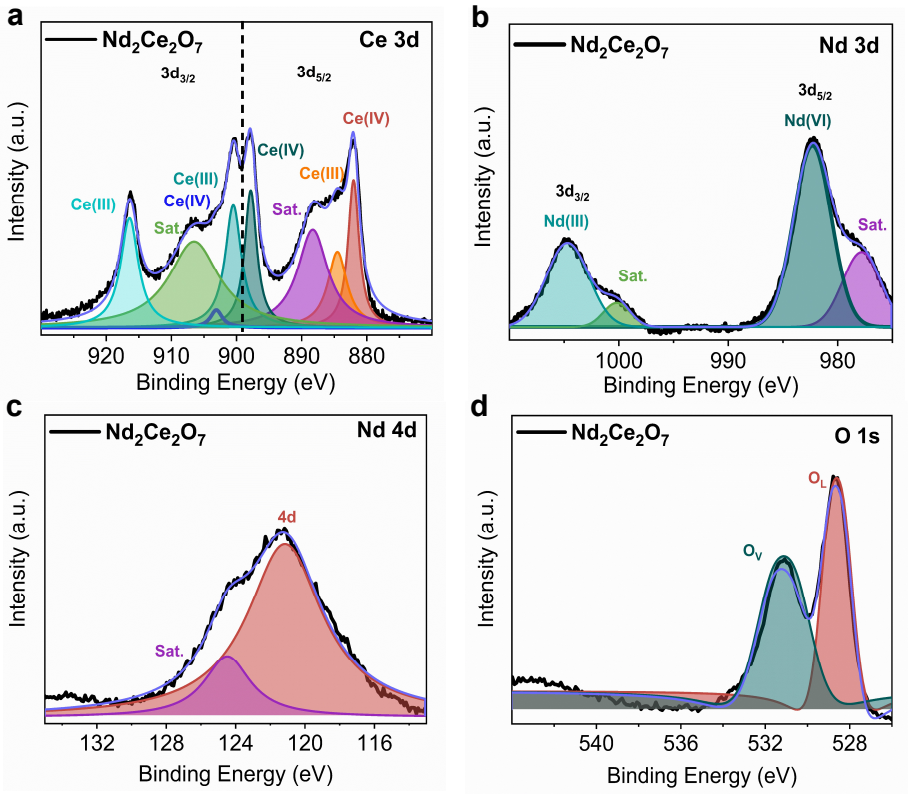


Figure S5.6: High resolution XPS spectra of $Nd_2Ce_2O_7$: (a) Ce 3d; (b)Nd 3d; (c) Nd 4d; (d) O 1.

Catalyst/electrode	Onset overpotential (V), η (*vs.* RHE)	Overpotential (mV), η (*vs.* RHE) at 10 $mAcm^{-2}$	Tafel slope ($mV\ dec^{-1}$)	Electrolyte	Substrate	Ref.
CeO_2	290	347	86.7	1 M KOH	CC	This work
$NdCeO_2$	180	243	47.9	1 M KOH	CC	This work
$RE_2Ce_2O_7$	150	210	43.1	1 M KOH	CC	This work
CeO_2	370	520	233	1 M KOH	CC	[220]
CeO_2	300	420	124.7	0.1 M KOH	GCE	[59]
CeO_2	360	410	146.7	1 M KOH	NF	[55]
CeO_2	355	370	58.9	1 M NaOH	NF	[232]
CeO_2	470	628	158.6	1 M KOH	GCE	[100]

Figure S5.7: Comparison of the catalytic performances between different Ceria-based catalysts.

Table S5.2: Parameters of equivalent circuit obtained from fitting of EIS experimental data.

Parameters	CeO_2	$Nd_2Ce_2O_7$	$RE_2Ce_2O_7$
R_{ct} (ohm)	7.83	3.54	0.97
Rs (ohm)	18.10	7.95	3.02
Cl / F	4.174×10^{-4}	$5.82 \times ^{-2}$	3.11×10^{-1}

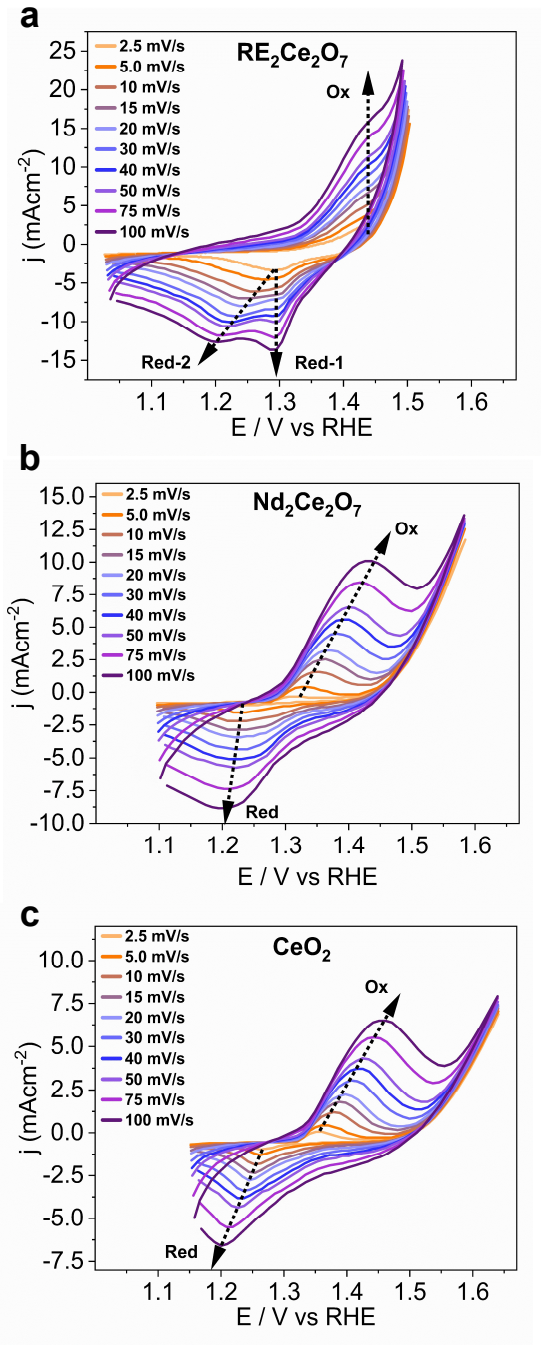


Figure S5.8: Electrocatalytic performance: cyclic voltammograms measured in N_2 saturated 1 M KOH at different scan rates for (a) $RE_2Ce_2O_7$; (b) $Nd_2Ce_2O_7$; and (c) CeO_2.

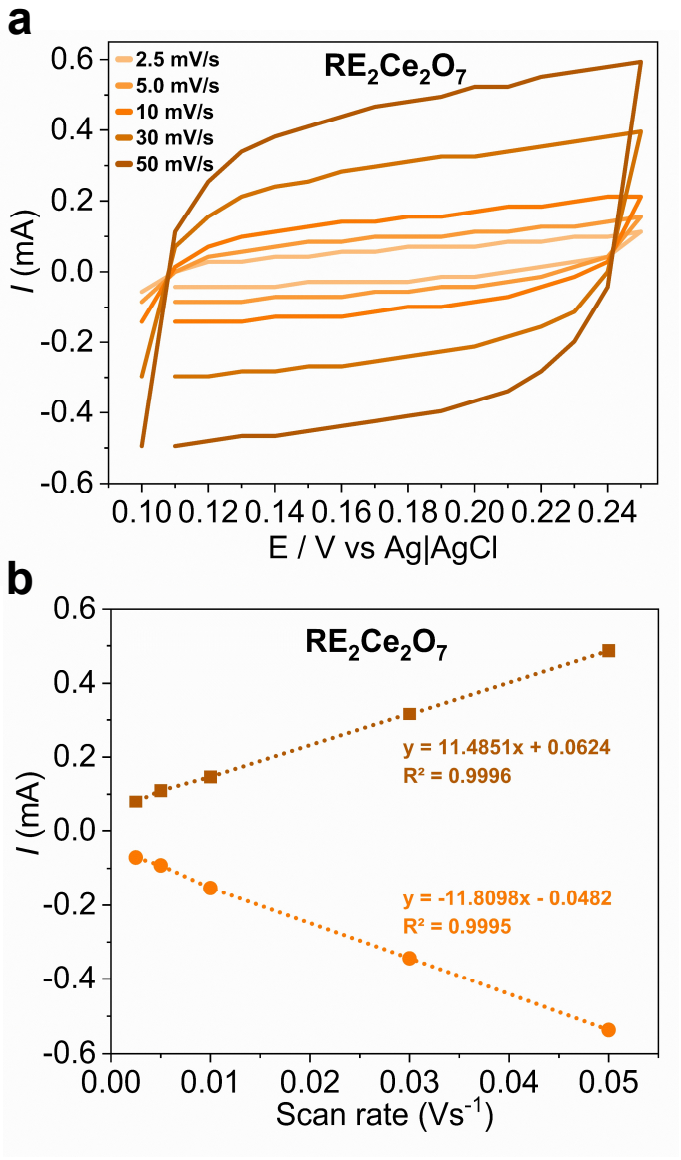


Figure S5.9: (a) Cyclic voltammograms in non-Faradaic region measured at different scan rates for $RE_2Ce_2O_7$. (b) Plots of anodic and cathodic currents measured as a function of different scan rates for $RE_2Ce_2O_7$.

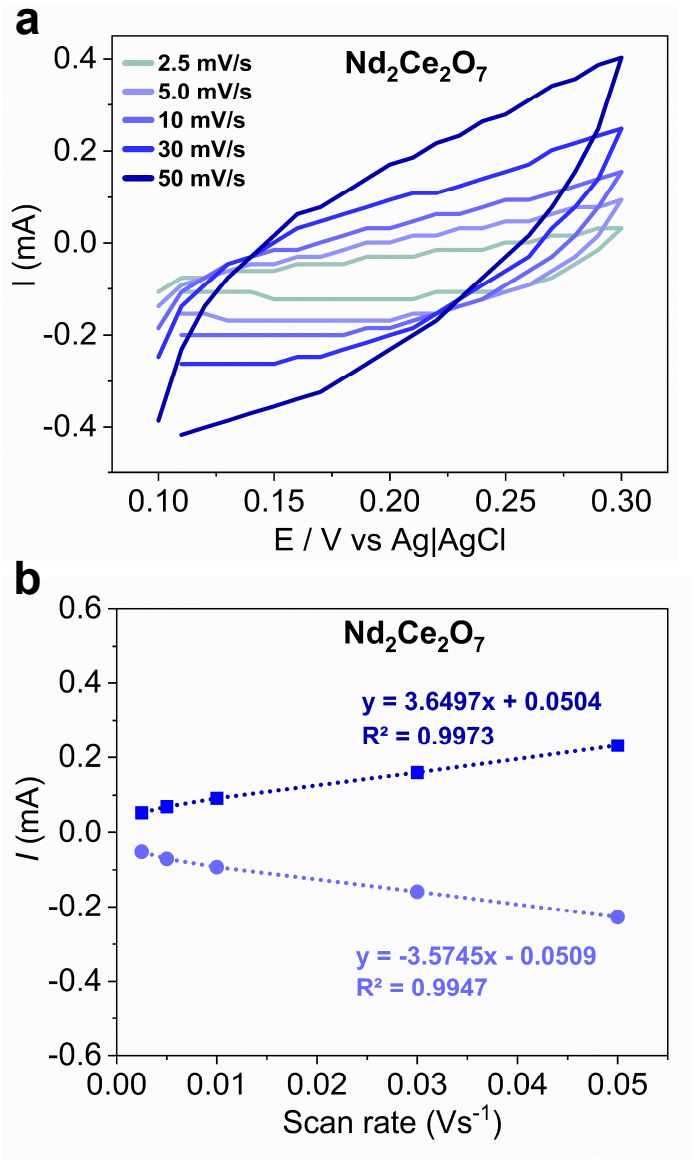


Figure S5.10: (a) Cyclic voltammograms in non-Faradaic region measured at different scan rates for $Nd_2Ce_2O_7$. (b) Plots of anodic and cathodic currents measured as a function of different scan rates for $Nd_2Ce_2O_7$.

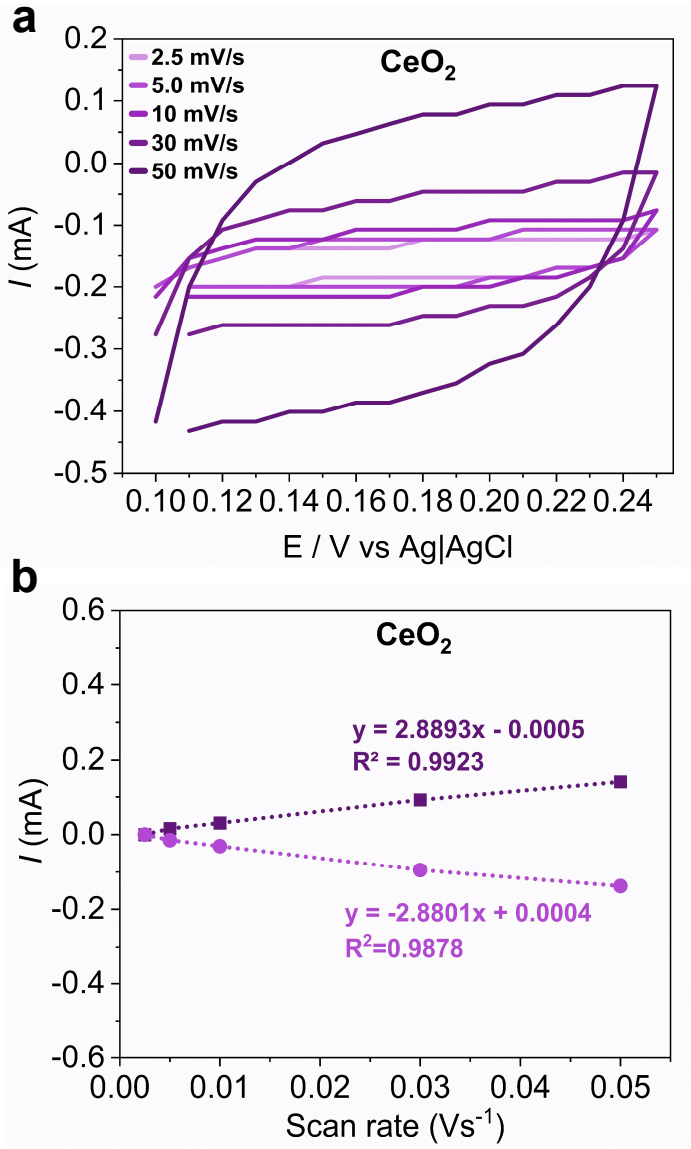


Figure S5.11: (a) Cyclic voltammograms in non-Faradaic region measured at different scan rates for CeO_2. (b) Plots of anodic and cathodic currents measured as a function of different scan rates for CeO_2.

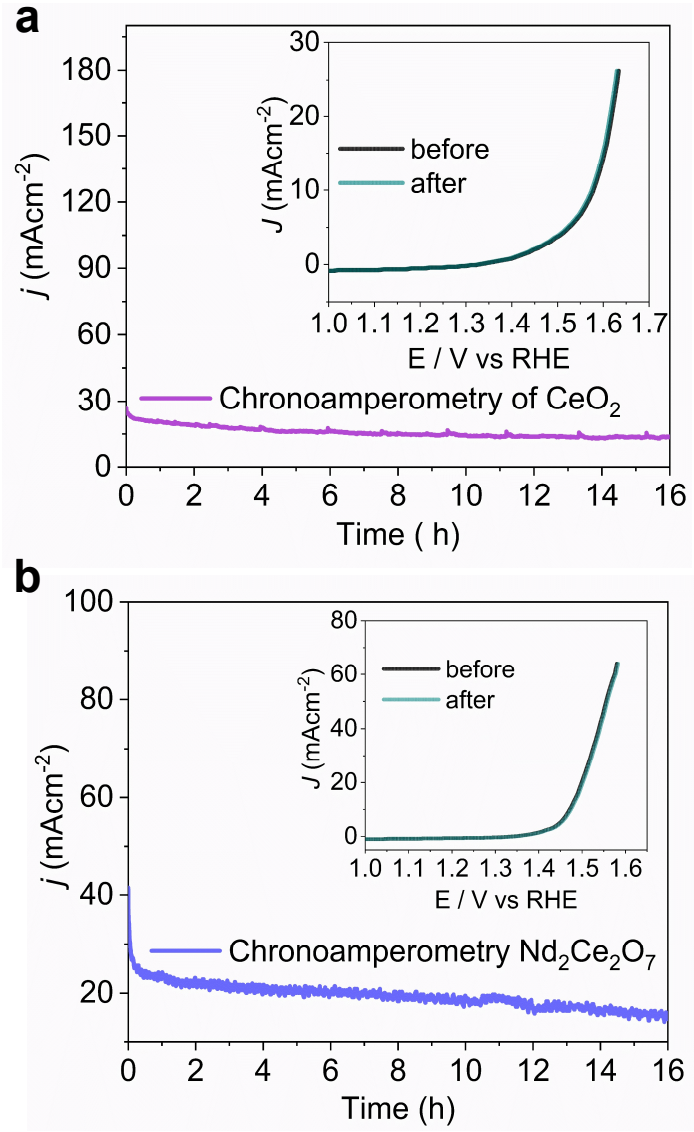


Figure S5.12: Electrocatalytic chronoamperometry stability of (a) CeO_2 at 0.65 V and (b) $Nd_2Ce_2O_7$ at 0.54 V measured in N_2 saturated 1 M KOH after 16h chronoamperometry.

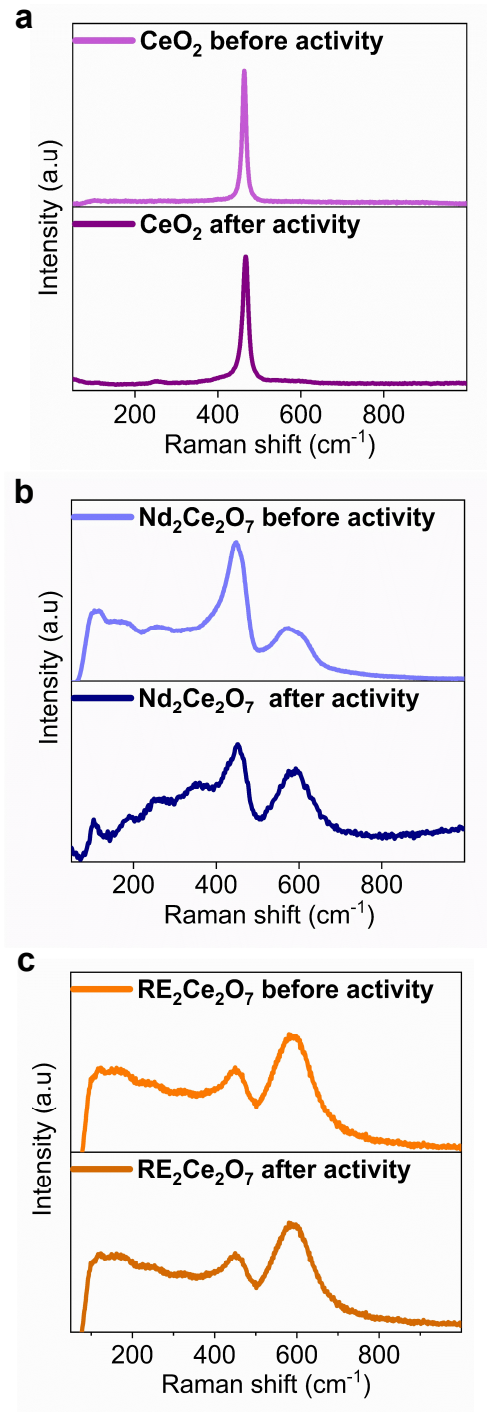


Figure S5.13: Raman Spectra before and after OER activity for (a) CeO_2, (b) $Nd_2Ce_2O_7$ and (c) $RE_2Ce_2O_7$ ($\lambda_{ex} = 632.8$ nm).

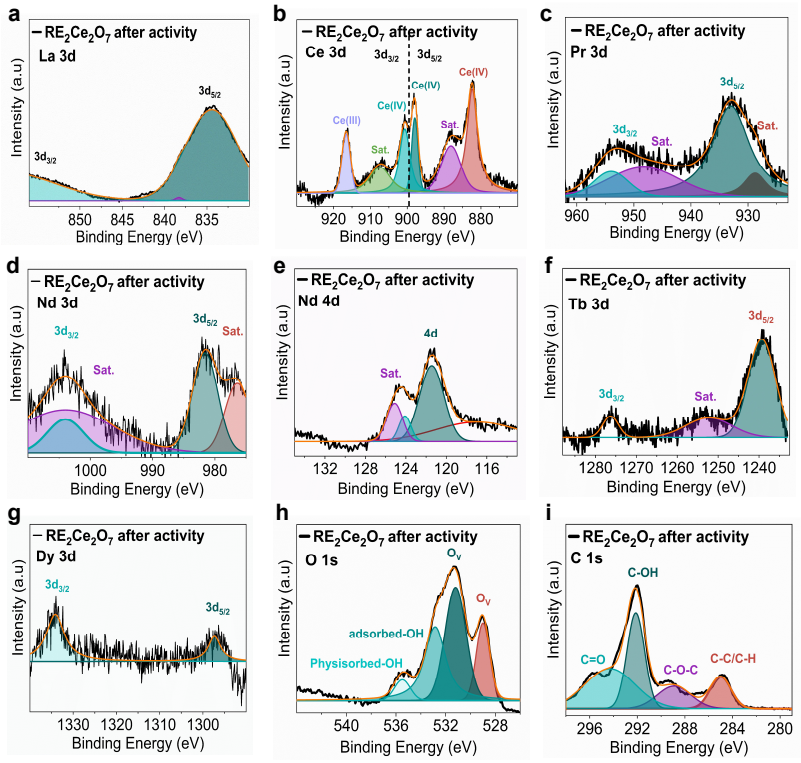


Figure S5.14: High resolution XPS spectra of $RE_2Ce_2O_7$ after OER activity: (a) La 3d; (b) Ce 3d; (c) Pr 4d; (d) Nd 3d; (e) Nd 4d; (f) Tb 3d; (g) Dy 3d; (h) O 1s and (h) C 1s.

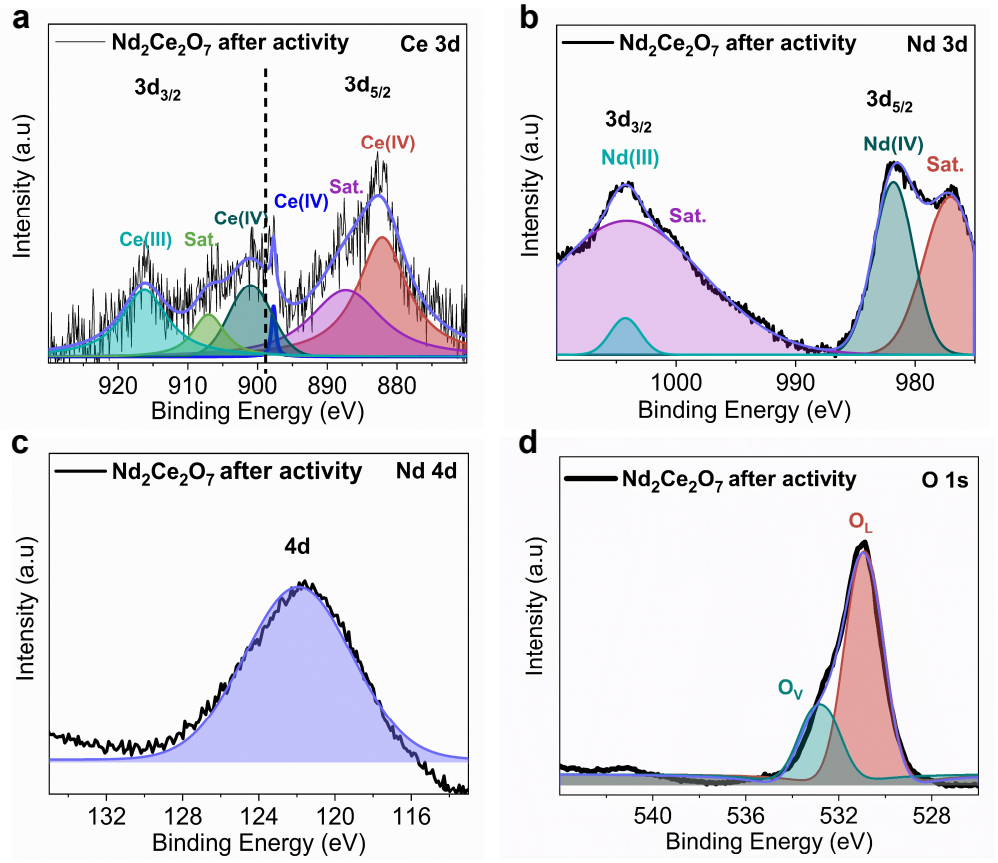


Figure S5.15: High resolution XPS spectra of $Nd_2Ce_2O_7$ after OER activity: (a) Ce 3d; (b) Nd 3d; (c) Nd 4d and (d) O 1s.

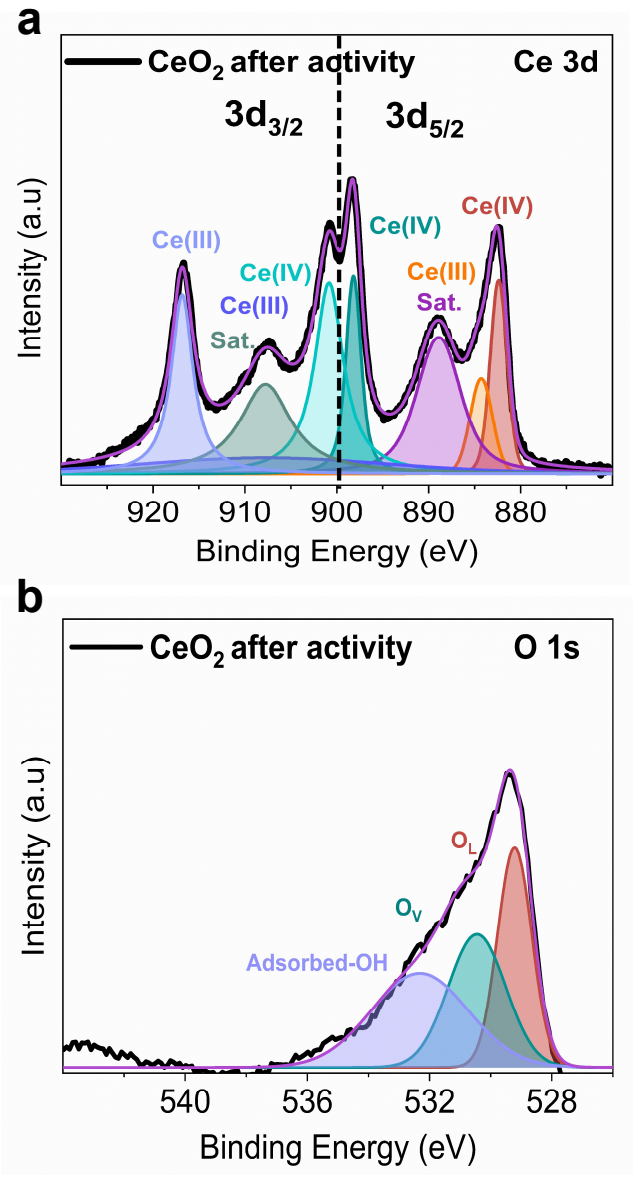


Figure S5.16: High resolution XPS spectra of CeO_2 after OER activity: (a) Ce 3d, (b) O 1s.

Chapter 6

Summary and Outlook

In this work, the fundamental role of structural defects and disorder on the properties of select metal oxide nanocatalysts was investigated for emissions control and energy conversion electrochemical catalytic applications. Findings from this series of studies unravel the intricate interplay between these factors, and provide valuable insights that can inform and direct future materials design strategies aimed at enhancing the efficiency and durability of metal oxide nanocatalysts.

6.1 Role of Noble Metals on Defect Formation in CeO_2-Based Oxides for Heterogeneous Catalysis

In Chapters 2 and 3, we evaluated the hypothesis that studying the structural evolution of metal oxide nanocatalysts impregnated with noble metals *in-situ* is crucial to elucidating the nature of defects and disorder and their role on the catalytic properties under real operating conditions.

In Chapter 2, an *in situ* investigation of CeO_2 and Pt-CeO_2 nanorods under oxidizing and reducing gas environments revealed that both samples share a similar bulk fluorite structure with the presence of surface Frenkel-type oxygen defects. Thus the enhanced reducibility resulting from Pt decoration of CeO_2, measured in this study as a larger concentration of Ce^{3+}, is ascribed to improved kinetics

of the oxygen and oxygen vacancy transport pathway between the surface and bulk. Importantly, while earlier *ex-situ* investigations suggest the presence of oxygen vacancy ordered surface reconstruction in CeO_2 nanorods, this work finds no evidence for the presence of an oxygen vacancy ordered phase under oxidizing and reducing environments. The discrepancy in *ex-situ* and *in-situ* structural observations of the oxygen vacancy defect structure from this study emphasizes the need for robust *in-situ* investigations of catalysts to confirm the mechanistic underpinnings of catalysts under operating conditions and to design industrially relevant materials.

In Chapter 3, the effect of Pd on the average and local structure of $CeZrO_4$ under oxidation, methane oxidation reaction and methane reduction reaction conditions was determined through an *in situ* neutron total scattering study. Analysis of the neutron diffraction data revealed that while $CeZrO_4$ maintains a fully occupied oxygen sub-lattice under all measured gas environments, Pd-$CeZrO_4$ exhibits an increased concentration of oxygen vacancies under methane oxidation reaction and reduction. Additionally, the formation of oxygen vacancies in Pd-$CeZrO_4$, when switching from methane reaction to reduction, is accompanied by a phase transition of Pd-$CeZrO_4$ from a tetragonal to a cubic average structure. These intriguing observations provide new insights into the improved reducibility and superior oxidation catalytic performance of Pd-$CeZrO_4$. Furthermore, *in-situ* neutron pair distribution function (PDF) analysis demonstrates that the generation of oxygen vacancies in Pd-$CeZrO_4$, when transitioning from methane oxidation to reduction, is associated with the evolution of distinct local cation environments for Ce and Zr, which influences oxygen mobility and thus overall catalytic performance. Overall, the presence of Pt and Pd in these two systems is found to have a profound impact on the evolution of the underlying structural supports.

6.2 *In situ* Neutron Total Scattering of Catalysts under Real Operating Conditions

In Chapters 2 and 3, *in situ* neutron total scattering is used as the primary characterization technique to develop a fundamental understanding of the structural evolution of metal oxide nanocatalysts under working conditions. Neutrons exhibit higher sensitivity to light elements present in heterogeneous catalytic reactions, relative to x-ray or electron probes, and thus offer valuable insights into the evolution of oxygen defects and the nature of active sites being formed during a catalytic reaction. These studies highlight that neutron total scattering provides valuable insights into the nature, extent, and evolution of oxygen vacancies, oxygen displacements, and local cation ordering within catalyst supports, which may be challenging to resolve using other structural characterization techniques. Additionally, the work in Chapter 3 commissioned a low background furnace and an improved gas flow cell for *in-situ* neutron total scattering studies, improving opportunities for studying real catalysts in industrially relevant environments.

Nonetheless, it is important to note that neutron total scattering is a bulk characterization technique, and surface interactions play a critical role in catalysis, directly influencing reaction efficiency and selectivity. The catalytic surface provides active sites where reactant molecules adsorb, undergo chemical transformations, and subsequently desorb as products. Neutron PDFs were not found sensitive to detection of adsorbed reactant molecules during reactions, presumably due to the limited surface-to-volume ratios of the samples in these studies. Understanding and controlling surface interactions are crucial for optimizing catalytic performance. To supplement neutron total scattering studies, it is essential to employ surface-sensitive techniques like X-ray Photoelectron Spectroscopy and/or X-ray Absorption Spectroscopy. These techniques provide a holistic understanding of the catalytic

system by offering insights into the surface properties and the contribution of noble metals that may be present in low percentages on catalytic supports.

Additionally, in some cases, catalytic reactions involve rapid dynamics occurring within microseconds to milliseconds. Surface absorbed species are often transient and may be highly disordered. Neutron total scattering measurements may require longer measurement times to achieve a satisfactory signal-to-noise ratio, making it challenging to capture the dynamics of such fast reactions. In such instances, complementary techniques such as inelastic neutron scattering and/or Fourier Transform Infrared (FTIR) spectroscopy can be employed to investigate the reaction mechanism and identify intermediates in conjunction with neutron total scattering.

6.3 Leveraging Compositional Complexity To Enhance Activity and Stability of Electrocatalysts for the Oxygen Evolution Reaction

In Chapters 4 and 5, we evaluate the hypothesis that compositional complexity can be leveraged as a materials design strategy to enhance catalytic activity and stability for the electrochemical OER, unrealized via more traditional materials approaches.

In Chapter 4, we demonstrate EISA as a promising, inexpensive and scalable route to synthesize OER catalysts with high surface area and mesoporosity, belonging to the cerate fluorite class of materials. We demonstrate that partial substitution of Ce^{4+} with a single, mainly RE^{3+}, cation results in an electronic structure perturbation and introduces oxygen vacancies into the lattice to maintain charge balance. Consequently, binary fluorite compositions are found to display lower OH* adsorption energy than pristine CeO_2, resulting in a lower overpotential and enhanced activity for the OER. Variation in OER activity among the various binary fluorite compositions investigated can be attributed to a difference in the electronic structure, concentrations of oxygen vacancies, morphology and surface area. Important considerations when selecting RE cations for substitution in the

fluorite lattice include the single/multivalent nature of the RE (affects oxygen vacancy concentration) and the decomposition temperature of the RE nitrate precursor which may influence oxide formation and morphology during sample calcination. Importantly, we demonstrate that rare-earth oxide OER catalysts with high activity and stability in an alkaline media, can be achieved using the EISA synthesis route, without the incorporation of transition or noble metals.

While Chapter 4 shows that RE substitution in the fluorite lattice of CeO_2 can lead to increased oxygen vacancy formation, significantly influencing OER activity, the nature of oxygen vacancies are not specifically investigated. In Chapter 5, the role of RE cation incorporation and the degree of compositional complexity (number of participating RE cations) in a fluorite lattice, studied by Raman spectroscopy and neutron total scattering, is found to have a significant influence on the type, concentration and length scale of oxygen vacancies and the observed OER activity. RE cation substitution was found to result in an increased concentration and longer correlation length scale of a partially reduced oxygen vacancy ordered $RE_{1.5}Ce_{1.5}O_{5+x}$ phase relative to the limited coherence length of the vacancy ordered Ce_3O_{5+x} phase in CeO_2. The correlation length scale of oxygen vacancies has been shown to strongly influence the redox properties and resulting catalytic performance of ceria-based mixed oxides and OER catalysts in general. Additionally, tuning the degree of compositional complexity was determined to enhance OER activity as the fluorite composition containing 5 mainly RE^{3+} cations ($RE_2Ce_2O_7$) displayed higher OER activity than the composition containing a single RE^{3+} cation ($Nd_2Ce_2O_7$). The superior intrinsic catalytic activity of $RE_2Ce_2O_7$ relative to $Nd_2Ce_2O_7$ and CeO_2, may be attributed to an increase in: (i) number of catalytically active sites, (ii) electronic structure perturbation and (iii) concentration of oxygen Frenkel defects and partially reduced $RE_{1.5}Ce_{1.5}O_{5+x}$ defect phase. The larger concentration of surface oxygen vacancies in $RE_2Ce_2O_7$ facilitates the pre-oxidation of RE sites, increases hydroxyl adsorption and promotes the reconstruction of the defective surface with applied potential.

In addition to an improvement in intrinsic catalytic activity, the large surface area resulting from the nanoarchitecture of the $RE_2Ce_2O_7$ catalyst plays a key role in improving OER activity by increasing the number of exposed electrochemically active sites, facilitating electrolyte infiltration and surface interaction with the electrocatalyst. Thus, this work suggests that tuning compositional complexity may offer promising improvements in OER catalytic activity. The determination of whether this enhancement is due to the presence of increased numbers of the types of catalytically active sites (cocktail effects), the increased configurational entropy arising from the high number of involved cations (improving the stability of oxygen defects, limiting cation diffusion, etc.) or a combination of factors deserves further investigation.

Overall, this research offers key insights into the underlying structural and morphological factors that govern the performance of metal oxide nanocatalysts in both emissions control catalysis and electrocatalysis. The results of *in-situ* studies highlight the significance of studying catalysts under working conditions and the value and considerations associated with utilizing neutron total scattering as a technique for studying the structure of metal oxide supports. Furthermore, we highlight a number of intriguing results that emerge from harnessing compositional complexity as a materials design tool, warranting further exploration and serving as a resource for researchers engaged in catalytic studies. Ultimately, the findings derived from these investigations serve as a guide for the development of metal oxide nanocatalysts with enhanced efficacy and stability for various energy applications.

Bibliography

[1] Debanjali Ghosh, Mopidevi Manikanta Kumar, C Retna Raj, and Debabrata Pradhan. Bifunctional Catalytic Activity of Solvothermally Synthesized CeO2 Nanosphere/NiO Nanoflake Nanocomposites. *ACS Applied Energy Materials*, 5(5):5666–5679, may 2022. doi: 10.1021/acsaem.1c04036. xxv, 92, 93, 153, 157, 158, 159

[2] Bocheng Qiu, Cong Wang, Ning Zhang, Lejuan Cai, Yujie Xiong, and Yang Chai. CeO2-Induced Interfacial Co2+ Octahedral Sites and Oxygen Vacancies for Water Oxidation. *ACS Catalysis*, 9(7):6484–6490, jul 2019. doi: 10.1021/acscatal.9b01819. xxv, 87, 93, 156, 158, 159

[3] Menghan Gao, Zhihong Wang, Shichao Sun, Deli Jiang, and Min Chen. Interfacial engineering of CeO(2) on NiCoP nanoarrays for efficient electrocatalytic oxygen evolution. *Nanotechnology*, 32(19):195704, may 2021. ISSN 1361-6528 (Electronic). doi: 10.1088/1361-6528/abe0e5. xxv, 92, 157, 158, 159

[4] Hongtao Xie, Qin Geng, Xiaoyue Liu, and Jian Mao. Interface engineering for enhancing electrocatalytic oxygen evolution reaction of CoS/CeO2 heterostructures. *Frontiers of Chemical Science and Engineering*, 16(3):376–383, 2022. ISSN 2095-0187. doi: 10.1007/s11705-021-2062-x. xxv, 92, 93, 157, 158, 159

[5] Zihao Zhang, Shize Yang, Xiaobing Hu, Haidi Xu, Honggen Peng, Miaomiao Liu, Bishnu Prasad Thapaliya, Kecheng Jie, Jiahua Zhao, Jixing Liu, Hao Chen, Yan Leng, Xiuyang Lu, Jie Fu, Pengfei Zhang, and Sheng Dai. Mechanochemical Nonhydrolytic Sol-Gel-Strategy for the Production of Mesoporous Multimetallic Oxides. *Chemistry of Materials*, 31(15):5529–5536, 2019. ISSN 15205002. doi: 10.1021/acs.chemmater.9b01244. xxv, 158, 159

[6] Arumugam Sivanantham, Pandian Ganesan, and Sangaraju Shanmugam. A synergistic effect of Co and CeO2 in nitrogen-doped carbon nanostructure for the enhanced oxygen electrode activity and stability. *Applied Catalysis B: Environmental*, 237:1148–1159, dec 2018. ISSN 0926-3373. doi: 10.1016/J.APCATB.2017.08.063. xxv, 158, 159

[7] Tongfei Li, Sulin Li, Qianyu Liu, Yechao Tian, Yiwei Zhang, Gengtao Fu, and Yawen Tang. Hollow Co3O4/CeO2 Heterostructures in Situ Embedded in N-Doped Carbon Nanofibers Enable Outstanding Oxygen Evolution. *ACS Sustainable Chemistry & Engineering*, 7(21):17950–17957, nov 2019. doi: 10.1021/acssuschemeng.9b04699. xxv, 158, 159

[8] Jinzhen Huang, Hongyuan Sheng, R Dominic Ross, Jiecai Han, Xianjie Wang, Bo Song, and Song Jin. Modifying redox properties and local bonding of Co3O4 by CeO2 enhances oxygen evolution catalysis in acid. *Nature Communications*, 12(1):3036, 2021. ISSN 2041-1723. doi: 10.1038/s41467-021-23390-8. xxv, 158, 159

[9] Jiangtian Li. Oxygen Evolution Reaction in Energy Conversion and Storage: Design Strategies Under and Beyond the Energy Scaling Relationship. *Nano-Micro Letters*, 14(1):112, 2022. ISSN 2150-5551. doi: 10.1007/s40820-022-00857-x. xxv, 13, 158, 159

[10] Dasol Jin, Jisoo Kang, Sampath Prabhakaran, Youngmi Lee, Myung Hwa Kim, Do Hwan Kim, and Chongmok Lee. Chromium-rich CrxIr1−xO2 wire-in-tube alloys for boosted water oxidation with long standing electrocatalytic activity. *J. Mater. Chem. A*, 10(26):13803–13813, 2022. doi: 10.1039/D2TA02984G. xxvi, 170

[11] Shaoxi Kong, Mengfei Lu, Shicheng Yan, and Zhigang Zou. High-valence chromium accelerated interface electron transfer for water oxidation. *Dalton Trans.*, 51(44):16890–16897, 2022. doi: 10.1039/D2DT02908A. xxvi, 170

[12] Sakila Khatun and Roy Poulomi. Cobalt chromium vanadium layered triple hydroxides as an efficient oxygen electrocatalyst for alkaline seawater splitting. *Chem. Commun.*, 58(8):1104–1107, 2022. doi: 10.1039/D1CC05745F. xxvi, 170

[13] Cynthia M Friend and Bingjun Xu. Heterogeneous Catalysis: A Central Science for a Sustainable Future. *Accounts of Chemical Research*, 50(3):517–521, mar 2017. ISSN 0001-4842. doi: 10.1021/acs.accounts.6b00510. 2

[14] B Delmon. Preparation of heterogeneous catalysts. *Journal of Thermal Analysis and Calorimetry*, 90(1):49–65, 2007. ISSN 1572-8943. doi: 10.1007/s10973-007-8476-y. 2

[15] Jacques C Vedrine. Importance, features and uses of metal oxide catalysts in heterogeneous catalysis. *Chinese Journal of Catalysis*, 40(11):1627–1636, 2019. ISSN 1872-2067. doi: https://doi.org/10.1016/S1872-2067(18)63162-6. 2

[16] Xijun Hu and Alex C K Yip. Heterogeneous Catalysis: Enabling a Sustainable Future. *Frontiers in Catalysis*, 1, 2021. ISSN 2673-7841. doi: 10.3389/fctls.2021.667675. 2

[17] Julian Ross. *Heterogeneous Catalysis – Chemistry in Two Dimensions*, pages 1–15. Elsevier, 2012. ISBN 9780444533630. doi: 10.1016/B978-0-444-53363-0.10001-5. 2

[18] Manoj B Gawande, Rajesh K Pandey, and Radha V Jayaram. Role of mixed metal oxides in catalysis science—versatile applications in organic synthesis. *Catal. Sci. Technol.*, 2(6):1113–1125, 2012. doi: 10.1039/C2CY00490A. 2

[19] Fan Yang, Dehui Deng, Xiulian Pan, Qiang Fu, and Xinhe Bao. Understanding nano effects in catalysis. *National Science Review*, 2(2):183–201, 2015. ISSN 2095-5138. doi: 10.1093/nsr/nwv024. 2

[20] Seunghyun Weon, Dahong Huang, Kali Rigby, Chiheng Chu, Xuanhao Wu, and Jae-Hong Kim. Environmental Materials beyond and below the Nanoscale: Single-Atom Catalysts. *ACS ES and T Engineering*, 1(2):157–172, feb 2021. doi: 10.1021/acsestengg.0c00136. 2

[21] Shuhua Liu, Shi-Qiang Bai, Yuangang Zheng, Kwok Wei Shah, and Ming-Yong Han. Composite Metal–Oxide Nanocatalysts. *ChemCatChem*, 4(10):1462–1484, 2012. doi: https://doi.org/10.1002/cctc.201200264. 2, 4

[22] Jawwad A Darr, Jingyi Zhang, Neel M Makwana, and Xiaole Weng. Continuous Hydrothermal Synthesis of Inorganic Nanoparticles: Applications and Future Directions. *Chemical Reviews*, 117(17):11125–11238, sep 2017. ISSN 0009-2665. doi: 10.1021/acs.chemrev.6b00417. 4

[23] Serena Esposito. "Traditional" Sol-Gel Chemistry as a Powerful Tool for the Preparation of Supported Metal and Metal Oxide Catalysts. *Materials (Basel, Switzerland)*, 12(4), feb 2019. ISSN 1996-1944 (Print). doi: 10.3390/ma12040668. 4

[24] David A Ward and Edmond I Ko. Preparing Catalytic Materials by the Sol-Gel Method. *Industrial and Engineering Chemistry Research*, 34(2):421–433, feb 1995. ISSN 0888-5885. doi: 10.1021/ie00041a001. 4

[25] Dong Won Lee and Bok Ryul Yoo. Advanced metal oxide (supported) catalysts: Synthesis and applications. *Journal of Industrial and Engineering Chemistry*, 20(6):3947–3959, 2014. ISSN 1226-086X. doi: https://doi.org/10.1016/j.jiec.2014.08.004. 4

[26] Jhumur Seth, Prashant Dubey, Vijay R Chaudhari, and Bhagavatula L V Prasad. Preparation of metal oxide supported catalysts and their utilization for understanding the effect of a support on the catalytic activity. *New J. Chem.*, 42(1):402–410, 2018. doi: 10.1039/C7NJ03753H. 4

[27] Guoming Huang, Chun-Hua Lu, and Huang-Hao Yang. Chapter 3 - Magnetic Nanomaterials for Magnetic Bioanalysis. In Xiaoru Wang and Xi B T Novel Nanomaterials for Biomedical Chen Environmental and Energy Applications, editors, *Micro and Nano Technologies*, pages 89–109. Elsevier, 2019. ISBN 978-0-12-814497-8. doi: https://doi.org/10.1016/B978-0-12-814497-8.00003-5. 4

[28] Bhim Prasad Kafle. Chapter 6 - Introduction to nanomaterials and application of UV–Visible spectroscopy for their characterization. In Bhim Prasad B T Chemical Analysis Kafle and Material Characterization by Spectrophotometry, editors, *Chemical Analysis and Material Characterization by Spectrometry*, pages 147–198. Elsevier, 2020. ISBN 978-0-12-814866-2. 4

[29] Peter Munnik, Petra E de Jongh, and Krijn P de Jong. Recent Developments in the Synthesis of Supported Catalysts. *Chemical Reviews*, 115(14):6687–6718, jul 2015. ISSN 0009-2665. doi: 10.1021/cr500486u. 4, 8

[30] Luther Mahoney and Ranjit T Koodali. Versatility of Evaporation-Induced Self-Assembly (EISA) Method for Preparation of Mesoporous TiO_2 for Energy and Environmental Applications. *Materials (Basel, Switzerland)*, 7(4):2697–2746, mar 2014. ISSN 1996-1944 (Print). doi: 10.3390/ma7042697. 6

[31] Clément Sanchez, Cédric Boissière, David Grosso, Christel Laberty, and Lionel Nicole. Design, Synthesis, and Properties of Inorganic and Hybrid Thin Films Having Periodically Organized Nanoporosity. *Chemistry of Materials*, 20(3):682–737, feb 2008. ISSN 0897-4756. doi: 10.1021/cm702100t. 6

[32] Nilofar Asim, Shideh Ahmadi, M A Alghoul, F Y Hammadi, Kasra Saeedfar, and K Sopian. Research and Development Aspects on Chemical Preparation Techniques of Photoanodes for Dye Sensitized Solar Cells. *International Journal of Photoenergy*, 2014:518156, 2014. ISSN 1110-662X. doi: 10.1155/2014/518156. 6

[33] Ankit Kashyap, Niraj Kumar Singh, Mahesh Soni, and Ajay Soni. Chapter 3 - Deposition of thin films by chemical solution-assisted techniques. In Soumen Das, Sandip B T Chemical Solution Synthesis for Materials Design Dhara, and Thin Film Device Applications, editors, *Chemical Solution Synthesis for Materials Design and Thin Film Device Applications*, pages 79–117. Elsevier, 2021. ISBN 978-0-12-819718-9. 6

[34] Ewelina Grabowska, Martyna Marchelek, Marta Paszkiewicz-Gawron, and Adriana Zaleska-Medynska. 3 - Metal oxide photocatalysts. In Adriana B T Metal Oxide-Based Photocatalysis Zaleska-Medynska, editor, *Metal Oxides*, pages 51–209. Elsevier, 2018. ISBN 978-0-12-811634-0. doi: https://doi.org/10.1016/B978-0-12-811634-0.00003-2. 6

[35] Géraldine Dantelle, Sandrine Beauquis, Ronan Le Dantec, Virginie Monnier, Christine Galez, and Yannick Mugnier. Solution-Based Synthesis Routes

for the Preparation of Noncentrosymmetric 0-D Oxide Nanocrystals with Perovskite and Nonperovskite Structures. *Small*, 18(30):2200992, jul 2022. ISSN 1613-6810. doi: https://doi.org/10.1002/smll.202200992. 6

[36] Gabor A Somorjai and Yimin Li. Impact of surface chemistry. *Proceedings of the National Academy of Sciences*, 108(3):917–924, 2011. doi: 10.1073/pnas.1006669107. 8, 9

[37] Tom W van Deelen, Carlos Hernández Mejía, and Krijn P de Jong. Control of metal-support interactions in heterogeneous catalysts to enhance activity and selectivity. *Nature Catalysis*, 2(11):955–970, 2019. ISSN 2520-1158. doi: 10.1038/s41929-019-0364-x. 8

[38] Y Lou, J Xu, Y Zhang, C Pan, Y Dong, and Y Zhu. Metal-support interaction for heterogeneous catalysis: from nanoparticles to single atoms. *Materials Today Nano*, 12:100093, 2020. ISSN 2588-8420. doi: https://doi.org/10.1016/j.mtnano.2020.100093. 8

[39] Yangyang Li, Yunshang Zhang, Kun Qian, and Weixin Huang. Metal–Support Interactions in Metal/Oxide Catalysts and Oxide–Metal Interactions in Oxide/Metal Inverse Catalysts. *ACS Catalysis*, 12(2):1268–1287, jan 2022. doi: 10.1021/acscatal.1c04854. 8

[40] Zheng Lu, Jacob Kunisch, Zhuoran Gan, Muntaseer Bunian, Tianpin Wu, and Yu Lei. Gold Catalysts Synthesized Using a Modified Incipient Wetness Impregnation Method for Propylene Epoxidation. *ChemCatChem*, 12(23):5993–5999, 2020. doi: https://doi.org/10.1002/cctc.202001053. 8

[41] Si Luo, Meijun Li, Victor Fung, Bobby G. Sumpter, Jue Liu, Zili Wu, and Katharine Page. New Insights into the Bulk and Surface Defect Structures of Ceria Nanocrystals from Neutron Scattering Study. *Chemistry of Materials*, 33

(11):3959–3970, jun 2021. ISSN 0897-4756. doi: 10.1021/acs.chemmater.1c00156. 9, 19, 37

[42] Chao Xie, Dafeng Yan, Hao Li, Shiqian Du, Wei Chen, Yanyong Wang, Yuqin Zou, Ru Chen, and Shuangyin Wang. Defect Chemistry in Heterogeneous Catalysis: Recognition, Understanding, and Utilization. *ACS Catalysis*, 10 (19):11082–11098, oct 2020. doi: 10.1021/acscatal.0c03034. 9

[43] Christina M Rost, Edward Sachet, Trent Borman, Ali Moballegh, Elizabeth C Dickey, Dong Hou, Jacob L Jones, Stefano Curtarolo, and Jon-Paul Maria. Entropy-stabilized oxides. *Nature Communications*, 6(1):8485, 2015. ISSN 2041-1723. doi: 10.1038/ncomms9485. 9

[44] Dawei Zhang, Yan Chen, Tianshi Feng, Dunji Yu, Ke An, Renkun Chen, and Jian Luo. Discovery of a reversible redox-induced order-disorder transition in a 10-component compositionally complex ceramic. *Scripta Materialia*, 215: 114699, 2022. ISSN 1359-6462. doi: https://doi.org/10.1016/j.scriptamat.2022.114699. 9

[45] Yifan Sun and Sheng Dai. High-entropy materials for catalysis: A new frontier. *Science Advances*, 7(20):eabg1600, sep 2022. doi: 10.1126/sciadv.abg1600. 9

[46] Shuangyang Zhao, Aihua Liu, Yonghe Li, Yanyan Wen, Xiaoqian Gao, and Qiaoli Chen. Boosting the Electrocatalytic CO(2) Reduction Reaction by Nanostructured Metal Materials via Defects Engineering. *Nanomaterials (Basel, Switzerland)*, 12(14), jul 2022. ISSN 2079-4991 (Print). doi: 10.3390/nano12142389. 9

[47] Shaima H Albedwawi, Asala AlJaberi, Gregory N Haidemenopoulos, and Kyriaki Polychronopoulou. High entropy oxides-exploring a paradigm of

promising catalysts: A review. *Materials and Design*, 202:109534, 2021. ISSN 0264-1275. doi: https://doi.org/10.1016/j.matdes.2021.109534. 11

[48] Yifan Sun and Sheng Dai. High-entropy materials for catalysis: A new frontier. *Science Advances*, 7(20):eabg1600, 2021. doi: 10.1126/sciadv.abg1600. 11

[49] Donald Stedman. Catalytic Converter, 2022. 11

[50] Emmy Kritsanaviparkporn, Francisco M Baena-Moreno, and T R Reina. Catalytic Converters for Vehicle Exhaust: Fundamental Aspects and Technology Overview for Newcomers to the Field. *Chemistry*, 3(2):630–646, 2021. ISSN 2624-8549. doi: 10.3390/chemistry3020044. 11

[51] Dong Jiang, Konstantin Khivantsev, and Yong Wang. Low-Temperature Methane Oxidation for Efficient Emission Control in Natural Gas Vehicles: Pd and Beyond. *ACS Catalysis*, 10(23):14304–14314, dec 2020. doi: 10.1021/acscatal.0c03338. 12, 49, 50

[52] A F Diwell, R R Rajaram, H A Shaw, and T J Truex. The Role of Ceria in Three-Way Catalysts. In A Crucq, editor, *Studies in Surface Science and Catalysis*, volume 71 of *Studies in Surface Science and Catalysis*, pages 139–152. Elsevier, 1991. doi: https://doi.org/10.1016/S0167-2991(08)62975-4. 12

[53] Spyridon Divanis, Tugce Kutlusoy, Ida Marie Ingmer Boye, Isabela Costinela Man, and Jan Rossmeisl. Oxygen evolution reaction: a perspective on a decade of atomic scale simulations. *Chem. Sci.*, 11(11):2943–2950, 2020. doi: 10.1039/C9SC05897D. 12, 13

[54] Takahiro Naito, Tatsuya Shinagawa, Takeshi Nishimoto, and Kazuhiro Takanabe. Recent advances in understanding oxygen evolution reaction

mechanisms over iridium oxide. *Inorg. Chem. Front.*, 8(11):2900–2917, 2021. doi: 10.1039/D0QI01465F. 12, 13

[55] Yanying Liu, Daojin Zhou, Tianyin Deng, Guangli He, Aibing Chen, Xiaoming Sun, Yuhua Yang, and Ping Miao. Research Progress of Oxygen Evolution Reaction Catalysts for Electrochemical Water Splitting. *ChemSusChem*, 14 (24):5359–5383, 2021. doi: https://doi.org/10.1002/cssc.202101898. 13

[56] David Stenzel, Bei Zhou, Chukwudalu Okafor, Mohana Veeraju Kante, Ling Lin, Georgian Melinte, Thomas Bergfeldt, Miriam Botros, Horst Hahn, Ben Breitung, and Simon Schweidler. High-entropy spinel-structure oxides as oxygen evolution reaction electrocatalyst . *Frontiers in Energy Research*, 10, 2022. 13

[57] Xinbin Yu, Yongqiang Cheng, Yuanyuan Li, Felipe Polo-Garzon, Jue Liu, Eugene Mamontov, Meijun Li, David Lennon, Stewart F Parker, Anibal J Ramirez-Cuesta, and Zili Wu. Neutron Scattering Studies of Heterogeneous Catalysis. *Chemical Reviews*, 123(13):8638–8700, jul 2023. ISSN 0009-2665. doi: 10.1021/acs.chemrev.3c00101. 13

[58] José A Rodriguez, Jonathan C Hanson, Peter J Chupas, Jose a Rodriguez, Jose a Rodriguez, Jonathan C Hanson, and Peter J Chupas. In-Situ Characterization of Heterogeneous Catalysts. In *In-Situ Characterization of Heterogeneous Catalysts*. John Wiley and Sons, Incorporated, Oxford, UNITED STATES, 2013. ISBN 9781118355909. 13, 14

[59] Nora K Zimmerli, Christoph R Müller, and Paula M Abdala. Deciphering the structure of heterogeneous catalysts across scales using pair distribution function analysis. *Trends in Chemistry*, 4(9):807–821, sep 2022. ISSN 2589-7209. doi: 10.1016/j.trechm.2022.06.006. 13

[60] Sreya Paladugu, Peter C Metz, Si Luo, Meijun Li, Jue Liu, Harry I I I Meyer, Yiqing Wu, Zili Wu, and Katharine Page. In Situ Neutron Scattering Studies on the Oxidation and Reduction of CeO2 and Pt–CeO2 Nanorods. *The Journal of Physical Chemistry C*, 127(7):3689–3697, feb 2023. ISSN 1932-7447. doi: 10.1021/acs.jpcc.2c07398. 17, 153, 155

[61] Tiziano Montini, Michele Melchionna, Matteo Monai, and Paolo Fornasiero. Fundamentals and Catalytic Applications of CeO2-Based Materials. *Chemical Reviews*, 116(10):5987–6041, may 2016. ISSN 0009-2665. doi: 10.1021/acs.chemrev.5b00603. 17, 24, 31

[62] Alessandro Trovarelli. Catalytic Properties of Ceria and CeO2-Containing Materials. *Catalysis Reviews*, 38(4):439–520, nov 1996. ISSN 0161-4940. doi: 10.1080/01614949608006464. 17, 18

[63] B Murugan and A V Ramaswamy. Defect-site promoted surface reorganization in nanocrystalline ceria for the low-temperature activation of ethylbenzene. *Journal of the American Chemical Society*, 129(11):3062–3063, mar 2007. ISSN 0002-7863 (Print). doi: 10.1021/ja066834k. 17

[64] Javier Guzman, Silvio Carrettin, and Avelino Corma. Spectroscopic evidence for the supply of reactive oxygen during CO oxidation catalyzed by gold supported on nanocrystalline CeO2. *Journal of the American Chemical Society*, 127(10):3286–3287, mar 2005. ISSN 0002-7863 (Print). doi: 10.1021/ja043752s. 17

[65] Laurence Vivier and Daniel Duprez. Ceria-Based Solid Catalysts for Organic Chemistry. *ChemSusChem*, 3(6):654–678, jun 2010. ISSN 1864-5631. doi: https://doi.org/10.1002/cssc.201000054. 17

[66] Jurriaan Beckers and Gadi Rothenberg. Sustainable selective oxidations using ceria-based materials. *Green Chemistry*, 12(6):939–948, 2010. ISSN 1463-9262. doi: 10.1039/C000191K. 17

[67] J. Kašpar, P. Fornasiero, and M. Graziani. Use of CeO2-based oxides in the three-way catalysis. *Catalysis Today*, 50(2):285–298, apr 1999. ISSN 0920-5861. doi: 10.1016/S0920-5861(98)00510-0. 17

[68] E. Mamontov, T. Egami, R. Brezny, M. Koranne, and S. Tyagi. Lattice defects and oxygen storage capacity of nanocrystalline ceria and ceria-zirconia. *Journal of Physical Chemistry B*, 104(47):11110–11116, 2000. ISSN 15206106. doi: 10.1021/jp0023011. 17, 24, 26, 84, 148

[69] Zili Wu, Meijun Li, David R Mullins, and Steven H Overbury. Probing the Surface Sites of CeO2 Nanocrystals with Well-Defined Surface Planes via Methanol Adsorption and Desorption. *ACS Catalysis*, 2(11):2224–2234, nov 2012. doi: 10.1021/cs300467p. 17

[70] Xiangwen Liu, Kebin Zhou, Lei Wang, Baoyi Wang, and Yadong Li. Oxygen Vacancy Clusters Promoting Reducibility and Activity of Ceria Nanorods. *Journal of the American Chemical Society*, 131(9):3140–3141, mar 2009. ISSN 0002-7863. doi: 10.1021/ja808433d. 17, 18, 31, 34

[71] Friedrich Esch, Stefano Fabris, Ling Zhou, Tiziano Montini, Cristina Africh, Paolo Fornasiero, Giovanni Comelli, and Renzo Rosei. Electron Localization Determines Defect Formation on Ceria Substrates. *Science*, 309(5735):752–755, jul 2005. doi: 10.1126/science.1111568. 17, 18, 137

[72] M. Verónica Ganduglia-Pirovano, Alexander Hofmann, and Joachim Sauer. Oxygen vacancies in transition metal and rare earth oxides: Current state of understanding and remaining challenges. *Surface Science Reports*, 62(6):

219–270, jun 2007. ISSN 0167-5729. doi: 10.1016/J.SURFREP.2007.03.002. 17

[73] H. He, H. X. Dai, and C. T. Au. Defective structure, oxygen mobility, oxygen storage capacity, and redox properties of RE-based (RE = Ce, Pr) solid solutions. *Catalysis Today*, 90(3-4):245–254, jul 2004. ISSN 0920-5861. doi: 10.1016/J.CATTOD.2004.04.033. 17, 18

[74] Alessandro Trovarelli. *Catalysis By Ceria And Related Materials*. World Scientific Publishing Company, Singapore, SINGAPORE, 2002. ISBN 9781860949654. 18

[75] H Nörenberg and J H Harding. The surface structure of CeO2(001) single crystals studied by elevated temperature STM. *Surface Science*, 477(1):17–24, 2001. ISSN 0039-6028. doi: https://doi.org/10.1016/S0039-6028(01)00700-2. 18

[76] M. Ozawa and C. K. Loong. In situ X-ray and neutron powder diffraction studies of redox behavior in CeO2-containing oxide catalysts. *Catalysis Today*, 50(2):329–342, apr 1999. ISSN 0920-5861. doi: 10.1016/S0920-5861(98)00513-6. 18

[77] P Dutta, S Pal, M S Seehra, Y Shi, E M Eyring, and R D Ernst. Concentration of Ce3+ and Oxygen Vacancies in Cerium Oxide Nanoparticles. *Chemistry of Materials*, 18(21):5144–5146, oct 2006. ISSN 0897-4756. doi: 10.1021/cm061580n. 18, 31

[78] Felipe Polo-Garzon, Zhenghong Bao, Xuanyu Zhang, Weixin Huang, and Zili Wu. Surface Reconstructions of Metal Oxides and the Consequences on Catalytic Chemistry. *ACS Catalysis*, 9(6):5692–5707, jun 2019. doi: 10.1021/acscatal.9b01097. 18

[79] Zili Wu, Meijun Li, Jane Howe, Harry M Meyer, and Steven H Overbury. Probing Defect Sites on CeO2 Nanocrystals with Well-Defined Surface Planes by Raman Spectroscopy and O2 Adsorption. *Langmuir*, 26(21):16595–16606, nov 2010. ISSN 0743-7463. doi: 10.1021/la101723w. 18, 20, 151, 153

[80] Zhen-An Qiao, Zili Wu, and Sheng Dai. Shape-controlled ceria-based nanostructures for catalysis applications. *ChemSusChem*, 6(10):1821–1833, oct 2013. ISSN 1864-564X (Electronic). doi: 10.1002/cssc.201300428. 18

[81] Yuyuan Lin, Zili Wu, Jianguo Wen, Kenneth R Poeppelmeier, and Laurence D Marks. Imaging the Atomic Surface Structures of CeO2 Nanoparticles. *Nano Letters*, 14(1):191–196, jan 2014. ISSN 1530-6984. doi: 10.1021/nl403713b. 18

[82] Zili Wu, Meijun Li, and Steven H Overbury. On the structure dependence of CO oxidation over CeO2 nanocrystals with well-defined surface planes. *Journal of Catalysis*, 285(1):61–73, 2012. ISSN 0021-9517. doi: https://doi.org/10.1016/j.jcat.2011.09.011. 18

[83] Leon A Avakyan, Natalia A Kolpacheva, Ekaterina V Paramonova, Jagdeep Singh, Urs Hartfelder, Jeroen A van Bokhoven, and Lusegen A Bugaev. Evolution of the Atomic Structure of Ceria-Supported Platinum Nanocatalysts: Formation of Single Layer Platinum Oxide and Pt-O-Ce and Pt-Ce Linkages. *The Journal of Physical Chemistry C*, 120(49):28057–28066, dec 2016. ISSN 1932-7447. doi: 10.1021/acs.jpcc.6b09824. 18

[84] Jaeha Lee, YoungSeok Ryou, Xiaojun Chan, Tae Jin Kim, and Do Heui Kim. How Pt Interacts with CeO2 under the Reducing and Oxidizing Environments at Elevated Temperature: The Origin of Improved Thermal Stability of Pt/CeO2 Compared to CeO2. *The Journal of Physical Chemistry C*, 120(45):

25870–25879, nov 2016. ISSN 1932-7447. doi: 10.1021/acs.jpcc.6b08656. 18, 37, 40

[85] Wenyong Lin, A A Herzing, C J Kiely, and I E Wachs. Probing Metal Support Interactions under Oxidizing and Reducing Conditions: In Situ Raman and Infrared Spectroscopic and Scanning Transmission Electron Microscopic-X-ray Energy-Dispersive Spectroscopic Investigation of Supported Platinum Catalysts. *The Journal of Physical Chemistry C*, 112(15):5942–5951, apr 2008. ISSN 1932-7447. doi: 10.1021/jp710591m. 18

[86] Elizaveta A Derevyannikova, Tatyana Yu Kardash, Andrey I Stadnichenko, Olga A Stonkus, Elena M Slavinskaya, Valery A Svetlichnyi, and Andrei I Boronin. Structural Insight into Strong PtCeO2 Interaction: From Single Pt Atoms to PtOx Clusters. *The Journal of Physical Chemistry C*, 123(2):1320–1334, jan 2019. ISSN 1932-7447. doi: 10.1021/acs.jpcc.8b11009. 18

[87] Albert Bruix, José A Rodriguez, Pedro J Ramírez, Sanjaya D Senanayake, Jaime Evans, Joon B Park, Dario Stacchiola, Ping Liu, Jan Hrbek, and Francesc Illas. A New Type of Strong Metal–Support Interaction and the Production of H2 through the Transformation of Water on Pt/CeO2(111) and Pt/CeOx/TiO2(110) Catalysts. *Journal of the American Chemical Society*, 134(21):8968–8974, may 2012. ISSN 0002-7863. doi: 10.1021/ja302070k. 18

[88] April Russell and William S Epling. Diesel Oxidation Catalysts. *Catalysis Reviews*, 53(4):337–423, oct 2011. ISSN 0161-4940. doi: 10.1080/01614940.2011.596429. 18

[89] Tianxiao Wu, Xiqiang Pan, Yibo Zhang, Zhenzhen Miao, Bin Zhang, Jingwei Li, and Xiangguang Yang. Investigation of the Redispersion of Pt Nanoparticles on Polyhedral Ceria Nanoparticles. *The Journal of Physical Chemistry Letters*, 5(14):2479–2483, jul 2014. doi: 10.1021/jz500839u. 19

[90] Hao-Xin Mai, Ling-Dong Sun, Ya-Wen Zhang, Rui Si, Wei Feng, Hong-Peng Zhang, Hai-Chao Liu, and Chun-Hua Yan. Shape-Selective Synthesis and Oxygen Storage Behavior of Ceria Nanopolyhedra, Nanorods, and Nanocubes. *The Journal of Physical Chemistry B*, 109(51):24380–24385, dec 2005. ISSN 1520-6106. doi: 10.1021/jp055584b. 20

[91] Lai Yan, Ranbo Yu, Jun Chen, and Xianran Xing. Template-Free Hydrothermal Synthesis of CeO2 Nano-octahedrons and Nanorods: Investigation of the Morphology Evolution. *Crystal Growth and Design*, 8(5):1474–1477, may 2008. ISSN 1528-7483. doi: 10.1021/cg800117v. 20

[92] Nina Perkas, Hadar Rotter, Leonid Vradman, Miron V Landau, and Aharon Gedanken. Sonochemically Prepared Pt/CeO2 and Its Application as a Catalyst in Ethyl Acetate Combustion. *Langmuir*, 22(16):7072–7077, aug 2006. ISSN 0743-7463. doi: 10.1021/la0600907. 20

[93] Piboon Pantu and George R Gavalas. Methane partial oxidation on Pt/CeO2 and Pt/Al2O3 catalysts. *Applied Catalysis A: General*, 223(1):253–260, 2002. ISSN 0926-860X. doi: https://doi.org/10.1016/S0926-860X(01)00761-X. 20

[94] Ya Dong Bi, Wei Zhang, Heng Yong Xu, and Wen Zhao Li. Nanocrystalline CeO2 in SBA-15: Performance of Pt/CeO2/SBA-15 Catalyst for Water-gas-shift Reaction. *Catalysis Letters*, 119(1):126–133, 2007. ISSN 1572-879X. doi: 10.1007/s10562-007-9209-3. 20

[95] Jörg Neuefeind, Mikhail Feygenson, John Carruth, Ron Hoffmann, and Kenneth K. Chipley. The Nanoscale Ordered MAterials Diffractometer NOMAD at the Spallation Neutron Source SNS. *Nuclear Instruments and Methods in Physics Research, Section B: Beam Interactions with Materials and Atoms*, 287:68–75, 2012. ISSN 0168583X. doi: 10.1016/j.nimb.2012.05.037. 20, 52, 143

[96] Daniel Olds, Katharine Page, Arnold Paecklar, Peter F. Peterson, Jue Liu, Gerald Rucker, Mariano Ruiz-Rodriguez, Michael Olsen, Michelle Pawel, Steven H. Overbury, and James R. Neilson. A high precision gas flow cell for performing in situ neutron studies of local atomic structure in catalytic materials. *Review of Scientific Instruments*, 88(3), 2017. ISSN 10897623. doi: 10.1063/1.4978287. 20

[97] Katharine Page, Claire E. White, Eben G. Estell, Reinhard B. Neder, Anna Llobet, and Thomas Proffen. Treatment of hydrogen background in bulk and nanocrystalline neutron total scattering experiments. *Journal of Applied Crystallography*, 44(3):532–539, 2011. ISSN 00218898. doi: 10.1107/S0021889811001609. 21, 56

[98] László Temleitner, Anne Stunault, Gabriel J. Cuello, and László Pusztai. Neutron diffraction of hydrogenous materials: Measuring incoherent and coherent intensities separately. *Physical Review B - Condensed Matter and Materials Physics*, 92(1):1–6, 2015. ISSN 1550235X. doi: 10.1103/PhysRevB.92.014201. 21, 56

[99] Anton Gagin and Igor Levin. A Bayesian approach to removal of incoherent scattering from neutron total-scattering data. *Journal of Applied Crystallography*, 47(6):2060–2068, 2014. ISSN 16005767. doi: 10.1107/S1600576714023796. 21, 56

[100] Peter F. Peterson, Daniel Olds, Marshall T. McDonnell, and Katharine Page. Illustrated formalisms for total scattering data: a guide for new practitioners. *Journal of Applied Crystallography*, 54(1):317–332, 2021. ISSN 1600-5767. doi: 10.1107/s1600576720015630. 23, 56

[101] Rafael Schmitt, Andreas Nenning, Olga Kraynis, Roman Korobko, Anatoly I. Frenkel, Igor Lubomirsky, Sossina M. Haile, and Jennifer L.M. Rupp. A review of defect structure and chemistry in ceria and its solid solutions.

Chemical Society Reviews, 49(2):554–592, 2020. ISSN 14604744. doi: 10.1039/c9cs00588a. 24, 84, 148

[102] E. Mamontov and T. Egami. Structural defects in a nano-scale powder of CeO2 studied by pulsed neutron diffraction. *Journal of Physics and Chemistry of Solids*, 61(8):1345–1356, 2000. ISSN 00223697. doi: 10.1016/S0022-3697(00)00003-2. 26

[103] Alan A. Coelho. TOPAS and TOPAS-Academic: An optimization program integrating computer algebra and crystallographic objects written in C++: An. *Journal of Applied Crystallography*, 51(1):210–218, 2018. ISSN 16005767. doi: 10.1107/S1600576718000183. 26, 56, 80, 143, 144

[104] Daniel Olds, Hsiu Wen Wang, and Katharine Page. DShaper: An approach for handling missing low-Q data in pair distribution function analysis of nanostructured systems. *Journal of Applied Crystallography*, 48:1651–1659, 2015. ISSN 16005767. doi: 10.1107/S1600576715016581. 26

[105] C. L. Farrow, P. Juhas, J. W. Liu, D. Bryndin, E. S. Boin, J. Bloch, Th Proffen, and S. J.L. Billinge. PDFfit2 and PDFgui: computer programs for studying nanostructure in crystals. *Journal of Physics: Condensed Matter*, 19(33): 335219, jul 2007. ISSN 0953-8984. doi: 10.1088/0953-8984/19/33/335219. 27

[106] Sameer Arun Deshpande, Swanand D Patil, Satyanarayana Vnt Kuchibhatla, and S Seal. Size dependency variation in lattice parameter and valency states in nanocrystalline cerium oxide. *Applied Physics Letters*, 87:133113, 2005. 31, 149

[107] Tedi Marie Usher, Daniel Olds, Jue Liu, and Katharine Page. A numerical method for deriving shape functions of nanoparticles for pair distribution function refinements. *Acta Crystallographica Section A: Foundations and*

Advances, 74(4):322–331, 2018. ISSN 20532733. doi: 10.1107/S2053273318004977. 31

[108] S Tsunekawa, R Sivamohan, S Ito, A Kasuya, and T Fukuda. Structural study on monosize CeO2-x nano-particles. *Nanostructured Materials*, 11(1):141–147, 1999. ISSN 0965-9773. doi: https://doi.org/10.1016/S0965-9773(99)00027-6. 31

[109] Feng Zhang, Qiang Jin, and Siu-Wai Chan. Ceria nanoparticles: Size, size distribution, and shape. *Journal of Applied Physics*, 95(8):4319–4326, mar 2004. ISSN 0021-8979. doi: 10.1063/1.1667251. 31

[110] Xuefei Wan, Daniel Goberman, Leon L Shaw, Guangshun Yi, and Gan-Moog Chow. Valence states of nanocrystalline Ceria under combined effects of hydrogen reduction and particle size. *Applied Physics Letters*, 96(12):123108, mar 2010. ISSN 0003-6951. doi: 10.1063/1.3371687. 31

[111] E A Kummerle and G Heger. The Structures of C-Ce2O3+δ, Ce7O12, and Ce11O20. *Journal of Solid State Chemistry*, 147(2):485–500, 1999. ISSN 0022-4596. doi: https://doi.org/10.1006/jssc.1999.8403. 37, 154

[112] Yasutaka Nagai, Takeshi Hirabayashi, Kazuhiko Dohmae, Nobuyuki Takagi, Takashi Minami, Hirofumi Shinjoh, and Shin'ichi Matsumoto. Sintering inhibition mechanism of platinum supported on ceria-based oxide and Pt-oxide–support interaction. *Journal of Catalysis*, 242(1):103–109, aug 2006. ISSN 0021-9517. doi: 10.1016/J.JCAT.2006.06.002. 40

[113] Jaeha Lee, YoungSeok Ryou, Jonghyun Kim, Xiaojun Chan, Tae Jin Kim, and Do Heui Kim. Influence of the Defect Concentration of Ceria on the Pt Dispersion and the CO Oxidation Activity of Pt/CeO2. *The Journal of Physical Chemistry C*, 122(9):4972–4983, mar 2018. ISSN 1932-7447. doi: 10.1021/acs.jpcc.8b00254. 40

[114] T V Choudhary, S Banerjee, and V R Choudhary. Catalysts for combustion of methane and lower alkanes. *Applied Catalysis A: General*, 234(1):1–23, 2002. ISSN 0926-860X. doi: https://doi.org/10.1016/S0926-860X(02)00231-4. 49

[115] Yuan Shu, Mengyao Wang, Xiaolan Duan, Dandan Liu, Shize Yang, and Pengfei Zhang. Low-temperature total oxidation of methane by pore- and vacancy-engineered NiO catalysts. *AIChE Journal*, 68(6):e17664, 2022. doi: https://doi.org/10.1002/aic.17664. 49

[116] Yuan Gao, Mingxin Jiang, Liuqingqing Yang, Zhuo Li, Fei-Xiang Tian, and Yulian He. Recent progress of catalytic methane combustion over transition metal oxide catalysts. *Frontiers in chemistry*, 10:959422, 2022. ISSN 2296-2646 (Print). doi: 10.3389/fchem.2022.959422. 49

[117] Benjamin Hmiel, V V Petrenko, M N Dyonisius, C Buizert, A M Smith, P F Place, C Harth, R Beaudette, Q Hua, B Yang, I Vimont, S E Michel, J P Severinghaus, D Etheridge, T Bromley, J Schmitt, X Faïn, R F Weiss, and E Dlugokencky. Preindustrial 14CH4 indicates greater anthropogenic fossil CH4 emissions. *Nature*, 578(7795):409–412, 2020. ISSN 1476-4687. doi: 10.1038/s41586-020-1991-8. 49

[118] Li He, Yilin Fan, Jérôme Bellettre, Jun Yue, and Lingai Luo. A review on catalytic methane combustion at low temperatures: Catalysts, mechanisms, reaction conditions and reactor designs. *Renewable and Sustainable Energy Reviews*, 119:109589, 2020. ISSN 1364-0321. doi: https://doi.org/10.1016/j.rser.2019.109589. 49

[119] R Burch and F J Urbano. Investigation of the active state of supported palladium catalysts in the combustion of methane. *Applied Catalysis A: General*, 124(1):121–138, 1995. ISSN 0926-860X. doi: https://doi.org/10.1016/0926-860X(94)00252-5. 49

[120] Jinghuan Chen, Hamidreza Arandiyan, Xiang Gao, and Junhua Li. Recent Advances in Catalysts for Methane Combustion. *Catalysis Surveys from Asia*, 19(3):140–171, 2015. ISSN 1574-9266. doi: 10.1007/s10563-015-9191-5. 49

[121] José A Rodriguez, David C Grinter, Zongyuan Liu, Robert M Palomino, and Sanjaya D Senanayake. Ceria-based model catalysts: fundamental studies on the importance of the metal–ceria interface in CO oxidation, the water–gas shift, CO2 hydrogenation, and methane and alcohol reforming. *Chem. Soc. Rev.*, 46(7):1824–1841, 2017. doi: 10.1039/C6CS00863A. 49

[122] M Cargnello, J J Delgado Jaén, J C Hernández Garrido, K Bakhmutsky, T Montini, J J Calvino Gámez, R J Gorte, and P Fornasiero. Exceptional activity for methane combustion over modular Pd@CeO2 subunits on functionalized Al2O3. *Science (New York, N.Y.)*, 337(6095):713–717, aug 2012. ISSN 1095-9203 (Electronic). doi: 10.1126/science.1222887. 49

[123] F Arosio, S Colussi, A Trovarelli, and G Groppi. Effect of alternate CH4-reducing/lean combustion treatments on the reactivity of fresh and S-poisoned Pd/CeO2/Al2O3 catalysts. *Applied Catalysis B: Environmental*, 80(3):335–342, 2008. ISSN 0926-3373. doi: https://doi.org/10.1016/j.apcatb.2007.11.030. 49, 50

[124] Patrick Gélin and Michel Primet. Complete oxidation of methane at low temperature over noble metal based catalysts: a review. *Applied Catalysis B: Environmental*, 39(1):1–37, 2002. ISSN 0926-3373. doi: https://doi.org/10.1016/S0926-3373(02)00076-0. 49

[125] Jordan K Lampert, M Shahjahan Kazi, and Robert J Farrauto. Palladium catalyst performance for methane emissions abatement from lean burn natural gas vehicles. *Applied Catalysis B: Environmental*, 14(3):211–223,

1997. ISSN 0926-3373. doi: https://doi.org/10.1016/S0926-3373(97)00024-6. 49

[126] Sara Colussi, Arup Gayen, Matteo F. Camellone, Marta Boaro, Jordi Llorca, Stefano Fabris, and Alessandro Trovarelli. Nanofaceted PdO Sites in PdCe Surface Superstructures: Enhanced Activity in Catalytic Combustion of Methane. *Angewandte Chemie International Edition*, 48(45):8481–8484, 2009. doi: https://doi.org/10.1002/anie.200903581. 49

[127] Maila Danielis, Sara Colussi, Carla de Leitenburg, Lluís Soler, Jordi Llorca, and Alessandro Trovarelli. Outstanding Methane Oxidation Performance of Palladium-Embedded Ceria Catalysts Prepared by a One-Step Dry Ball-Milling Method. *Angewandte Chemie International Edition*, 57(32):10212–10216, 2018. doi: https://doi.org/10.1002/anie.201805929. 49

[128] Baohua Yue, Renxian Zhou, Yuejuan Wang, and Xiaoming Zheng. Study of the methane combustion and TPR/TPO properties of Pd/Ce–Zr–M/Al2O3 catalysts with M=Mg, Ca, Sr, Ba. *Journal of Molecular Catalysis A: Chemical*, 238(1):241–249, 2005. ISSN 1381-1169. doi: https://doi.org/10.1016/j.molcata.2005.05.027. 49

[129] Tongfei Li, Sulin Li, Qianyu Liu, Yechao Tian, Yiwei Zhang, Gengtao Fu, and Yawen Tang. Hollow Co3O4/CeO2 Heterostructures in Situ Embedded in N-Doped Carbon Nanofibers Enable Outstanding Oxygen Evolution. *ACS Sustainable Chemistry and Engineering*, 7(21):17950–17957, nov 2019. doi: 10.1021/acssuschemeng.9b04699. 49, 93, 137

[130] Guohui Cai, Wei Luo, Yihong Xiao, Yong Zheng, Fulan Zhong, Yingying Zhan, and Lilong Jiang. Synthesis of a Highly Stable Pd@CeO2 Catalyst for Methane Combustion with the Synergistic Effect of Urea and Citric Acid. *ACS Omega*, 3(12):16769–16776, dec 2018. doi: 10.1021/acsomega.8b02556. 49

[131] Yuanqing Ding, Qingqing Wu, Bo Lin, Yanglong Guo, Yun Guo, Yunsong Wang, Li Wang, and Wangcheng Zhan. Superior catalytic activity of a Pd catalyst in methane combustion by fine-tuning the phase of ceria-zirconia support. *Applied Catalysis B: Environmental*, 266:118631, 2020. ISSN 0926-3373. doi: 10.1016/j.apcatb.2020.118631. 49, 50

[132] Alessandro Trovarelli, Francesca Zamar, Jordi Llorca, Carla de Leitenburg, Giuliano Dolcetti, and Janos T Kiss. Nanophase Fluorite-Structured CeO2–ZrO2Catalysts Prepared by High-Energy Mechanical Milling. *Journal of Catalysis*, 169(2):490–502, 1997. ISSN 0021-9517. doi: https://doi.org/10.1006/jcat.1997.1705. 49

[133] Alessandra Toso, Sara Colussi, Shiva Padigapaty, Carla de Leitenburg, and Alessandro Trovarelli. High stability and activity of solution combustion synthesized Pd-based catalysts for methane combustion in presence of water. *Applied Catalysis B: Environmental*, 230:237–245, 2018. ISSN 0926-3373. doi: https://doi.org/10.1016/j.apcatb.2018.02.049. 50

[134] A Iglesias-Juez, A Martínez-Arias, and M Fernández-García. Metal–promoter interface in Pd/(Ce,Zr)Ox/Al2O3 catalysts: effect of thermal aging. *Journal of Catalysis*, 221(1):148–161, 2004. ISSN 0021-9517. doi: https://doi.org/10.1016/j.jcat.2003.07.010. 50

[135] Anand S Burange, Kasala Prabhakar Reddy, Chinnakonda S Gopinath, Rakesh Shukla, and Avesh K Tyagi. Role of palladium crystallite size on CO oxidation over CeZrO4-δ supported Pd catalysts. *Molecular Catalysis*, 455: 1–5, 2018. ISSN 2468-8231. doi: https://doi.org/10.1016/j.mcat.2018.05.021. 50

[136] Andrey W Petrov, Davide Ferri, Frank Krumeich, Maarten Nachtegaal, Jeroen A van Bokhoven, and Oliver Kröcher. Stable complete methane oxidation over palladium based zeolite catalysts. *Nature Communications*,

9(1):2545, 2018. ISSN 2041-1723. doi: 10.1038/s41467-018-04748-x. 50, 51

[137] Andreas Gremminger, Patrick Lott, Menno Merts, Maria Casapu, Jan-Dierk Grunwaldt, and Olaf Deutschmann. Sulfur poisoning and regeneration of bimetallic Pd-Pt methane oxidation catalysts. *Applied Catalysis B: Environmental*, 218:833–843, 2017. ISSN 0926-3373. doi: https://doi.org/10.1016/j.apcatb.2017.06.048. 50

[138] Daniel Olds, Rebecca A. Mills, Marshall T. McDonnell, Jue Liu, Joshua R. Kim, Matthew T. Dunstan, Michael W. Gaultois, S. Michelle Everett, Matthew G. Tucker, and Katharine Page. A high temperature gas flow environment for neutron total scattering studies of complex materials. *Review of Scientific Instruments*, 89(9), 2018. ISSN 10897623. doi: 10.1063/1.5033464. 51

[139] C L Farrow, P Juhas, J W Liu, D Bryndin, E S Božin, J Bloch, Th Proffen, and S J L Billinge. PDFfit2 and PDFgui: computer programs for studying nanostructure in crystals. *Journal of Physics: Condensed Matter*, 19(33): 335219, 2007. ISSN 0953-8984. doi: 10.1088/0953-8984/19/33/335219. 57, 144

[140] Masatomo Yashima, Kenji Morimoto, Nobuo Ishizawa, and Masahiro Yoshimura. Diffusionless Tetragonal–Cubic Transformation Temperature in Zirconia–Ceria Solid Solutions. *Journal of the American Ceramic Society*, 76(11):2865–2868, 1993. doi: https://doi.org/10.1111/j.1151-2916.1993.tb04028.x. 57, 58, 60

[141] Masatomo Yashima, Haruo Arashi, Masato Kakihana, and Masahiro Yoshimura. Raman Scattering Study of Cubic–Tetragonal Phase Transition in Zr1−xCexO2 Solid Solution. *Journal of the American Ceramic Society*,

77(4):1067–1071, 1994. doi: https://doi.org/10.1111/j.1151-2916.1994.tb07270.x. 57, 58, 60

[142] Takahiro Wakita and Masatomo Yashima. In situ observation of the tetragonal-cubic phase transition in the CeZrO4 solid solution–a high-temperature neutron diffraction study. *Acta crystallographica. Section B, Structural science*, 63(Pt 3):384–389, jun 2007. ISSN 0108-7681 (Print). doi: 10.1107/S0108768107007720. 57, 58, 60

[143] Sasaki Tsuyoshi, Yoshio Usko, Suda Akihiko, Suguira Masahiro, Kotaro Kuroda, Shigeo Arai, and Hiroyasu Saka. Oxygen Absorption Behavior of Ce2Zr2O7+x and Formation of Ce2Zr2O7.5. *Journal of the Ceramic Society of Japan*, 11(1294):382–385, 2003. 57, 66, 71

[144] S Nagabhusan Achary, Sanjay K Sali, Narendra K Kulkarni, P Siva Ram Krishna, Anil B Shinde, and Avesh K Tyagi. Intercalation/Deintercalation of Oxygen: A Sequential Evolution of Phases in Ce2O3/CeO2−ZrO2 Pyrochlores. *Chemistry of Materials*, 21(24):5848–5859, dec 2009. ISSN 0897-4756. doi: 10.1021/cm902450q. URL https://doi.org/10.1021/cm902450q. 57

[145] Alexander N Shmakov, Svetlana V Cherepanova, Dmitrii A Zyuzin, Yulia E Fedorova, Ivan A Bobrikov, Anne-Cecile Roger, Andrzej Adamski, and Vladislav A Sadykov. The crystal structure of compositionally homogeneous mixed ceria-zirconia oxides by high resolution X-ray and neutron diffraction methods. *Open Chemistry*, 15(1):438–445, 2017. doi: doi:10.1515/chem-2017-0044. 66

[146] Haruo Kishimoto, Takahisa Omata, Shinya Otsuka-Yao-Matsuo, Kazushige Ueda, Hideo Hosono, and Hiroshi Kawazoe. Crystal structure of metastable κ-CeZrO4 phase possessing an ordered arrangement of Ce and Zr ions.

Journal of Alloys and Compounds, 312(1):94–103, 2000. ISSN 0925-8388. doi: https://doi.org/10.1016/S0925-8388(00)01168-3. 66

[147] Yoshio UKYO, Kae YAMAMURA, Hideo SOBUKAWA, Tsuyoshi Sasaki, Yasutaka Nagai, Toshitaka Tanabe, and Masahiro Sugiura. Effect of Ordered Arrangement of Ce and Zr Ions on Oxygen Storage Capacity of Ceria-Zirconia Solid Solution. *Journal of The Ceramic Society of Japan - J CERAMIC SOC JPN*, 112:586–589, 2004. doi: 10.2109/jcersj.112.586. 71

[148] Xue Zhi Song, Wen Yu Zhu, Xiao Feng Wang, and Zhenquan Tan. Recent Advances of CeO2-Based Electrocatalysts for Oxygen and Hydrogen Evolution as well as Nitrogen Reduction. *ChemElectroChem*, 8(6):996–1020, 2021. ISSN 21960216. doi: 10.1002/celc.202001614. 76, 77, 78, 137, 139

[149] Qingqing Li, Lianpeng Song, Zhong Liang, Mingzi Sun, Tong Wu, Bolong Huang, Feng Luo, Yaping Du, and Chun-Hua Yan. A Review on Ceo2-Based Electrocatalyst and Photocatalyst in Energy Conversion. *Advanced Energy and Sustainability Research*, 2(2):2000063, 2021. doi: https://doi.org/10.1002/aesr.202000063. 76, 137

[150] Alberto Bucci, Miguel García-Tecedor, Sacha Corby, Reshma R Rao, Vlad Martin-Diaconescu, Freddy E Oropeza, Víctor A de la Peña O'Shea, James R Durrant, Sixto Giménez, and Julio Lloret-Fillol. Self-supported ultra-active NiO-based electrocatalysts for the oxygen evolution reaction by solution combustion. *J. Mater. Chem. A*, 9(21):12700–12710, 2021. doi: 10.1039/D1TA00072A. 76

[151] Nian-Tzu Suen, Sung-Fu Hung, Quan Quan, Nan Zhang, Yi-Jun Xu, and Hao Ming Chen. Electrocatalysis for the oxygen evolution reaction: recent development and future perspectives. *Chem. Soc. Rev.*, 46(2):337–365, 2017. doi: 10.1039/C6CS00328A. 76, 137

[152] Sehkyu Park, Yuyan Shao, Jun Liu, and Yong Wang. Oxygen electrocatalysts for water electrolyzers and reversible fuel cells: status and perspective. *Energy Environ. Sci.*, 5(11):9331–9344, 2012. doi: 10.1039/C2EE22554A. 76, 137

[153] Ashalatha Vazhayil, Linsha Vazhayal, Jasmine Thomas, Shyamli Ashok C, and Nygil Thomas. A comprehensive review on the recent developments in transition metal-based electrocatalysts for oxygen evolution reaction. *Applied Surface Science Advances*, 6:100184, 2021. ISSN 2666-5239. doi: https://doi.org/10.1016/j.apsadv.2021.100184. 76

[154] Fang Song, Lichen Bai, Aliki Moysiadou, Seunghwa Lee, Chao Hu, Laurent Liardet, and Xile Hu. Transition Metal Oxides as Electrocatalysts for the Oxygen Evolution Reaction in Alkaline Solutions: An Application-Inspired Renaissance. *Journal of the American Chemical Society*, 140(25):7748–7759, jun 2018. ISSN 0002-7863. doi: 10.1021/jacs.8b04546. 76

[155] Bryan M Hunter, Harry B Gray, and Astrid M Müller. Earth-Abundant Heterogeneous Water Oxidation Catalysts. *Chemical Reviews*, 116(22): 14120–14136, nov 2016. ISSN 0009-2665. doi: 10.1021/acs.chemrev.6b00398. 76

[156] Jiangtian Li, Deryn Chu, David R Baker, Asher Leff, Peng Zheng, and Rongzhong Jiang. Earth-Abundant Fe and Ni Dually Doped Co2P for Superior Oxygen Evolution Reactivity and as a Bifunctional Electrocatalyst toward Renewable Energy-Powered Overall Alkaline Water Splitting. *ACS Applied Energy Materials*, 4(9):9969–9981, sep 2021. doi: 10.1021/acsaem.1c01926. 76

[157] Jiajia Song, Chao Wei, Zhen-Feng Huang, Chuntai Liu, Lin Zeng, Xin Wang, and Zhichuan J Xu. A review on fundamentals for designing oxygen

evolution electrocatalysts. *Chem. Soc. Rev.*, 49(7):2196–2214, 2020. doi: 10.1039/C9CS00607A. 76

[158] Zhaohui Xiao, Yu-Cheng Huang, Chung-Li Dong, Chao Xie, Zhijuan Liu, Shiqian Du, Wei Chen, Dafeng Yan, Li Tao, Zhiwen Shu, Guanhua Zhang, Huigao Duan, Yanyong Wang, Yuqin Zou, Ru Chen, and Shuangyin Wang. Operando Identification of the Dynamic Behavior of Oxygen Vacancy-Rich Co3O4 for Oxygen Evolution Reaction. *Journal of the American Chemical Society*, 142(28):12087–12095, jul 2020. ISSN 0002-7863. doi: 10.1021/jacs.0c00257. 77, 97, 162

[159] Chanqin Duan, Xinglong Li, Dan Wang, Zhiyuan Wang, Hongyu Sun, Runguo Zheng, and Yanguo Liu. Nanosized high entropy spinel oxide (FeCoNiCrMn)3O4 as a highly active and ultra-stable electrocatalyst for the oxygen evolution reaction. *Sustainable Energy Fuels*, 6(6):1479–1488, 2022. doi: 10.1039/D1SE02038B. 77, 138, 139

[160] Mauro Coduri, Stefano Checchia, Mariangela Longhi, Davide Ceresoli, and Marco Scavini. Rare Earth Doped Ceria: The Complex Connection Between Structure and Properties. *Frontiers in Chemistry*, 6, 2018. ISSN 2296-2646. doi: 10.3389/fchem.2018.00526. 77, 84, 137, 139, 148, 149

[161] U Aarthi, Dhananjaya Shukla, S Rengaraj, and K Suresh Babu. Ordered to defect fluorite structural transition in Ce1-xNdxO2-δ system and its influence on ionic conductivity. *Journal of Alloys and Compounds*, 838:155534, 2020. ISSN 0925-8388. doi: https://doi.org/10.1016/j.jallcom.2020.155534. 77, 148

[162] R D Shannon and C T Prewitt. Effective ionic radii in oxides and fluorides. *Acta Crystallographica Section B*, 25(5):925–946, may 1969. doi: 10.1107/S0567740869003220. 84, 149

[163] R D Shannon. Revised effective ionic radii and systematic studies of interatomic distances in halides and chalcogenides. *Acta Crystallographica Section A*, 32(5):751–767, sep 1976. doi: 10.1107/S0567739476001551. 84, 149

[164] Carmelo Giacovazzo, Hugo Monaco Luis, Gilberto Artioli, Davide Viterbo, Marco Milanesio, Gastone Gilli, Paola Gilli, Giuseppe Zanotti, and Giovanni Ferraris. Fundamentals of crystallography. *Acta Crystallographica Section A*, 49:373–374, 1993. 84, 149

[165] Longkang Cong, Shouyang Zhang, Shengyue Gu, and Wei Li. Thermophysical properties of a novel high entropy hafnate ceramic. *Journal of Materials Science and Technology*, 85:152–157, 2021. ISSN 10050302. doi: 10.1016/j.jmst.2021.02.005. 85, 150

[166] Elizabeth A. Cochran, Keenan N. Woods, Darren W. Johnson, Catherine J. Page, and Shannon W. Boettcher. Unique chemistries of metal-nitrate precursors to form metal-oxide thin films from solution: Materials for electronic and energy applications. *Journal of Materials Chemistry A*, 7(42): 24124–24149, 2019. ISSN 20507496. doi: 10.1039/c9ta07727h. 85

[167] Konstantin I Maslakov, Yury A Teterin, Aleksej J Popel, Anton Yu. Teterin, Kirill E Ivanov, Stepan N Kalmykov, Vladimir G Petrov, Peter K Petrov, and Ian Farnan. XPS study of ion irradiated and unirradiated CeO2 bulk and thin film samples. *Applied Surface Science*, 448:154–162, 2018. ISSN 0169-4332. doi: https://doi.org/10.1016/j.apsusc.2018.04.077. 87

[168] Yan Zhu, Nikhil Jain, Mantu Hudait, Deepam Maurya, Ronnie Varghese, and S.Jeba Priya. X-ray photoelectron spectroscopy analysis and band offset determination of CeO2 deposited on epitaxial (100), (110), and (111)Ge. *Journal of vacuum science and technology. B, Microelectronics and nanometer*

structures: processing, measurement, and phenomena: an official journal of the American Vacuum Society, 32:–, 2014. doi: 10.1116/1.4862160. 87

[169] Thi Xuyen Nguyen, Yi-Cheng Liao, Chia-Chun Lin, Yen-Hsun Su, and Jyh-Ming Ting. Advanced High Entropy Perovskite Oxide Electrocatalyst for Oxygen Evolution Reaction. *Advanced Functional Materials*, 31(27): 2101632, 2021. doi: https://doi.org/10.1002/adfm.202101632. 87, 90, 155, 157

[170] Jiali Zhao, Chen Liu, Jinmei Li, Rui Wu, Jiaou Wang, Haijie Qian, Haizhong Guo, Jiankun Li, and Kurash Ibrahim. Oxygen vacancy induced electronic structure variation in the La0.2Sr0.8MnO3 thin film. *AIP Advances*, 9(5): 55208, 2019. doi: 10.1063/1.5088738. 87, 88

[171] Fermin H Aragón, Ismael Gonzalez, José. A H Coaquira, Pilar Hidalgo, Hermi F Brito, José. D Ardisson, Waldemar A A Macedo, and Paulo C Morais. Structural and Surface Study of Praseodymium-Doped SnO2 Nanoparticles Prepared by the Polymeric Precursor Method. *The Journal of Physical Chemistry C*, 119(16):8711–8717, apr 2015. ISSN 1932-7447. doi: 10.1021/acs.jpcc.5b00761. 87, 156

[172] D. D. Koelling, A. M. Boring, and J. H. Wood. The electronic structure of CeO2 and PrO2. *Solid State Communications*, 47(4):227–232, jul 1983. ISSN 0038-1098. doi: 10.1016/0038-1098(83)90550-1. 87, 156

[173] Helena Brunckova, Hristo Kolev, and Maria Kanuchova. X-ray photoelectron spectroscopy study of neodymium niobate and tantalate precursors and thin films. *Surface and Interface Analysis*, 51(3):326–335, 2019. doi: https://doi.org/10.1002/sia.6583. 87, 139, 156

[174] John P Baltrus and Murphy J Keller. Rare earth oxides Eu2O3 and Nd2O3 analyzed by XPS. *Surface Science Spectra*, 26(1):14001, 2019. doi: 10.1116/1.5085768. 87, 139, 156

[175] John F Moulder, William F Stickle, Warren M Sobol, and Kenneth D Bomben. Handbook of X-Ray Photoelectron Spectroscopy. In *Handbook of X-ray Photoelectron Spectroscopy: A Reference Book of Standard Spectra for Identification and Interpretation of XPS Data*, 1992. 87, 139, 156

[176] G Blanco, J M Pintado, S Bernal, M A Cauqui, M P Corchado, A Galtayries, J Ghijsen, R Sporken, T Eickhoff, and W Drube. Influence of the nature of the noble metal (Rh,Pt) on the low-temperature reducibility of a Ce/Tb mixed oxide with application as TWC component. *Surface and Interface Analysis*, 34 (1):120–124, 2002. doi: https://doi.org/10.1002/sia.1266. 88, 156

[177] Yushuang Zhao, Ji-Guang Li, Mengxi Guo, and Xiaojing Yang. Structural and photoluminescent investigation of LTbH/LEuH nanosheets and their color-tunable colloidal hybrids. *J. Mater. Chem. C*, 1(22):3584–3592, 2013. doi: 10.1039/C3TC30205A. 88

[178] Vassilis Tangoulis, Nikolia Lalioti, John Parthenios, Nikos Boukos, Ondřej Malina, Jiří Tuček, and Radek Zbořil. Noncovalent Grafting of a DyIII2 Single-Molecule Magnet onto Chemically Modified Multiwalled Carbon Nanotubes. *Inorganic Chemistry*, 57(11):6391–6400, jun 2018. ISSN 0020-1669. doi: 10.1021/acs.inorgchem.8b00472. 88, 139, 156

[179] Yolimar Gil, Raquel Gimeno-Muñoz, Ricardo Costa de Santana, Núria Aliaga-Alcalde, Pablo Fuentealba, Daniel Aravena, Arántzazu González-Campo, and Evgenia Spodine. Luminescence of Macrocyclic Mononuclear DyIII Complexes and Their Immobilization on Functionalized Silicon-Based Surfaces. *Inorganic Chemistry*, 61(41):16347–16355, oct 2022. ISSN 0020-1669. doi: 10.1021/acs.inorgchem.2c02342. 88

[180] Yi Wang, Jinxing Mi, and Zhong-Shuai Wu. Recent status and challenging perspective of high entropy oxides for chemical catalysis. *Chem Catalysis*, 2 (7):1624–1656, jul 2022. ISSN 2667-1107. doi: 10.1016/j.checat.2022.05.003. 88, 138

[181] Bin Hua, Ya-Qian Zhang, Ning Yan, Meng Li, Yi-Fei Sun, Jian Chen, Jian Li, and Jing-Li Luo. The Excellence of Both Worlds: Developing Effective Double Perovskite Oxide Catalyst of Oxygen Reduction Reaction for Room and Elevated Temperature Applications. *Advanced Functional Materials*, 26 (23):4106–4112, 2016. doi: https://doi.org/10.1002/adfm.201600339. 88, 156

[182] Lina Tang, Yanling Yang, Hongquan Guo, Yue Wang, Mengjie Wang, Zuoqing Liu, Guangming Yang, Xianzhu Fu, Yang Luo, Chenxing Jiang, Yingru Zhao, Zongping Shao, and Yifei Sun. High Configuration Entropy Activated Lattice Oxygen for O2 Formation on Perovskite Electrocatalyst. *Advanced Functional Materials*, 32(28):2112157, 2022. doi: https://doi.org/10.1002/adfm.202112157. 88, 156

[183] Yinlong Zhu, Wei Zhou, Jie Yu, Yubo Chen, Meilin Liu, and Zongping Shao. Enhancing Electrocatalytic Activity of Perovskite Oxides by Tuning Cation Deficiency for Oxygen Reduction and Evolution Reactions. *Chemistry of Materials*, 28(6):1691–1697, mar 2016. ISSN 0897-4756. doi: 10.1021/acs.chemmater.5b04457. 90, 157

[184] Michele Pavone, Andrew M Ritzmann, and Emily A Carter. Quantum-mechanics-based design principles for solid oxide fuel cell cathode materials. *Energy Environ. Sci.*, 4(12):4933–4937, 2011. doi: 10.1039/C1EE02377B. 90

[185] Tridip Das, Jason D Nicholas, and Yue Qi. Long-range charge transfer and oxygen vacancy interactions in strontium ferrite. *J. Mater. Chem. A*, 5(9): 4493–4506, 2017. doi: 10.1039/C6TA10357J. 90

[186] Tridip Das, Jason D Nicholas, and Yue Qi. Polaron size and shape effects on oxygen vacancy interactions in lanthanum strontium ferrite. *J. Mater. Chem. A*, 5(47):25031–25043, 2017. doi: 10.1039/C7TA06948K. 90, 93

[187] E Lewin, P O Å Persson, M Lattemann, M Stüber, M Gorgoi, A Sandell, C Ziebert, F Schäfers, W Braun, J Halbritter, S Ulrich, W Eberhardt, L Hultman, H Siegbahn, S Svensson, and U Jansson. On the origin of a third spectral component of C1s XPS-spectra for nc-TiC/a-C nanocomposite thin films. *Surface and Coatings Technology*, 202(15):3563–3570, 2008. ISSN 0257-8972. doi: https://doi.org/10.1016/j.surfcoat.2007.12.038. 90

[188] Jerry Pui Ho Li, Xiaohong Zhou, Yaoqi Pang, Liang Zhu, Evgeny I Vovk, Linna Cong, Alexander P van Bavel, Shenggang Li, and Yong Yang. Understanding of binding energy calibration in XPS of lanthanum oxide by in situ treatment. *Phys. Chem. Chem. Phys.*, 21(40):22351–22358, 2019. doi: 10.1039/C9CP04187G. 90

[189] Haoyu Zhang. Synthesis and Characterization of Fe3+ and CeO2 Co-decorated NiOOH Electrocatalysts Supported by Nickel Foam for the Oxygen Evolution Reaction. *International Journal of Electrochemical Science*, pages 6532–6545, 2019. doi: 10.20964/2019.07.52. 93

[190] Jinzhen Huang, Hongyuan Sheng, R. Dominic Ross, Jiecai Han, Xianjie Wang, Bo Song, and Song Jin. Modifying redox properties and local bonding of Co3O4 by CeO2 enhances oxygen evolution catalysis in acid. *Nature Communications*, 12(1), 2021. ISSN 20411723. doi: 10.1038/s41467-021-23390-8. 93

[191] Yanyan Li, Xinyu Zhang, and Zhiping Zheng. CeO2 Functionalized Cobalt Layered Double Hydroxide for Efficient Catalytic Oxygen-Evolving Reaction. *Small*, 18(17):2107594, 2022. doi: https://doi.org/10.1002/smll.202107594. 93

[192] Haizhen Wang, Xinqi Chen, Di Huang, Meng Zhou, Dong Ding, and Hongmei Luo. Cation Deficiency Tuning of LaCoO3 Perovskite as Bifunctional Oxygen Electrocatalyst. *ChemCatChem*, 12(10):2768–2775, 2020. doi: https://doi.org/10.1002/cctc.201902392. 93, 159

[193] Kun Liu, Zhuoya Zhu, Mengqi Jiang, Liangcheng Li, Linfei Ding, Meng Li, Dongmei Sun, Gaixiu Yang, Gengtao Fu, and Yawen Tang. Boosting Electrocatalytic Oxygen Evolution over Ce−Co9S8 Core–Shell Nanoneedle Arrays by Electronic and Architectural Dual Engineering. *Chemistry – A European Journal*, 28(32):e202200664, 2022. doi: https://doi.org/10.1002/chem.202200664. 97

[194] Tao Wang, Hao Chen, Zhenzhen Yang, Jiyuan Liang, and Sheng Dai. High-Entropy Perovskite Fluorides: A New Platform for Oxygen Evolution Catalysis. *Journal of the American Chemical Society*, 142(10):4550–4554, mar 2020. ISSN 0002-7863. doi: 10.1021/jacs.9b12377. 97, 160

[195] Sarah C Petitto, Erin M Marsh, Gregory A Carson, and Marjorie A Langell. Cobalt oxide surface chemistry: The interaction of CoO(100), Co3O4(110) and Co3O4(111) with oxygen and water. *Journal of Molecular Catalysis A: Chemical*, 281(1):49–58, 2008. ISSN 1381-1169. doi: https://doi.org/10.1016/j.molcata.2007.08.023. 97

[196] Kamalakannan Ranganathan, Andreia Morais, Isaac Nongwe, Claudia Longo, Ana F Nogueira, and Neil J Coville. Study of photoelectrochemical water splitting using composite films based on TiO2 nanoparticles and nitrogen or boron doped hollow carbon spheres as photoanodes. *Journal*

of Molecular Catalysis A: Chemical, 422:165–174, 2016. ISSN 1381-1169. doi: https://doi.org/10.1016/j.molcata.2015.10.024. 101

[197] Erik Lewin and P.O. Persson. On the origin of a third spectral component of C1s XPS-spectra for nc-TiC/a-C nanocomposite thin films. *Surface and Coatings Technology*, 202(15):3563–3570, 2008. ISSN 0257-8972. doi: https://doi.org/10.1016/j.surfcoat.2007.12.038. 101

[198] Charles C L McCrory, Suho Jung, Jonas C Peters, and Thomas F Jaramillo. Benchmarking Heterogeneous Electrocatalysts for the Oxygen Evolution Reaction. *Journal of the American Chemical Society*, 135(45):16977–16987, nov 2013. ISSN 0002-7863. doi: 10.1021/ja407115p. 108

[199] Ibrahim Munkaila Abdullahi and Manashi Nath. Molecular Cluster Complex of High-Valence Chromium Selenide Carbonyl as Effective Electrocatalyst for Water Oxidation. *Catalysts*, 13(4), 2023. ISSN 2073-4344. doi: 10.3390/catal13040721. 108

[200] Harry B Gray. Powering the planet with solar fuel. *Nature Chemistry*, 1(1):7, 2009. ISSN 1755-4349. doi: 10.1038/nchem.141. 137

[201] Jeferson A Dias, Marcos A S Andrade Jr, Hugo L S Santos, Márcio R Morelli, and Lucia H Mascaro. Lanthanum-Based Perovskites for Catalytic Oxygen Evolution Reaction. *ChemElectroChem*, 7(15):3173–3192, 2020. doi: https://doi.org/10.1002/celc.202000451. 137

[202] Bryan H R Suryanto, Yun Wang, Rosalie K Hocking, William Adamson, and Chuan Zhao. Overall electrochemical splitting of water at the heterogeneous interface of nickel and iron oxide. *Nature Communications*, 10(1):5599, 2019. ISSN 2041-1723. doi: 10.1038/s41467-019-13415-8. 137

[203] Sengeni Anantharaj, Sivasankara Rao Ede, Kuppan Sakthikumar, Kannimuthu Karthick, Soumyaranjan Mishra, and Subrata Kundu. Recent Trends

and Perspectives in Electrochemical Water Splitting with an Emphasis on Sulfide, Selenide, and Phosphide Catalysts of Fe, Co, and Ni: A Review. *ACS Catalysis*, 6(12):8069–8097, dec 2016. doi: 10.1021/acscatal.6b02479. 137

[204] Qiurong Shi, Chengzhou Zhu, Dan Du, and Yuehe Lin. Robust noble metal-based electrocatalysts for oxygen evolution reaction. *Chem. Soc. Rev.*, 48 (12):3181–3192, 2019. doi: 10.1039/C8CS00671G. 137

[205] Lei Xu, Qianqian Jiang, Zhaohui Xiao, Xingyue Li, Jia Huo, Shuangyin Wang, and Liming Dai. Plasma-Engraved Co3O4 Nanosheets with Oxygen Vacancies and High Surface Area for the Oxygen Evolution Reaction. *Angewandte Chemie International Edition*, 55(17):5277–5281, 2016. doi: https://doi.org/10.1002/anie.201600687. 137

[206] Linsey C Seitz, Colin F Dickens, Kazunori Nishio, Yasuyuki Hikita, Joseph Montoya, Andrew Doyle, Charlotte Kirk, Aleksandra Vojvodic, Harold Y Hwang, Jens K Norskov, and Thomas F Jaramillo. A highly active and stable IrO_x/SrIrO₃ catalyst for the oxygen evolution reaction. *Science*, 353(6303):1011–1014, 2016. doi: 10.1126/science.aaf5050. 137

[207] U Aarthi, Dhananjaya Shukla, S Rengaraj, and K Suresh Babu. Ordered to defect fluorite structural transition in Ce1-xNdxO2-δ system and its influence on ionic conductivity. *Journal of Alloys and Compounds*, 838:155534, 2020. ISSN 0925-8388. doi: https://doi.org/10.1016/j.jallcom.2020.155534. 137, 139

[208] Kaiyue Zhu, Fang Shi, Xuefeng Zhu, and Weishen Yang. The roles of oxygen vacancies in electrocatalytic oxygen evolution reaction. *Nano Energy*, 73: 104761, 2020. ISSN 2211-2855. doi: https://doi.org/10.1016/j.nanoen.2020.104761. 138, 151

[209] Elena Marelli, Jaume Gazquez, Emiliya Poghosyan, Elisabeth Müller, Dariusz J Gawryluk, Ekaterina Pomjakushina, Denis Sheptyakov, Cinthia Piamonteze, Dino Aegerter, Thomas J Schmidt, Marisa Medarde, and Emiliana Fabbri. Correlation between Oxygen Vacancies and Oxygen Evolution Reaction Activity for a Model Electrode: PrBaCo2O5+δ. *Angewandte Chemie International Edition*, 60(26):14609–14619, jun 2021. ISSN 1433-7851. doi: https://doi.org/10.1002/anie.202103151. 138, 151, 153, 155

[210] Yao Xiao, Yibo Wang, Meiling Xiao, Changpeng Liu, Shuai Hou, Junjie Ge, and Wei Xing. Regulating the pore structure and oxygen vacancies of cobaltosic oxide hollow dodecahedra for an enhanced oxygen evolution reaction. *NPG Asia Materials*, 12(1):73, 2020. ISSN 1884-4057. doi: 10.1038/s41427-020-00255-y. 138, 151

[211] Matthew Brahlek, Maria Gazda, Veerle Keppens, Alessandro R Mazza, Scott J McCormack, Aleksandra Mielewczyk-Gryń, Brianna Musico, Katharine Page, Christina M Rost, Susan B Sinnott, Cormac Toher, Thomas Z Ward, and Ayako Yamamoto. What is in a name: Defining "high entropy" oxides. *APL Materials*, 10(11):110902, 2022. doi: 10.1063/5.0122727. 138

[212] Andrew J Wright and Jian Luo. A step forward from high-entropy ceramics to compositionally complex ceramics: a new perspective. *Journal of Materials Science*, 55(23):9812–9827, 2020. ISSN 1573-4803. doi: 10.1007/s10853-020-04583-w. 138

[213] Mingede Qin, Heidy Vega, Dawei Zhang, Sarath Adapa, Andrew J Wright, Renkun Chen, and Jian Luo. 21-Component compositionally complex ceramics: Discovery of ultrahigh-entropy weberite and fergusonite phases and a pyrochlore-weberite transition. *Journal of Advanced Ceramics*, 11(4): 641–655, 2022. ISSN 2227-8508. doi: 10.1007/s40145-022-0575-5. 138

[214] Dawei Zhang, Héctor A De Santiago, Boyuan Xu, Cijie Liu, Jamie A Trindell, Wei Li, Jiyun Park, Mark A Rodriguez, Eric N Coker, Joshua D Sugar, Anthony H McDaniel, Stephan Lany, Liang Ma, Yi Wang, Gregory Collins, Hanchen Tian, Wenyuan Li, Yue Qi, Xingbo Liu, and Jian Luo. Compositionally Complex Perovskite Oxides for Solar Thermochemical Water Splitting. *Chemistry of Materials*, 35(5):1901–1915, mar 2023. ISSN 0897-4756. doi: 10.1021/acs.chemmater.2c03054. 138

[215] Min-Ju Choi, Le Wang, Kelsey A Stoerzinger, Sung-Yoon Chung, Scott A Chambers, and Yingge Du. Epitaxial Design of Complex Nickelates as Electrocatalysts for the Oxygen Evolution Reaction. *Advanced Energy Materials*, page 2300239, 2023. ISSN 1614-6832. doi: https://doi.org/10.1002/aenm.202300239. 138

[216] Ya-Rong Zheng, Min-Rui Gao, Qiang Gao, Hui-Hui Li, Jie Xu, Zhen-Yu Wu, and Shu-Hong Yu. An Efficient CeO2/CoSe2 Nanobelt Composite for Electrochemical Water Oxidation. *Small*, 11(2):182–188, 2015. doi: https://doi.org/10.1002/smll.201401423. 139

[217] Jia Wei Desmond Ng, Max García-Melchor, Michal Bajdich, Pongkarn Chakthranont, Charlotte Kirk, Aleksandra Vojvodic, and Thomas F Jaramillo. Gold-supported cerium-doped NiOx catalysts for water oxidation. *Nature Energy*, 1(5):16053, 2016. ISSN 2058-7546. doi: 10.1038/nenergy.2016.53. 139

[218] Taiwo Odedairo, Xuecheng Yan, Xiangdong Yao, Kostya (Ken) Ostrikov, and Zhonghua Zhu. Hexagonal Sphericon Hematite with High Performance for Water Oxidation. *Advanced Materials*, 29(46):1703792, 2017. doi: https://doi.org/10.1002/adma.201703792. 139

[219] M T McDonnell, D P Olds, K L Page, J C Neufeind, M G Tucker, J C Bilheux, W Zhou, and P F Peterson. ADDIE: ADvanced DIffraction

Environment – a software environment for analyzing neutron diffraction data. *Acta Crystallographica Section A*, A73:a377, may 2017. doi: 10.1107/S0108767317096325. 144

[220] Ibrahim Munkaila Abdullahi, Martin Langenderfer, Olga Shenderova, Nicholas Nunn, Marco D. Torelli, Catherine E. Johnson, and Vadym N. Mochalin. Explosive fragmentation of luminescent diamond particles. *Carbon*, 164:442–450, aug 2020. ISSN 0008-6223. doi: 10.1016/J.CARBON.2020.03.057. 144

[221] Joey A Lussier, Diego H P Souza, Pamela S Whitfield, and Mario Bieringer. Structural Competition and Reactivity of Rare-Earth Oxide Phases in YxPr2–xO3 ($0.05 \leq x \leq 0.80$). *Inorganic Chemistry*, 57(22):14106–14115, nov 2018. ISSN 0020-1669. doi: 10.1021/acs.inorgchem.8b01911. 148

[222] Takeshi Hagiwara, Zuiho Kyo, Akitaka Manabe, Hiroshi Yamamura, and Katsuhiro Nomura. Formation of C-type rare earth structures in the Ce1-xNdxO2-δ system: a factor in the decrease in oxide-ion conductivity. *Journal of the Ceramic Society of Japan*, 117:1306–1310, 2009. 148

[223] Liv-Elisif Kalland, Andreas Løken, Tor S Bjørheim, Reidar Haugsrud, and Truls Norby. Structure, hydration, and proton conductivity in 50CeO2 – La2Ce2O7 and Nd2Ce2O7 – and their solid solutions. *Solid State Ionics*, 354:115401, 2020. ISSN 0167-2738. doi: https://doi.org/10.1016/j.ssi.2020.115401. 148

[224] Jordi Ibáñez, Juan Ángel Sans, Vanesa Cuenca-Gotor, Robert Oliva, Óscar Gomis, Plácida Rodríguez-Hernández, Alfonso Muñoz, Ulises Rodríguez-Mendoza, Matías Velázquez, Philippe Veber, Catalin Popescu, and Francisco Javier Manjón. Structural and Lattice-Dynamical Properties of Tb2O3 under Compression: A Comparative Study with Rare Earth and

Related Sesquioxides. *Inorganic Chemistry*, 59(14):9648–9666, jul 2020. ISSN 0020-1669. doi: 10.1021/acs.inorgchem.0c00834. 148, 149

[225] Hiroaki Nitani, Takashi Nakagawa, Masaya Yamanouchi, Takahiro Osuki, Masato Yuya, and Takao A Yamamoto. XAFS and XRD study of ceria doped with Pr, Nd or Sm. *Materials Letters*, 58(15):2076–2081, 2004. ISSN 0167-577X. doi: https://doi.org/10.1016/j.matlet.2004.01.005. 149

[226] Alexander E Baranchikov, Olga S Polezhaeva, Vladimir K Ivanov, and Yuri D Tretyakov. Lattice expansion and oxygen non-stoichiometry of nanocrystalline ceria. *CrystEngComm*, 12(11):3531–3533, 2010. doi: 10.1039/C0CE00245C. 149

[227] Lan Chen, Pete Fleming, Virginia Morris, Justin D Holmes, and Michael A Morris. Size-Related Lattice Parameter Changes and Surface Defects in Ceria Nanocrystals. *The Journal of Physical Chemistry C*, 114(30):12909–12919, aug 2010. ISSN 1932-7447. doi: 10.1021/jp1031465. 149

[228] Jonathan E Spanier, Richard D Robinson, Feng Zhang, Siu-Wai Chan, and Irving P Herman. Size-dependent properties of CeO_{2-y} nanoparticles as studied by Raman scattering. *Phys. Rev. B*, 64(24):245407, nov 2001. doi: 10.1103/PhysRevB.64.245407. 151

[229] Takaaki Taniguchi, Tomoaki Watanabe, Naota Sugiyama, A K Subramani, Hajime Wagata, Nobuhiro Matsushita, and Masahiro Yoshimura. Identifying Defects in Ceria-Based Nanocrystals by UV Resonance Raman Spectroscopy. *The Journal of Physical Chemistry C*, 113(46):19789–19793, nov 2009. ISSN 1932-7447. doi: 10.1021/jp9049457. 151, 153

[230] A Nakajima, A Yoshihara, and M Ishigame. Defect-induced Raman spectra in doped CeO_2. *Phys. Rev. B*, 50(18):13297–13307, nov 1994. doi: 10.1103/PhysRevB.50.13297. 153

[231] Kun Liu, Zhuoya Zhu, Mengqi Jiang, Liangcheng Li, Linfei Ding, Meng Li, Dongmei Sun, Gaixiu Yang, Gengtao Fu, and Yawen Tang. Boosting Electrocatalytic Oxygen Evolution over Ce−Co9S8 Core–Shell Nanoneedle Arrays by Electronic and Architectural Dual Engineering. *Chemistry – A European Journal*, 28(32):e202200664, 2022. doi: https://doi.org/10.1002/chem.202200664. 153, 154, 155, 160

[232] Srijita Nundy, Dalibor Tatar, Jelena Kojčinović, Habib Ullah, Aritra Ghosh, Tapas Mallick, Rafael Meinusch, Bernd Smarsly, Asif Tahir, and Igor Djerdj. Bandgap Engineering in Novel Fluorite-Type Rare Earth High-Entropy Oxides (RE-HEOs) with Computational and Experimental Validation for Photocatalytic Water Splitting Applications. *Advanced Sustainable Systems*, 6, 2022. doi: 10.1002/adsu.202200067. 155

[233] Konstantin I. Maslakov, Yury A. Teterin, Aleksej J. Popel, Anton Yu Teterin, Kirill E. Ivanov, Stepan N. Kalmykov, Vladimir G. Petrov, Ross Springell, Thomas B. Scott, and Ian Farnan. XPS study of the surface chemistry of UO2 (111) single crystal film. *Applied Surface Science*, 433:582–588, mar 2018. ISSN 0169-4332. doi: 10.1016/J.APSUSC.2017.10.019. 155

[234] Yan Zhu, Nikhil Jain, Mantu Hudait, Deepam Maurya, Ronnie Varghese, and S.Jeba Priya. X-ray photoelectron spectroscopy analysis and band offset determination of CeO2 deposited on epitaxial (100), (110), and (111)Ge. *Journal of vacuum science and technology. B, Microelectronics and nanometer structures: processing, measurement, and phenomena: an official journal of the American Vacuum Society*, 32:–, 2014. doi: 10.1116/1.4862160. 155

[235] Yushuang Zhao, Ji-Guang Li, Mengxi Guo, and Xiaojing Yang. Structural and photoluminescent investigation of LTbH/LEuH nanosheets and their color-tunable colloidal hybrids. *J. Mater. Chem. C*, 1(22):3584–3592, 2013. doi: 10.1039/C3TC30205A. 156

[236] Yolimar Gil, Ricardo Costa de Santana, Andréa Simone Stucchi de Camargo, Leonnam Gotardo Merízio, Patricia Farías Carreño, Pablo Fuentealba, Jorge Manzur, and Evgenia Spodine. Dual visible and near-infrared luminescence in mononuclear macrocyclic erbium(iii) complexes via ligand and metal centred excitation. *Dalton Trans.*, 52(10):3158–3168, 2023. doi: 10.1039/D2DT03447F. 156

[237] Jiali Zhao, Chen Liu, Jinmei Li, Rui Wu, Jiaou Wang, Haijie Qian, Haizhong Guo, Jiankun Li, and Kurash Ibrahim. Oxygen vacancy induced electronic structure variation in the La0.2Sr0.8MnO3 thin film. *AIP Advances*, 9(5): 55208, 2019. doi: 10.1063/1.5088738. 157

[238] Sarah C. Petitto, Erin M. Marsh, Gregory A. Carson, and Marjorie A. Langell. Cobalt oxide surface chemistry: The interaction of CoO(1 0 0), Co3O4(1 1 0) and Co3O4(1 1 1) with oxygen and water. *Journal of Molecular Catalysis A: Chemical*, 281(1-2):49–58, feb 2008. ISSN 1381-1169. doi: 10.1016/J.MOLCATA.2007.08.023. 162

[239] A T Swesi, J Masud, and M Nath. Nickel selenide as a high-efficiency catalyst for oxygen evolution reaction. *Energy Environ. Sci.*, 9(5):1771–1782, 2016. doi: 10.1039/C5EE02463C. 165

Vita

Sreya Paladugu was born in Wisconsin, USA and grew up in India and China. She received her B.S. degree in Nanoscience at Virginia Tech in 2018, where her research focused on the mechanical and drug release properties of bio compatible polymer composites. She went on to pursue an integrated M.S. and Ph.D degree in Materials Science and Engineering at The University of Tennessee, Knoxville. Her dissertation is focused on understanding the structure-property relationships of metal oxide nanocatalysts.